The Dissertation Committee for Lauren Stafford Richardson Certifies that this is the approved version of the following dissertation:

Maintenance of fetal membrane integrity by cyclic cellular transitions during gestation and parturition

Committee:

Ramkumar Menon, Ph.D., Mentor

Richard Pyles, Ph.D., Committee chair

Hal Hawkins, MD, Ph.D.

Giulio Taglialatela, Ph.D.

Robert Taylor, MD, Ph.D.

Dean, Graduate School

Maintenance of fetal membrane integrity by cyclic cellular transitions during gestation and parturition

by

Lauren Stafford Richardson, B.S.

Dissertation

Presented to the Faculty of the Graduate School of

The University of Texas Medical Branch

in Partial Fulfillment

of the Requirements

for the Degree of

Doctor of Philosophy

The University of Texas Medical Branch

July, 2019

Dedication

This work is dedicated to my parents, Ben and Laura Stafford, and my husband, Alex Richardson, whose love, support, and faith in me allowed me to pursue my education.

This work is dedicated to my two grandmothers for motivating me to study cancer-related pathways and for inspiring me to pursue science.

Acknowledgments

I would like to thank my mentor, Dr. Ramkumar Menon, for allowing me the independence and resources to grow as a scientist, as well as the opportunity to present my work at national and international conferences. Without his guidance and supervision throughout my Ph.D. I would not have been able to achieve my goals. I would also like to thank the many individuals who assisted me in the laboratory, including all of the visiting and local graduate students, rotating maternal-fetal medical fellows, and technicians who contributed to this work mentally or physically. Additionally, thank you to my committee members who supported me throughout this process and who continue to help me refine my critical thinking skills. Many thanks to the predoctoral Environmental Toxicology Training Program (T32ES007254), which is supported by the National Institute of Environmental Health Sciences (NIEHS) for funding the last two years of my Ph.D. Lastly, I would like to thank my family and husband for their constant support and patience.

Maintenance of fetal membrane integrity by cyclic cellular transitions during gestation and parturition

Publication No._____

Lauren Richardson, Ph.D.

The University of Texas Medical Branch, 2019

Supervisor: Ramkumar Menon

Fetal membranes line the intra-uterine cavity and perform protective functions during pregnancy. Rupture of membranes before term is deemed 'catastrophic' and contributes to infection, preterm birth, and neonatal death. During gestation, membranes repair and remodel through a balanced collagenolytic process of the matrix. Individual sites of membrane remodeling have been identified and termed 'microfractures.' However, the roles of membrane cells, amnion epithelial (AEC) and mesenchymal (AMC), and their ability to migrate, insert themselves, and repair these damaged sites (e.g., microfractures) remains unclear. We report that injury to AECs forces proliferation and cellular transitions including epithelial-to-mesenchymal transition (EMT) during migration and the reverse (MET) during wound resealing. Multiple assays established that oxidative stress (OS) at term induces EMT, mediated in part by transforming growth factor beta 1 (TGF-β), TGF-β activated kinase binding protein (TAB1), and p38 mitogen-activated protein kinase (p38 MAPK) signaling in human and mice membranes. This process is balanced during gestation by progesterone (P4) which transitions 'reservoir' stromal AMCs into epithelial cells (MET) through its progesterone membrane receptor (PGRMC2) and c-Myc. We speculate, during pregnancy, fetal membrane cells alternatively undergo cyclic transitions (EMT-MET) to maintain membrane homeostasis. Overwhelming OS at term inhibits MET and promotes an overall mesenchymal phenotype by inducing a terminal state of EMT, senescence, and inflammation which contributes to labor initiation. An amnion membrane-organ-on-chip model corroborated these findings. Understanding cellular transitions and signaling mediators at term can help us derive novel therapeutic targets for preterm birth.

TABLE OF CONTENTS

List of Tables

List of Figures

List of Abbreviations

3D	3 Dimensional
3-NT	3-Nitrotyrosine
AEC	Amnion Epithelial Cells
AF	Amniotic Fluid
AMC	Amnion Mesenchymal Cells
AM-OOC	Amnion Membrane Organ-On-Chip
ASK	Apoptosis Signal-regulating Kinase
CD-1	Cluster of Differentiation 1
CK-18	Cytokeratin-18
CRH	Corticotrophin-Releasing Hormone
CSE	Cigarette Smoke Extract
D18	Day 18
D19	Day 19
DAMPs	Damage Associated Molecular Patterns
DMEM	Dulbecco's Modified Eagle's Medium
DNA	Deoxyribonucleic Acid
ECM	Extracellular Matrix
ELISA	Enzyme-Linked Immunosorbent Assay
EMT	Epithelial to Mesenchymal Transition
ERK	Extracellular Signal-Regulated Kinases
FITC	Fluorescein Isothiocyanate
FM-OO-C	Fetal Membrane Organ-On-Chip
GM-CSF	Granulocyte-Macrophage Colony-Stimulating Factor
HPA	Hypothalamic-Pituitary-Adrenal
IHC	Immunohistochemistry
IL-1β	Interleukin 1 Beta
IL-6	Interleukin 6
IL-8	Interleukin 8
IACUC	Institutional Animal Care and Use Committee
JNK	c-Jun N-terminal Kinases
MAPKK	Mitogen-Activated Protein Kinase Kinase
MAPKKK	Mitogen-Activated Protein Kinase Kinase Kinase
MET	Mesenchymal to Epithelial Transition
MMP9	Matrix Metallopeptidase 9
MPAM	Multiphoton Autofluorescent Microscopy
NAC	N-Acetyl-L-Cysteine
NADH	Nicotinamide Adenine Dinucleotide
NLOM	Nonlinear Optical Microscopy
NT siRNA	Non-Target Ribonucleic Acid
OC	Optical Clearing
OCT4	Octamer-Binding Transcription Factor 4
OOC	Organ-On-Chip

OS	Oxidative Stress
P0	Passage Zero
P1	Passage One
p38 MAPK	p38 Mitogen-Activated Protein Kinase
P4	Progesterone
PBS	Phosphate-Buffered Saline
PE	Preeclampsia
PFA	Paraformaldehyde
PGRMC1	Progesterone Receptor Membrane Component 1
PGRMC2	Progesterone Receptor Membrane Component 2
pPROM	Preterm Premature Rupture Of Membrane
PDMS	Polydimethylsiloxane
PTB	Preterm Birth
qRT-PCR	Quantitative Reverse Transcription Polymerase chain reaction
ROI	Region Of Interest
ROS	Reactive Oxygen Species
SASP	Senescence Associate Secretory Phenotype
SA-β-Gal	Senescence Associate Beta-Galactosidase
SB	SB203580
SD	Standard Deviation
SEM	Standard Error of the Mean
SHGM	Second Harmonic Generation Microscopy
siRNA	Small Interfering Ribonucleic Acid
SPTB	Spontaneous Preterm Birth
TAB1	TGF-beta Activated Kinase 1 Binding Protein
TAK1	TGF-beta Activated Kinase 1
TDE	2,2'-Thiodiethanol
TEM	Transmission Electron Microscopy
TGFR1	Transforming Growth Factor Receptor 1
TGF-β	Transforming Growth Factor Beta
TIMP	Tissue Inhibitor of Metalloproteinase
TL	Term Labor
TNF-α	Tumor Necrosis Factor Alpha
TNIL	Term Not In Labor
Trx	Thioredoxin
UTMB	University of Texas Medical Branch
ZEB1	Zinc Finger E-box Binding Homeobox 1

INTRODUCTION

Chapter 1. Background and significance

OVERVIEW OF HUMAN GESTATION

During human pregnancy, fetal development occurs inside the maternal uterine cavity for ~ 40 weeks ending in labor and delivery (parturition). This process begins with the fusion of male and female gametes which develop into a blastocyst containing two differentiated pluripotent cells types: 1) the inner mass cells (inside; fetal lineage), and 2) the trophoblast cells (outside), which will become the fetal membranes and placenta respectively [1]. These two cell types grow, differentiate, and are regulated by a variety of genetic, epigenetic, and environmental signals throughout gestation. Hormones like progesterone (P4) (a pro-gestational hormone)[2], estrogen (a pro-labor hormone) [3], and corticotrophin-releasing hormone (CRH) [3], all play vital roles in the stepwise development, maintenance, and delivery of fetal and placental tissues at term. Perturbation of intra-uterine tissue signaling, or functional roles, could lead to adverse pregnancy outcomes such as preterm birth (PTB) [4, 5]. PTB is defined as birth before 37 weeks gestation [6] and is a major pregnancy complication contributing to one million neonatal deaths/year around the globe [7].

PATHWAYS OF HUMAN LABOR

Both preterm and term deliveries are initiated by multiple endocrine and physiological factors operating together to control the timing and building of inflammation in utero, one of the key effectors of labor process. These pathways rely on both maternal and fetal components working in unison to initiate parturition (Fig. 1.1). Throughout pregnancy, the ovaries, placenta, and fetal membranes produce P4 helping maintain myometrium quiescence, promote uterine growth, and produce an anti-inflammatory environment [2]. However, closer to term the dynamic balance between P4 and estrogen switches to favor estrogen, promoting contractions and differential regulation of P4 receptors. This dynamic switch is aided by the fetal hypothalamus-pituitary-adrenal axis

(HPA) [3]. The HPA axis triggers a cascade of events that increase fetal cortisol levels, production of prostaglandins and cyclooxygenase-2 in the fetal membranes, and oxytocin receptors in the myometrium [8]. Additionally, mechanical stretch [9] and increased reactive oxygen species (ROS) levels are present in utero at term. ROS and HPA axis signaling, along with many other synergistic pathways increase inflammatory mediators in the intrauterine cavity that will be propagated to activate the decidua, induce a contractile state in the myometrium, and cause cervical ripening [2]. These well-coordinated events are prerequisite for labor at term.

PATHWAYS OF HUMAN LABOR: A FETAL PERSPECTIVE

Human labor has been well studied at the maternal tissue level as well as from the endocrine perspective as mentioned above. Besides, the fetal HPA axis, the contributions by the fetus are hardly been studied. Recently, fetal components of the intra-uterine cavity have also been shown to play an important role in human labor and delivery. Although it is clear that inflammation results from complex tissue-specific, molecular and cellular interactions, these are not well delineated in uterine tissues in the context of normal pregnancy and parturition. It is known that in normal pregnancy fetal hormones (CRH) [2, 8], surfactant protein-A [10], and brain-derived neurotrophic factor, released from a mature fetus, play a critical role in the priming of the intra-uterine cavity by increasing oxidative stress (OS). Recent data from our lab showed that term, non-laboring (TNIL), fetal membranes from human and murine models treated with cigarette smoke extract (CSE) (a potent OS inducer to mimic term labor [TL] signaling) produced ROS leading to a telomere-dependent activation of p38 mitogen-activated protein kinase (p38 MAPK) [11, 12]. Increased p38 MAPK activation at term causes fetal membrane senescence, or tissue aging, as well as secretion of senescence-associated secretory phenotypes (SASP) [13]. SASP represents sterile inflammation in fetal tissues that propagates to the maternal side and transition the quiescent myometrium and cervix into a contractile (active/labor) phenotype. By studying the fetal membranes throughout gestation and at term, researchers can delineate both fetal and maternal signals, and how they complement each other by overloading the inflammatory system to induce labor. Due to the impracticality of longitudinal fetal tissue samples from humans, animal models were used to delineate these

signals. Similarities in SASP and paracrine signaling mechanisms between human and mouse models allowed us to use murine models to study fetal membrane structure, function, remodeling, and molecular/cellular level changes associated with parturition [11, 14, 15].

FUNCTIONAL ROLE OF UTERINE TISSUES THROUGHOUT GESTATION AND AT TERM

The intra-uterine cavity is composed of both fetal and maternal tissues (Fig. 1.1) each with important roles contributing to the development and protection of the fetus [2]. Maternal tissues including the cervix, myometrium, decidualized endometrium, and vagina have been studied extensively in pregnant and non-pregnant conditions, while fetal compartments including the: fetal membranes, placenta, and umbilical cord have not been well studied as they are not accessible until after delivery. Fetal membranes are connected to the placenta and are an integral component of the uterine cavity, providing structural and mechanical support for the growing fetus until their disruption at term [9]. The fetal membranes are composed of amnion and chorion epithelial layers connected by a collagen-rich extracellular matrix (ECM) [16, 17]. While the placenta provides oxygen, nutrients, and filters waste from fetal blood [18], the fetal membranes provide mechanical, immune, and endocrine functions to contain and protect the fetus [19]. Thus, fetal membranes are unique in function and distinct from the placenta. The placenta is the most studied fetal tissue due to its functional significance, whereas the fetal membranes have hardly been studied at all. Thus, the fetal membranes will the focus of the work in this dissertation.

ROLE OF FETAL MEMBRANES THROUGHOUT GESTATION AND AT TERM

Fetal membranes develop alongside the fetus and become a fully formed amniochorionic membrane by 15 weeks gestation. Membranes provide mechanical support and compartmentalization for the developing fetus until their disruption at term [20-24]. Balanced collagenolytic remodeling is vital to maintain membrane homeostasis during pregnancy [25, 26]. ROS from intra-uterine redox reactions maintains their structural and functional integrity [27] until stress kinase p38 MAPK-mediated senescence is initiated as previously described [28]. However, significant knowledge gaps still exist in our understanding of senescence-associated inflammation at term and PTB [29]. Premature

activation of senescence in response to OS-inducing risk factors (i.e., infection, high body mass index, and stress) can trigger PTB [30-33]. Thus, the membranes play a vital role throughout gestation and in both term [10, 13, 34-36] and preterm [30, 37, 38] labor, but how the membranes maintain their integrity during pregnancy, and whether if senescence disrupts their equilibrium, remain unknown.

FETAL MEMBRANE MICROARCHITECTURE

Human fetal membranes (amniochorionic or placental membrane) are avascular and their structure is detailed in Figure 1.2. The amnion epithelial cell (AEC) layer (blue cell layer) is bathed in amniotic fluid (AF) and is a single layer of cuboidal epithelial cells held together by neighboring cell junctions [39, 40]. This layer is under constant turnover as epithelial cells shed forming gaps and fissures due to apoptosis [12, 26] or senescence [2, 13, 15, 41] throughout their lifetime. AECs secrete type IV collagen and glycoproteins, forming the basement membrane of the ECM (Fig. 1.2) [17, 22]. This type IV collagen rich basement membrane forms a junction and facilitates communication between the cellular and stromal layers.

Stromal cells, such as amnion mesenchymal cells (AMC) (purple cells), secrete various collagen types including type I and III, forming the compact and fibroblast layers of the ECM [17, 22, 42]. The fibroblast layer is connected to the spongy layer, which is made up of proteoglycans, glycoproteins and type III collagen, resulting in a spongy meshwork (black lines). The reticular layer, made up of fibrillar bundles of collagen [39], is attached to the spongy layer on its apical side, and the chorion on its basal side [17, 22]. The ECM layers, filled with AMCs, that can interact with each other, degrade collagen layers, and communicate with other cellular layers to help with fetal membrane remodeling. Due to their epiblast origin, amnion cells express pluripotency markers (Nanog/Octamer-binding Transcription Factor 4 [OCT4][43]) and are commonly used in other fields for treatment of healing wounds [44-47] due to their ability to differentiate [48, 49] into other tissues because of their pluripotency status. However, reproductive scientists have overlooked this characteristic and possible role in membrane remodeling during labor.

STUDY FOCUS – HOW FETAL MEMBRANE INTEGRITY MAINTAINS PREGNANCY AND HOW ITS PERTURBATION CONTRIBUTES TO PARTURITION

Acting as the fetal-maternal interface, the fetal membranes compartmentalize potential fetal or maternal threats (e.g., maternal infection, AF inflammatory cytokines) that could lead to pregnancy dysfunction if not contained. The amnion component of the fetal membrane predominantly contributes to this barrier function by 1) supporting the fetal and amniotic fluid load, 1) withstanding local deformation and mechanical stretch [23, 24, 50-53], 2) preserving an intact amnion epithelial layer [39], 3) testing the environment and responding to local insults (e.g., ROS), and 4) undergoing remodeling to maintain ECM homeostasis. All are critical for maintaining membrane integrity during pregnancy.

During gestation, membranes are repaired and remodeled through a balanced collagenolytic process of the ECM. However, the remodeling of cellular components (epithelial and mesenchymal layers) to fill any gaps or aberrations are not fully studied. The ability of amnion cells to migrate and insert themselves to repair damage in the membranes is unclear. Because remodeling is essential to maintain membrane homeostasis and protect pregnancy, understanding this process is critical for membrane integrity. Fetal membrane, like other tissues (e.g., intestine), is composed of an epithelial layer connected to an ECM that contains mesenchymal cells where ECM remodeling via cellular transitions have been well-reported [54-58]. However, though similar in structure and cellular turnovers, this phenomenon has not been studied in fetal membranes.

One form of cellular transitions is called epithelial to mesenchymal transitions (EMT), and it is defined as epithelial cells transitioning into mobile mesenchymal cells that can migrate and the remodel ECM [59-61]. This transition is important in wound healing and contributes pathologically to fibrosis and cancer progression [59-63]. This transition occurs by 1) loss of microvilli and epithelial adherence junctions between neighboring cells (e.g., switch from E-cadherin to N-cadherin adherence junctions), 2) disassociation of desmosomes, 3) cytoskeleton rearrangement (e.g., switch from cytokeratin to vimentin intermediate filaments), and 4) gain in migratory phenotype. Some of the central signaling pathways that cause EMT include upstream regulators [63-65]: Transforming growth factor beta (TGF-β), Notch1, inflammation, and tyrosine kinase receptors. Induction of mesenchymal transcription factors [60] including: Zinc Finger E-Box Binding Homeobox

1 (ZEB), TWIST, SNAIL and SLUG are also known to promote EMT. In AECs TGF-β has been shown to induce EMT by changes in E-cadherin/N-cadherin ratio [66]. Cellular senescence has also been linked to EMT suggesting this connection could be made in fetal membranes at term [67].

Amnion membranes have also been shown to have wound healing properties [44, 47, 68]. This is likely through mesenchymal to epithelial transitions (MET) [69-71]. Though mesenchymal stromal cells are known to be reservoir cells that help with wound healing and membrane maintenance in the intestines [54], reproductive health scientist have not looked at AMCs in this manner. It is likely that specific microenvironments can promote MET to fill gaps created by epithelial shedding by forcing AMCs to 1) form E-cadherin adhesive junctions, 2), rearrange their cytoskeleton, and 3) express microvilli [71]. During pregnancy, we speculate that P4 promotes MET as a part of pregnancy maintenance. Both types of transitions described above can promote cellular remodeling [39] and producing collagen to allow growth of membranes and stretch alongside the maturing fetus.

The cell and molecular mechanisms by which this multilayer tissue stretches and expands throughout gestation are still unknown, highlighting the importance of studying fetal membrane remodeling and its mediators. It has been well documented that membranes undergo biaxial stretch and strain as they expand throughout gestation and that uterine pressure induced distention which peaks at term [72, 73]. These physiological changes have been documented to upregulate several cytokines and matrix metalloproteinases [74] that can contribute to collagen degradation (e.g., collagen type I), SASP production, and membrane weakening. Traditionally, loss in ECM integrity or weakening has been thought to be initiated by cellular prostaglandin synthesis and metabolism [75-77]. Increase in the bioavailability of prostaglandins (i.e., prostaglandin E2, prostaglandin F2α) before initiation of labor has been reported in amnion membrane cells [78] and contributes to membrane ECM degradation at term. However, prostaglandins bioavailability alone is not sufficient to induce membrane weakening (e.g., prostaglandin induction of labor does not always work clinically). Therefore, additional mechanisms of ECM remodeling need to be investigated.

ECM remodeling is known to involve a balance of collagenolytic activity between matrix-degrading enzymes (e.g., matrix metallopeptidase 9 [MMP9]) and their inhibitors (e.g., Tissue inhibitor of metalloproteinase [TIMPs]), in order to maintain collagen homeostasis [25, 56, 57, 79-81]. A disruption in this homeostasis was recently documented by our lab with transmission electron microscopy (TEM) microscopy showing areas of altered cell morphology and ECM degradation. MMPs mediated controlled collagenolytic processes have been reported as one of the key mechanisms of membrane remodeling [81]. However, the mechanistic events leading to MMP activation is unclear. Herein, we postulate that cell injury and cellular level remodeling generates localized inflammation and promotes membrane restructuring that is critical for the maintenance of membrane integrity.

PRIOR WORK ON SENESCENCE DEVELOPMENT WHILE TRANSITIONING FROM TERM NOT IN LABOR TO LABOR

Recently, our lab has documented another labor-associated phenotype, cellular senescence (i.e., mechanism of aging), that contributes to membrane dysfunction at term. This process promotes the transition from a TNIL phenotype in the fetal membranes. At term, significant levels of OS along with decreased levels of maternal antioxidants increase inflammation and ROS in utero. TL fetal membranes compared to TNIL samples contained: 1) higher levels of protein, lipid, and deoxyribonucleic acid (DNA) oxidation, 2) rounded mitochondria and swollen endoplasmic reticulum, 3) shorter telomeres, 4) activation of stress response kinase p38 MAPK, 5) increased production of cell cycle inhibitors (e.g., p21, p19, p16), 6) contained senescence-associated-β-Galactosidase (SA-β-Gal) positive cells, 7) show loss of nuclear envelope proteins (e.g., laminin B1), and 8) increased production of SASP and damage associated molecular patterns (DAMPs)[4, 13]. Thus histologic and molecular evidence determined an association between senescence and term labor in human. Even though endocrine differences exist between human and mice parturition, OS-induced p38 MAPK mediated senescence is similar in both humans and in murine models [11, 14, 15].

At the cellular level, previous data shows that AECs [28], AMCs, and chorion cells treated with CSE [82], a well know OS inducer, lead to ROS build up and DNA damage.

This DNA damage is mostly made up of loss of 8-oxoG base pairs in the telomere region which causes cells to release DAMPs (e.g., high-mobility group box B 1, heat shock protein 70, and uric acid). DAMPs can cause tissue injury and enhance the inflammatory load of the uterine cavity [19, 83]. This induces stress-activated p38 MAPK via telomere-dependent DNA damage, causing fetal membrane cells to undergo senescence and secrete SASPs comprised of pro-inflammatory cytokines, chemokines, growth factors, and MMPs [15, 34, 83]. SASPs create an environment of sterile inflammation in the uterus and propagate the inflammatory signal to the maternal side contributing to labor initiation.

THE SIGNIFICANCE OF SENESCENCE AND FETAL MEMBRANE FUNCTIONS IN ADVERSE PREGNANCY OUTCOME

Annually, 15 million babies are born preterm (i.e., before 37 weeks gestation) around the world, affecting about 5-18% of pregnancies [6, 7, 84]. Despite the medical advancements in the country, one out of ten babies in the United States is born preterm [7]. PTB is one of the leading causes of death amongst neonates. Premature babies that survive have an increased risk of not only short-term complications such as respiratory distress [85], but also long-term complications including early onset diabetes, cardiovascular risks, various forms of cancers [6], neurodevelopmental disorders, and defects in vision and hearing.

Preterm labor can be induced, in cases of maternal-fetal complications during pregnancy (e.g., preeclampsia [PE]), or can be spontaneous, which is characterized by uterine contractions with (e.g., pPROM) or without early rupture of fetal membranes (e.g., SPTB). Fetal membrane rupture is described as ‘catastrophic’ tissue failure and a unique event occurring in normal term labor membranes; however, rupture preterm can result in adverse pregnancy outcomes such as increased fetal death as well as infection in mothers [73, 86]. Infection within the amniotic cavity, OS, mechanical pressure, or early separation of the placenta (i.e., placental abruption), can potentially activate early contractions of the uterus and cause subsequent delivery [87-90]. Though a common pathway of labor in humans has been speculated, the precise mechanism is still unclear which is why further examination of fetal membranes, including mechanisms of membrane remodeling, resealing, and the pathological processes of its absence are needed to better understand the

trigger for term parturition. Fetal membrane remodeling is a key event required throughout pregnancy [26] involving balanced collagenolytic activity between matrix-degrading enzymes and their inhibitors to maintain collagen homeostasis in the ECM [91]. Overwhelming collagenolytic activity and mechanical disruption collapse the integrity of membranes, predisposing them to pPROM. Though the mechanism triggering term and preterm parturition is still unidentified, failure to remodel fetal membranes and dysfunctional status could play a critical role in increasing the inflammatory load throughout gestation. Premature senescence activation of the fetal membranes in response to pregnancy-associated risk factors has been reported as one of the key initiators of SPTB and pPROM.

THE RELEVANCE OF THIS STUDY

Physiologic labor activation at term (e.g., fetal signals of organ maturity, fetal and maternal endocrine factors, and immune cell activation) or preterm (e.g., infection-associated inflammation, sterile inflammation, and/or OS) propagates parturition associated signal cascades, increases inflammation, activates the myometrium, and cumulates in labor and delivery [2]. Over the last decade, clinical trials and treatments with P4 to inhibit inflammation [92], tocolytics to inhibit myometrial contacts [93, 94], or antioxidants to reduce OS [95] have not decreased the rate of PTB. Therefore, a better understanding of labor-associated cellular changes might provide new targets for clinical intervention.

Specifically, at term, fetal membranes undergo OS-induced, p38MAPK-mediated senescence, and generate inflammation to promote labor and delivery. Thus, fetal membranes play a critical role during parturition. Throughout gestation, membranes repair and remodel through a balanced collagenolytic process of the matrix. However, the role of amnion membrane cells to repair sites of damage through cellular transitions (e.g., EMT-MET) remains unclear. As remodeling is essential to maintain membrane homeostasis and protect pregnancy, understanding this process is critical.

Therefore, we hypothesize that during pregnancy, fetal membrane cells are plastic and alternatively undergo cyclic transition (EMT-MET) to maintain membrane homeostasis via a balance between TGF-β and P4 pathways. Overwhelming OS at term

drives the former pathway, leading to p38MAPK-mediated senescence, an irreversible state of EMT, and inflammation to promote labor. The following three aims will determine the contributions of cellular transitions, specifically EMT and MET, in membrane remodeling throughout gestation and its disruption at term:

Specific Aim 1: To characterize histological changes associated with fetal membranes and to determine cytological and extracellular level matrix aberrations as functional areas of membrane remodeling in normal pregnancy and sites of membrane dysfunction in pathologic pregnancies.

To identify, quantify, and characterize areas of cell shedding and matrix degradation as functional areas of fetal membrane remodeling in normal term membranes (***Sub Aim 1)*** and as areas of remodeling failure in preterm delivered membranes (***Sub Aim 2)*** using MPAM/SHGM. To recreate histological changes associated with fetal membrane remodeling in vitro using normal TNIL fetal membranes maintained under normal and OS environment that mimic pregnancy and parturition respectively (***Sub Aim 3)***.

Specific Aim #2: To determine cellular and molecular level changes associated with fetal membrane remodeling through cellular proliferation and transitions during pregnancy and parturition.

To determine mediators of cyclic transitions of amnion membrane cells, TGF-β-induced EMT in AECs and P4-mediated MET in AMCs, in *in vitro* conditions often associated with pregnancy (***Sub Aim 1)*** and under OS conditions often associated with parturition (***Sub Aim 2)***.

Specific Aim #3: To overcome limitations of the 2D cell culture system (Aims 1 and 2), which lacks intercellular and cell-environmental interactions, this aim intends to recreate the entire amnion membrane in an organ-on-chip in order to study the transitioning properties of amnion cells in a co-culture environment.

To determine the role of intercellular and cell-environmental interactions impacting amnion cell migration and cyclic transitions in an amnion membrane organ-on-chip under normal cell culture conditions mimicking pregnancy (***Sub Aim 1)*** and under OS conditions mimicking parturition (***Sub Aim 2)***.

This study is poised to discover a novel labor initiation mechanism mediated by fetal membrane senescence, regulation of cellular transitions, and inflammation. The nodes identified along these signaling pathways are candidate targets for the prevention of preterm labor pathways initiated by OS and inflammation.

A

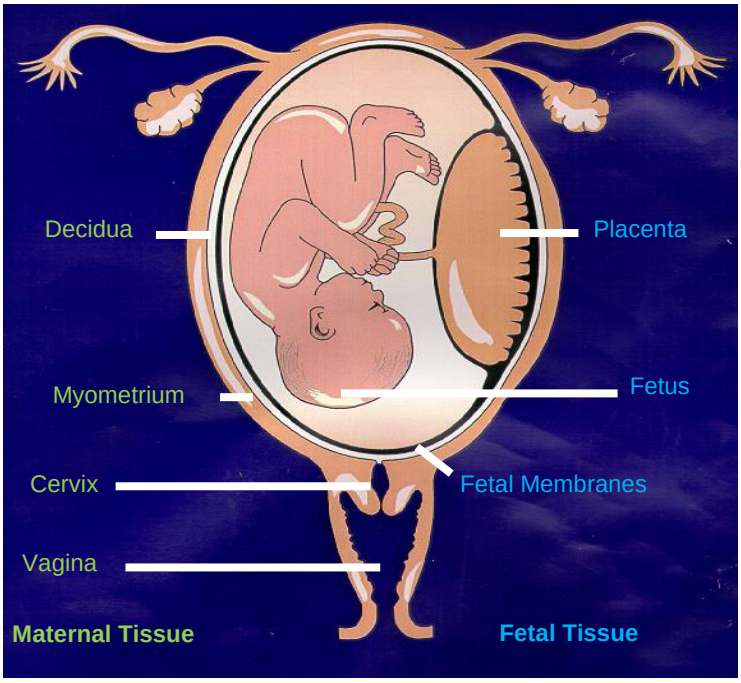

Figure 1.1: Intra-uterine tissues anatomy

A) A cartoon representation of the intra-uterine tissues broken down into maternal and fetal components. Maternal tissues (in green) comprised of: decidua (white line), myometrium (orange line), and cervix and vagina on the left hand side of the image, while the fetal tissues (blue) inducing: placenta (orange tissue), fetus, and fetal membranes (black line) are located on the right side of the image.

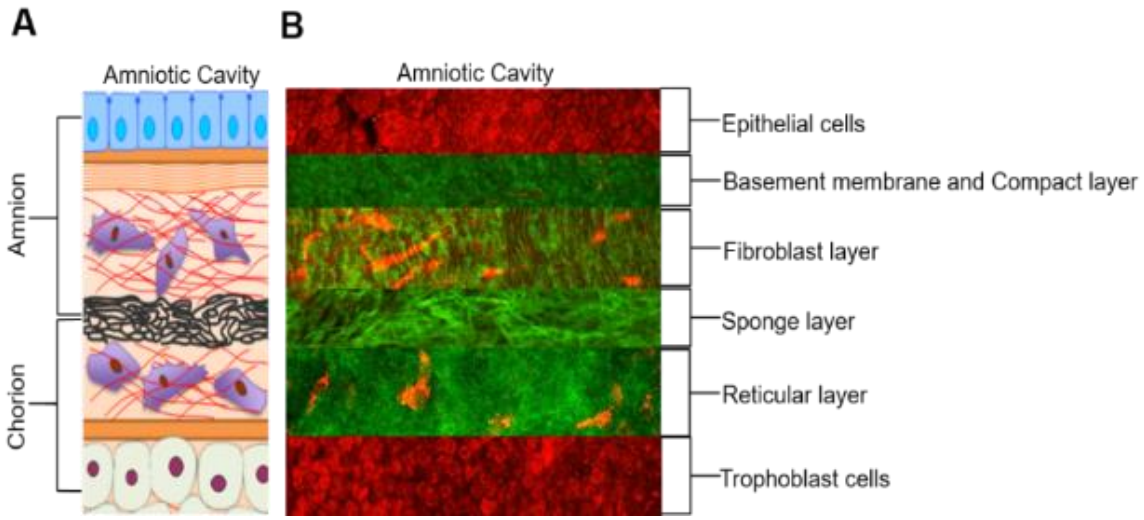

Figure 1.2 Fetal membrane structure

A) Cartoon representation of fetal membranes. Description will start from the inner most layer (amnion) facing the amniotic cavity and end with chorion. AEC (blue) are connected to the first layer of the ECM called the basement membrane (orange)/ compact layer (orange strips). The fibroblast (top red), spongy (black), and reticular layers (bottom red) follow, containing stromal cells (purple). The chorion (yellow) is connected to the ECM through a basement membrane (orange). B) MPAM (red) shows cuboidal AEC in a monolayer attached to the basement membrane in green as delineated by second harmonic generation microscopy. The layers of the ECM (green) including the basement membrane/compact layer, fibroblast, spongy, and reticular layers exhibit unique collagen characteristics and contain stromal cells (red). Chorion trophoblast cells (red) are connected to the ECM[39].

What other cellular levels changes are occurring in senescent fetal membranes?

Prior to our work with advanced microscopy techniques, TEM was used to study OS and labor associated changes in human fetal membranes. TL fetal membrane explants exhibit unique aging features compared to TNIL. At the organelle level, TEM microscopy showed swollen mitochondria and endoplasmic reticulum suggestive of senescence-associated changes [13]. However, at the cellular level, OS-treated AECs expressed desmosome and morphology changes. Morphometric AEC changes included a reduction in height and an increase in width (i.e., elongation), compared to non-treated explants. AECs altered morphology also correlated with regions of collagen degradation in the ECM.

Results from these studies, which are typically not senescence-associated changes, prompted further analysis of TL and OS treated fetal membrane explants. Due to fetal membrane thickness, most microscopy techniques require sliced or 'sectioned' samples in order to visualize amniochorion layers. However, tissue processing can skew the interpretation of cell-cell and cell-collagen interactions by only studying a single plane. Instead, fetal membrane analysis was conducted using a deep imaging advanced microscopy method called nonlinear optical miscopy (NLOM) which allows for whole membrane visualization. Specifically, multiphoton autofluorescence microscopy (MPAM) and second harmonic generation microscopy (SHGM) were used to visualize cellular and ECM components of full thickness, unsliced, fetal membranes (amnion-chorion-decidua) (**Chapter 2**). Additional methods were adapted from other fields to create novel techniques for imaging. By conducting 'image tiling' and 'optical clearing' whole 6mm full thickness explants could be visualized for the first time.

Once these methods were validated (**Chapter 2**)[39] we were able to study additional cellular level changes occurring in senescent fetal membranes at cell-cell and cell-collagen interfaces (**Chapter 3**)[96]. The results of these studies will contribute to an overall better understanding of micro-architecture as well as OS-labor associated morphology changes in fetal membranes.

Chapter 2. Redefining 3 dimensional placental membrane microarchitecture using multiphoton microscopy and optical clearing [39]

INTRODUCTION

Placental membranes (amniochorionic membranes or fetal membranes) are the innermost lining of the intra-uterine cavity that protects the fetus during pregnancy. These avascular membranes are composed of simple cuboidal amnion epithelium, multilayered ECM, and the chorion, which connects to the maternal decidua [16, 17]. Membranes are fully formed by week 15; however, they undergo constant remodeling throughout gestation involving collagen metabolism to maintain structural and functional homeostasis [26]. The amnion layer is the most elastic component of the placental membranes, and its remodeling is essential to maintain membrane integrity. During the remodeling process throughout gestation, epithelial cells are likely shed and replaced, and the basement membrane is replaced with nascent type IV collagen [22]. A shedding cell in a tissue is defined by the loosening of its junctions with its neighboring cells and basement membrane, leading to its expulsion and the development of a gap [97]. These gaps appear as areas of smooth basement membrane void of cellular components. Shedding and gap formation are well reported in intestinal epithelial cells [97, 98] as a part of remodeling of this tissue, and overwhelming shedding is linked to pathologic conditions, such as Crohn's disease [99]. We speculate that epithelial cell shedding, gap formation and resealing with new cells and nascent collagen are a part of tissue remodeling throughout pregnancy. Previous imaging studies using fetal membrane tissues after term deliveries have not reported well-defined shedding or gap formation, possibly because they are unlikely to be detected using thin 4-

10μm single-plane transverse views in histological or immunohistological methods. Limitations of advanced microscopic approaches (e.g., high-resolution imaging like confocal fluorescence microscopy or optical coherence tomography) also make it hard to study shedding and gap formation. To overcome some of the limitations of current methodologies and better understand shedding, gap formation, and other structural changes to the membrane, we used the NLOM method of MPAM and SHG microscopy. This approach provides imaging of tissues to hundreds of micrometers in depth, with a subcellular resolution comparable to confocal microscopy [100]. A significant advantage of MPAM and SHG is that they can provide label-free images of cells/tissues through the collection of intrinsic signals (e.g., autofluorescence) [101], useful in cases where full depth labeling is a challenge. Optical clearing (OC) is a process that renders tissue optically transparent and can be used to extend the imaging depth of microscopy. A variety of OC protocols have been reported [102-104], though to our current knowledge, no studies of OC in the placental membrane have been reported.

The primary objective of this study was to visualize and study membrane architecture at term fetal membranes using MPAM/SHG to better understand structural changes. Additionally, OC was used to render tissues optically transparent/clear to extend the depth of imaging by microscopy. MPAM/SHG with and without OC was used to reconstruct the multilayered three dimensional (3D) micro-organization of human placental membranes without the use of exogenous contrast agents.

MATERIALS AND METHODS

Placental samples were collected for this study from John Sealy Hospital at The University of Texas Medical Branch (UTMB) at Galveston, TX, USA under a discarded tissue IRB (institutional review board) protocol. The study protocol was submitted and approved by the IRB at UTMB (UTMB, Galveston, TX; protocol 11- 251).

Fetal membrane collection for multiphoton microscopy analysis

Placental membranes (combined amniochorion and decidua) were collected from TNIL cesarean deliveries (N=7) with no documented pregnancy complications. Placental membranes were dissected from the placenta, washed three times in normal saline, and cleansed of blood clots using cotton gauze. Six-millimeter biopsies (explants) were then cut from the midzone portion of the membranes, avoiding the regions overlying the cervix or placenta. Explants were stored in 500mL of 10% formalin in 1.5mL Eppendorf tubes until imaging.

MPAM/SHG of membrane explants

In this study, the combined methods of MPAM and SHG were applied to investigate the multilayered 3D micro-organization of human placental membranes without the use of exogenous contrast agents. The primary fluorophores collected in MPAM are the reduced form of nicotinamide adenine dinucleotide (NADH) and flavin adenine dinucleotides [101]. SHG arises from noncentrosymmetric molecules, including fibrillar collagen of the ECM, and has been applied for evaluating ECM organization in the placental membranes, but has not been combined with MPAM to our current knowledge. MPAM and SHG were conducted using a Prairie Ultima IV (Prairie Technologies/Bruker, Middleton, WI) upright microscope using excitation from a Ti:sapphire femtosecond laser (Mai Tai, Spectra-Physics, Santa Clara CA) (Fig. 1.1A). A 25x objective with 1.05NA. (XLPlanN, Olympus, Tokyo, Japan) was used for image collection. Samples were illuminated at 840nm for generation of both MPAM fluorescence and SHG, collected in a backscattering (epi-illumination) geometry. A 500nm dichroic mirror in the detection path split autofluorescence emission (>500nm) from SHG (centered at 420nm), and MPAM/SHG were collected simultaneously in a two-channel configuration. Gallium arsenide phosphide photo-multiplier tube detectors were used (Hamamatsu, Japan). For mounting, the tissue was placed with the amnion side facing a #1.5 cover glass in a mounting chamber (30mm cage platedThorLabs, Newton, NJ), with a second cover-glass

placed on the chorion side; 300mL of phosphate-buffered saline (PBS) was added to the tissue, and the coverslips were tightened to secure the PBS and tissue in the imaging chamber. The amnion layer was then oriented toward the objective on the up-right microscope and centered with the help of an aiming beam from the excitation source. Regions of interest (ROI) were obtained (1s per frame; 512x512). Depth scans were obtained using a z-interval of 1µm, with an imaging depth ranging from 110 to 400µm (Fig. 1.1D). Images were obtained using a digital zoom factor of 1.19 resulting in a field-of-view of 408x408µm. Image stacks were analyzed for epithelial characteristics, including morphology, shedding, gaps, the thickness of layers, and collagen alterations using ImageJ/FIJI (NIH) software, while IMARIS (Bitplane, Concord, MA) was used for 3D reconstructions of MPAM/SHG stacks (Fig. 1.1E). Imaging of the full explants in some samples was accomplished using image mosaic tiling (Fig. 1.1B). In these cases, z-stacks were obtained using a 10x (0.3NA) objective (UPlanFI, Olympus) with a z-interval of 2µm. An overlap region of 10% was used between acquired z-stacks (tiles) of the mosaic for optimal stitching between neighboring regions (Fig. 1.1C).

MPAM/SHG mosaic tiling of full intact explants

We characterized the amnion layer with MPAM and SHG and specifically examined cellular and matrix morphology characteristics (at the epithelial-connective tissue interface, then beyond into the matrix layers). Besides imaging of innate placental membranes, we explored the possibility of extended depth of imaging after OC. Using intact placental membranes, we optically cleared the tissue with 2,2'-thiodiethanol (TDE; described below). We employed mosaic tiling as employed similar to the Tadokoro study, in which mosaic tiling was applied to the uterine horn [105]. For acquisition of images to encompass the full lateral dimension of intact explants, z-stacks were taken across a predetermined grid of the sample using the 10x objective, with neighboring regions sampled in a mosaic configuration (Fig. 1.1B). The mosaic was reconstructed using a

custom algorithm. An overlap of 10% (controlled during acquisition) was used between neighboring fields for optimal stitching of adjacent regions. The grid was initiated at the upper left corner, and it progressed in the positive "x" direction. A grid size of 5x5 images was used to acquire images across the full explants. To account for topography, the full depth of z-stacks was set large enough to capture the surface and at least 350µm below the surface across the full sample. After the grid was set for the entire area of imaging, each grid was checked to ensure the XYZ-axis coordinates were appropriate. The same filter cube and filters for single z-stacks, as described above, were used for mosaic tiling using an average dwell time of 5.2µs and z-step size of 2µm.

Epithelial shedding and identification of epithelial gaps

MPAM/SHG z-stack images of placental membranes were examined for epithelial cell characteristics. Sites of epithelial shedding were identified by a dark area either due to missing cells or cells attached to the ECM because they were displaced from intact membranes [97]. Epithelial gaps were identified by empty areas in the amnion epithelial layer and contained organized collagen underneath, which was visible from the surface due to the gap. Analyses were carried out on two different sets of placental membranes with two ROIs obtained per explant. ROIs were assessed for the presence of epithelial shedding and gaps separately, and samples were marked positive if they contained one or more of these features. Results were then recorded showing the number of positive images for epithelial shedding and gaps per every ten images evaluated.

OC of fetal membranes

OC of whole tissue explants was performed by incubation of fixed fetal membrane explants in TDE (refractive index 1.52; Sigma-Aldrich St. Louis, MO). TDE solutions (50% and 100% [w/w]) were prepared in Milli-Q water at room temperature. Fixed tissue was completely immersed in 50% TDE for 2 hours and then in 100% TDE overnight at

room temperature. Samples were then switched to fresh 100% TDE for mounting and imaging as described above. OC allowed visualization of amniochorion along with maternal decidua to be studied as a single unit structure in vitro.

Measuring layer thickness with MPAM and SHG

MPAM/SHG z-stack images of native placental membranes were analyzed in ImageJ for the average thickness of each of the following layers: amnion epithelium, basement membrane compact layer, fibrous layer, spongy layer, and reticular layer. In this approach, individual image planes were observed in depth for observed transitions between layers based on observed collagen morphological shifts, and the distance between transitions was used to determine individual layer thickness. We termed this measurement approach "morphologic analysis" below. Additionally, the full thickness was measured in orthogonal views using ImageJ with the help of a line measurement tool. An average of six measurements was taken along the membranes of each sample in both cases and compared to immunohistochemistry (IHC) measurements. These measurements were performed on five separate placental membranes, and the averages were taken.

Trichrome staining for collagen

Tissue sections were fixed in 4% paraformaldehyde (PFA) for 48 hours and embedded in paraffin. Sections were cut at 5mm thickness and adhered to a positively charged slide and attached by keeping them at 57ºC for 45 min. Slides were deparaffinized using Xylene and rehydrated with 100% alcohol, 95% alcohol, and normal saline (pH 7.4) and stained using the Masson Trichrome method to identify collagen components. The amnion epithelium was identified by a single layer of cells, while the ECM was identified as the area in between the amnion epithelium and the chorion layer. Single microscopic fields were captured. The thicknesses of the amnion epithelium and layers of the ECM were measured using a scale bar and line tool across the layers.

Analysis and statistics

Comparisons were made between thicknesses obtained by IHC and MPAM/SHG. SPSS software (IBM, Armonk, NY) was used for statistical evaluation. IHC and MPAM/SHG sample thicknesses were analyzed using the Kruskal-Wallis Assigned Ranks test with a P value less than 0.05 considered statistically significant.

RESULTS

Placental membrane architecture as determined by MPAM/SHG

The combination of MPAM and SHG imaging allowed us to reconstruct the multilayered architecture of placental membranes as shown in Figure 2.2 Autofluorescence resulting from endogenous cytoplasmic fluorophores (primarily NADH) from cells and matrix (determined by MPAM in red) permitted delineation of the highly cellular amnion and chorion layers as well as identification of mesenchymal cells in the ECM. SHG, shown in green, resulted from fibrillar collagen in the ECM layers. Importantly, the combination of MPAM with SHG depicted the basement membrane and compact layers where the amnion interfaces with the underlying ECM. The depth of imaging provided by MPAM/SHG in native explants allowed assessment beyond the reticular layer. By separating the co-registered MPAM and SHG signals (Fig. 2.2; middle and right columns), the architecture of the individual components comprising various cell and distinct matrix layers was gained, which included 1) the topography of the amnion epithelium, 2) morphology shifts in collagen structure that occur from one ECM layer to the next, 3) the cellular morphology of epithelial and stromal cells, and 4) variations in the stromal cells in the various matrix layers (Fig. 2.2B and C). The 3D reconstruction of a full image stack shown in Figure 2.2 with MPAM and SHG co-registration was obtained using IMARIS software, which provided a volumetric view of the placental membranes and the individual layers up to the reticular layer (Fig. 2.2D).

MPAM of amnion epithelium reveals shedding and gaps

The characterization of the amnion epithelium revealed tightly packed cuboidal epithelial cells that occasionally contained sites of epithelial shedding (Fig. 2.3A) and epithelial gaps, in which the underlying ECM was visible (Fig. 2.3B). The dark areas shown in Figure 2.3 were attributed to shedding created either by vacated cells or detachment of cells that have once migrated. IMARIS was used to identify both the loss cells in epithelial shedding (Fig. 3.3A2) and the areas of smooth uniform collagen that define the lower surface of epithelial gaps (Fig. 3.3B2). Unpublished data showed an increasing trend in the number of epithelial gaps and shedding found in laboring membranes suggesting its relevance in parturition.

SHG reveals ECM layers

Samples of membranes were further analyzed with SHG and compared to trichrome staining for collagen (Fig. 2.4). In both the trichrome and the SHG images, the basement membrane and compact layers showed tightly packed organized collagen forming a tight interface between the epithelial and the mesenchymal cells of the matrix. In the fibrous layer, the collagen wave amplitudes begin to increase and continue to increase in the spongy layer, in which we saw small tightly compacted collagen waves, represented in both trichrome and SHG. In the reticular layer, the morphology shifted to larger more diffuse bundles of collagen forming, large wave amplitudes visualized in both methods.

Quantitation of ECM layer thickness

MPAM and SHG (NLOM) were used for qualitative and quantitative studies. Statistical analysis showed that fixed vs. live tissue samples (20%) were not statistically different relative to the loss of shrinkage affecting fixed tissues full thickness (amnion through ECM) ($P=0.770$). Following this analysis, we measured the average thickness of native (not cleared) fixed membranes and individual layers designated by morphology

along with the overall thickness measured by orthogonal view analysis (Table 1). We report that the morphologic, orthogonal view and IHC thicknesses did not show any significant difference in thickness (P=0.775). This observation further verified that our methods of morphologic and orthogonal view measurements are accurate for measuring fixed tissue with NLOM.

Full-depth imaging using optical clearing

To visualize the complete full-thickness fetal membrane structure, OC was applied to placental membranes before imaging by MPAM/SHG, which allowed us to view the overall topography (comparable to native tissue), additional cellular details, and matrix interfaces (Fig. 2.5). The general topography and integration of all fetal membrane layers remained the same as the native tissue (Fig. 2.5A), including the cellular and matrix interfaces of the basement membrane and compact layer and the fibrous, spongy, and reticular layers. Overall, the characteristics of the cellular layers, shedding and gaps were not altered by the image clearing process (Sup. Fig. 2.1A-B). However, using this technique enhanced the depth of imaging and improved details to visualize cellularity at deeper layers.

Chorion morphology

OC facilitated visualization of the chorion portion of the membranes. This method provided detailed cellularity of the chorion next to its basement membrane (at 114μm depth) and revealed no areas of shedding or gaps as seen in the amnion epithelial layer. Separation and enlargement of chorionic trophoblast cells close to the decidua (Fig. 2.5C) wew also evident here, though in the native (noncleared) explants limited depth of imaging precluded this observation.

Decidual morphology

In addition to examining amnion, chorion, and their ECM, OC also allowed us to examine decidual cells due to the enhanced imaging depth. Imaging of the decidua revealed large elongated cells with mesenchymal-like morphologies normally too deep to visualize in native explants. A comparison of the orthogonal view of native (Fig. 2.5D) and cleared (Fig. 2.5E) placental membranes are shown to document the impact that OC can have on revealing deep levels of cellularity in tissues.

MPAM/SHG mosaic tiling for imaging of full diameter native explants

MPAM and SHG were also used to scan an entire 6mm native explant to demonstrate the advantages of mosaic tiling when studying placental membranes (Fig. 2.6). Though time-consuming, MPAM and SHG have the capability to scan and collect z-stacks across a set area to create full 3D representations of a biopsy (Fig. 2.6A and B). This technique allowed overall analysis of apical epithelium and matrix layers as well as the ability to examine the individual fields of view for a closer look at the topography or cell-to-matrix interactions (Fig. 2.6A1 and 6B1).

DISCUSSION

This study demonstrated the usefulness of MPAM/SHG imaging to reveal the complex, multilayered organization of the placental membranes, with attention to cellular and extracellular organization. We determined the following: 1) MPAM revealed the overall topography of AEC and visualization of epithelial shedding with visible gaps in the amnion layer; 2) SHG revealed fibrillar collagen organization throughout the ECM, making it possible to determine individual layer transitions and thicknesses showing a high degree of agreement with histology; 3) there was a lack of any visual evidence of cell shedding and gaps in chorion and 4) OC prior to microscopy determined full-depth imaging (visualization of the full thickness amniochorion as well as decidua); 5) Mosaic tiling of MPAM/SHG image stacks captured entire 6mm biopsies of the placental membranes.

While SHG has been applied in a number of studies to examine fetal membrane ECM characteristics [23, 50, 52, 106], we are unaware of any studies using MPAM in placental membranes. The combined contrast provided by MPAM based on intrinsic autofluorescence and SHG presents a new way to examine the 3D multilayered tissue characteristics. This approach is expected to help future examination of placental membranes, including examining mechanisms of membrane remodeling, resealing, and pathological processes, in which membrane remodeling and resealing are ineffective, causing adverse pregnancy outcomes.

This approach provided several advantages over routinely used methods. High-resolution imaging approaches, such as confocal fluorescence microscopy or optical coherence tomography, offer an alternate approach to study intact biopsies without sectioning or disrupting the multilayered tissue. These approaches have provided multilayer assessment of ex vivo fetal membrane [40]. However, the resolution of 10μm provided by optical coherence tomography is not sufficient for resolving cellular detail or epithelial shedding/gap closure. Confocal microscopy provides subcellular resolution of microscopic structure and cellular and molecular composition [107]. The depth of imaging, however, is limited to tens of microns, so deep tissue images of the multilayer fetal membrane are difficult to obtain. Confocal fluorescence microscopy also requires the use of a fluorophore for contrast [101]. Further, distinct signals from cellular vs. ECM collagen components is not possible with confocal microscopy and a unique characteristic of MPAM-SHGM.

The use of NLOM to visualize cellular (MPAM) and collagen (SHG) signals in whole tissue is an idea that has been around since the late 1990s in many fields of medicine [108-112]; however, only in the last few years, NLOM has been utilized to study the placenta and membranes. Recently, SHG and multiphoton microscopy using exogenous labels (DAPI to label cell nuclei) have been used to study mechanical tension-strain [51] and cyclic stretch [50] of the ECM in placental membranes. This technique helps to

determine collagen deformation. MPAM/SHG also allows for thickness measurements of individual layers (Table 1) and, in cases where changes are expected, could provide an indication of cellular density and migration. There are no set standards in the literature to measure membrane thickness, and different investigators prefer to test different sampling locations (Zone of Altered Morphology, peri-placental, cervical, midzone, or reflective membranes), group different layers, and analyze different tissue states (fixed or Ringer's lactate solution) [23, 50, 51, 106].

The technique described here could be used for measuring membranes thickness due to its unique ability to capture images at great depths [113]. Although we used fixed tissue for this study, this method applies to fresh specimens, except the OC by TDE, and is being explored. However, in the case of fresh samples, a live tissue OC approach, such as that previously used by our group in vivo for other epithelial tissues, could be applied and is being explored [114, 115]. In situ imaging of live explants by MPAM/SHG could be a very powerful approach to visualize longitudinal events, such as the migration of cells and remodeling of the ECM, as may occur with perturbation modeling gestational or pathologic conditions that can lead to PTB or other adverse pregnancy events.

This study did not examine the physiologic or pathologic changes associated with placental membranes at term. We used midzone portions of the membranes to characterize membrane architecture as this area has minimal alterations due to other confounding factors and avoided well-reported structural changes, such as the zone of altered morphology [116]. We incorporated mosaic tiling of MPAM/SHG image stacks to provide more comprehensive assessment across the whole membrane, demonstrating the potential to capture much greater depth of fetal membrane tissue by microscopy than has previously been demonstrated. Although 6mm biopsies were imaged for this study, larger areas could be analyzed to understand better membrane remodeling or rupture-associated changes in future studies. One limitation is that the significant amount of imaging data obtained which poses potential challenges if quantification of features (manual or automated) is desired.

We used a lower magnification objective, though the 25x could be employed (at the cost of even greater datasets and time to image each sample). Imaging time for the case presented was around 6 hours.

In summary, this study introduced a new approach by which the multilayered organization of placental membranes can be investigated in 3D through the use of MPAM and SHGM. Additionally, novel elements, such as OC and the use of mosaic tiling, were applied for amnion-to-decidua full thickness imaging. These methods expand current capabilities to investigate cellular and ECM characteristics and interactions and may be applied for studies of fetal membrane remodeling and rupture [117].

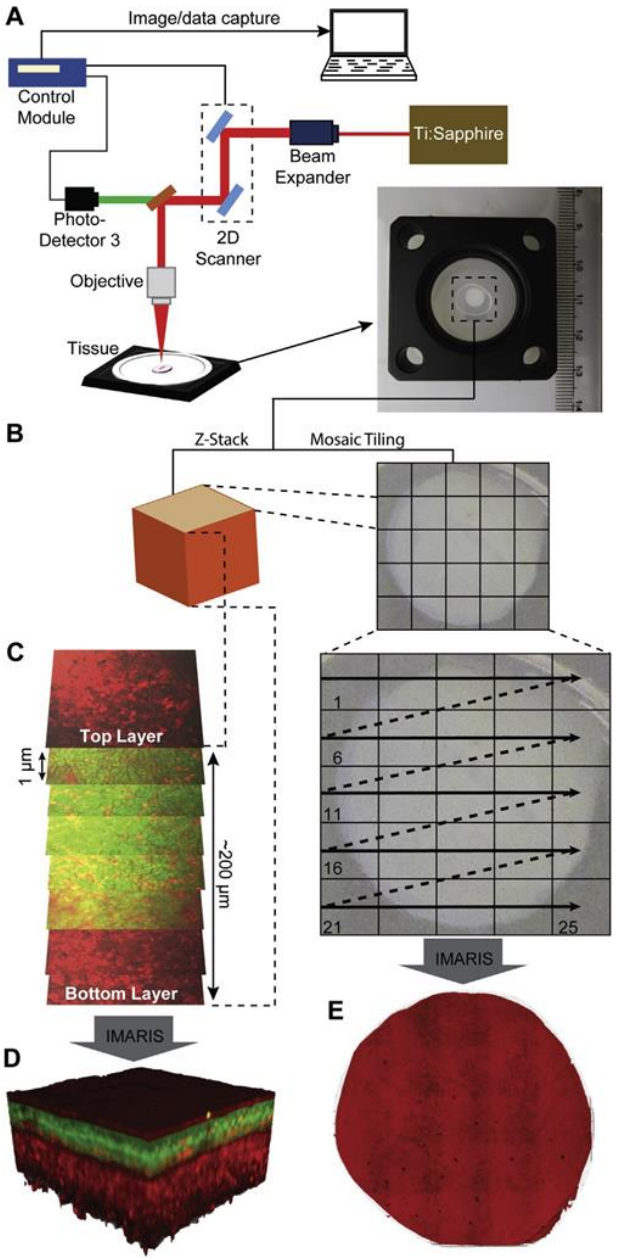

Fig. 2.1 Microscope layout and cartoon of mosaic tiling and Z-stacks.

A) A schematic of the Prairie Ultima IV setup (Prairie Technologies/Bruker, Middleton, WI). B) The depiction of single z-stack volume acquisition processed by ImageJ and IMARIS. C) The depiction of grid pattern to capture z-stacks across the full surface of the biopsy. D) Planer slices at a z-interval of 1µm were captured from the AEC to the chorion. E) Z-stack processed by IMARIS to display a 3D volume.

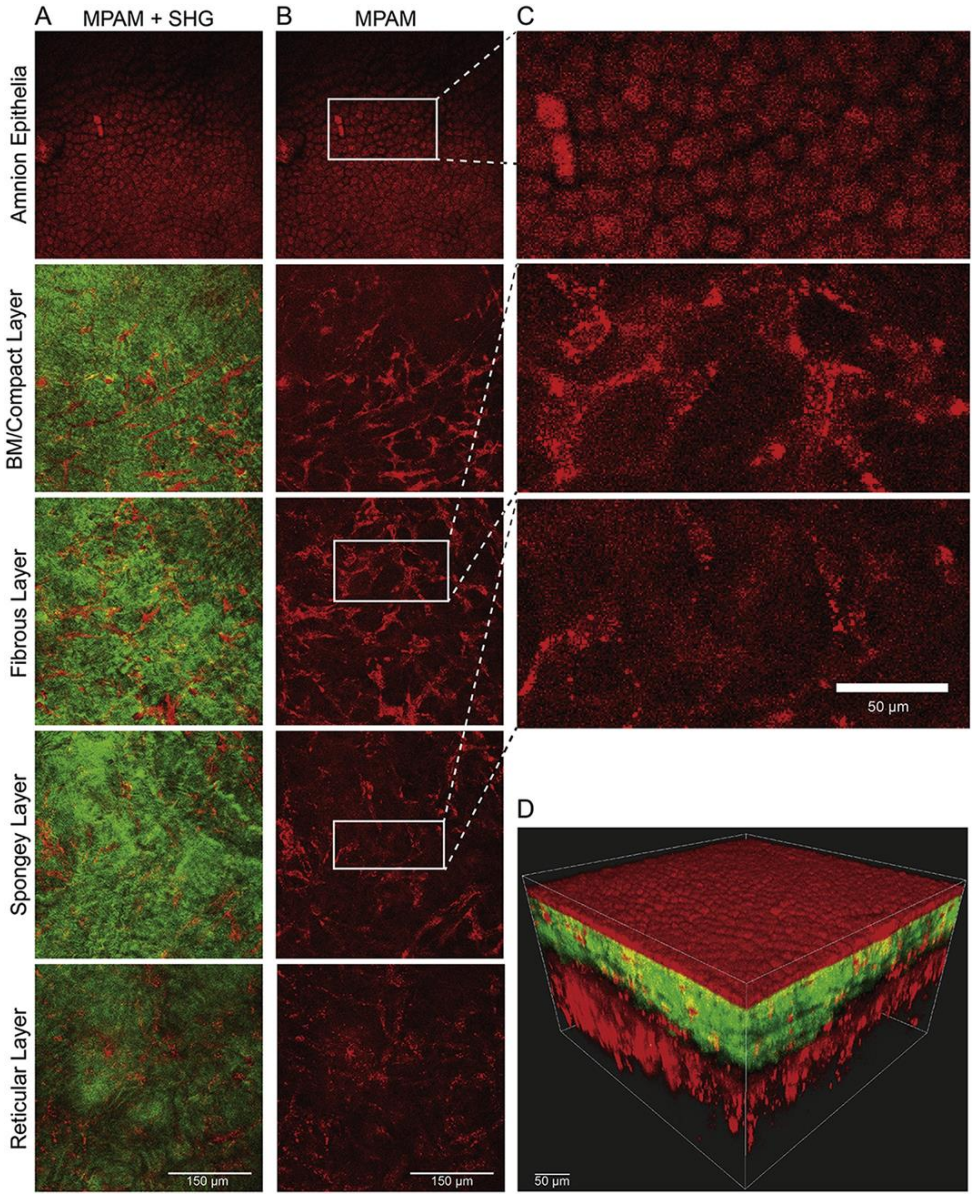

Fig. 2.2 Overall imaging capability of MPAM/SHG on native explants.

A) MPAM/SHG single plane images captured from the amnion epithelium, basement membrane and compact layer, fibrous layer, spongy layer, and reticular layer, showing the interface between the cells and matrix. Measurement bar is 150µm. B) MPAM single plane images corresponding to the images in column A, representing the cellular components of each of the layers. Measurement bar is 150µm. C) Cropped 200x100µm MPAM single plane images showing a close up of the AEC and a low and high density of mesenchymal cells from the matrix. Measurement bar is 50µm. D) MPAM/SHG 3D volume of placental membranes reconstructed with IMARIS software. Contrast and brightness were adjusted to enhance visibility keeping adjustments comparable between images.

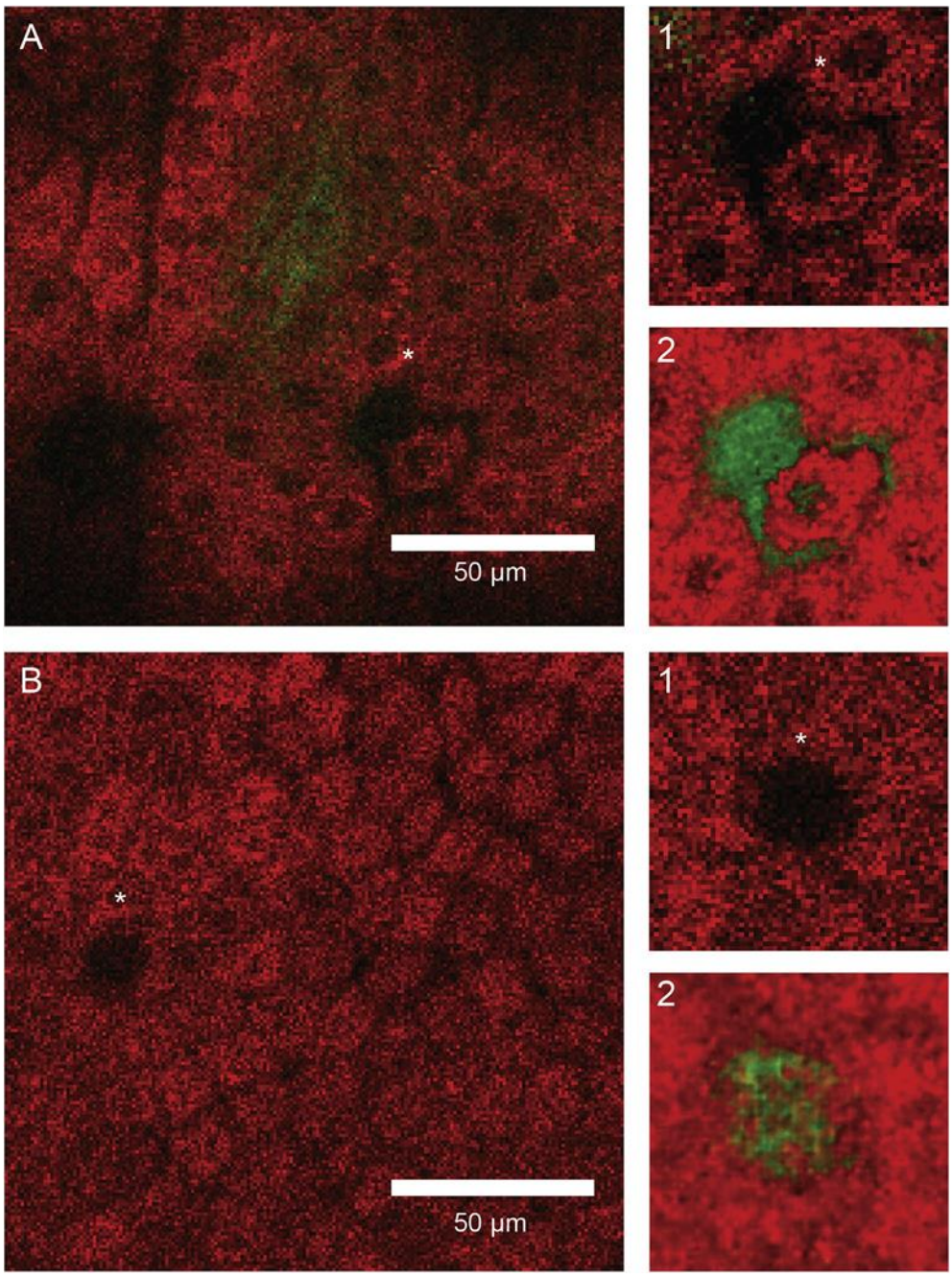

Fig. 2.3 Cellular characteristics of native explants using MPAM/SHG.

A) A cropped 150x150µm MPAM/SHG single-plane image. *represents an area of epithelial shedding. 1) A cropped 50x50µm close-up of the epithelial shedding. 2) An IMARIS 3D reconstruction of the epithelial shedding. B) A cropped 150x150µm MPAM/SHG single-plane image; *represents an epithelial gap. 1) A cropped 50x50µm close-up of the epithelial gap. 2) An IMARIS 3D reconstruction of the epithelial gap. Measurement bar is 50µm, and contrast and brightness were adjusted to enhance visibility keeping adjustments comparable between images.

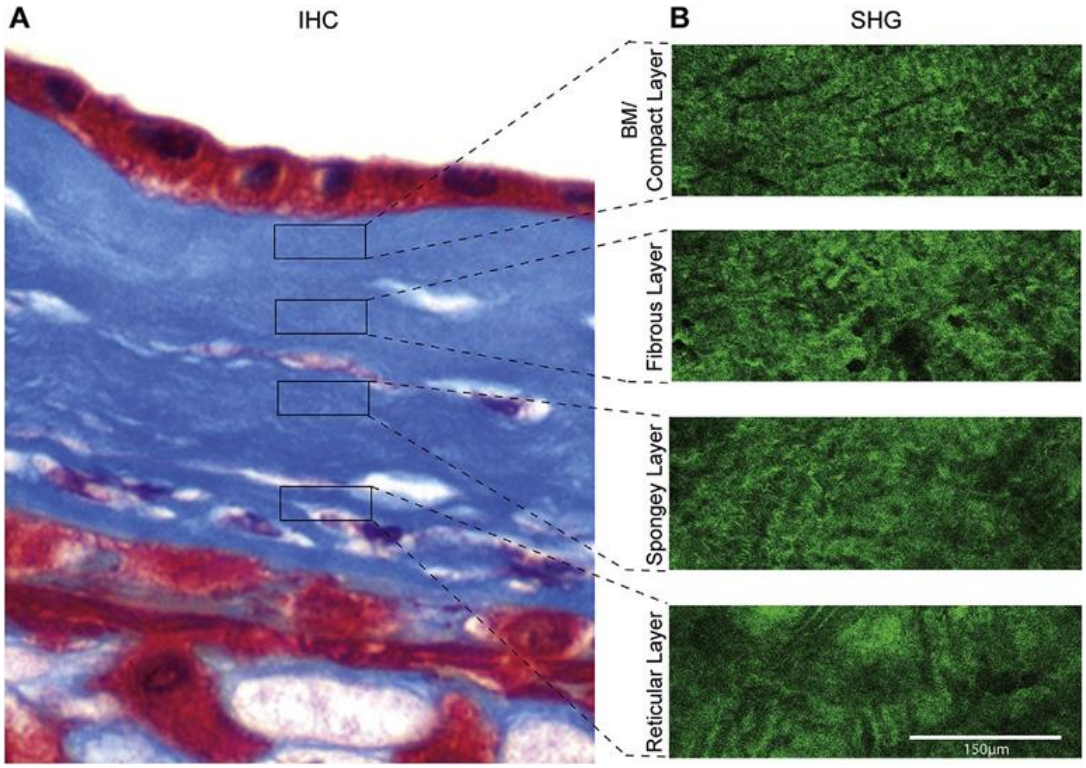

Fig. 2.4 Collagen characterization with SHG.

A) Masson trichrome stain of TNIL placental membranes for comparison of collagen layers in IHC techniques. Red is cells and blue is collagen B) Cropped 407x100µm SHG images of collagen at the basement membrane and compact layer, fibrous layer, spongy layer, and reticular layer. Measurement bar is 150µm, and contrast and brightness were adjusted to enhance visibility keeping adjustments comparable between images.

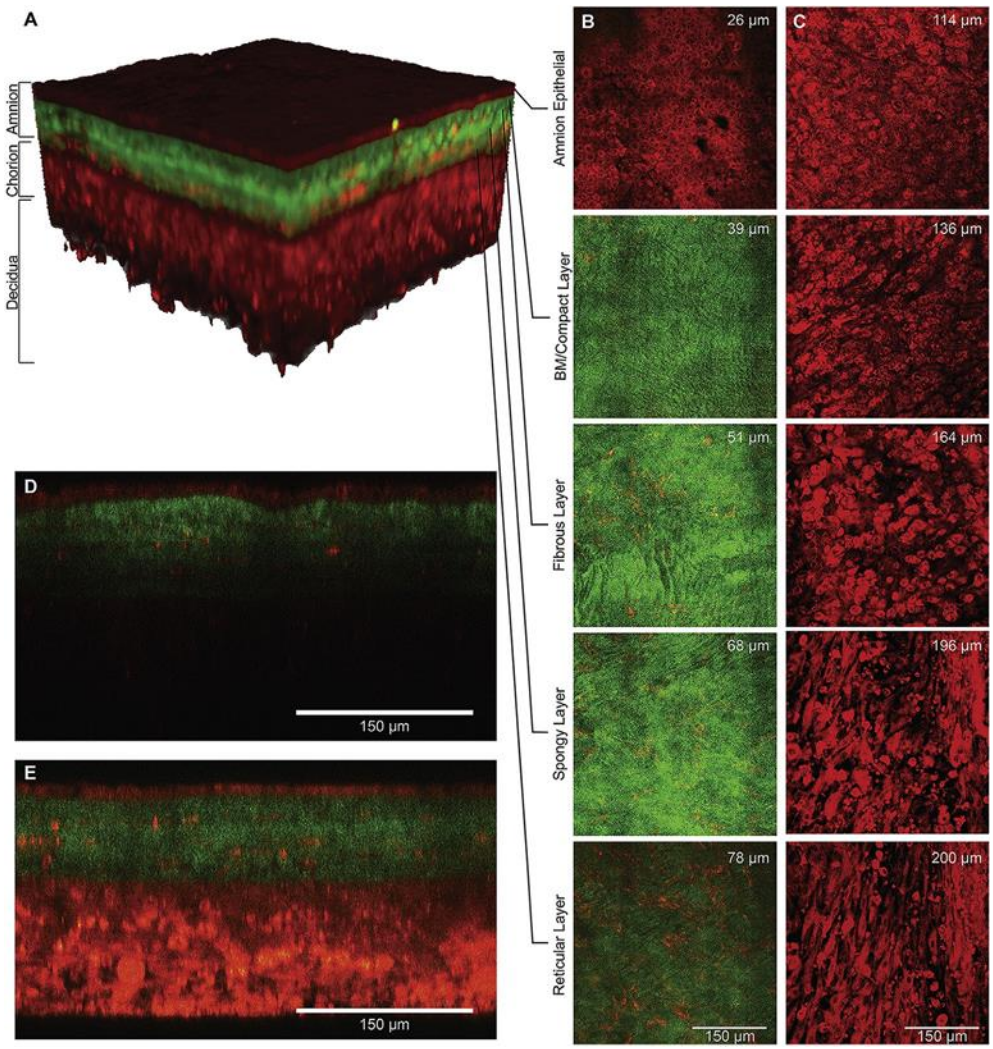

Fig. 2.5 Overall imaging capability of MPAM/SHG on optically cleared explants.

Image depth is recorded at the top right corner of each image in columns B and C. A) IMARIS 3D reconstruction of an optically cleared fetal membrane explant imaged with MPAM/SHG showing the amnion, chorion, and decidua layers. B) MPAM/SHG single-plane images captured from the amnion epithelium, basement membrane, and compact layer, fibrous layer, spongy layer, and reticular layers, representing what is normally visible in native tissue. Measurement bar is 150µm. C) MPAM/SHG single-plane images captured from the beginning of the chorion to the decidua, representing the advantage of image clearing. Measurement bar is 150µm. D) MPAM/SHG orthogonal view of a native explant. Measurement bar is 150µm. E) MPAM/SHG orthogonal view of an optically cleared explant. Measurement bar is 150µm. Contrast and brightness were adjusted to enhance visibility keeping adjustments comparable between images.

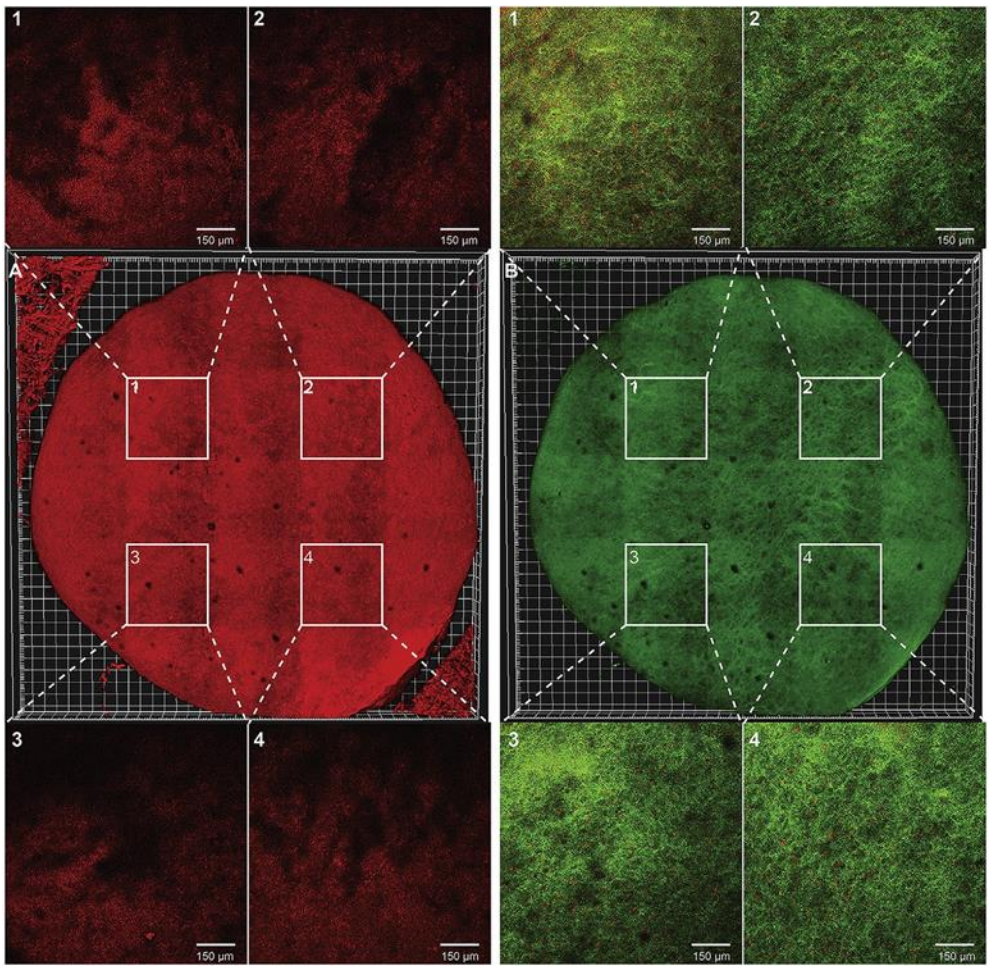

Fig. 2.6 MPAM/SHG mosaic tiling for imaging of full diameter native fetal membrane explants.

A) Apical cellular layer of an overall mosaic tiling of an explant comprising 25 images with a 10% overlap processed with IMARIS. Images 1-4 are single-plane MPAM images showing the differences in the overall topography of the amnion epithelium of a native explant in different areas. Measurement bar is 150µm. B) Apical matrix layer of an overall image mosaic tiling of explant comprised of 25 images. Images 1-4 are single-plane MPAM/SHG images showing the differences in the collagen and cellular interface of a native explant in different areas. Measurement bar is 150µm. Contrast and brightness were adjusted to enhance visibility keeping adjustments comparable between images.

Areas	Morphologic analysis
Amnion epithelium	12.2 ± 2.79 μ m
Basement membrane and compact layer	13.4 ± 2.42 μ m
Fibrous layer	12.8 ± 4.35 μ m
Spongy layer	12.2 ± 3.25 μ m
Reticular layer	39.2 ± 7.47 μ m
Total thickness	89.4 ± 14.32 μ m
	89 ± 13.55 μ m (Orthogonal view analysis)
	102.92 ± 21.39 μ m (Immunohistochemistry analysis)

Table 2.1: MPAM/SHG quantitation of placental membranes through ECM thickness.

Fetal membrane thickness was determined by morphological, orthogonal view, and IHC analysis. Each category contained five samples. Data is represented as Mean±standard deviation (SD).

Chapter 3: Discovery and characterization of human amniochorionic membrane microfractures [96]

INTRODUCTION

Fetal membranes comprise a vital intra-uterine compartment, where they perform mechanical, immune, and endocrine functions to promote the growth of the fetus and protection from environmental adversity [19]. Membrane integrity is normally maintained throughout gestation, mediated by well-balanced homeostasis involving matrix-degrading collagenolytic enzymes and their inhibitors [118-120]. Recently, we reported that amniochorionic membrane senescence occurs as a concomitant of fetal growth and tissue aging [34]. Tissue damage arising from amniochorion senescence produces a sterile inflammatory response associated with parturition [2]. Thus, amniochorionic membranes play major roles during gestation and parturition.

Amniochorionic membranes anatomically consist of a single layer of cuboidal AEC, chorionic trophoblasts, and scattered fibroblasts connected by a layer of type IV collagen-rich ECM [20]. Basement membrane degradation by specific matrix-degrading enzymes, as well as generalized proteolysis, is a factor predisposing to mechanical rupture of membranes before parturition at term or preterm [20]. A reported feature of amniochorionic membrane rupture that provides evidence of these structural changes is the so-called zone of altered morphology that overlies the site of rupture [121]. Morphometric characteristics of the zone of altered morphology are also suggestive of membrane aging because cells and organelles are often enlarged and express sterile inflammatory markers such as matrix metalloproteinase [4]. Although these changes may be expected in membranes at term, similar features were seen in cases with early (<34 weeks) preterm pPROM and spontaneous PTB [4].

Understanding the progressive morphological changes that occur in human amniochorionic membranes in utero is challenging because prospective, invasive sampling is unethical. Noninvasive imaging technologies to reliably scan amniochorionic membranes are yet to be developed. Even if such methodologies were discovered, structural alterations indicating imminent rupture or predicting preterm labor need to be established. We have embarked on the first step of this approach by applying sophisticated microscopic techniques to define structural changes in amniochorionic membranes in normal and pathologic pregnancies. By annotating amniochorionic membrane structural changes, we hope to provide insights into the mechanistic pathways contributing to such changes.

In the current studies, a combination of MPAM and SHG was employed to generate 3D multilayer representations of the surface organization of amniochorionic membranes [122]. This approach, a combination of MPAM and SHG, allows label-free, deep-tissue imaging of cellular and extracellular components of the amniochorionic membranes, through the collection of intrinsic autofluorescent signals [23, 39, 50, 52, 101, 106, 123]. Using this approach, we were able to observe amnion epithelial cell shedding and gap formation at term, along with evidence of loosened collagen in the underlying ECM [39].

The current study was undertaken to develop a microscopic method to allow more accurate volumetric characterization of amniochorionic membrane microstructural organization and to compare features between normal term births and pregnancies complicated by preterm delivery. Regions spanning the amniochorion and ECM extending all of the way to the maternal decidua were examined, and cellular morphology was determined and specifically examined for structural alterations. The discovery of unique microdomains referred to as microfractures in the amniochorionic membranes is reported. These microfractures are a structural feature in the fetal membrane and represent a break (fissure) in the continuity of the amnion surface that extends through the spongy layer and areas of sparse collagen, through to the reticular layer of the chorion basement membranes.

We have categorized characteristic morphometric features of these microfractures and discuss their physiological and pathologic significance.

METHODS

Amniochorionic membrane samples were obtained for this study from John Sealy Hospital at UTMB at Galveston, Texas, under an approved institutional review board protocol (UTMB 11-251).

Amniochorionic membrane collection for multiphoton microscopy analysis

Gestational age-matched term amniochorionic membranes were used for this study. Amniochorionic membranes were collected from TNIL cesarean deliveries, laboring vaginal deliveries after spontaneous onset of labor, and artificial rupture of the membranes (between 39 and 41 weeks) before delivery with no prior history of PTB or pPROM. Term membranes included in this study were limited to artificial rupture of the membranes because factors associated with spontaneous rupture of the membranes (at term) can be confounded by a variety of factors that could manifest in multiple structural outcomes. The collection, processing, and preparation of tissues for imaging are detailed in our prior publication [39]. The methods used did not have any impact on collagen or other cellular features reported in this paper. Amniochorionic membranes from cesarean deliveries after pPROM, SPTB, PE were also collected. Membranes were dissected from the placenta, washed three times in normal saline, and then cleaned of decidua and blood clots using cotton gauze. Biopsies 6mm in diameter (explants) were then cut from the midzone of the reflected membranes, approximately 2.5 inches away from the cervix or placenta. Explants were then stored in 500mL of 10% formalin in 1.5mL Eppendorf tubes until imaging.

For membranes from case groups from preterm births, the following factors were matched: gestational age, maternal age, and other sociodemographic variables (e.g., race/ ethnicity, education, income, and marital and insurance status). Latency between labor (all

subjects had a minimum rate of two contractions per ten minutes) leading to delivery were matched in PTB and pPROM cases.

INCLUSION CRITERIA

Women who had PTB were diagnosed with contractions (rate of two contractions per ten minutes) leading to delivery with intact membranes or with pPROM (as determined by nitrazine test or amniotic fluid pooling) between $24^{0/7}$ weeks and $33^{6/7}$ weeks). PE was defined in our study as blood pressure 140/90 mm Hg on two occasions at least four hours apart after 20 weeks' gestation with new-onset proteinuria. Normal term birth was defined as TL and delivery (>39 weeks) with no pregnancy-related complications.

EXCLUSION CRITERIA

Subjects with multiple gestations, placenta previa, fetal anomalies, and/or medical treatment or surgeries (interventions for clinical conditions that are not linked to pregnancy) during pregnancy were excluded. Severe cases of PE (persistent symptoms (headache, vision changes, right upper quadrant pain), abnormal laboratory findings (thrombocytopenia, repeated abnormal liver function tests, creatinine doubling or >1.2, or HELLP syndrome), or clinical findings (pulmonary edema or eclampsia) were excluded. Subjects who had any surgical procedures during pregnancy or who were treated for hypertension, preterm labor, or for suspected intra-amniotic infection (e.g., reports of foul-smelling vaginal discharge, high levels of c-reactive protein, fetal tachycardia) and delivered at term were excluded from the control groups.

In vitro amniochorionic membrane organ culture and stimulation with CSE

The in vitro organ explant culture system for human amniochorionic membranes and stimulation of membranes with CSE were as previously reported [4]. In this study, CSE was used to mimic the OS experienced by amniochorionic membranes at term before

labor that transition the membrane into a labor phenotype [34]. In short, 6mm biopsies of amniochorionic membranes were collected from TNIL cesarean deliveries and placed in an organ explant system for 24 hours. CSE was prepared by bubbling smoke drawn from a single lit commercial cigarette (unfiltered Camel; R.J. Reynolds Tobacco Co., Winston Salem, NC) through 50mL of tissue culture medium (Ham's F12/Dulbecco's modified Eagle's medium (DMEM) mixture with antimicrobial agents), which was then filter sterilized through a 0.22μm filter (Millipore, Bedford, MA) to remove contaminant microbes and insoluble particles. Amniochorionic membranes were then stimulated with CSE (1:25 dilution) for 48 hours (N=5), whereas the TNIL control medium was replaced with tissue culture medium (N=5). After a 48 hour treatment, the explants were removed and placed into 500mL of 10% formalin in 1.5mL Eppendorf tubes for fixation before imaging.

Optical clearing

OC of whole tissue explants to render the amniochorionic membranes optically transparent was performed by incubation of fixed amniochorionic membrane explants in TDE (refractive index 1.52), (Sigma-Aldrich St. Louis, MO). TDE solutions (50% and 100% w/w) were prepared in Milli-Q water (Merck Millipore, Billerica, MA) at room temperature. Fixed tissue was completely immersed in 50% TDE for 2 hours, and then in 100% TDE overnight at room temperature. Samples were then switched to fresh 100% TDE for mounting and imaging as described above.

Tissue mounting

For mounting, the tissue was placed with the amnion side facing a #1.5mm cover glass in a mounting chamber (30mm cage plate; ThorLabs, Newton, NJ), with a second cover glass placed on the chorion side; 300μl of PBS was added to the tissue, and the coverslips were tightened to secure the PBS and tissue in the imaging chamber. The amnion

epithelium was then oriented toward the objective on the upright microscope and centered with the help of an aiming beam from the excitation source.

Imaging

MICROSCOPY

To determine the cellular and structural alterations in detail, a combination of MPAM and SHG microscopy was used. This approach was used to investigate the multilayered 3D micro-organization of human amniochorionic membranes without the use of exogenous contrast agents, as previously applied by our group [39]. MPAM and SHGM were conducted using a Prairie Ultima IV upright microscope (Prairie Technologies/Bruker, Middleton, WI) using excitation from a Ti:sapphire femtosecond laser (Mai Tai; Spectra-Physics, Santa Clara, CA). A 25x objective with 1.05 numerical aperture (XLPlanN; Olympus, Tokyo, Japan) was used for image collection. Samples were illuminated at 840nm for generation of both MPAM and SHG microscopy, collected in an epi-illumination geometry. Collected autofluorescence and SHG microscopy was split into two detection paths using a dichroic mirror, and auto-fluorescence emission was detected at >500nm, whereas SHGM collected at 420nm. MPAM and SHGM were collected simultaneously in a two-channel configuration using Gallium arsenide phosphide photo-multiplier tubes (Hamamatsu Photonics, Hamamatsu, Japan) for detection.

IMAGE COLLECTION

Regions of interest were obtained (1s per frame; 512x512µm or 1024x1024µm). Depth scans were obtained using a z-interval of 1µm, with imaging depth ranging from 110 to 400µm depending on sample preparation as specified below. Images were obtained using a digital zoom factor of 1.19, resulting in a field of view of 408x408µm. Image stacks were analyzed for epithelial characteristics, epithelial shedding and gaps, and collagen alterations using ImageJ software bundled with 64-bit Java version 1.8.0_112

(NIH, Bethesda, MD; http://imagej.nih.gov/ij), whereas IMARIS software version 7.6.5 (Bitplane, Concord, MA) was used for 3D reconstructions of MPAM and SHGM stacks.

Microfracture quantification

The total area of a 6mm explant can be imaged by taking 25 to 30 individual images (mosaic tiling as reported earlier [chapter 2] [39]) and stitching them together with ImageJ. The center nine images, captured with a 25x objective, were used as the normalizing surface area to serve as the common denominator for microfracture quantification. Microfractures in membranes were counted in a $1.50x106\mu m^3$ area with ImageJ. This allowed us to normalize the surface area scanned for determining microfracture quantities. Microfractures were sliced, and 3D reconstructed with IMARIS software to determine depth and width for each category studied. Kruskal-Wallis followed by Dunn's comparison between groups, and U-test statistics were used to compare the clinical groups; significant differences were defined as $P<0.05$ in two-tailed tests.

RESULTS

Amniochorionic membrane architecture as determined by MPAM/SHGM

The multilayered architecture of the human amniochorionic membranes were analyzed by reconstructed MPAM and SHGM methods as shown in Figure 3.1, A and B. MPAM was generated from endogenous cytoplasmic fluorophores and pseudocolored red in all images; fibrillar collagen autofluorescence in the ECM was captured by SHGM and pseudocolored green (Fig. 3.1B). Features associated with each layer are shown, with the signal arising from the amnion being due to cellular autofluorescence because no fibrillar collagen to produce SHGM is found in that layer (thus, no green signal). MPAM allowed for visualization of cells in the fibroblast and reticular layers embedded within the ECM. The amnion, stromal cells, and chorion cells were studied in the context of their ECM interfaces. As previously described, this method allows the identification of surface

topography, collagen distribution, and cellular density within unique cell layers [39]. Characterization of the amnion epithelial layer topography specifically revealed areas of surface disturbances (Fig. 3.1C), epithelial shedding (Fig. 3.1D), and epithelial gaps (voids lacking an epithelial cell, that extend through the single amnion layer, exposing the ECM) (Fig. 3.1E).

Discovery and characterization of microfractures

Analysis of amnion topography identified areas within the epithelial monolayer that showed intercellular gaps (Fig. 3.2, A and B). This is consistent with epithelial cell shedding. Morphological puckering (Fig. 3.2C) or indentation of the monolayer surface was also noted. Analysis of orthogonally sliced sections showed areas of degraded basement membrane (Fig. 3.2C) containing migrating epithelial cells (Fig. 3.2D). These are shed or migratory cells that appear to invade degraded collagen (visualized as tunnels) in the ECM, where proteolysis of collagen appeared to extend deeply into the ECM (Fig. 3.2E). This constellation of morphological features, with tunnels extending through damaged basement membrane containing migrating cells, is termed microfracture because it appears to represent detachments between the epithelium and matrix.

Four characteristic features for a microfracture in human amniochorionic membranes are reported. This description is based on the analysis of membranes from TNIL (Fig. 3.3A-E) and TL (Fig. 3.3 F-J) membranes, as well as in vitro cultures in response to CSE (Fig. 3.3K-O) that mimicked the OS conditions experienced in utero before and during TL. The main features of microfracture are: i) altered amnion epithelial layer (puckering) or site of epithelial shedding (Fig. 3.3B, G, and L); ii) deterioration and damage of the basement membrane (Fig. 3.3, C, H, and M); iii) tunnels representative of collagen degradation in the ECM that extend from the basement membrane through the spongy layer (Fig. 3.3D, I, and N); and iv) the presence of migrating cells in the tunnel (Fig. 3.3, E, J, and O). Identification of microfractures, regardless of condition, suggests

that microfractures are a normal constituent of membranes at term. Additionally, membranes from each clinical group also contained microfractures based on the characteristics described above; however, the density, depth, and width of the microfractures differed among the groups. MPAM and SHGM membrane images (1.50x106μm^3 area) analyzed by ImageJ allowed the quantification of differences between TNIL, TL, and CSE treated tissues. Microfracture numbers were similar between the TNIL and TL groups (Fig. 3.3P).

In vitro induction of microfractures in response to OS

To determine whether OS can increase microfractures, TNIL were exposed in culture to CSE (N=5). CSE treatment increased the number of microfractures by 1.62-fold compared to TNIL (control) (Fig. 3.3P). IMARIS software was used to create the 3D reconstruction of the collagen matrix region, allowing microfractures to be sliced showing width and depth. CSE induced deeper ($P<0.001$) (Fig. 3.3Q) and wider ($P=0.03$) microfractures (Fig. 3.3R) than what was seen in TNIL controls, suggesting that OS can cause an increased number of microfractures with increased morphometry. Although the numbers of microfractures are similar in width and depth (range, 10 to 50μm) regardless of labor status, there is an increasing trend in each characteristic compared to TNIL and TL membranes. We have already reported that the number of senescent cells are higher in TL compared to TNIL membranes [13]. This suggests the possibility that the migratory cells seen in the microfractures at TL are either shed or senescent cells, which could potentially traverse through these fractures, though further investigation is required to test this hypothesis.

Microfracture characteristics of the chorion and its extracellular region

The microfractures that are in chorion and its ECM were also examined. Like the amnion membrane, the chorion layer also had microfractures pointing toward the amnion

and extending through the reticular layer. Although it is difficult to confirm that the chorion has cell shedding or gap formation (due to its multilayer composition), distorted areas extended toward the matrix region. The reticular layer of the amniochorionic membranes is located on the basal side of the spongy layer and the apical side of the chorion. SHG microscopy microcopy identified loose fibrillar collagen [39] (Fig. 3.4A) in the reticular layer; here, we add to this description by identifying gaps, potential fractures, in the reticular layer ECM (Fig. 3.4B-D), which could be caused by migrating fibroblast or chorion cells. Thus, if microfractures span the gap between the amnion and spongy layer, collagen degradation in the reticular layer could bridge the gap between AEC and the chorion layer, and thus allow the microfractures to span across the membranes.

Microfractures are more frequent and structurally different in pPROM than PTB and PE

Increased microfracture density and altered morphometry are responses to OS and led us to examine membranes from pPROM and PTB with no rupture. pPROM has also been termed a "disease of the amniochorionic membranes."[117] pPROM membranes also exhibit increased levels of OS and collagen degradation [124, 125]. In our study, membranes from gestational, age-matched, mild PE were included for two reasons: i) PTB following PE is an indicated delivery, and ii) PE is not normally associated with membrane dysfunction. Therefore, it may provide a good gestational age matching control for our pPROM and PTB groups, and PE is often associated with OS and may provide an OS-induced effect on membranes that is yet to be reported in this condition. We do acknowledge that membranes in PE may often show non-inflammatory choriodecidual necrosis and/or old retro-membranous blood clots. Membranes from pPROM, PTB, and PE were compared for microfractures and their characteristics (Fig. 3.5A-L) using MPAM and SHG microscopy as above. Comparison between PTB and term birth (regardless of labor status) membranes did not show any difference in the number of microfractures (Fig.

3.5M). The number of microfractures in pPROM membranes was (4.6-fold) higher than PTB membranes (Fig. 3.5M). Microfractures in pPROM are also deeper (Fig. 3.5N) and wider than in PTB membranes (Fig. 3.5O) when 3D reconstructions were formed. To note, the morphometric changes were similar between TL and PTB microfractures, though pre-term birth microfractures were significantly wider (P=0.01) than those of TL.

When membranes from PE were compared with PTB membranes, no significant differences in microfractures (number and dimensions) were seen between the groups. However, the comparison between microfractures in PE and pPROM membranes had similar differences as those seen between pPROM and PTB. However, pPROM microfractures are significantly deeper than those seen in PE (P=0.04). This suggests that the pathologies of PTB and PE are not affecting changes in membrane microfractures. Here, results indicating pPROM had extensive areas of collagen degradation resulting in broader and deeper microfractures are shown. We postulate that these microfractures are areas of insufficient tissue remodeling due to the underlying pathologic condition or premature senescence. Persistent microfractures can act as channels for amniotic fluid leak and inflammatory cell infiltration as often seen in pPROM. In summary, microfractures appear as tunnels of degraded collagen, possibly vacated by a shed or senescent amnion cells. These microfractures could also arise by displacement of chorion laeve or trophoblast cells. Collagen degradation, a key characteristic feature of microfractures, extends through the spongy layer of the ECM, connecting its contents with the dispersed collagen of the reticular layer. The connection created by microfractures between the amnion and chorion may facilitate communication via signals including inflammatory cells and exosomes.

DISCUSSION

Using a combination of the innovative microscopic techniques of multiphoton autofluorescence and SHG microscopy, a thorough examination of structural characteristics of normal term amniochorionic membranes (Fig. 3.1) obtained from

laboring and non-laboring women at term and in spontaneous and indicated preterm births was performed. In addition, an established amniochorionic membrane explant system under control and OS conditions was used. The principal finding of this study is the discovery of structural defects in human amniochorionic membranes that we have termed microfractures. These lesions were characterized using the following four morphological criteria: i) the amnion epithelial monolayer showing regions of cell shedding or puckering of amnion cells; ii) localized degradation of the sub-epithelial basement membrane; iii) fissures or tunnels that extend into the remodeled collagen matrix; and iv) migrating or shed cells that can be identified within the matrix tunnels (Fig. 3.2 and 3.3). In summary, microfractures represent structural defects that extend into the sub-epithelial matrix, creating tunnels that can contain satellite amnion cells or other migrating cells. Microfractures can span the thickness of the ECM, which is around 80μm [39], and can allow whole amnion cells or their exosomes (microvesicles that are inter-tissue communication mediators) access to the chorion layer through the loose sub-epithelial reticulum (Fig. 3.4).

Although collagen and basement membrane degradations are well-reported features in term and pPROM membranes, through the use of advanced 3D multimodal microscopic imaging used in this report, we report for the first time the presence of a characteristic feature termed microfracture that extends from the amnion through the ECM and that reaches the chorion layer with altered cellular and matrix morphology. Microfractures are likely developed due to a structural alteration created by biochemical and cellular-level changes (Fig. 3.5). These findings were not possible previously, because traditional histologic and microscopic approaches such as IHC or confocal microscopy are not adequately sensitive, either lacking the ability for volumetric 3D assessment or lacking the specific contrast from collagen provided by SHG microscopy. Microfractures may develop when amniochorionic membranes expand and grow to support fetal development. Membrane growth and extension involve amnion cell shedding and gap formation, leading

to microfracture formation. Our ongoing studies and recently reported findings suggest that distorted or displaced AEC can be recycled or transitioned to become mesenchymal cells (EMT) [126], and this transition involves localized inflammation that involves collagen metabolism. This will lead to microfracture resealing, a mechanism to remodel membranes. Microfractures are likely areas where active remodeling takes place during gestation, and their development and resealing are essential to main membrane integrity. Data from mild PE (a condition where amniochorionic membrane dysfunctions are not reported) may support this concept, where a small number of microfractures along with collagen rearrangement was seen (Fig. 3.5). Increased quantity of microfractures and pathologic conditions that will fail to reseal may predispose membranes to rupture, resulting in an adverse pregnancy.

An increase in the number of microfractures and their dimensions was visible after OS induction in vitro and in membranes from pPROM (Fig. 3.5), a condition associated with increased OS [31]. Development of microfractures in response to OS inducing risk factors (e.g., infection, poor nutrition, high body mass index, behavioral risks) can be a predisposing factor for pPROM because microfractures can provide channels for amniotic fluid leak and inflammatory cell migration. We also speculate that microfractures can act as channels of communication by fetal cell-derived exosomes that also carry inflammatory signals at term or in response to OS [127].

Our prior reports showed several biochemical and histologic senescence and OS-associated markers that were similar in TL and pPROM membranes [4]. However, microfractures are not similar in numbers or morphometry between TL and pPROM membranes. Although senescence is a factor associated with both conditions [4], microfractures are likely independent of senescence-associated changes. As mentioned above, microfractures are likely sites of membrane remodeling, and pPROM is a condition associated with tissue destruction due to remodeling failures. The lack of differences in the number of microfractures between two different term groups (TNIL and TL) suggests the

pluripotency of cells in the membrane. These cells retain the ability to reseal microfractures even at term, whereas pPROM membranes have a diminished capacity to reseal.

Due to limited sample sizes in each of the categories, the specific role of histologic chorioamnionitis or microbial invasion in the spontaneous PTB or pPROM groups were not examined. Although this was not one of the objectives of this study, some of these factors may affect microfracture development, resealing, and/or its persistence leading to rupture. These pathologic factors along with other OS inducing risk factors and their impact on microfracture formation/tissue remodeling or destruction are the focus of our ongoing studies. Another limitation of this study comes in sample preparation due to tissue fixation preventing directionality studies. Future studies will use live tissues to better document this remodeling process.

In summary, the clinical significance of microfractures is highlighted. We postulate that persistence of microfractures or failure to repair them might lead to pockets of inflammation in the membranes. Our ongoing studies have shown MMP9 immunostaining, suggesting inflammatory and matrix degradation related changes. Microfractures can function as channels of amniotic fluid leak, and failure to reseal microfractures can be considered as a predisposing factor for membrane rupture. Several pioneering studies have reported ECM remodeling and collagen metabolism in amniochorionic membranes and their overwhelming activities in response to infection and other risk factors causing membrane rupture. This report provides more evidence to suggest that pPROM is a disease of the fetal membranes. Further studies centered on microfractures could provide valuable insights into their development and other functional roles, as well as how they contribute to membrane dysfunctions.

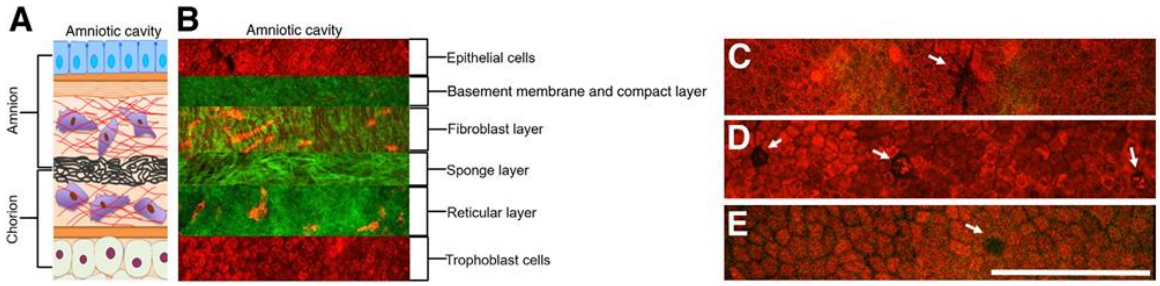

Fig. 3.1 Characterization of amniochorionic membranes with NLOM

Compared to the layers imaged by a two-photon laser using MPAM (red) and SHG microscopy (green) A). A schematic of the amniochorionic membrane layers: Description starts from the innermost layer (amnion) facing the amniotic cavity and ends with the chorion. AEC (blue) are connected to the first layer of the ECM, called the basement membrane (orange)/compact layer (orange strips). The fibroblast (top red), spongy (black), and reticular layers (bottom red) follow, containing stromal cells (purple). The chorion (tan) is connected to the ECM through a basement membrane (orange). B) MPAM and SHG microscopy of fetal membranes: MPAM (red) shows cuboidal AEC in a monolayer attached to the basement membrane in green as delineated by SHG microscopy. The layers of the ECM (green), including the basement membrane/compact layer and fibroblast, spongy, and reticular layers, exhibit unique collagen characteristics and contain stromal cells (red). Chorion trophoblast cells (red) are connected to the ECM. C) AEC forming an area of altered morphology, puckering, as indicated by the white arrow. D) AEC (white arrows) that are shedding away from the monolayer by losing junctions to neighboring cells. E) Amnion epithelial cell gap (white arrow), which leave holes in the epithelial layer. Scale bar=150µm (C-E). Images in B obtained with a 25x objective.

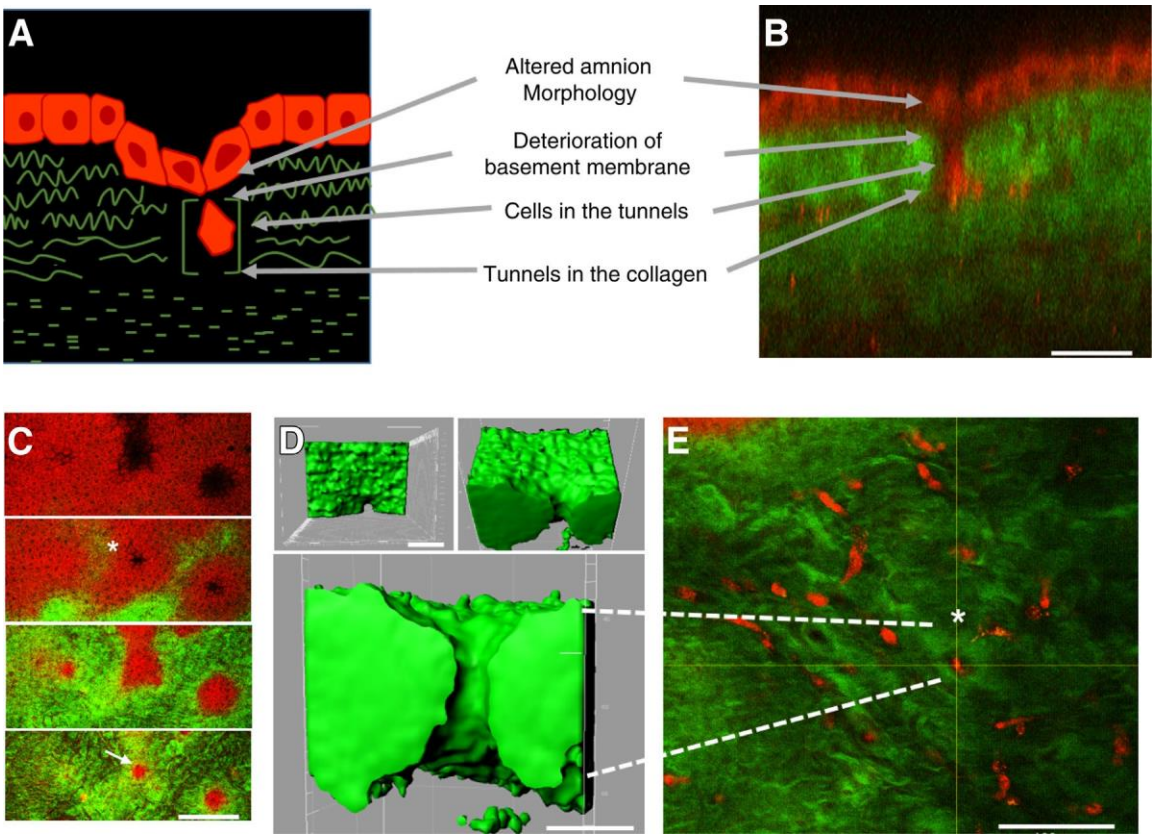

Fig. 3.2 Characteristics of microfractures.

A) Cartoon representation of a microfracture visualized by a degraded tunnel of collagen containing a migrating cell. B) Multiphoton image of microfracture. Cells are red, and collagen, green. C) Multiphoton image of a degraded basement membrane: Representative image of a degraded type IV rich basement membrane (arrow) around an area of altered amnion morphology (asterisk). D) IMARIS software reconstruction of a degraded tunnel of collagen. E: Multiphoton image of a cell migrating through a degraded collagen tunnel (asterisk). Other stromal cells represented in this image are not in collagen tunnels. Scale bars: 30µm (B); 150µm (C); 10µm (D); 100µm (E).

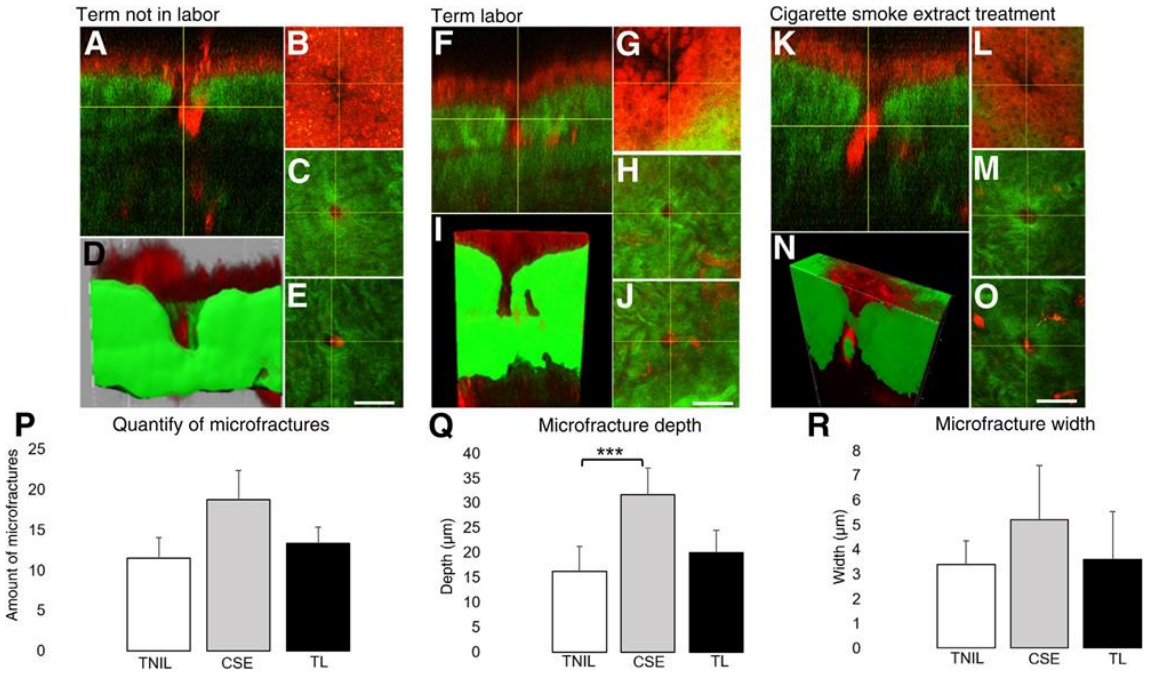

Fig. 3.3 Characteristics and quantification of microfractures in term fetal membrane samples and in membranes exposed to OS by CSE.

A-O) Microfractures in TNIL (A-E), TL (F-J), and CSE: A-O) Microfractures in TNIL (A-E), TL (F-J), and CSE treated tissue in vitro in an organ explant system for 24 hours (K-O). The yellow crosshairs pinpoint the migrating cell of interest throughout each group of images. A, F, and K) Orthogonal views of a microfracture. B, G, and L) Amnion morphology above the microfracture. C, H, and M) Degraded basement membrane around the migrating cell. D, I, and N) 3D collagen reconstruction by IMARIS software of a sliced microfracture showing a tunnel of degraded collagen. E, J, and O) Degraded collagen tunnel with a migratory cell. P-R) Quantitation and morphometric measures of microfractures in TNIL, TL, and CSE exposed fetal membranes in vitro. P) Number of microfractures: Multiphoton images add up to a 1.5008x106µm^3 area that was analyzed for microfracture quantity. Numbers of microfractures were higher after CSE of TNIL membranes in culture, followed by TL membranes. Q) Depth of microfractures: TL explants contained deeper microfractures then TNIL membranes. CSE treatment produced significantly deeper microfractures than TNIL controls in vitro or TL membranes (P=0.002). R) Width of microfractures: CSE treatment induced wider microfractures compared to TNIL control cultures (P=0.032) in vitro. TL microfractures were only slightly wider than the TNIL controls, and they were not significantly different.

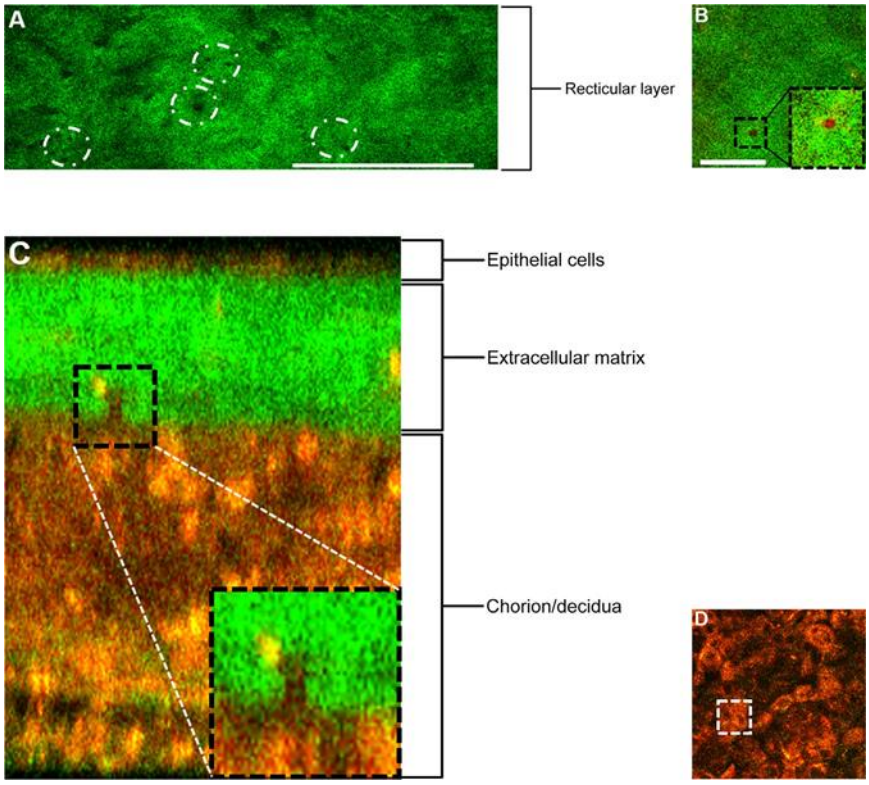

Fig. 3.4 Characterization of the reticular layer.

A) SHG microscopy image of the reticular layer of amniochorionic membranes. The reticular layer of the chorionic ECM demonstrates loose collagen and areas of collagen degradation that connect to the chorion (dashed circles). B-D) Multiphoton autofluorescence and SHG microscopy images of collagen degradation in the reticular layer of the chorion: shown are tunnels of degraded collagen (black box, B), connecting to the chorion layer (white box, D). An overall view of this collagen degradation is depicted in (black box, C). Insets show a higher magnification of the boxed areas. Scale bars: 150µm (A); 40µm (B). Images in C and D were obtained with a 25x objective.

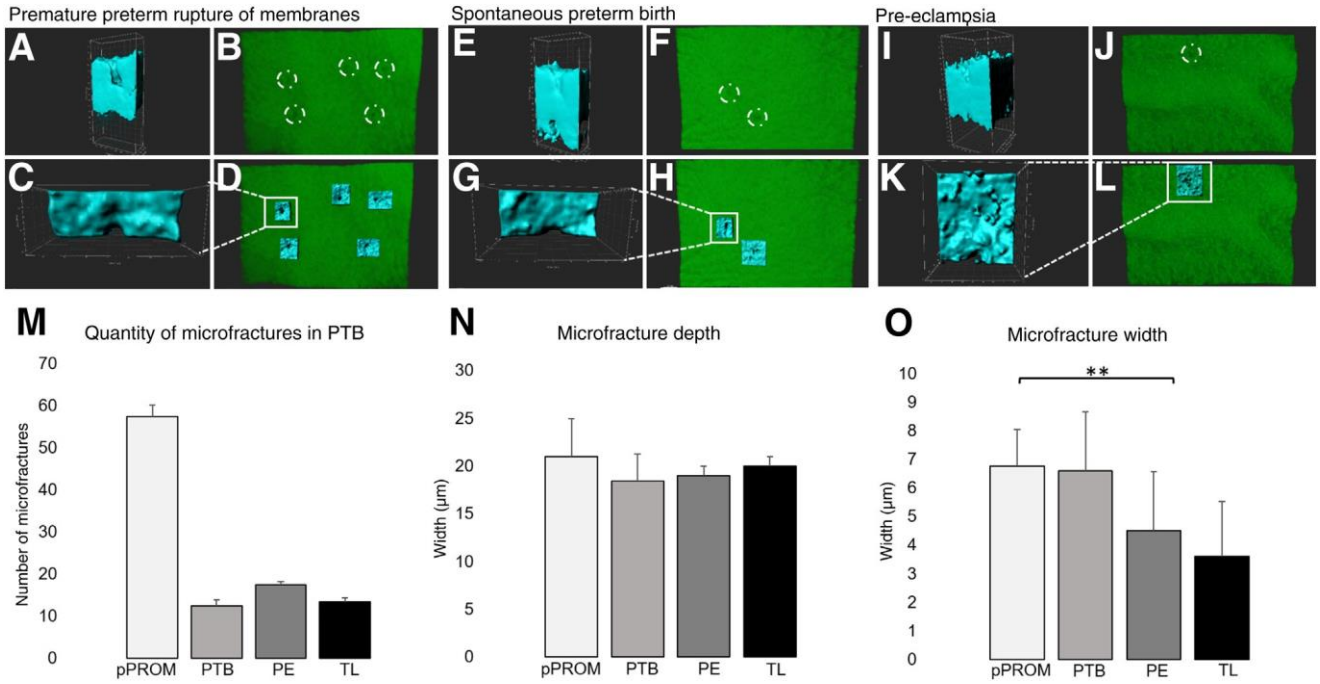

Fig. 3.5 Analysis and quantification of collagen degradation in fetal membranes from PTB.

NOLM analysis of collagen degradation by SHG microscopy of standardized surface area of fetal membranes from pPROM (A-D), PTB (E-H), and PE (I-L). Surface areas studied [regions of 360x260µm (9.4x104µm^3)] were similar in the pPROM, spontaneous PTB, and PE samples that were analyzed. A-D) Fetal membranes from pPROM imaged with SHG microscopy visualizing areas of collagen degradation (dashed circles, B). These areas of collagen degradation, or microfractures, were reconstructed in blue as seen in A, C, and D, highlighting the depth, width, and location of microfractures. pPROM samples had wider and larger numbers of microfractures compared to spontaneous PTB and PE samples. E-H) Fetal membranes from spontaneous PTB only contained one true microfracture that was reconstructed and sliced as seen in images E, G, and H. SHG microscopy visualized areas of collagen degradation (dashed circles, F). The second blue area in panel H (not in the white square) may also suggest the beginning of microfracture formation due to the indentation, but not tunnel formation, seen at this location. I-L) Fetal membranes from PE also showed low numbers and smaller microfractures compared to membranes from pPROM. SHG microscopy visualized an area of collagen degradation (dashed circle, J). Boxed areas in D, H, and L correspond to higher-magnification images in C, G, and K. M-O) Quantitation and morphometric measures of microfractures in PTB membranes and TL. M) Number of microfractures: Fetal membranes from pPROM contained a 4.6-fold higher number of microfractures than PTB and 3.3-fold higher than PE samples. N) Depth of microfractures: Microfracture depth did not change much between PTB categories or TL, though PPROM depth is significantly greater than in PTB (P=0.04). O) Width of microfractures: Microfracture widths were not different between pPROM and PTB samples (P=0.005); however, compared to TL, pPROM and PTB microfractures were wider.

What type of cellular processes could heal microfractures or wounds in utero?

NLOM allowed for comprehensive analysis of TNIL fetal membrane micro-architecture highlighting the overall topography and visualization of epithelial shedding, gaps, and altered morphology in the amnion layer. Additionally, SHG revealed fibrillar collagen organization throughout the ECM, making it possible to determine individual layer transitions (e.g., cell-collagen and collagen-collagen interactions), thickness, and fiber morphology (**Chapter 2**)[39]. From this analysis, specific areas of fetal membranes remodeling were identified and termed biological 'microfractures' (**Chapter 3**)[96]. Morphometries (e.g., depth and width) and quantity of microfractures increased in term labor and preterm (i.e., pPROM) membranes showing their physiological and mechanistic relevance in parturition. Microfracture resealing and gap filling of areas vacated by epithelial cell shedding likely occur; However, how these sites are formed or sealed remain unknown.

This data induced speculation regarding what type of cellular processes could heal microfractures (i.e., wounds) in utero and what stimulant might expedite or inhibit healing. Cellular transitions between epithelial and mesenchymal phenotypes (e.g., EMT and MET) are well documented in other fields to contribute to tissue remodeling [54-58]. However, currently, it is unknown if amnion membrane cells are able to undergo transitions in vitro or in utero and how this could affect wound healing. To study this question, an AEC scratch assay was used to mimic wound healing in vitro (**Capture 4**)[128]. This model will elucidate AECs wound healing properties, cellular transitions contribute to this process, and how treatments mimicking gestation (i.e., AF) or term labor (i.e., CSE) affect these outcomes.

Chapter 4: Proliferative, migratory, and transition properties revel metastate of human amnion cells [128]

INTRODUCTION

During pregnancy, placental membranes provide mechanical support and immune tolerance for the growing fetus until their disruption at term [19]. Placental membranes are composed of AECs and chorion trophoblast cells, connected by a collagen-rich ECM that also contains amnion mesenchymal stromal cells [23, 39, 106]. Membranes expand with the developing embryo, undergoing continuous remodeling throughout gestation to maintain structural integrity and accommodate fetal growth [2, 23, 52]. Membranes, specifically the amnion layer, are highly elastic, allowing them to withstand the stretch and strain endured during fetal growth [129]. We recently reported that the membranes undergo telomere-dependent [15] senescence via OS-induced p38 MAPK [28, 41]. Both human and animal models suggest that development of senescence and senescence-associated inflammation are progressive events that peak at term as the membranes reach their longevity [14, 41, 127, 130]. Senescent membranes fail to remodel [96], lose their structural integrity and generate various inflammatory signals that can cause a transition of a quiescent uterus to an active (in labor) status. Thus, membranes can alternatively support a pregnancy or promote labor. Because premature senescence is associated with preterm delivery [4, 131], understanding the mechanisms that regulate placental membrane homeostasis will help to elucidate causes of PTB and preterm pPROM, two major pregnancy complications.

Placental membrane cells are pluripotent, with stem-like characteristics (self-renewal and capable of differentiation when stimulated under appropriate conditions) and

the ability to remodel through a well-balanced inflammatory process during gestation. This is supported by self-healing of wounds after fetoscopy [132, 133], as well as minimal incidence of placental membrane rupture after invasive procedures, such as amniocentesis, where incision injuries are often self-limiting, repaired, and heal spontaneously [134]. A recent report by Carvalho et al. [135] noted reparative activity at the placental membrane surgical sites after open fetal surgery. This activity was characterized by a significant increase in nascent collagen synthesis, tissue remodeling, and repair of suture site, mechanisms likely to prevent AF leakage and to maintain pregnancy. Human amniotic membranes are shown to promote healing of iatrogenic placental membrane defect sites [136-138]. However, ambiguity [139] and lack of understanding of the mechanisms involved in wound healing has hindered the advancement of intra-uterine interventions to prevent various fetal anomalies. Effective interventions for pPROM, a disease of the placental membranes that affects approximately 40% of all spontaneous PTB that results from failure to heal membranes, are also elusive because of gaps in knowledge of the mechanisms of membrane remolding.

Recently, we reported certain unique features in placental membranes from TL delivery compared with TNIL delivery. Multiphoton microscopy of membranes showed amnion cell shedding and/or puckering, basement membrane and ECM degradation, and migration of cells through tunnels in the ECM [96]. These structures are collectively called microfractures, and TL microfractures are distinct from those in TNIL. Microfractures are more frequent in TL than TNIL membranes from cesarean sections. In vitro, TNIL membranes exposed to OS inducers, increased microfractures, and their morphometry were similar to those seen in TL [96]. Similarly, microfractures were more frequent in pPROM and PTB with intact membranes than gestational age-matched membranes from PE [140]. We postulate that microfractures are areas of membrane remodeling and are increased in response to OS at term or preterm. At term, this could be considered as a normal physiologic response, ensuring fetal and membrane/placental delivery. However, failure to

repair and heal microfractures may predispose them to rupture and/or delivery in PTB, when pregnancy-associated risk factors increase intra-amniotic OS.

Although the mechanisms of wound healings are not well characterized, several studies have found wound healing properties of placental membranes, specifically the amnion layer. In a recent study, Janzen et al. [126] proposed transition of AECs to mesenchymal cells (EMT), a process associated with inflammation and accelerated by inflammatory mediators. In support of this study, Mogami et al. [141] reported that small ruptures of the placental membrane (generated by a 26-gauge needle) closed within 72 hours in a preclinical mouse model on day 15 of gestation, whereas limited healing capacity was associated with large ruptures (generated by a 20-gauge needle). Small ruptures induced transient up-regulation of cytokines, whereas large ruptures elicited sustained up-regulation of proinflammatory cytokines in the placental membranes. Fetal macrophages facilitated localized inflammation, EMT, and epithelial cell migration in this model, enabling wound healing.

On the basis of these reports, it is hypothesized that OS inducers compromise membrane microfracture remodeling and healing capacity, leading to persistence of wounds or fractures that cause dysfunctional membranes with inflammation. To further investigate the kinetics and mechanisms of the wound healing and transition capacity of AECs under normal and OS conditions, an in vitro scratch assay was performed and their transition during the wound healing process studied. In addition, it was demonstrated how OS compromises and AF nurtures the healing capacity of amnion cells. We report that AECs from term membranes can proliferate, undergo EMT for cell propagation, and heal a scratch when cells regain epithelial phenotype through MET.

METHODS

Study design

This study protocol was approved by the institutional review board at UTMB at Galveston, TX, as an exempt protocol for using discarded placenta after normal term cesarean deliveries (project 69693). No subject recruitment or consent was required for this study.

AEC culture

Primary AECs were isolated from TNIL amnion (approximately 10g), peeled from the chorion layer, and dispersed by successive treatments with 0.125% collagenase and 1.2% trypsin. All cell culture reagents were purchased from Sigma-Aldrich (St. Louis, MO), and details of AEC isolation protocols can be found in previous reports [15, 28, 41]. This isolation method has been optimized to eliminate AMC contamination as verified by cytologic evaluation of all the preparations on seeding. The dispersed cells were plated in a 1:1 mixture of Ham's F12/DMEM, supplemented with 10% heat-inactivated fetal bovine serum (FBS), 10 ng/mL of epidermal growth factor, 2 mmol/L L-glutamine, 100 U/mL of penicillin G, and 100 mg/mL of streptomycin at a density of 3 million to 5 million cells per T75 and incubated at 37ºC with 5% CO_2 until 80% to 90% confluence was achieved. Although there are limitations to culturing AECs with epidermal growth factor and FBS as primary cells they require such growth factors to survive in vitro. Growth factors in AEC medium did not promote additional proliferation and migration of cells as documents by the OS treatments.

AF collection

TNIL AF was used from our existing biobanks. AF samples were collected from women undergoing cesarean delivery by transabdominal amniocentesis. Samples were immediately centrifuged three times at 3000g to remove all cells and particulate debris. Aliquots of supernatant were stored at 80ºC until further use. Inclusion criteria included elective cesareans after an uncomplicated pregnancy before the initiation of labor.

Exclusion criteria included history of antimicrobial treatments during pregnancy, any surgical procedures, smoking during pregnancy, positive screening for group B Streptococcus between 35 and 37 weeks of gestation, body mass index >25, prior history of preterm labor or other complications of pregnancy, and bacterial vaginosis.

Scratch assay and cell culture treatments

Passage (P) 1 AECs were seeded at approximately 80% confluence in four-well coverslips and incubated at 37ºC with 5% CO2 for 24 hours. AECs were then serum starved for 1 hour, rinsed with sterile 1x PBS, and then scratched evenly down the middle of the well, in a straight line, with a 200µL pipet tip. Cells were washed with sterile 1x PBS four times to remove any cell debris [142]. To measure cellular proliferation versus migration, P1 AECs were plated for scratch assay after being incubated with 5µmol/L of carboxyfluorescein succinimidyl ester for 20 minutes, rinsed with PBS, and re-suspended. Carboxyfluorescein succinimidyl ester stains cells green and only loses its intensity after cell division. This identified cells that proliferated (lost their initial green fluorescent protein intensity) versus migrated (maintained their initial intensity) to seal the wound.

Exposure of scratch to OS conditions and normal term AF

To test the effect of OS on wound healing and the effect of AF in nurturing AECs, scratch wounds were treated with one of the following: i) control Dulbecco's modified Eagle's medium/F12 medium, ii) OS inducer CSE 1:25 medium [28], iii) CSE and antioxidant (15 mmol/L; Sigma-Aldrich), or iv) AF samples from TNIL cesareans (TNIL AF; 1:1 dilution in AEC culture medium) and incubated at 37ºC, 5% CO2, and 95% air humidity for up to 38 hours.

Immunocytochemical localization of intermediate filaments CK-18 and vimentin

AEC immunocytochemical staining for vimentin (3.7µL/mL; ab92547; Abcam, Cambridge, MA) and cytokeratin-18 (CK-18) (1µL/mL; ab668; Abcam) were performed at 1 hour, 10 hours, 22 hours, and 38 hours after the initial scratch was made. Manufacturer's instructions were used to calculate staining dilutions to ensure uniform staining. After each time point, parallel cultures of cells were fixed with 4% PFA, permeabilized with 0.5% Triton X, and blocked with 3% bovine serum albumin in PBS before incubation with primary antibodies overnight at 4ºC [143]. This protocol is adequate to remove nonspecific binding of primary antibodies in our system. After washing with PBS, slides were incubated with Alexa Fluor 488 and Alexa Fluor 594 conjugated secondary antibodies (Life Technologies, Carlsbad, CA) and diluted 1:1000 in PBS for 1 hour in the dark. Slides were washed with PBS, treated with NucBlue Live ReadyProbes Reagent (Life Technologies), and then mounted using Mowiol 4 to 88 mounting medium (Sigma-Aldrich).

Microscopy and image analysis

Images of scratch sites were recorded and medium were collected 1 hour, 22 hours, and 38 hours after the initial scratch. Bright field microscopy images were captured using a Nikon Eclipse TS100 microscope (10x) (Nikon, Melville, NY). Five regions of interest per condition were used to determine the overall cell morphologic features. Confocal microscopy images were captured using a Zeiss 880 confocal microscope (10x) (Zeiss, Oberkochen, Germany). Five random regions of interest per field were used to determine red (CK-18) and green (vimentin) fluorescence intensity. Uniform laser settings, brightness, contrast, and collection settings were matched for all images collected. Images were not modified (brightness, contrast, and smoothing) for intensity analysis. ImageJ software version 1.51J (NIH, Bethesda, MD; http://imagej.nih.gov/ij) was used to measure vimentin and CK-18 staining intensity from two focal planes of three different regions per

treatment condition at each time point. Image analysis was conducted in triplicate for all cell experiments.

SA-β-Gal assay

The presence of the SA-β-Gal distinguishes senescent cells from quiescent cells [13, 28, 144, 145]. This enzymatic activity is distinct from the ubiquitous acidic b-galactosidase and can be detected at pH 6.0 using the chromogenic substrate X-Gal. Senescent cells were identified using a histochemical staining kit (Sigma-Aldrich), with blue cells visualized by light microscopy 38 hours after treatment. Four regions of interest per condition were captured by bright-field microscopy using a Nikon Eclipse TS100 microscope (10x). Uniform brightness, contrast, and collection settings were matched for all images collected. Image modifications (brightness, contrast, and smoothing) were applied to entire image sets using Lightroom software version 7.4 (Adobe, San Jose, CA) and ImageJ software. The total number of cells in each bright-field was counted, and the number of SA-β-Gal positive cells was divided over the total amount of cells to show the percentage of SA-β-Gal stained cells per condition.

Total collagen type 1 assay

A total collagen type 1 assay kit was purchased through Abcam, and kit instructions were modified to run cell culture medium. Cell supernatants were mixed with equal volumes of sodium hydroxide (10N) and hydrolyzed individually at 120ºC for 1 hour. Samples were then cooled on ice, and the hydrolysate was neutralized by adding an equivalent volume of hydrogen chloride (10N). Supernatants were decolorized by adding 4mg of activated charcoal to the neutralized hydrolysate and centrifuged at 10,000g for 5 minutes to remove precipitate and activated charcoal. Clear supernatant (10mL) was added to a 96-well plate. The standards and samples were evaporated by heating at 65ºC on a hot plate. Oxidation mix (100µL) was added and the plate incubated at room temperature for

20 minutes. Developer (50mL) was then added to each well and kept at 37ºC for 5 minutes. 4-(Dimethylamino)-benzaldehyde concentrate solution (50μL) was added and the plate placed on a hot plate at 65ºC for 45 minutes. Absorbance of each sample was then measured at OD 560 nm using a microplate reader. Standard curves were developed with samples of known quantities of recombinant proteins that were provided by the manufacturer. Sample concentrations were determined by relating the absorbance values obtained to the standard curve by linear regression analysis. Manufacturer's instructions were followed to calculate the hydrolysate and total collagen production in micrograms per microliter.

Enzyme-linked immunosorbent assay (ELISA) for inflammatory marker Interleukin-8 (IL-8)

ELISA was performed for IL-8 (Biosource International, Camarillo, CA, and Luminex Corporation, Austin, TX) as an indicator of general inflammation. As a chemokine, IL-8 has been associated with EMT [146], senescence [13], and wound healing [147]. Standard curves were developed with duplicate samples of known quantities of recombinant proteins that were provided by the manufacturer. Sample concentrations were determined by relating the absorbance values that were obtained to the standard curve by linear regression analysis.

Statistical analysis

Data were analyzed for significant differences using GraphPad Prism software version 7 (GraphPad Software, San Diego, CA). One-way analysis of variance followed by the Tukey multiple comparison posthoc test or the t-test were used for comparison of the studied groups. Statistically significant difference was indicated by a $P < 0.05$.

RESULTS

Innate state of AECs

To determine the innate transition state of primary AECs in culture, immunocytochemical analyses of epithelial and mesenchymal intermediate filaments, CK-18, and vimentin, respectively, were performed, followed by confocal microscopy. To rule out any deleterious effects of processing of placental membranes for cell cultures, AECs at passage zero (P0) and P1 were immunostained. P0 AECs stained 24 hours after isolation showed expression of both CK-18 and vimentin and had round morphologic features, which is as expected and normal before attachment to the culture plates. Cells attained the typical cobblestone morphologic features of epithelial cells in P1, with enhanced expression of both intermediate filaments (Fig. 4.1). Freshly harvested AECs contained both CK-18 and vimentin, two key components of epithelial and mesenchymal cells, suggesting that they were at an in-between state of transition termed metastate.

Migratory and transition potential of AECs

The migratory potential of metastate AECs was studied under normal in vitro conditions. Wounds inflicted by scratch on AECs healed naturally within 38 hours that included AEC proliferation, migration, and transition (Fig. 4.2, A and B, and Sup. Fig. 4.1). Specifically, cell morphologic changes and changes in the expression pattern of CK-18 and vimentin were examined to determine changes associated with wound healing. Co-expression of CK-18 and vimentin were seen before scratch and up to 10 hours after the initial wound. After 22 hours, the dominance of vimentin-positive cells with mesenchymal morphologic features at the leading edge were seen (Fig. 4.2C). Mesenchymal cells are more migratory [148], and the CK-18/vimentin staining pattern suggests that EMT promoted cellular migration to heal the wound. Wounds were healed within 38 hours, and examination of these sites showed the dominance of intermediate filament CK-18 cells with a morphologic finding that indicated MET (Fig. 4.2C). Confocal microscopic analysis confirmed that perinuclear vimentin-stained cells with epithelial morphologic features were predominant before scratch, whereas proliferating cells at leading edges showed

increased vimentin staining at the periphery of cells (Fig. 4.3, left column). After 38 hours, AECs with perinuclear vimentin and epithelial morphologic features dominated the healed wound. CK-18 was diffused throughout the cytoplasm and did not follow the same reorganization trend as vimentin during wound healing (Fig. 4.3, right column). The EMT and MET not only produced differential expression of intermediate filaments but also caused cytoskeletal reorganization.

OS prevents wound closures

Intra-amniotic OS and ROS are required for cellular proliferation and fetoplacental growth [149]. At term, increased OS and reduced antioxidant levels promote OS-induced cellular damage [2, 13, 19, 28]. To test the ability of AECs to undergo transition and their wound healing capacity under OS, we conducted scratch assays after exposing the cells to CSE, an inducer of OS [28]. The water-soluble portion of CSE is used exclusively as a laboratory reagent because it is a well-reported OS inducer and produces changes in AECs in culture to mimic fetal membranes at TL. Examination of various CSE components and their potential risk during pregnancy are beyond the scope of this study. CSE treatment of cells that mimicked OS experienced at TL prevented wound healing. This was noted based on the distance between the two scratch edges which was significantly shorter (108.2±45.06μm) in the CSE-treated group compared with controls (867±96.01μm) ($P<0.0001$) after 38 hours. OS caused by CSE was reversed by co-treatment with N-Acetyl-L-Cysteine (NAC). Co-treatment with NAC and CSE in culture medium significantly improved wound healing because the distance traveled by cells to heal the wound was higher compared with CSE alone (655.41±9.27μm; $P<0.001$) (Fig. 4.4A and B).

AF accelerates wound healing

The amniotic membrane, composed of a single layer of AECs, is constantly bathed in AF that contains but is not limited to growth factors, cytokines, and exosomes [150,

151]. We tested the hypothesis that nutrient-rich AF can nourish and nurture amniotic membranes to heal any gaps generated by cell shedding. Scratch wounds were treated with TNIL AF because these samples have lower levels of ROS and markers of OS compared with TL samples [19]. Treatment with TNIL AF healed wound edges by inducing cell migration that covered a greater distance between the two scratch edges compared with controls (1193±23.79μm versus 867±96.01μm; $P<0.01$), therefore consistent with supporting our hypothesis.

OS induces a constant state of EMT

Immunocytochemistry followed by confocal microscopy and ImageJ analysis of vimentin/CK-18 ratios was used to determine the transition potential of AECs during wound healing. On the basis of staining intensity, wound healing involved both EMT and reversal of this process (MET). Control cells (P1 cells in normal culture conditions) healed the wound by undergoing EMT, visualized at 22 hours by high vimentin/CK-18 ratios at the leading edge ($P<0.0001$), and MET, visualized at 38 hours by low vimentin/CK-18 ratios at healed edges ($P<0.0001$) (Fig. 4.5A and B). CSE treatment did not heal the wound and induced a constant state of EMT (Fig. 4.5C), which was demonstrated by high vimentin/CK-18 ratios at 22 and 38 hours (Fig. 4.5A and C). Co-treatment with NAC (EMT: $P<0.001$; MET: $P<0.01$) (Fig. 4.5A and D) improved wound healing similar to that of controls and AF (EMT: $P<0.01$; MET: $P<0.01$) (Fig. 4.5A and E). These results support our hypothesis that OS can generate a terminal state in cells, preventing their transition to a normal state.

OS induces senescence and increases collagen production

As mentioned in the opening paragraphs of this chapter, CSE causes senescence of AECs in culture after 24 hours, a phenomenon seen in membranes at TL and a condition associated with parturition [28, 152]. Therefore, whether CSE caused AEC senescence,

preventing cell proliferation and migration, was tested. AECs were stained for SA-β-Gal as a marker of senescent cells. Bright-field microscopy demonstrated a significantly higher amount of SA-β-Gal-positive cells (blue cells) after CSE treatment compared with controls ($P<0.05$) (Fig. 4.6A and B). SA-β-Gal-positive cells were recorded at the wound site and throughout the general cell population of CSE-treated cells. Medium samples were analyzed for total collagen production and inflammatory mediators to determine collagen concentration at the scratch site. CSE treatment significantly stimulated collagen production ($P<0.0001$) compared with controls; co-treatment with NAC did not decrease collagen production to a statistically significant level (Fig. 4.6C). AF treatment also significantly increased collagen concentration in the medium compared with control AECs ($P<0.0001$) (Fig. 4.6D). Nascent collagen production can be considered as an inflammatory process associated with remodeling, and it is likely that OS-induced damage, as well as AF nurturing of cells to proliferate and migrate, is associated with collagen synthesis.

Inflammation is associated with wound healing

The proinflammatory cytokine IL-8 was observed at the wound healing site. Although IL-8 was induced by CSE (19.67±11.44pg/mL) after 38 hours, it was not significantly different from controls (11.92 ±4.738pg/mL) (Fig. 4.6E). Co-treatment of CSE with NAC (12.13 ±5.947pg/mL) decreased IL-8, although this decrease was not significant (Fig. 4.6E). Cellular senescence caused by CSE diminished tissue remodeling capacity of AECs, even with a mild increase in local proinflammatory cytokines. IL-8 progressively increased in both control and AF-treated cell cultures, and a maximum value was seen at 38 hours. IL-8 was significantly higher in AF-treated cells (75.49±17.25pg/mL) at 38 hours compared with control cells (17.25±8.45pg/mL) ($P<0.05$) (Fig. 4.6F), supporting the view that pro-inflammatory cytokines contribute to wound healing. The term AF samples that were used contained IL-8, which can confound the increased IL-8 that occurs in the medium. To control for this, IL-8 ELISA of AF samples was conducted,

and values were deducted from the medium IL-8 concentrations reported here. Wound healing is an inflammatory process, and IL-8 chemoattracts neutrophils to aid wound healing. Accelerated healing of wounds by AF compared with controls is likely to be aided by increased localized proinflammatory cytokines, as indicated by IL-8 increase in the medium.

DISCUSSION

OS and inflammation are physiologic components of pregnancy that help to promote tissue remodeling and membrane integrity maintenance [96]. As previously reported by us, microfractures develop during membrane growth in gestation because of shedding of senescent or apoptotic cells, characterized by degradation of basement membranes and ECM collagen [96, 140]. However, these microfractures do not threaten pregnancy status or membrane integrity because they are healed by tissue and collagen remodeling. This process is aided by ROS mediated signaling and localized inflammation similar to what is documented in wound healing [153]. This physiologic process of tissue remodeling is likely to be aided by nutrient-rich AF and is a balanced process throughout pregnancy. However, at term, increased fetal metabolic demands and decreased feto-maternal antioxidants lead to OS build-up in the amniotic cavity, which perturbs remodeling [41]. This build-up leads to a terminal state of EMT, senescence, and inflammation, preventing recycling of transitioned mesenchymal cells back to their epithelial state.

In this study, these scenarios were tested by inflicting a wound in cultured AECs, and the ability to seal these sites of insult was investigated. Whether AECs are stem cells or cells that exhibit stemness within the right environment has been debated. Regardless, tissue regeneration properties are widely used in a variety of clinical fields to promote wound healing [46, 47]. In this study, AECs were shown to proliferate, migrate, transition, and heal wounds in vitro (Sup. Fig. 4.1). In addition, the effect of the excessive OS (similar

to that seen at TL) was tested in reducing migratory and proliferative (Sup. Fig. 4.1) capability of cells that could prevent wound healing and the capacity of AF to promote healing and wound closure during gestation.

The key findings from this study are as follows: i) AECs at term gestation are not dead cells and are capable of proliferation, migration, transition, and self-renewal, which indicates their stemness; ii) amnion cells show innate expression of both epithelial and mesenchymal intermediate filaments, causing them to be in a metastate phenotype; iii) wound healing of amnion involves proliferation and migration of cells with cytoskeletal reorganization, while undergoing transition between EMT and MET; iv) AF expedites wound healing, aided by low levels of inflammation, stimulation of collagen synthesis, nourishment of AECs, and a likely reduction in OS; and v) on the contrary, OS induces a terminal state of EMT, senescence, and inflammation, which compromises wound healing. This effect of OS can lead to membrane dysfunction and mechanical instability [53]. These changes can also predispose membranes to rupture, although this depends on the strength of redox imbalance. The OS-induced outcome was partially reversed by co-treatment with NAC, thus supporting our hypothesis. In summary, we determined that AECs, through a regulated EMT and MET transition (Fig. 4.7), can heal gaps or microfractures, and this process is likely to be facilitated by AF. Increased OS at term [154] or in response to OS-inducing risk factors at preterm reduces the capacity for microfracture healing, which can predispose membranes to rupture.

AECs are unique because of their pluripotent status as stem cells [155], as well as their co-expression and localization of epithelial and mesenchymal markers. The ability of cells to express both epithelial and mesenchymal phenotypes was first reported by Savagner as a metastable phenotype, documented in his studies of Rac distribution in cancer cells [61, 70]. Here we describe AECs in an in-between state of epithelial and mesenchymal transition that we term a metastate, which is critical for AEC survival and maintenance of membrane integrity. Metastate is a response to changes in the membrane

microenvironment, which helps maintain homeostasis and promotes wound healing during pregnancy. As previously reported [96], microfractures should not persist because they present likely channels for trafficking of shed AECs, immune cells, and leakage of AF. Although these characteristics have been overlooked in recent years, heterogenous populations of AECs expressing both vimentin and cytokeratin were first documented in the early 1980s [156, 157]. Our ongoing studies support these findings, and additional EMT/MET-associated changes, such as differential expression of E-cadherin and N-cadherin expression, changes in stem cell transcription factors Nanog and OCT4, and other EMT/ MET transcription factors in cultured AECs and tissue explants, have been observed. These metastate qualities of AECs are consistent with the expression of stem cells undergoing EMT, which is likely the reason that AECs are used as progenitor cells to generate various organs [49]. These properties of AECs and amnion membranes are also used extensively for wound healing in burn patients [44-46, 68, 158].

Similar to some cancer cells, AECs can undergo EMT to migrate followed by MET at a secondary site to perform specific functional roles, such as sealing the site to complete the repair process. These morphologic changes are also supported by the occurrence of vimentin localization (Fig. 4.3) that has been documented to be vital for cell proliferation and migration in cancer cells [62, 159]. Cells with perinuclear vimentin staining with epithelial morphologic features were predominant before scratch and at healed edges, whereas leading and migratory edges had vimentin staining at the periphery of cells with mesenchymal morphologic features. This type of vimentin re-localization has been previously reported, and we were able to recapitulate this in our model [159, 160].

CK-18 localization was diffused throughout the cytoplasm and did not follow the same reorganization trend as vimentin during wound healing. This finding suggests that vimentin expression and localization play a vital role in transitioning AECs and can be used as a marker to document cells undergoing EMT or MET. The vimentin/CK-18 ratio may be used to monitor the state (epithelial vs. mesenchymal) of cells before conducting

experiments with AECs. These cells are always in a state of transition under specific environmental conditions, and their functional roles may be dependent on the dominant state of cells.

Throughout gestation, amnion membranes maintain their structural integrity by growing, healing microfractures, and adapting to changes in the endocrine and immune milieu. This adaptation is feasible because of their metastate qualities. The inflammatory environment observed in response to various treatments in our study indicates how AECs will respond to changes in the microenvironment. Here we document the existence of generalized inflammation at wound healing sites, consistent with the role of inflammation (i.e., walling of the spread of an infection at the injury site and remodeling of tissue). Homogeneity in the inflammatory profile (collagen and chemokine increase irrespective of AF or CSE treatment) does not necessarily indicate functional harmony. In fact, these changes are indicative of distinct mechanisms in which the same inflammatory mediator may show uniformity in its concentration. Control and AF treatments tend to produce inflammation that is likely to promote remodeling [146] and wound healing [147], whereas inflammation associated with CSE treatment is likely caused by cellular senescence [28], the latter being a detrimental factor for membrane survival. However, there are limitations in using some inflammatory mediators as biomarkers associated with pregnancy complications. On the basis of the underlying physiologic or pathophysiologic mechanisms, these biomarkers may be indicative of distinct underlying functions, and an increase in a cytokine/chemokine does not always reflect a pathologic condition.

Here we also document the natural ability of AECs to proliferate, migrate, and heal wounds via EMT and MET transition (Fig. 4.2) and how AF supports the metastate qualities of AECs in enhancing wound closure (Fig. 4.5). The data above suggest that nutrient-rich AF stimulates low levels of IL-8 (Fig. 4.6), causing metastate AECs to undergo EMT and MET transition and promoting collagen synthesis to heal wounds. The levels of IL-8 seen during wound closure (approximately 60pg/mL of IL-8) (Fig. 4.6) are

much lower than IL-8 levels reported in TNIL (2941pg/mL) and TL (5571pg/mL) AF [13], suggesting that treatments with AF can stimulate low levels of IL-8 that do not harm the cells but help them to remodel. This study did not examine specific factors involved in AF promotion of cellular transitions and/ or its remodeling properties, although AF has various growth factors, cytokines, and exosomes with a potential role in wound healing [150, 151]. Analysis of the specific AF constituent responsible for promoting AECs properties described here is beyond the scope of this work. We postulate that this well-balanced process of cellular transition, collagen production, and inflammation plays a role in the healing of placental membranes after fetal surgery in women who have a balanced intra-uterine redox status. However, exposure of placental membranes to the excessive OS, at term or preterm, induces a terminal state of EMT, causing senescence and senescence-associated inflammation that will prevent repair capabilities. The CSE data support this concept that OS could be a contributor of membrane rupture at term or preterm gestation, specifically in cases of pPROM, where an increased number of microfractures [96] or lack of microfracture healing can compromise fetal membrane integrity. Although lack of remodeling, senescence, and inflammation are likely to be physiologic requirements for promoting parturition at term, all these factors could also cause premature rupture of the membranes leading to PTB.

In summary, we report certain unique features of fetal AECs. These cells exist in a metastate, undergoing constant transitions that will help to maintain membrane structural and mechanical integrity. Stemness of AECs and their remodeling capabilities are aided by nourishment by AF. Excessive OS disrupts transitions and the remodeling process and can contribute to membrane dysfunction. We have already shown pathways of senescence and how senescence can disrupt membrane integrity. Herein, we provide additional information on the process by which membrane healing can be disrupted by senescent cells. Understanding the mechanisms and mediators of EMT and MET will increase our knowledge of the contribution of membranes to human pregnancy and parturition.

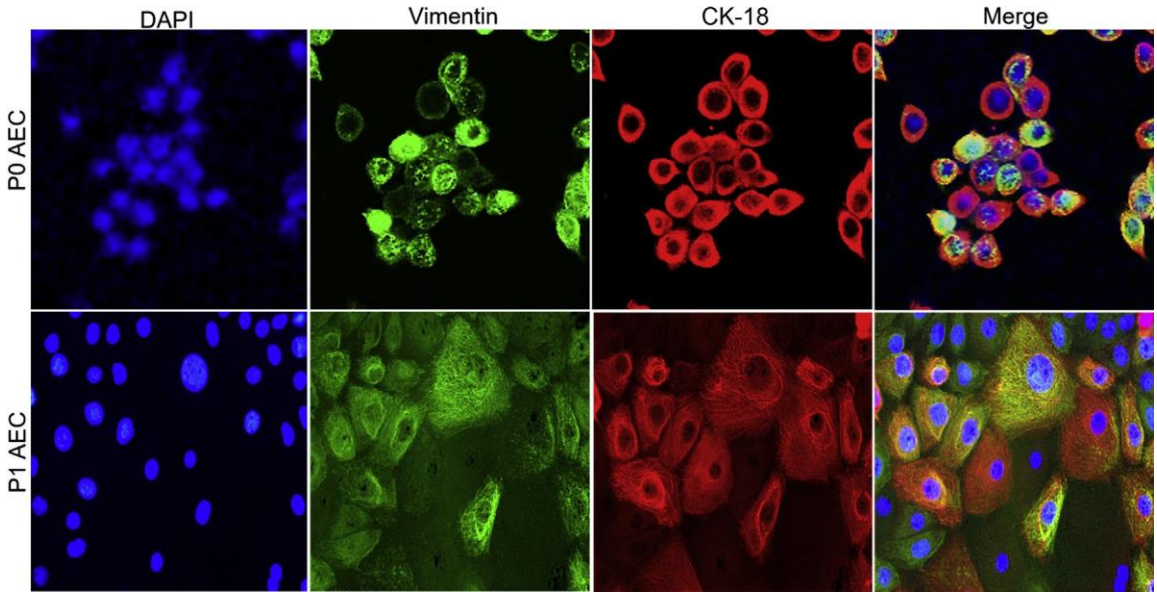

Fig. 4.1 Characteristics of metastate AECs in culture.

Confocal microscopy showing vimentin (green) and CK-18 (red) localized in the cytoplasm of both P0 and P1 AECs. Perinuclear localization of vimentin and CK-18 is expected in P0 cells. Fully attached P1 cells show cytoplasmic localization of both vimentin and CK-18. Original magnification, 63x.

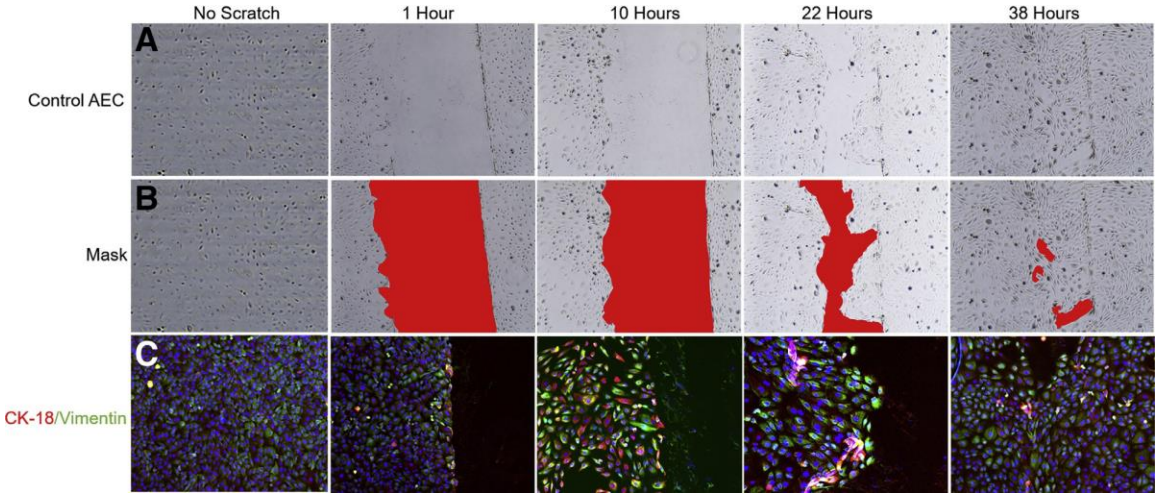

Fig. 4.2 Scratch assay demonstrates that AECs naturally heal wounds.

A) Bright-field microscopy of AECs under normal cell culture conditions showing wound healing at 38 hours. B) A red mask was overlaid on the wound to highlight the area of AEC proliferation and migration throughout the 38 hour period. C) Fluorescence microscopy showing vimentin (green) and CK-18 (red) localized in the cytoplasm of AECs at various time points after the scratch and in no-scratch control cells. A heterogeneous population of cells co-expressing both markers was recorded at 1 hour and 10 hours, as well as in the no-scratch control experiment. At 22 hours, AECs were predominantly vimentin positive at the leading edge. After healing of the wound at 38 hours, AECs reverted to metastate, co-expressing both intermediate filaments with the dominance of CK-18. Original magnification, 10x.

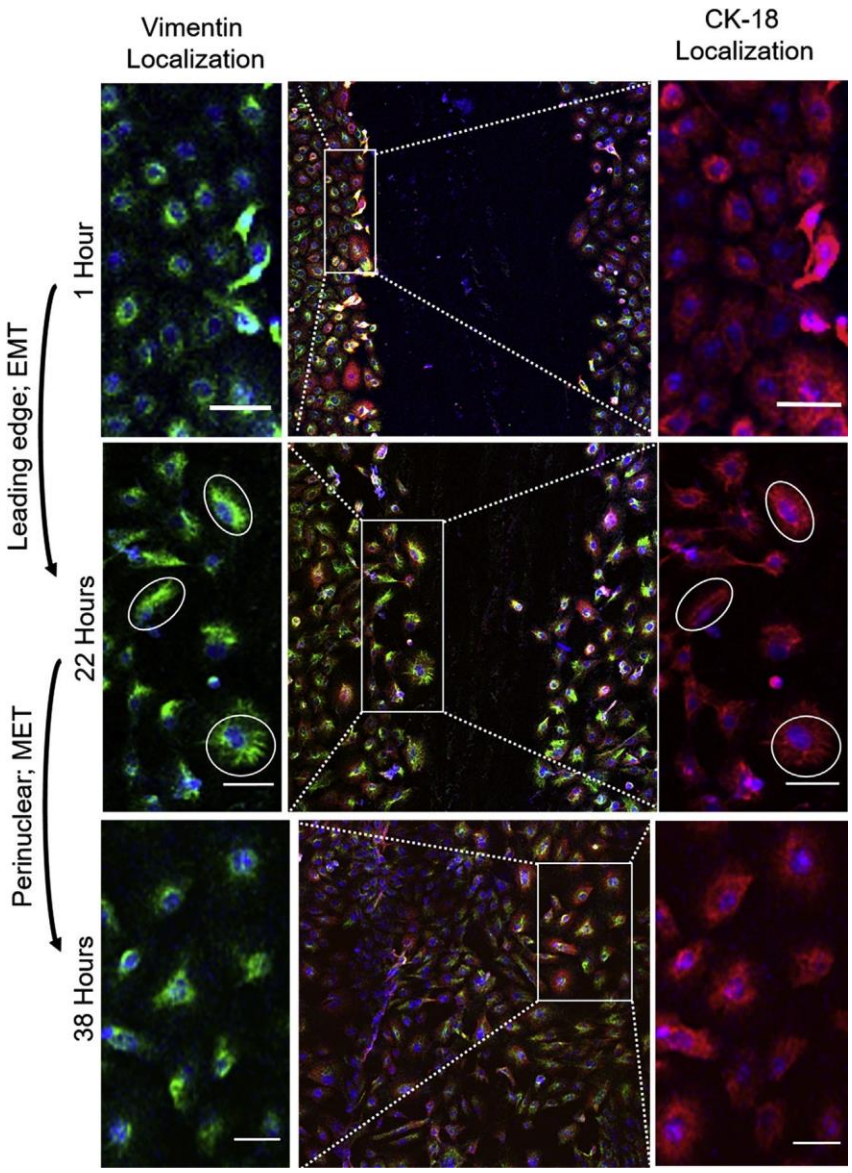

Fig. 4.3 Vimentin relocalization during wound healing.

Confocal microscopic images showing vimentin (green) and CK-18 (red) localized in AEC healing a wound. At the scratch site (left column), vimentin is located in the perinuclear region of predominantly epithelial amnion cells. This localization shifts to the periphery of cells at the migratory edges, where cells start to acquire mesenchymal morphologic features, indicating EMT. White circles highlight vimentin localization on the leading edge. Wound healing site is characterized by perinuclear localization of vimentin along with cells acquiring epithelial morphologic features, suggesting MET. Right column: Although expression levels change, unlike vimentin, localization of CK-18 does not change during the EMT or MET process (white circles). Boxed areas in the center column are enlarged in both the left and right columns. Scale bars=50μm. Original magnification, 10x.

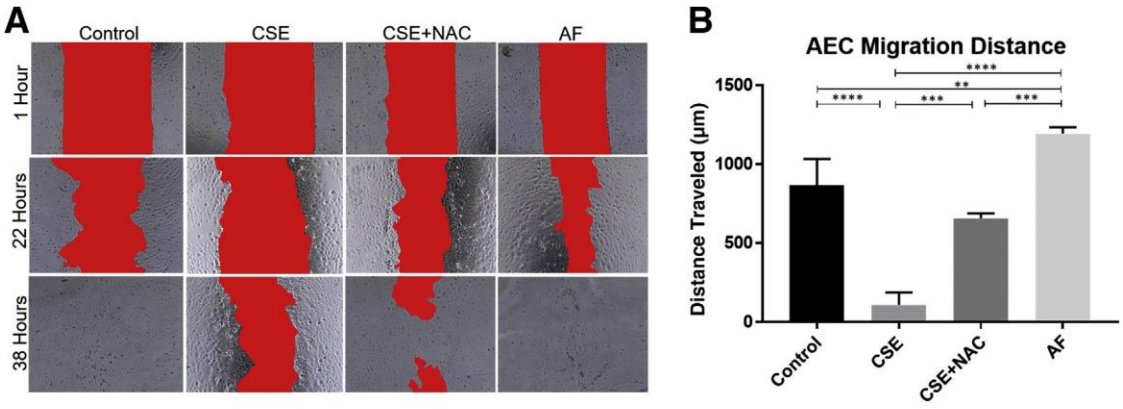

Fig. 4.4 Documentation of cellular migration and wound healing under normal OS conditions and after treatment with amniotic fluid.

A red mask was applied to help visualization of the wound field and distance was measured at different time points. AECs under normal cell culture conditions show their natural ability to heal a wound within 38 hours. CSE prevents wound healing, indicated by a migration distance between the two scratch edges that is significantly shorter (108.2±45.06µm) in CSE-treated group compared with controls (867±96.01µm) after 38 hours. Co-treatment with antioxidant NAC significantly increases the distance traveled by cells to heal the wound (655.4±19.27µm) compared with CSE alone. Treatments with TNIL AF heals wound edges by increasing migration distance between the two scratch edges compared with controls (1193±23.79µm vs. 867±96.01µm). Data are expressed as means±SD (B). **P < 0.01, ***P < 0.001, and ****P < 0.0001. Original magnification, 10x.

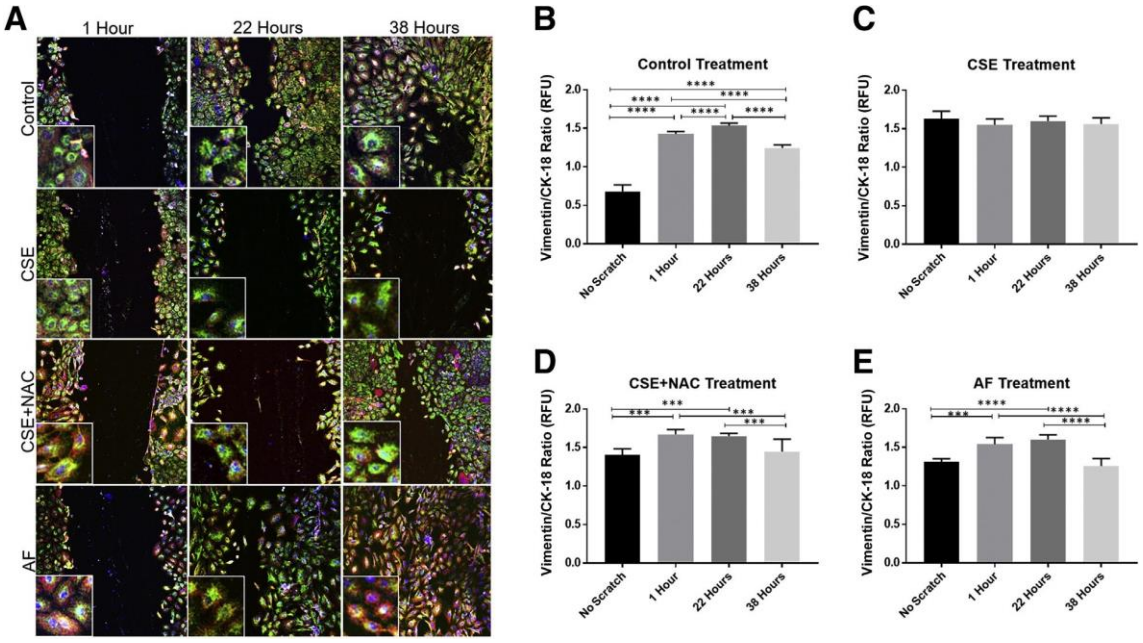

Fig. 4.5 AECs heal wounds by undergoing EMT and MET.

A) Confocal microscopy image showing vimentin (green) and CK-18 (red) localization in AEC wound healing after different treatments. Insets show the overall staining pattern for each treatment. B) Under normal cell culture conditions, EMT was demonstrated at 22 hours with high vimentin/CK-18 ratios at the leading edge, and MET was demonstrated at 38 hours by low vimentin/CK-18 ratios at healed edges. C) CSE treatment induces a constant state of EMT compared with controls. D) The effect of CSE is inhibited by co-treatment with antioxidant NAC, which enables wound healing by promoting EMT, demonstrated at 22 hours by high vimentin/CK-18 ratios at the leading edge, and MET demonstrated at 38 hours by low vimentin/CK-18 ratios at healed edges. E) AF treatments of cells produce changes similar to that of control. Wounds heal by EMT, demonstrated at 22 hours by high vimentin/CK-18 ratios at the leading edge, and MET, demonstrated at 38 hours by low vimentin/CK-18 ratios at healed edges. Data are expressed as means±SD (B). ***P<0.001, ****P<0.0001. Original magnification, 10x. RFU, relative fluorescence units.

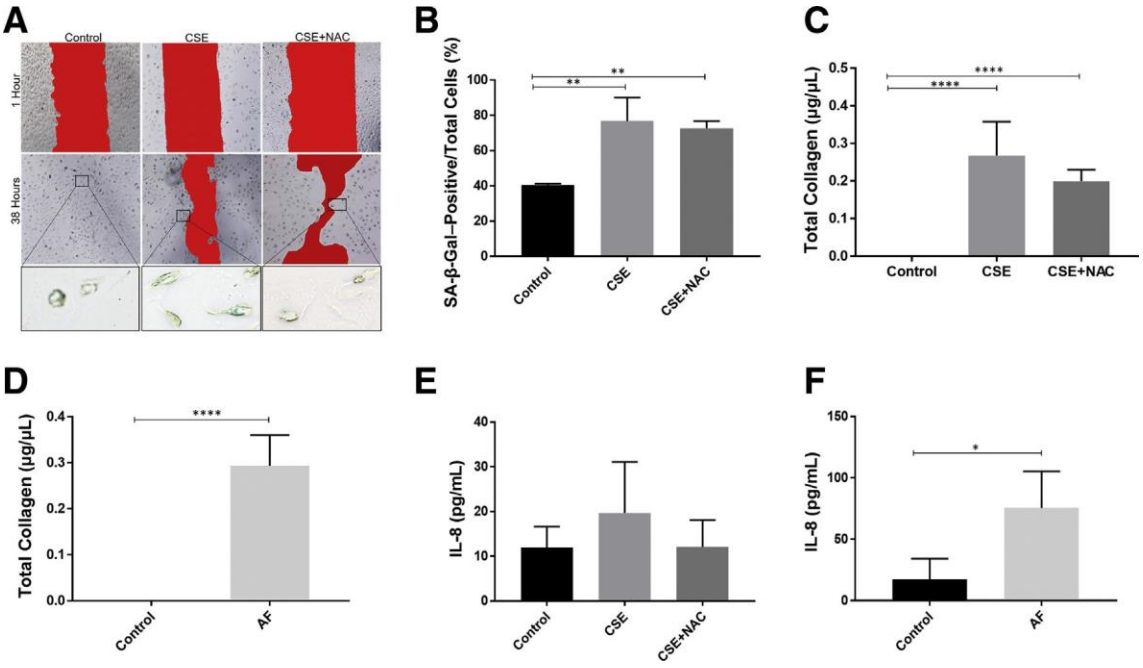

Fig. 4.6 EMT is associated with senescence, collagen production, and inflammation.

A and B) SA-β-Gal: CSE induced senescence (blue stain) in a larger population of AECs healing the wound compared with controls, as seen in A and quantified in B. Boxed areas in the middle row of A are shown at higher magnification in the bottom row. C and D) Collagen assay. C) CSE treatment significantly stimulates collagen production compared with controls, whereas antioxidant NAC decreases collagen production. D) AF treatment also significantly stimulates collagen production compared with controls. E and F) Chemokine IL-8 release. E) After 38 hours of exposure, CSE-treated AECs release more IL-8 than controls and CSE plus NAC. F) AF induces a significant amount of IL-8 production after healing the wound for 38 hours compared with controls. Data are expressed as means±SD (B-F). *P<0.05, **P<0.01, and ****P<0.0001. Original magnification: 10x (A, top and middle rows); 40x (A, bottom row).

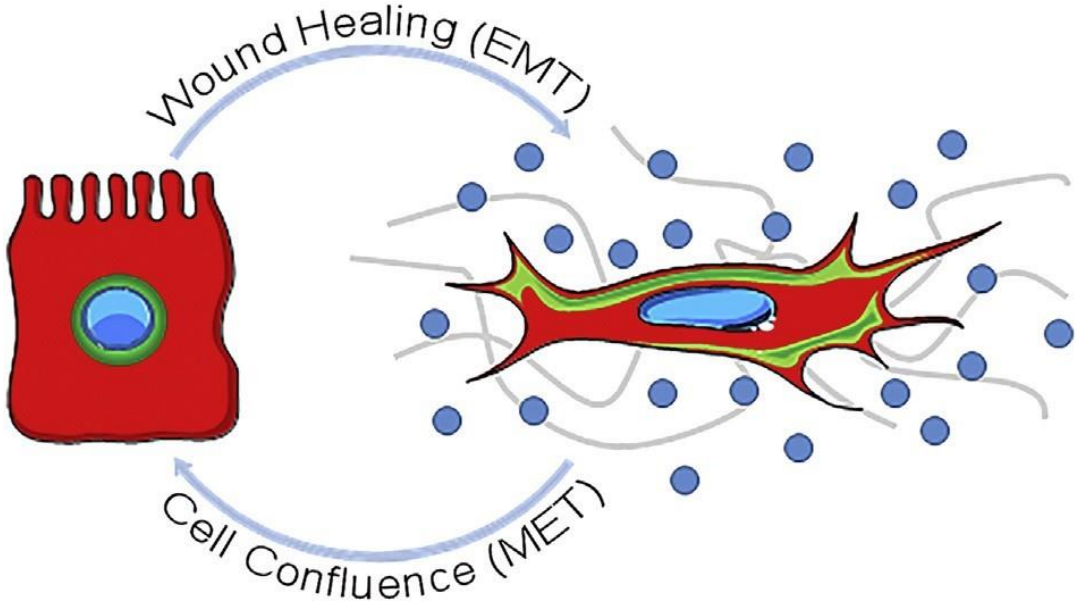

Fig. 4.7 AECs undergo EMT and MET to remodel placental membranes.

Diagram representing metastate AECs. AECs undergo EMT to heal a wound in which perinuclear vimentin (green) is increased and relocalized to the periphery and leading edges of cells along with increased collagen (gray lines) and inflammatory mediator (blue circles) production. The transition is complete when epithelioid morphologic features are transformed into a mesenchymal shape. Wound closure is facilitated when cells revert to MET when epithelial morphologic features are reinstated to perinuclear localization of vimentin. This process promotes recycling and remodeling of AECs in the placental membranes. Cytokeratin-18-red, vimentin-green.

Mechanisms of EMT and MET: Can they play a role in fetal membrane homeostasis?

This study shows that injury to AECs forces proliferation and cellular transitions such as EMT during migration and the reverse (MET) during wound resealing (**Chapter 4**)[128]. Due to the pluripotent 'metastate' status of amnion cells, AECs are primed to respond, transition (EMT-MET), and adapt to micro-environmental stimuli throughout gestation to maintain the amnion membrane barrier function. Cellular transitions could contribute to cells specific acts of membrane remodeling such as 1) filling or resealing a gap due to cell shedding or cell death or 2) regeneration of ECM collagen in void regions of the stroma [39, 96]; Both of which help maintain fetal membrane homeostasis. TNIL AFs ability to expedite wound healing, likely due to its nourishing components and anti-inflammatory profile (e.g., P4), could counteract injury due to localized ROS production. Conversely, increased OS at term (i.e., CSE treatment), leads to persistence of microfractures (i.e., prevention of wound healing), a terminal state of EMT, senescence, and inflammation contributing to membrane dysfunction. Though this data suggests cellular transitions could play a vital role in membrane homeostasis during gestation and its disruption at term, the signaling pathways regulated these cellular changes remain unknown.

In the fetal membranes, term labor status is associated with OS-induced p38 MAPK activation [13, 28]; therefore understanding OS-induced signaling in AEC might elucidate pathways associated with EMT, senescence, and inflammation. Recent data from our lab showed that exosomes collected from OS-treated, AECs dominantly express proteins related to TGF-β signaling pathways compared to control cells [143]. TGF-β is a known p38 MAPK activator and EMT inducer [161, 162]. Due to the exosomes' ability to represent the physiological state of its origin cells, TGF-β could be a potential mediator in OS-induced EMT. We systematically tested this hypothesis by studying all of the OS-induced upstream regulators of p38 MAPK activation that could be responsible for labor-associated changes (**Chapter 5**).

Chapter 5. OS-induced TGF-β/TAB1-mediated p38 MAPK activation in human AECs [224]

INTRODUCTION

The global PTB rate is approximately 10% of all pregnancies, contributing to one million neonatal deaths/year and other health complications for survivors [163-165]. The majority of PTBs are spontaneous with unknown etiologies but are pathologically highlighted by infection/inflammation and OS [166-169]. Similarly, normal term labor and delivery is also affected by sterile inflammation and OS, compared to normal TNIL cesarean deliveries [29, 170-172]. It is difficult to ascertain the cause and origin of sterile inflammation in PTB [13, 14, 173-175]. Senescence of feto-maternal tissues, often characterized by chronic sterile inflammation, has recently been linked to term and PTB [29, 165, 172, 174, 175]. Further, studies using human and murine fetal membranes (amniochorion) determined that OS is one of the promoters of cellular senescence that generates sterile inflammation [13-15, 19, 41, 176]. Fetal membranes encounter increased OS at term due to metabolic demands that expand in response to fetal growth, heightened respiratory needs, and altered maternal metabolic supply [19, 35, 177]. Inflammatory markers from senescent cells are inherently uterotonic and capable of transitioning quiescent uterine tissues to an active contractile state (labor) at term [13, 176]. Conversely, premature senescence activation caused by various risk factors can trigger PTB [2, 31].

Mechanistically, OS-induced senescence in fetal membranes, at term and preterm, is mediated through the stress signaler p38 MAPK [13-15, 41]. p38 MAPK, including all four of its isoform (α, β, γ, and δ), are part of a 14 member MAPK superfamily containing extracellular signal-regulated kinases (ERK)1/2, ERK5, and c-Jun N-terminal kinases

(JNK) are the others [178]. In general, all MAPK pathways consist of three dependent kinases activated in a sequential manner that include Mitogen-Activated Protein Kinase Kinase Kinase (MAPKKKs), MAPK kinases (MAPKKs), and MAPKs. Dual phosphorylation of tyrosine and threonine residues, which can be activated by one or two kinases in the activation loop of kinase subdomain, phosphorylate all four isoforms of MAPK [179].

p38 MAPK also consists of four signaling isoforms (p38 MAPK α, β, γ, and δ) that are evolutionarily conserved serine/threonine kinases whose functions differ significantly [179, 180]. The p38 MAPK α isoform is the most dominant of the four in reproductive tissues; its activities are essential for normal development [179] and other physiological processes [181, 182]. Multifactorial functions of p38 MAPK in reproduction [183] include preimplantation [184], embryogenesis [185, 186], placental function and development [182, 186], and decidualization [187, 188]. p38 MAPK is also a mediator of cellular senescence, a mechanism of aging, which is a non-reversible process. Senescent cells can remain in the tissue environment without undergoing cell death and constantly secret inflammatory mediators and damage-associated molecular pattern markers.

In fetal membranes, OS increases p38 MAPK activation (P-p38 MAPK alpha), leading to senescence and sterile inflammation seen in normal term [13] and PTB [4, 31]. In vitro, primary cultures of fetal membrane cells (AECs) exposed to OS showed p38 MAPK-mediated senescence and inflammation that was reduced by p38 MAPK inhibitor SB203580 (SB) [28]. Similarly, a progressive increase in p38 MAPK in fetal membranes and placenta in murine pregnancy that peaked on days 15–18 of gestation also correlated with OS and senescence [14]. Exogenous signals such as environmental pollutants [152], cigarette smoke [34], infection and inflammation, and cell damage-associated molecular pattern markers [41] were all shown to induce p38 MAPK-mediated senescence and inflammation in AECs. These data support the hypothesis that p38 MAPK-mediated premature senescence activation can contribute to PTB. Thus, p38 MAPK plays a role in

generating inflammation at term and preterm. We postulate that minimizing its activation in gestational tissues can reduce the risk of OS-associated PTB. As p38 MAPK activation can occur through multitudes of pathways in a cell-type-dependent manner [179], a precise mechanism of activation in fetal membrane cells is required to design intervention strategies to minimize p38 MAPK-mediated PTB risks.

OS in AECs is expected to cause two major pathways of p38 MAPK activation: (1) one path is mediated by activation of apoptosis signal-regulating kinase (ASK1)-signalosome [189-191] and (2) the second is caused by activation of TGF-β activated kinase binding protein 1 (TAB1)-mediated p38 autophosphorylation [192-194]. Briefly, the ASK1-signalosome-mediated activation involves antioxidant Thioredoxin 1 (Trx). Reduced Trx forms an inhibitory Trx(SH)2-ASK1 complex that can attenuate ASK1-signalosome-mediated p38 MAPK activation [195]. In this mechanism, Trx(SH)2 interacts with the N-terminal domain of ASK1 and serves as a negative regulator of ASK1 and attenuator of p38 MAPK activity [190, 195, 196]. The OS-mediated oxidation of ASK1-bound Trx(SH)2 dissociates this complex, creating free and activated ASK1-signalosome and leading to p38 MAPK activation [197]. TGF-β is an OS-responding growth factor involved in embryogenesis [198] and tissue remodeling [199]. Interaction between TGF-β-TGF receptors I (TGFR1) and II activates TGF-activated kinase (TAK1), leading to its interaction with TAB1 [198]. TGF-β/TAK1/TAB1 complex, either through canonical MAPKKKs or TGF-β directly through TAB1 (independent of TAK1) by autophosphorylation, results in p38 MAPK activation [200-202]. We tested the mode of activation of p38 MAPK in AECs through these two pathways because both ASK1 [143] and TGF-β pathways [143] were reportedly activated in oxidatively stressed AECs. We found the existence of the ASK1- signalosome in AECs, but an absence of the ASK1-signalosome complex-mediated p38 activation; however, CSE-induced OS in AECs causes TGF-β to increase, leading to a TGF-β-TAB1-mediated p38 MAPK activation.

MATERIALS AND METHODS

This study protocol was approved by the Institutional Review Board at UTMB at Galveston, Texas, as an exempt protocol to use discarded placenta after normal term cesarean deliveries (UTMB 11-251). No subject recruitment or consenting was done for this study. All placental collection methods were performed in accordance with the relevant guidelines and regulations of the IRB.

Clinical samples and cell culture

Fetal membrane samples for this study were obtained from John Sealy Hospital at UTMB at Galveston, Texas, USA. Primary AECs were isolated from reflected amnion (about 10g), peeled from the chorion layer, and dispersed by successive treatments with 0.024% collagenase and 1.2% trypsin. This processing was completed within 2–3 hours of getting the placenta. The dispersed cells were plated in a 1:1 mixture of Ham's F12/DMEM, supplemented with 10% heat-inactivated FBS, 10ng/mL EGF, 2 mM L-glutamine, 100 U/mL penicillin G, and 100 mg/mL streptomycin at a density of 3–5 million cells per T75 [28], and incubated at 37◦C with 5% CO2 for 4–5 days until the cells were ready to be passaged for treatment. CK-18 staining and vimentin staining were conducted to determine epithelial characteristics of amnion cells in culture.

Cell culture treatments

To induce OS in AECs, we used CSE as previously described [28, 203], with slight modifications. CSE is a validated and reproducible OS inducer in our system and we do not use CSE in our experiments as a risk factor of pregnancy. Smoke from a single lit commercial cigarette (unfiltered Camel, R.J. Reynolds Tobacco Co, Winston Salem, NC) was infused into 25mL of medium, consisting of DMEM/F12 supplemented with 10% FBS (System Biosciences, Mountain View, CA). The stock CSE was sterilized using a 0.22μm Steriflip filter unit (Millipore, Billerica, MA). CSE concentrate was diluted 1:10 in

complete DMEM medium prior to use. Once AECs reached 70%–80% confluence, AECs were passaged (P1), allowed to establish baseline characteristics for 24 hours prior to performing additional treatments. Each flask was serum starved for 1 hour and rinsed with sterile 1x PBS followed by treatment with medium (control), CSE containing medium, TGF-β receptor 1, 2, and 3 antagonist (3ng/mL) (R&D, Minneapolis, MN), or TGF-β 2ng/Ml (R&D, Minneapolis, MN). Then, they were incubated at 37C, 5% CO2, and 95% air humidity for 1 hour. The culture medium were collected and stored at −80◦C for evaluation by ELISA.

AEC siRNA transfections

To determine the potential role of each of the two investigated signaling pathways leading to activation of p38 MAPK by CSE, we individually downregulated ASK1, MKK3/6, TAK1, and TAB1 in AECs using siGENOME small interfering ribonucleic acid (siRNA) (GE Healthcare Dharmacon) (Dharmacon, Thermo Fisher Scientific (Rockford, IL); Table 1). Briefly, AECs were cultured to nearly 50% confluence in DMEM/F12 medium supplemented with 10% FBS and antimicrobial agents (Penicillin/Streptomycin, Amphotericin). Prior to siRNA transfection, cells were incubated with antimicrobial-free medium overnight. Next, cells were incubated for 4 hours with siRNA complexes, which were freshly prepared using either 150nM siRNA to specific genes or Non-Target Ribonucleic Acid (NT siRNA) as control and 0.3% Lipofectamine RNAiMAX (Invitrogen, Eugene, OR) in Opti-MEM I Reduced Serum Medium. Cells were further incubated in growth medium for 48 hours. Downregulation efficiency of the target genes was validated by quantitative real-time polymerase chain reaction (qRT-PCR). Gene expression was normalized to nontransfected control.

Crystal violet proliferation assay

AECs were seeded in a 12-well plate (90,000 per well) and treated in replicates of six with control or CSE 1:10 medium for 1 hour. After 1 hour, cells were washed with 1× PBS, fixed with 4% PFA for 15 min, washed with water, and stained with 0.1% crystal violet for 20 min. After 20 min, cells are washed, allowed to dry, and 10% acetic acid was added to each well. A 1:4 dilution of the colored supernatant was measured at an absorbance of 590nm.

Quantitative RT-PCR

To determine the expression levels of TAB1, ASK1, MKK3, MKK6, and MKK4 after treatments, cells were collected and lysed using lysis buffer (Qiagen, Valencia, CA, USA). RNA was extracted using an RNeasy kit (Qiagen) per the manufacturer's instructions. Total RNA (1μg) was reverse-transcribed using a High-Capacity RNA-to-cDNA Kit (Applied Biosystems, Foster City, CA). qRT-PCR was performed on an ABI7500 Fast Real-Time PCR System (Applied Biosystems) using Fast SYBR Green Master Mix (Applied Biosystems). The amplification thermal profile was 20s at 95◦C and 3s 95◦C, followed by 30s 60◦C (40 cycles). To confirm the presence of a single amplicon, a melt curve stage was carried out: 15s at 95◦C, 1min at 60◦C, 15s at 95◦C, and 1s at 60◦C. Changes in gene expression levels were calculated by using the ΔΔCt method [204]. We used predesigned primers from Integrated DNA Technologies (Table 2).

Protein extraction and immunoblot assay

Portions of these cells were collected using NE-PER nuclear and cytoplasmic extraction reagents (Thermo fisher #78835), while the rest of the cells were lysed with Pierce Lysis Buffer for separate ASK1 and Trx pulldown assays. Cells and tissue were lysed with RIPA lysis buffer (50mM Tris pH 8.0, 150mM NaCl, 1% Triton X-100, and 1.0mM EDTA pH 8.0, 0.1% SDS) supplemented with protease and phosphatase inhibitor cocktail and phenylmethylsulfonyl fluoride. After centrifugation at 10,000rpm for 20min,

the supernatant was collected, and protein concentrations were determined using BCA (Pierce, Rockford, IL). The protein samples were separated using SDS-PAGE on a gradient (4%–15%) Mini-PROTEAN TGX Precast Gels (Bio-Rad, Hercules, CA) and transferred to the membrane using iBlot Gel Transfer Device (Thermo Fisher Scientific). Membranes were blocked in 5% nonfat milk in 1× Tris-buffered saline-Tween 20 or in 5% BSA buffer for a minimum of 1 hour at room temperature and then probed (or reprobed) with primary antibody overnight at 4◦C. The membrane was incubated with appropriate secondary antibody conjugated with horseradish peroxidase and immunoreactive proteins were visualized using Luminata Forte Western HRP substrate (Millipore, Billerica, MA). The stripping protocol followed the instructions of Restore Western Blot Stripping Buffer (Thermo Fisher). No blots were used more than three times. The following anti-human antibodies were used for western blot: ASK1 (1:750, Cell Signaling, Danvers, MA), TRX (1:1000, Abcam, Cambridge, United Kingdom), TAB1 (1:1000, R&D, Minneapolis, MN), P-TAB1 (1:800, Milipore, Thr431, Burlington, MA), P-p38 MAPK (1:300, Cell Signaling, T180/Y182), p38 MAPK (1:1000, Cell Signaling) (Table 3).

Immunochemical localization

For immunocytochemistry of CK-18 (1:300, Abcam), ASK1 (1:250, Cell Signaling), Trx (1:500, Abcam), P-p38 MAPK (1:300, Cell Signaling, T180/Y182), TAK1 (1:300, Santa Cruz), and TAB1 (1:300, R&D). AECs were seeded on glass coverslips at a density of 30,000 cells per slip and incubated overnight prior to treatment with control or CSE 1:10 medium. After a 1 hour serum starvation, cells were treated for 1 hour and promptly fixed with 4% PFA, permeabilized with 0.5% Triton X, and blocked with 3% BSA in PBS prior to incubation with primary antibodies overnight at 4◦C. After washing with PBS, slides were incubated in Alexa Fluor 488 or 594 conjugated secondary antibodies (Life Technologies) diluted 1:1000 in PBS for 1 hour in the dark. Slides were

washed with PBS and then treated with NucBlue Live ReadyProbes Reagent (Life Technologies) and mounted using Mowiol 4–88 mounting medium (Sigma-Aldrich).

Confocal microscopy and image analysis

Images were captured using LSM 510 Meta UV confocal microscope (63×; Zeiss, Germany). Five regions of interest per image were used to determine red and green fluorescence intensity. Image modifications (brightness, contrast, and smoothing) were applied to the entire image using Image J (open source).

Pull down assay

ASK-1-Trx pull-down assays were conducted based on methods previously reported by Hsieh and Papaconstantinou [196]. Varying concentrations of protein (500, 1000, and 500μg plus 1% formalin fixed protein) coming from total cell lysates of both control and treated cells were incubated overnight with ASK1 antibody (1:100) or GSK3beta antibody (1:100) (control) rocking at 4◦C (Fig. 5.3). The next day 40μL of protein-A agarose beads were added and incubated at 4◦C for 1 hour. Samples were then spun down at 6000g, and the beads were washed three times with 1mL of ice cold PBS. Blue dye was added, and the samples were heated for 5 min at 95◦C and loaded onto a Western blot to look for ASK1 and Trx pool levels. Trx pulldowns were carried out with 500μg of control and CSE total cell lysates and followed the same protocol as the ASK1 pulldown.

TGF-β ELISA

AEC conditioned medium were collected from control and CSE after 48 hours of treatment. Human AF was collected at term vaginal deliveries and TNIL, and a human/mouse TGF-β 1 ELISA Ready-SET-Go! ELISA (second generation) (Affymetrix eBioscience) was conducted following the manufacturer's instructions. Standard curves

were developed with recombinant protein samples of known quantities. Sample concentrations were determined by correlating the absorbance of the sample to the standard curve by linear regression analysis.

Statistics

Statistical analyses for normally distributed data were performed using an ANOVA with the Tukey Multiple Comparisons and Test t-tests. Statistical values were calculated using PRISM or IBM SPSS. P values of less than .05 were considered significant.

RESULTS

Characterization of the ASK1-signalosome in AECs

To determine the role of the ASK1-signalosome, we first studied the expression of the ASK-1/Trx complex in primary AECs in culture. AECs were grown to confluence under standard cell culture conditions, and they showed the expression of CK-18 (Fig. 5.1A). AECs contain both ASK1 and Trx in total cell lysates, the two key components of the ASK1-signalosome complex, in cells grown under standard cell culture conditions (control) as well as in cells treated with OS inducer CSE (Fig. 5.1B) (Sup. Fig. 5.1A). Cytotoxicity experiments showed the viability of AECs after 1 hour treatment with CSE (Fig. 5.1C). As expected and shown before [28], CSE treatment induced p38 MAPK phosphorylation in AECs, which was inhibited by the antioxidant NAC ($P<.05$) (Fig. 5.1D and E) (Sup. Fig. 5.1B). These data (Fig. 5.1B and D) confirmed that AECs contain both components of the ASK1-signalosome complex, and OS causes p38 MAPK activation. To determine the existence of the ASK1-Trx signalosome as a complex in AECs, we conducted a series of pulldown assays (Fig. 5.1F) (Sup. Fig. 5.1C). These assays included testing with different protein concentrations as well as strengthening the covalent bonds between the molecules using formalin. First, ASK1 was pulled down using 500μg of total protein from both control and CSE. Western blot (Fig. 5.1F) data showed that ASK1 was

not associated with Trx in AECs. Reversing this experiment, a Trx pulldown was carried out using 500μg of total protein from both control and CSE, revealing that Trx was not associated with ASK1. Next, we tested the existence of this complex by strengthening the bond between the molecules. To strengthen the covalent bonds connecting ASK1-Trx, total cell protein was fixed with 1% formalin, and then ASK1 was pulled down from 500μg of protein in both groups. Western blot analysis still showed a dissociated complex, regardless of treatment. To confirm this finding and rule out issues of low amounts of proteins in our lysates, we increased the protein concentration to 1000μg and repeated these experiments. As shown in the last column of Figure 5.1F, we were able to reproduce the same findings as with low protein concentration and note that ASK1 and Trx are not complexed in AECs, regardless of culture condition.

Localization of ASK1-signalosome in AECs

Immunocytochemistry followed by confocal microscopy and line graphing colocalization was used to validate western blot and pull-down findings concerning the localization of the ASK1-Trx complex in AECs. To rule out any deleterious effects of processing fetal membranes, AECs at P0 and P1 were immunostained. As shown in Figure 5.2A, AECs in P0 and P1 under normal cell culture conditions (control) and after CSE treatment showed ASK1 in both their cytoplasm and nuclei. Localization of ASK1 in the nucleus is rather unique and a non-canonical phenomenon. Trx was mainly localized in the cytoplasm, but staining was seen in the nucleus as well. P1 cells were further characterized since those cells were used for the rest of the experiments. Colocalization of ASK1-Trx across the total cell area was measured, and it showed low levels of association in control or CSE P1 cells (e.g., P1 cells-Pearson's r coefficient 0.57 control and 0.41 CSE). Line graphs of select regions (Fig. 5.2A, white bars) confirmed the above findings showing minimal colocalization, regardless of culture condition or treatment (Fig. 5.2B). We further verified the existence of ASK1-Trx complex components within the nucleus of P1 cells

(area within the blue line in Fig. 5.2B) by western blot analysis. Figure 5.2C (Sup. Fig. 5.1C) revealed ASK1 and Trx in both cytoplasmic and nuclear extracts of lysed cells. Confirming immunolocalization analysis, western blots also showed ASK1 in the cytoplasm and nucleus, whereas Trx was predominantly in the cytoplasm.

Inhibition of ASK1 does not inhibit p38 MAPK activation

The above experiments led us to think that OS-induced p38 MAPK activation is independent of ASK1-Trx complex dissociation, which would result in ASK1 release and canonical ASK1-MKK3/6-mediated p38 MAPK activation. siRNA to ASK1 (Fig. 5.3A and B) and MKK3/6 (Fig. 5.3C and D) were used to test ASK1-independent activation of p38 MAPK. AECs transfected with ASK1siRNA had 89.10% downregulation of the gene as determined by qRT-PCR (Fig. 5.3S) and downregulation of protein levels compared to controls (without siRNA and NT siRNA). This downregulation of ASK1 gene expression did not affect p38 MAPK activation when AECs were simultaneously treated with siRNA to ASK1 and CSE (P=.77; Fig. 3B and E).

Inhibition of MKK3/6 does not prevent p38 MAPK activation

To verify that ASK1-independent activation of MKK3/6 was contributing to p38 MAPK activation, similar experiments were carried out with siRNA to MKK3/6, the upstream kinase to p38 MAPK, which can be activated via phosphorylation by ASK1. Although MKK3/6 gene expression (92.40%; Fig. 5.3C) and protein expression was knocked down compared to controls (without siRNA and NT siRNA); surprisingly, it did not affect p38 MAPK activation after CSE cotreatment (Fig. 5.3D and E; P=.65). These data suggested that ASK1 and MKK3/6 activations are not required for p38 MAPK activation by CSE-mediated OS.

AECs increase TGF-β production when treated with CSE

The above data suggest that p38 MAPK activation in response to CSE is unlikely mediated through ASK1-Trx signalosome dissociation or downstream activation of ASK1-mediated MKK3/6. An alternate pathway of p38 MAPK activation is through TGF-β-mediated TAK1, TAB1 signaling. As shown in Figure 5.4A, 48 hour treatment of AECs with CSE increased (70.95pg/mL) TGF-β 1 release compared to control (49.23pg/mL; P<.05) as determined by ELISA. The CSE-induced increase was downregulated by antioxidant NAC (20.46pg/mL; P<.05), suggesting an OS effect on AEC TGF-β production (Fig. 5.4A). In addition, we have also shown that CSE-treated, AEC-derived exosomes also carry TGF-β signaling molecules compared to AECs grown under normal cell culture conditions [143]. This is the first report to document that OS causes AECs to increase TGF-β release. This finding rationalizes our approach to investigate OS-induced TGF-β increase as a potential activator of p38 MAPK activation. Consequently, AECs treated with TGF-β (2ng/mL) resulted in p38 MAPK activation via phosphorylation within 1 hour (2-fold change; Fig. 5.4B) while cotreatment with a TGF receptor antagonist significantly prevented p38 MAPK activation (P=0.04) (Fig. 5.4C) (Sup. Fig.5.1D). AF ELISA analysis of TGF-β showed that TL samples had a higher concentration of TGF-β (72.55pg/mL) compared to samples from TNIL (15.40pg/mL; P<.05; Fig. 5.4D).

OS activation of the TGF-β -signaling pathway is independent of TAK1 in AECs

To test the role of OS-induced TGF-β signaling, its downstream effects on TAK1 and TAB1 were examined. To rule out that TAK1-TAB1 are still linked, dual immunofluorescence staining was performed for TAK1-TAB1. Data showed colocalization of TAK1-TAB1 (Fig. 5.4E), suggested that TAB1 is associated with TAK1 expression. Western blot analysis showed an increase in P-TAB1 after CSE treatment (P=.047), an effect that was prevented by NAC (P=.057; Fig. 5.4F and G) (Sup. Fig.5.1E). Though western blot analysis did not yield data on P-TAK1, siRNA to TAK1was used to validate its role in TGF-β TAK1-TAB1-mediated p38 MAPK activation. AECs were

transfected with siRNA to TAK1 in control and OS conditions. Control AECs transfected with siRNA to TAK1 showed (91%; P=.003) reduction of TAK1 gene expression, while control AECs transfected with NT siRNA did not produce any change, as expected (6%; P=.58; Fig. 5.5A). Although TAK1 gene expression and protein expression was knocked down, interestingly, it did not affect p38 MAPK activation after CSE co-treatment (Fig. 5.5B and C; P=1.00). These data suggest that TAK1 activation is not required for p38 MAPK activation by CSE-mediated OS in AECs.

OS induces a TGF-β–TAB1-dependent activation of p38 MAPK

To confirm the role of the TGF-β pathway mediators in inducing p38 MAPK activation under OS conditions, AECs were transfected with siRNA to TAB1 (Fig. 5.6). TAB1 gene expression was downregulated 90.33%, as documented by qRT-PCR (Fig. 5.6A). Protein level downregulation of TAB1 was documented by western blot analysis. Surprisingly, downregulation of TAB1decreased the phosphorylation of p38 MAPK by 40.18% (P=.03) in CSE-treated AECs (Fig. 5.6B and C) compared to controls (without siRNA and NT siRNA), which suggested TAB1-mediated activation of p38 MAPK was occurring. As shown in other systems [200, 202], we report that p38 MAPK activation in AECs under CSE-induced OS conditions are likely mediated through an autophosphorylation pathway that has not been reported previously in AECs, likely through TAB1-mediated autophosphorylation.

DISCUSSION

ROS generated as a result of intra-uterine OS are essential for fetal and fetal tissue (placenta and membrane) growth during pregnancy [27, 32, 205]. At term, increased OS causes telomere-dependent, p38 MAPK-mediated senescence of fetal membrane tissues, elevating an intra-uterine inflammatory load capable of promoting labor and delivery [4, 14]. Similar mechanistic events of senescence have been reported in placenta and other

uterine tissues, suggesting fetal tissue aging as a physiologic contributor of parturition [14, 32, 172, 206]. Premature activation of senescence can occur when tissues are exposed to OS-inducing risk factors. Premature senescence and untimely activation of uterotonic inflammatory cascade are associated with PTB, especially when complicated by pPROM membranes [31, 165]. Therefore, reducing PTB risk requires a much better understanding of molecular signalers of OS-associated events. p38 MAPK is implicated as a central regulator of the senescence process and preventing its activation can be one strategy [207, 208]. Understanding novel mechanisms and molecular targets that cause p38 MAPK activation are needed to stop the p38 MAPK effect. As currently tested, p38 MAPK inhibitors are found to be unsuitable for clinical use [207]. Activation of the ASK1-signalosome or existence of the canonical pathway can be detrimental to the growth and survival of the fetus by causing premature aging of fetal tissues, leading to a dysfunctional status.

TGF-β, a growth factor and OS responder, produces its effects through the TGF-β/TGF receptor pathway that involves MAPKKK family member TAK1 and scaffold protein TAB1 [209]. OS in AECs increased TGF-β and led to p38 MAPK activation, an effect that was prevented by TAB1 silencing. The TGF-β-TGFR1-TAB1 axis causing p38 MAPK activation through allosteric autophosphorylation has been reported in many other systems under specific conditions [210, 211]. TAB1 has been shown to activate TAK1, which can cause activation of MKK3 and 6, precursors of p38 MAPK activation through classic pathways [209]. Silencing of ASK1, MKK3/6, and TAK1 did not reduce p38 MAPK activation in AECs, suggesting that p38 MAPK activation in AECs is independent of canonical elements. Silencing of TAB1 prevented this effect, supporting that p38 MAPK activation in AECs is likely autophosphorylation by TAB1, an alternate pathway. As pointed out by DeNicola et al., since p38 MAPK is a serine/threonine kinase, it is theoretically difficult to accept the autophosphorylation of Thr180 and Tyr182 within the activation loop; however, the existence of such an autophosphorylation mechanism has

been reported to cause p38 MAPK activation [212]. It is also to be noted that TAB1-dependent autophosphorylation is limited to p38 MAPK α and not the other three isoforms. It is likely that the classic pathway may still be operational for activation p38 MAPK β, the other form seen in fetal cells.

The biologic relevance of TAB1-dependent activation of p38 MAPK in AECs is unclear. The existence of other upstream activators and their increased expression under OS does not rule out redundancy in p38 MAPK activation. Involvement of other activators and activation of the classical pathway are likely stimulant-dependent and required to maintain base level activation of p38 MAPK required for various other cellular function. As murine pregnancy models indicate, p38 MAPK is a constitutively expressed protein in fetal membranes from day 9 of gestation, and it peaks at day 15 [14]. Senescence is not observed until day 15, suggesting other functional roles for p38 MAPK in tissue remodeling. Early indications from our ongoing studies suggest that p38 MAPK activation is required for collagenolytic processes and replenishment of cells shed from the fetal membranes to maintain membrane homeostasis. Therefore, it is likely that redox changes in fetal tissues can activate p38 MAPK through canonical pathways for tissue remodeling. We have already reported the roles of lysyl oxidase and lysyl oxidase-like enzyme in OS-induced tissue remodeling [213] suggesting that besides p38 MAPK, other enzymes may also contribute to ECM remodeling. Overwhelming OS experienced at term, or untimely OS in response to pregnancy risk factors as seen in PTB, may cause alternative pathway activation and p38 MAPK autophosphorylation to facilitate parturition to avoid a hostile environment for the growing fetus.

In summary, we report, for the first time, non-canonical activation of p38 MAPK in fetal cells exposed to OS. An OS-mediated TGF-β increase can lead to TAB1-mediated activation of p38 MAPK. Because many pregnancy complications are associated with increased OS and OS-associated damages that can activate p38 MAPK, identification of this pathway is relevant in translational medicine in designing interventional strategies to

prevent p38 MAPK-mediated deleterious effects on cells and adverse events during pregnancy.

Gene Symbol	Target sequence 1	Target sequence 2	Target sequence 3	Target sequence 4
TAB1	GAUGAGCUCUUCCGUCUUU	GAACAACUGCUUCCUGUAU	GGAGAUUGCUGCGAUGAUU	AAAUAUGGCUACACGGACA
ASK1	CAGGAAAGCUCGUAAUUUA	GGAAAGCUCGUAAUUUAUA	GAUGUUCUCUACUAUGUUA	UAAGUAGUCUUCUUGGUAA
MKK3	GGUGGAGGCUGAUGACUUG	CCGCAGAGCGUAUGAGCUA	CCAAUGUCCUUAUCAACAA	GGAGAUUGCUGUGUCUAUC
MKK4	GGACAGAAGUGGAAAUAUU	GACAGAAGUGGAAAUAUUA	GCGCAUCACGACAAGGAUA	UCCCAUGUAUGUCGAUUGA
MKK6	CCAAAGAACGGCCUACAUA	GAUAAAGGCCAGACAAUUC	GCUCAUGGAUACAUCACUA	CAUCAAUGCUCUCGGUCAA
TAK1	CCCAAUGGCUUAUCUUACA	GGACAGCCAAGACGUAGAU	UACACUGGAUCACCAACUA	AGUGAUAACGCGUCGGAAA
NT siRNA	UAAGGCUAUGAAGAGAUAC	AUGUAUUGGCCUGUAUUAG	AUGAACGUGAAUUGCUCAA	UGGUUUACAUGUCGACUAA

Table 5.1: List of siRNA target sequences.

Gene symbol	GenBank/Ref-Seq ID	Forward 5^{l}-3^{l}	Reverse 5^{l}-3^{l}
TAB1	NM 006116	TCTGCTTGGCAAACTCAGTG	CTTGGTGCTGATGTCGGA
ASK1	NM 005923	TGTAGTTCCCAGTGCACATAG	GCCAACAACATCATCCTCTACT
MKK3	NM 145109	GGCTTGGACATGCAGGATA	GCAGTCCTCTAGATTAGTCTCCA
MKK4	NM 003010	TCAAACGAGGTAGACATGAGTTC	TTTGGATGTAGTAATGCGGAGT
MKK6	NM 002758	TGGAACTGGTCTGAGGTTGT	GAAGAGAAGCAAGGCAAAGTC

Table 5.2: List of quantitative reverse transcription–polymerase chain reaction (qRT-PCR) assays primers for AEC experiments.

Protein Name	Catalog Number	Company	Dilution	Method
ASK1	D11C9	Cell Signaling	1:750	Western Blot
TRX	Ab16965	Abcam	1:1000	Western Blot
TAB1	AF3578	R&D	1:1000	Western Blot
P-TAB1(Thr431)	06–1334	Milipore	1:800	Western Blot
P-p38 MAPK (T180/y182)	9211L	Cell Signaling	1:300	Western Blot
p38 MAPK	9212S	Cell Signaling	1:1000	Western Blot
B-Actin	A5441	Sigma-Aldrich	1:20,000	Western Blot
Cytokeratin-18	Ab668	Abcam	1:300	Immunofluorescence
ASK1	Ab45178	Abcam	1:250	Immunofluorescence
TRX	Ab16965	Abcam	1:500	Immunofluorescence
P-p38 MAPK (T180/y182)	9211L	Cell Signaling	1:300	Immunofluorescence
TAK1	Sc-7967	Santa Cruz	1:300	Immunofluorescence
TAB1	AF3578	R&D	1:300	Immunofluorescence
ASK1	D11C9	Cell Signaling	1:100	Immunoprecipitation
TRX	Ab16965	Abcam	1:100	Immunoprecipitation
GSK3B	mAb#9832	Cell Signaling	1:100	Immunoprecipitation

Table 5.3: Antibodies used for the western blot

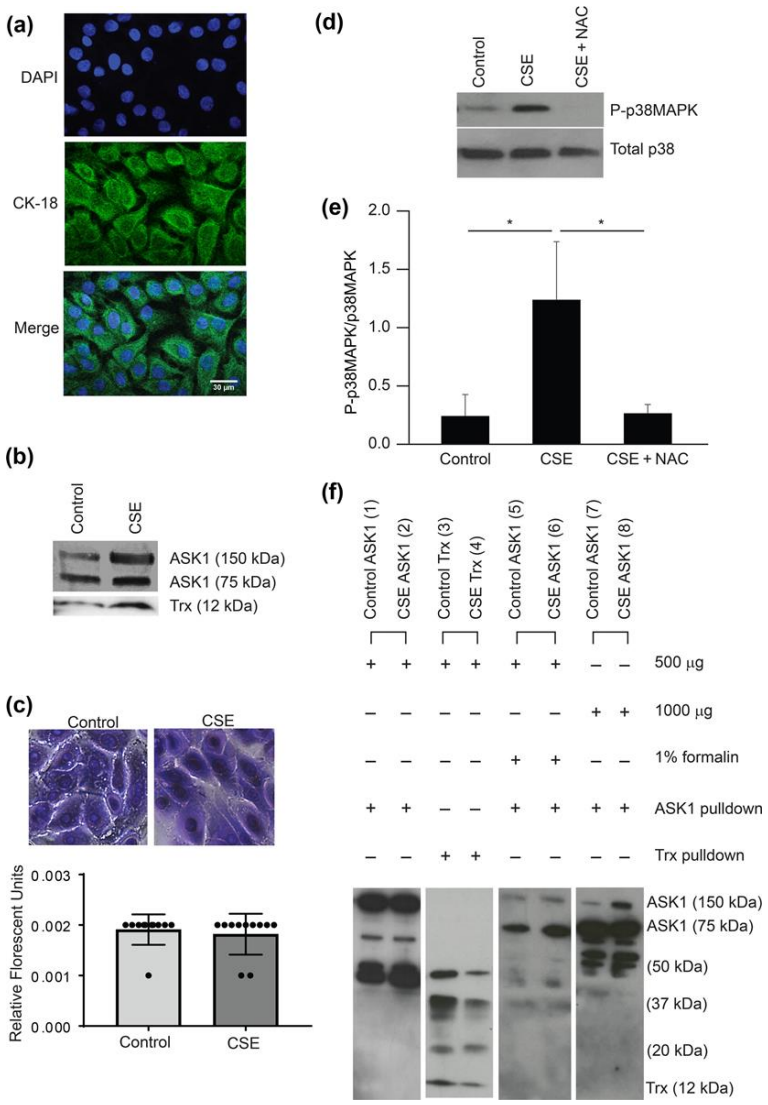

Fig. 5.1 ASK1-Signalosome in AECs.

A) Immunofluorescence images of CK-18 positive (green) AECs. Scale bar is set to 30μM. B) Western blot analysis-ASK1 (dimer 150kDa top band, monomer 75kDa lower band) and Trx are present in AECs, regardless of treatment. C) Crystal violet stain (purple) was not expelled from AECs after CSE 1:10 treatment for 1 hour. This was confirmed by plate reader analysis showing no difference in crystal violet intensity. D) CSE treatment induced P-p38 MAPK ($P<.05$), while NAC ($P<.05$) prevented its activation. E) Densitometry of P-p38 MAPK (1C) over total p38 MAPK in CSE and CSE+NAC exposed AECs. A one-way ANOVA with the Tukey Multiple Comparisons Test was used to test statistical significance. F) ASK1 pulldowns in columns 1, 2, 5, 6, 7, and 8 all show ASK1 present, but not Trx, in both control and CSE bead samples, while the Trx Pulldown in columns 3 and 4 show Trx present, but not ASK1, in both control and CSE bead samples.

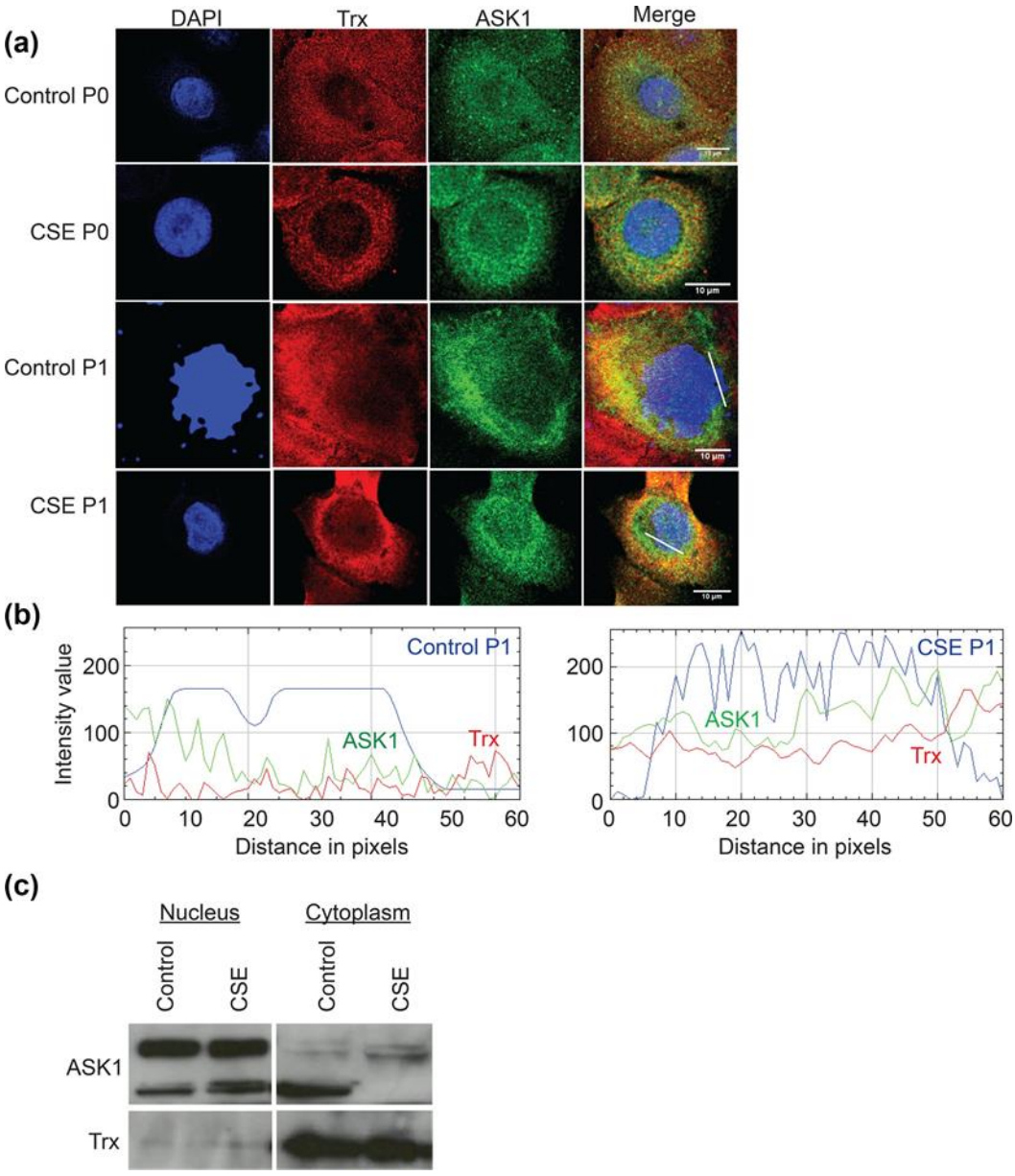

Fig. 5.2 Immunofluorescence staining and Western blots of ASK1 and Trx in AECs.

A) Confocal microscopy was used to analyze the ratio of ASK1 and Trx in AECs. Trx (red) and ASK1 (green) staining can be seen in the cytoplasm and nuclei of control AECs. White lines represent regions of interest to look for ASK1-Trx colocalization. Scale bar is set to 10μM. B) Control and CSE graphs of ASK1-Trx showing no colocalization and ASK1 in the nucleus. C) Western blot analysis of nuclear and cytoplasmic lysates confirms ASK1 (dimer 150kDa top band, monomer 75kDa lower band) in the nucleus and Trx in the cytoplasm.

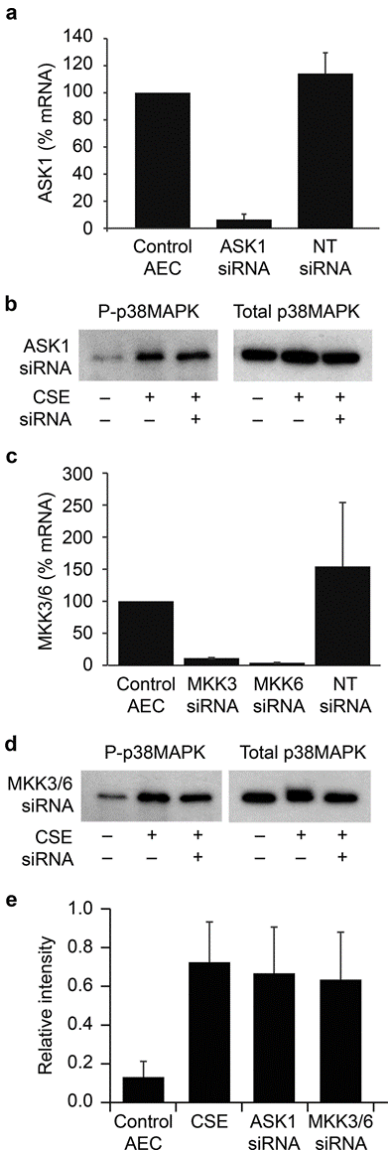

Fig. 5.3 Inhibition of ASK1 and MKK3/6 does not inhibit p38 MAPK activation.

A) mRNA levels of ASK1 showed siRNA to ASK1 decreases its expression by 89% (P<.0001) compared to NT siRNA. A two-tailed t-test was used to test statistical significance. B) AECs treated with CSE induced P-p38 MAPK, but treatment with siRNA to ASK1 and CSE did not reduce p38 MAPK phosphorylation. C) mRNA levels of MKK3/6 showed siRNA to MKK3/6 decreases its expression by 90% (P<.0002) compared to NT siRNA. A two-tailed t-test was used to test statistical significance. D) AECs treated with CSE induced P-p38 MAPK, as seen previously, but treatment with siRNA to MKK3/6 and CSE did not reduce P38 MAPK phosphorylation. E) Quantitative densitometry (B and D) of P-p38 MAPK over total p38 MAPK shows a significant increase of activated p38 MAPK when treated with CSE (P<.003); however, its phosphorylation is not inhibited when treated with siRNA to ASK1 or MKK3/6 and CSE.

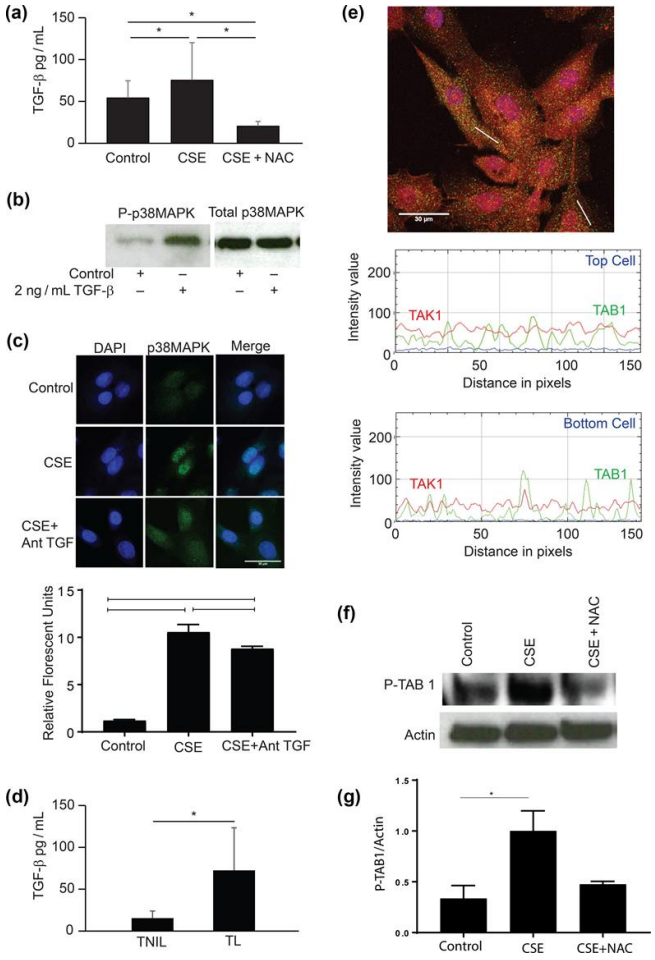

Fig. 5.4 Production and function of TGF-β in AECs.

A) ELISA for TGF-β conducted on AEC supernatant that had been stimulated with CSE for 48 hours. AECs showed a significantly increased production of TGF-β when stimulated with CSE ($P<.05$) and NAC can inhibit this production ($P<.05$). A one-way ANOVA with the Tukey Multiple Comparisons Test was used to test statistical significance. B) AECs treated with 2ng/mL of TGF-β for up to 1 hour caused activation of p38 MAPK (2-fold) compared to control treated AECs. C) AECs treated with CSE for 1 hour significantly induced p38 MAPK activation ($P<0.0001$) while TGF receptor antagonist prevented p38 MAPK activation ($P=0.03$). D) ELISA for TGF-β conducted on AF of TNIL or TL deliveries showed significant expression of TGF-β at term ($P<.05$). A one-tailed t-test was used to test statistical significance. E) Immunofluorescence colocalized TAK (red) and TAB1 (green) inside control treated AECs. White lines represent regions of interest to look for TAK1-TAB1 colocalization. Both cells showed overlapping line graphs of TAK1-TAB1 documenting colocalization within the cytoplasm. Scale bar is set to 30μM. F) Western blot analysis confirmed that TAB1 can be significantly ($P=.047$) activated by CSE and antioxidant NAC can significantly prevent this activation ($P=.057$). G) Quantitative densitometry of P-TAB1 over actin for panel f showing statistical significance. A one-way ANOVA with the Tukey Multiple Comparisons Test was used to test statistical significance.

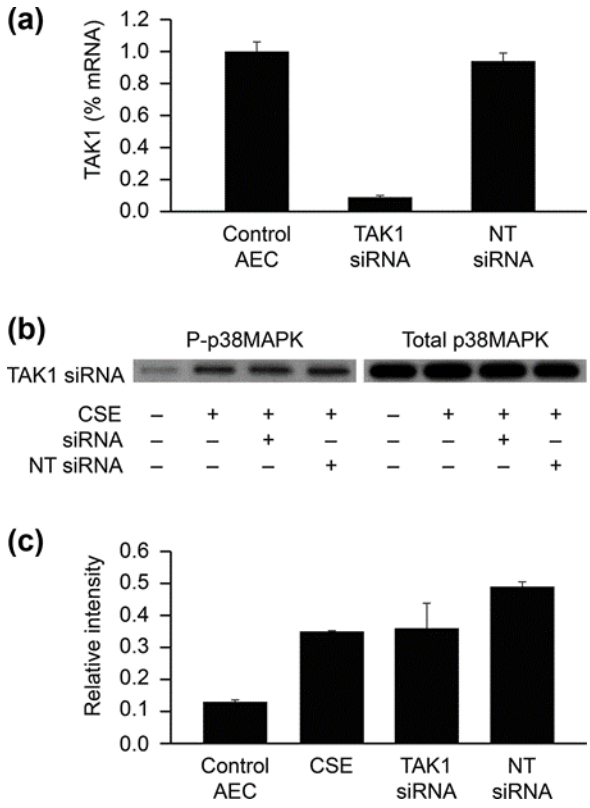

Fig. 5.5 Inhibition of TAK1 does not inhibit p38 MAPK activation.

A) mRNA levels of TAK1 showed siRNA to TAK1 decrease its expression by 91% (P=.003), but NT siRNA does not decrease TAK1 gene expression 6% (P=.58). A two-tailed t-test was used to test statistical significance. B) AECs treated with CSE and siRNA to TAK1 did not significantly reduce p38 MAPK phosphorylation. C) Quantitative densitometry (B) of P-p38 MAPK over total p38 MAPK showed a significant increase of p38 MAPK phosphorylation in AECs when treated with CSE (P=.001) and NT siRNA (P=.001); however, there was no significant difference of activated p38 MAPK phosphorylation when treated with siRNA to TAK1+CSE (P=1.00). Surprisingly, NT siRNA + CSE also significantly upregulated p38 MAPK activation compared to CSE alone (P=.006). A two-tailed t-test was used to test statistical significance.

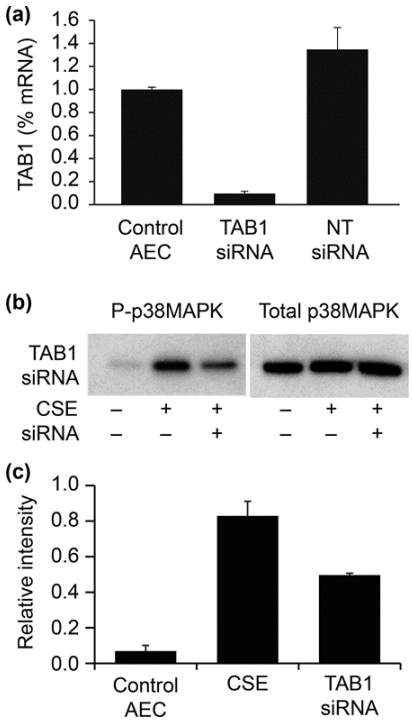

Fig. 5.6 OS induces a TGF-β–TAB1-dependent activation of p38 MAPK.

A) mRNA levels of TAB1 showed siRNA to TAB1 decrease its expression by 91% (P<.0001) compared to NT siRNA. B) AECs treated with CSE and siRNA to TAB1 significantly reduce p38 MAPK phosphorylation (P=.0295). A two-tailed t-test was used to test statistical significance. C) Quantitative densitometry (B) of P-p38 MAPK over total p38 MAPK shows a significant decrease of activated p38 MAPK phosphorylation when treated with siRNA to TAB1 and CSE (P=.0295). A two-tailed t-test was used to test statistical significance.

Does TGF-β induce EMT in fetal membranes at term labor?

At term, increased OS causes telomere-dependent, p38 MAPK-mediated senescence of fetal membrane tissues, elevating the intra-uterine inflammatory load, which is capable of promoting labor and delivery. Here siRNA was used to rigorously define the pathway of p38 MAPK activation (i.e., phosphorylation at Threonine-180 and Tyrosine-182) (**Chapter 5**). Surprisingly, OS-inducer CSE did not activate the canonical MAPKKK cascade (e.g., MAPK3, MAPK6, MAPK4, ASK1) but instead p38 MAPK activation was dependent on TGF-β induced signaling protein, TAB1. In immune cells, TAB1 has been shown to directly bind to p38 MAPK and induce its autophosphorylation [210, 211]. This is a unique and non-canonical pathway of activation which is a novel finding in AECs. Which raises the question, if TGF-β is responsible for OS-induced p38 MAPK at term, what other TGF-β specific pathways are being activated?

Physiologically, amnion cells are exposed continuously to TGF-β through autocrine and paracrine secretion (e.g., due to local OS stimulation) or through the AF. As a redox status indicator, TGF-β performs dual functions in AECs 1) maintaining cell growth and proliferation at low concentrations, and 2) inducing dysfunction (e.g., EMT pathways) at high concentrations [214]. Previously, autocrine secretion of TGF-β or TGF-β treatment of AECs has been documented to induce EMT in culture [66, 215]; Suggesting, AECs have the ability to undergo cellular transitions in vitro. However, these transitions have never been related to term labor associated changes.

TGF-β-TAB1 mediated p38 MAPK activation has now been shown in AECs, but mediation of p38 MAPK-induced EMT remains unknown. To determine if TGF-β can induce EMT in fetal membranes at term labor, ultrastructural, immunohistochemical, gene silencing, and western blotting experiments were conducted to establish that fetal membranes are subject to EMT, mediated in part by p38 MAPK pathways responding to OS (**Chapter 6**). A mouse model of parturition was also used to recapitulate these findings for further validation.

Chapter 6. Regulation of dynamic amnion membrane remodeling via reversible EMT and MET

INTRODUCTION

Human fetal membranes are composed of an inner amnion layer and chorion trophoblast layer connected by a type IV collagen-rich basement membrane and other ECM components [49, 124]. ECM is traversed by embedded mesenchymal cells providing a structural scaffold for the avascular fetal membranes [20, 96]. These membranes define the intra-uterine cavity and protect the fetus during gestation, primarily by the highly elastic amnion. The amnion layer grows with the fetus from the time of embryogenesis and provides immune and mechanical protection as well as endocrine functions [216]. The amnion and chorion layers expand throughout gestation to accommodate the increasing volume of the fetus and AF and fuse by the late first or early second trimester. Expansion of the fetal membranes requires a constant physiological remodeling process that is accompanied by cellular shedding (exfoliation) and repair of accumulated membrane microfractures [96]. Failure to seal these microfracture defects can lead to degradation and loss of structural integrity of the membranes and appears to be a cause of PTB [96]. Although ECM remodeling is reported to be mediated by MMPs [22, 124], the regulation of fetal membrane cellular remodeling is unclear.

As the innermost lining of the uterine cavity and structural barrier, the fetal membranes provide homeostasis critical for successful maintenance of pregnancy. Senescence of the fetal membrane cells also occurs as a physiological process that peaks due to mounting OS and inflammation in the intra-uterine cavity at term, mediated

predominantly by p38 MAPK [2, 28]. Aging of the membranes can lead to parturition in both human and animal models [14, 217]. Premature activation of fetal membrane senescence, in response to a variety of pregnancy-associated risk factors, can predispose membranes to dysfunction and rupture. pPROM is a common complication of pregnancy and accounts for ~ 40% of spontaneous PTBs [218, 219]. pPROM contributes to significant neonatal morbidity and mortality, yet no diagnostic or clinical indicators exist to predict high risk. Current diagnostic tests only detect pPROM after its occurrence, creating a clinical quandary as to how to intervene for preventing PTB. To understand predisposing factors that contribute to membrane weakening, specifically amnion stress, and stretching, we tested the mechanisms by which epithelial and mesenchymal cells in the amnion layer [124] undergo remodeling or seal the gaps created by cell shedding.

Amnion cells are capable of proliferation, migration and pluripotent transition (i.e., epithelial-to-mesenchymal transition [EMT] and its reverse [MET]) durring remodeling [128]. Additionally, OS can prevent remodeling by increasing senescence and inflammation; by contrast, nutrient-rich AF accelerates remodeling [128, 220]. Two key factors that likely mediate cellular transitions during gestation are TGF-β and P4. TGF-β is an established promoter of EMT [66, 221, 222] and P4, the dominant pregnancy maintenance hormone, is known to minimize EMT [223], in part by promoting MET. We determined that normal term parturition is associated with fetal membrane EMT in both humans and mice, which also coincided with increased cellular and AF TGF-β levels. We further tested the mechanisms of cellular transitions and the roles played by TGF-β and P4 and reported that TGF-β ligation of TGFR1 leads to activation of TAB1 complex that autophosphorylates p38 MAPK [224] promoting amnion epithelial cell EMT. We also report a unique dual role for P4 in the membranes: P4 maintains amnion epithelial phenotype by 1. Downregulating mesenchymal transcription factors, and 2. By complexing with its membrane receptor 2 (PGRMC2), P4 causes MET in AMCs, through c-MYC proto-oncogene signaling.

MATERIALS AND METHODS

This study protocol is approved by the Institutional Review Board at UTMB at Galveston, TX, as an exempt protocol to use discarded placenta after normal term cesarean deliveries (UTMB 11-251). No subject recruitment or consenting was done for this study.

Clinical samples

Fetal membranes (combined amniochorion and decidua) were collected from TNIL cesarean deliveries (N=5) with no documented pregnancy complications and TL vaginal deliveries (N=5). Fetal membranes were dissected from the placenta, washed three times in normal saline, and cleansed of blood clots using cotton gauze. Six-millimeter biopsies (explants) were then cut from the midzone portion of the membranes, avoiding the regions overlying the cervix or placenta. The amnion was then separated from the chorion and explants were processed for a variety of assays.

INCLUSION CRITERIA

Normal term birth were classified as TL (> 390/7 weeks) with no pregnancy-related complications.

EXCLUSION CRITERIA

Subjects with multiple gestations, placenta previa, fetal anomalies, and/or medical or surgeries (intervention for clinical conditions that are not linked to pregnancy) during pregnancy were excluded. Severe cases of PE or persistent symptoms (headache, vision changes, RUQ pain) or abnormal laboratory findings (thrombocytopenia, repeated abnormal liver function tests, creatinine doubling or > 1.2, or HELLP syndrome) or clinical findings (pulmonary edema or eclampsia) were excluded. Subjects who had any surgical procedures during pregnancy or who were treated for hypertension, preterm labor or for suspected clinical chorioamnionitis (reports on foul-smelling vaginal discharge, high levels

of CRP, fetal tachycardia), positive GBS screening or diagnosis of bacterial vaginosis, behavioral issues (cigarette smoking, drug or alcohol abuse) and delivered at term were excluded from the control groups.

In vitro explant culture and stimulation with CSE

The in vitro organ explant culture system for human fetal membranes and stimulation of membranes with CSE was performed as previously reported [4]. In this study, CSE was used to mimic the OS experienced by fetal membranes at term prior to labor that will transition the membrane into a labor phenotype [34]. In short, 6mm biopsies of fetal membranes were collected from not laboring cesarean deliveries and placed in an organ explant system for 24 hours. CSE was prepared by bubbling smoke drawn from a single lit commercial cigarette (unfiltered Camel; R.J. Reynolds Tobacco Co., Winston Salem, NC) through 50mL of tissue culture medium (Ham's F12/Dulbecco's modified Eagle's medium mixture with antimicrobial agents) which was then filter sterilized through a 0.22μm filter (Millipore, Bedford, MA) to remove contaminant microbes and insoluble particles. Fetal membranes were then stimulated with CSE (1:25 dilution) for 48 hours (N=4), while the cesarean explants were replaced with tissue culture medium (N=4). After a 48 hour treatment, the explants were removed the amnion was separated from the chorion and processed for a variety of assays.

Collection of CD-1 fetal membranes

The Institutional Animal Care and Use Committee (IACUC) at the University of Texas Medical Branch at Galveston approved the study protocol. CD-1 pregnant mice were purchased from Charles River Laboratories (Wilmington, MA). Animals were shipped on day 10 of gestation and acclimated in a temperature and humidity controlled facility with automatically controlled 12:12 hour light and dark cycles. Mice were allowed to consume regular chow and drinking solution ad libitum.

At day 14th of pregnancy, the pregnant CD-1 mice (N=3/group) were weighed and subjected to minilaparotomy in the lower abdomen and injection of 150uL of the treatment into uteri in between 2-3 gestational sacs according to the following experimental groups: 1) water-soluble CSE (CSE; 1:10) diluted in saline; 2) CSE in combination with SB (p38 MAPK inhibitor) and 3) saline (control). After sacrificing the animals by using carbon dioxide inhalation according to the IACUC and American Veterinary Medical Association guidelines on day 18, maternal, fetal, and placental weight was documented and pup loss/reabsorption was counted. Amniotic sacs and placentae were collected and collected in either 10% formalin or fresh frozen in liquid nitrogen and stored at -80ºC until further analysis.

Additionally, CD-1 mice at embryonic day 9, 13, 18, and 19 of pregnancy (N=5/group) were sacrificed using carbon dioxide inhalation according to the IACUC and American Veterinary Medical Association guidelines. Fetal membranes were collected and collected in either 10% formalin or fresh frozen in liquid nitrogen and stored at -80ºC until further analysis.

AEC in vitro culture:

Primary AECs (N=4) were isolated from TNIL amnion (about 10g), peeled from the chorion layer and dispersed by successive treatments with 0.125% collagenase and 1.2% Trypsin [28]. The dispersed cells were plated in a 1:1 mixture of Ham's F12/DMEM, supplemented with 10% heat-inactivated FBS, 10 ng/ml EGF, 2mM L-Glutamine, 100U/ml Penicillin G and 100mg/ml Streptomycin at a density of 3-5 million cells per T75 and incubated at 37°C with 5% CO2 until they were 80-90% confluent.

AMC in vitro culture:

AMCs were isolated from fetal membranes as previously described by Kendal-Wright et al. [42, 225] with slight modifications. Primary AMCs (N=4) were isolated from

the placental membranes of women experiencing normal parturient at term (e.g., not in labor) and undergoing a repeat elective cesarean section. Reflected amnion (~10 g) was peeled from the chorion layer and rinsed three or four times in sterile Hanks' Balanced Salt Solution (Cat# 21-021-CV, Corning) to remove blood debris. The sample was then incubated with 0.05% trypsin/EDTA (Cat# 25-053-CI, Corning) for 1 hour at 37°C (water bath) to disperse the cells and remove the epithelial cell layer. The membrane pieces were then washed three to four times using cold HBSS to inactivate the enzyme. The washed membrane was transferred into a second digestion buffer containing Minimum Essential Eagle Medium (Cat# 10-010-CV, Corning), 1mg/mL collagenase type IV, and 25 μg/mL DNase I and incubated in a rotator at 37°C for 1 hour. The digested membrane solution was neutralized using DMEM/F12 medium (Cat# 16-405-CV, Corning), filtered using a 70μm cell strainer, and centrifuged at 3000rpm for 10 min. The cell pellet was resuspended in complete DMEM/F12 media supplemented with 5% heat-inactivated FBS (Cat# 35-010-CV, Corning), 100U/ml penicillin G, and 100mg/mL streptomycin (Cat# 30-001-CI, Corning), plated at 3-5 million cells per T75, and incubated at 37°C with 5% CO2 until they were 80-90% confluent.

Quantitation of AEC and AEC from fetal membranes

Fetal membranes were collected from TNIL cesarean deliveries (N=3) with no documented pregnancy complications and TL vaginal deliveries (N=3). Fetal membranes were dissected from the placenta, washed three times in normal saline, and cleansed of blood clots using cotton gauze. $0.0006m^2$ sections were then cut from three different regions of the midzone, avoiding the regions overlying the cervix or placenta. The amnion membrane was then separated from the chorion, and the sections were processed using the AMC collection method. AECs were removed after the first digestion and AMCs were removed after the second digestion. Cells were counted manually as well as using an automatic cell counter (Countless 2 FL automated cell counter, ThermoFisher, Waltham,

MA). These data were then used for analysis to determine the changes in AEC/AMC ratio at TNIL and TL.

Cell culture treatments

To induce cellular transitions in AECs, once cells reached 40–50% confluence, each flask was serum starved for 1 hour, rinsed with sterile 1x PBS followed by treatment with medium (control), 15ng/ml TGF-β containing medium, TGF-β+SB (10μm) a p38 MAPK functional inhibitor, SB alone, TGF-β+siRNA to TAB1 (150nM), or P4 (30ng/mL) and incubated at 37°C, 5% CO2, and 95% air humidity for 6 days. To induce MET in AMCs, once cells reached 40–50% confluence, each flask was serum starved for 1 hour, rinsed with sterile 1x PBS followed by treatment with medium (control), 200ng/mL P4 containing medium, P4+10058 (75μM) a pharmaceutical inhibitor of c-MYC, or P4+siRNA to PGRMC2 (150nM) and incubated at 37°C, 5% CO2, and 95% air humidity for 6 days. Cells were collected for qRT-PCR and western blots analysis.

siRNA transfection

To determine the potential role of TAB1 regulation of TGFβ induced EMT in AEC, and PGRMC2 induced MET in AMCs, we downregulated TAB1 and PGRMC2 using siGENOME siRNA (GE Healthcare Dharmacon) (Thermo Fisher Scientific, Rockford, IL) (Table 2). Briefly, AECs and AMCs were cultured to nearly 50% confluence in DMEM/F12 medium supplemented with 10% FBS and antimicrobial agents (Penicillin/Streptomycin, Amphotericin). Prior to siRNA transfection, cells were incubated with antimicrobial-free medium overnight. Next, cells were incubated for 4 hours with siRNA complexes, which were freshly prepared using either 150 nM siRNA to specific genes or NT siRNA as control and 0.3% Lipofectamine® RNAiMAX (Invitrogen, Eugene, OR) in Opti-MEM™ I Reduced Serum Medium. Cells were further incubated in growth

medium for 6 Days. Downregulation efficiency of the target genes was validated by qRT-PCR. Gene expression was normalized to non-transfected control.

Overexpression of PGRMC2 in AMCs

To determine if OS-induced functional P4 withdrawal in AMCs occurs through PGRMC2. Overexpression studies were carried out. AMCs were cultured to nearly 50% confluence in DMEM/F12 medium supplemented with 10% FBS and antimicrobial agents (Penicillin/Streptomycin, Amphotericin) then transfected with 800ng of GFP-PGRMC2 expression plasmids (Table 3) with FuGENE ® (1:3 plasmid weight) (Promega, Madison, WI) in Opti-MEM™ I Reduced Serum Medium. After 24 hours, Opti-MEM was removed, and cells were treated with control, CSE (1:50), or CSE+P4 (200ng/mL) for 48 hours.

Scratch assay and cell culture treatments

P1 AECs were seeded at approximately at 80% confluence in 4-well coverslips and incubated at 37°C with 5% CO2 for 24 hours (N=3). AECs were then serum-starved for 1 hour, rinsed with sterile 1× PBS, and then scratched evenly down the middle of the well, in a straight line, with a 200µl pipet tip [128]. Cells were washed with sterile 1× PBS four times to remove any cell debris. Cell were then treated with 15ng/ml TGFβ or P4 (30ng/mL) for 1 hour, 24, and 38 hours. Bright field and confocal microscopy documented wound closure, morphology, and vimentin/CK-18 staining.

Microscopy

TRANSMISSION ELECTRON MICROSCOPY

Fetal membranes from cesarean and vaginal deliveries (N=3) and fetal membrane explants from normal-term pregnancies with or without CSE exposure (N=3) were fixed, stained, and embedded in PolyBed 812. Initial fixation was for 24 hours at 4°C in a fixative with 2.5% PFA, 0.2% glutaraldehyde, and 0.03% picric acid in 0.05mol/L cacodylate

buffer. After fixation, samples were rinsed three times with cacodylate buffer and postfixed with 1% osmium tetroxide in 0.1mol/L cacodylate buffer. Osmicated tissue was rinsed twice with deionized water and stained in blocking reagent with 2% aqueous uranyl acetate for 1 hour at 60°C. The samples were then dehydrated by a series of ethanol-water solutions (50%, 75%, 95%, and 100% ethanol for three exchanges). Dehydrated tissue was infiltrated with two exchanges of propylene oxide, then with propylene oxide-diluted PolyBed resin at 1:1 ratio and 1:2 ratio, and then twice with pure PolyBed 812. Finally, the samples were embedded in PolyBed 812 and cured overnight at 60°C. Because precise tissue orientation could not be maintained during curing of the resin, the first resin blocks were cut to give a wide flat face for the desired sectioning plane, replaced into new embedding molds, and cured again. Samples were cut as 90nm sections, placed on Formvar-coated slotted grids, and poststained for three minutes with a solution of Reynold's lead citrate. Images were taken with a JEM 1400 electron microscope (JEOL, Tokyo, Japan).

BRIGHT FIELD MICROSCOPY

Bright-field microscopy images were captured using a Nikon Eclipse TS100 microscope (4x, 10x, 20x) (Nikon, Melville, NY, USA). Three regions of interest per condition were used to determine the overall cell morphology.

CONFOCAL MICROSCOPY

Confocal microscopy images were captured using a Zeiss 880 confocal microscope (10x, 40x, or 63x) (Zeiss, Germany). Three random regions of interest per field were used to determine red (CK-18) and green (vimentin) fluorescence intensity. Uniform laser settings, brightness, contrast, and collection settings were matched for all images collected. Images were not modified (brightness, contrast, and smoothing) for intensity analysis. ImageJ software (National Institutes of Health, rsbweb.nih.gov/ij; version 1.51J) was used to measure vimentin and CK-18 staining intensity from two focal plans of three different

regions per treatment condition at each time point. Image analysis was conducted in triplicate for all cell experiments.

Immunohistochemistry

Human and mice fetal membrane tissue sections were fixed in 4% PFA for 48 hours and embedded in paraffin. Sections were cut at 5μm thickness and adhered to a positively charged slide and attached by keeping them at 57°C for 45min. Slides were deparaffinized using Xylene and rehydrated with 100% alcohol, 95% alcohol, and normal saline (pH 7.4) and stained. Three images for each category were taken at 10x and 40x magnification. Images were processed with ImageJ and staining intensity was measured in a uniform manner. The following anti-human/mouse antibodies were used for IHC: Vimentin, CK-18, N-cadherin, E-cadherin, MMP9, TGF-β, c-MYC, and 3-Nitrotyrosine modified proteins (3-NT).

SA-β-Gal

The SA-β-Gal, a senescence cellular marker, was evaluated by using a commercial histochemical staining assay, following the manufactures instructions (Senescence cells Histochemical Staining Kit; Sigma-Aldrich). Briefly, paraffin murine amnion sac and placental samples were fixed for 6-7 min using the provided Fixation Buffer, washed in PBS and incubated for 1 hour at 37ºC with a fresh β-Gal solution. Following incubation, tissues were evaluated using a standard light microscope for SA-β-Gal blue staining (dark grey in black and white images).

Trichrome staining for collagen

Tissue sections were fixed in 4% PFA for 48 hours and embedded in paraffin. Sections were cut at 5μm thickness and adhered to a positively charged slide and attached by keeping them at 57°C for 45 min. Slides were deparaffinized using Xylene and

rehydrated with 100% alcohol, 95% alcohol, and normal saline (pH 7.4) and stained using the Masson Trichrome method to identify collagen components. The amnion epithelium was identified by a single layer of cells, while the ECM was identified as the area in between the amnion epithelium and the chorion layer. Three microscopic fields were captured at 10x and 40x.

Protein extraction and immunoblot assay

AECs, AMCs, human, and murine tissue were lysed with RIPA lysis buffer (50mM Tris pH 8.0, 150mM NaCl, 1% Triton X-100, and 1.0mM EDTA pH 8.0, 0.1% SDS) supplemented with protease and phosphatase inhibitor cocktail and phenylmethylsulfonyl fluoride. After centrifugation at 10,000rpm for 20 minutes, the supernatant was collected, and protein concentrations were determined using BCA (Pierce, Rockford, IL). The protein samples were separated using SDS-PAGE on a gradient (4–15%) Mini-PROTEAN® TGX™ Precast Gels (Bio-Rad, Hercules, CA) and transferred to the membrane using iBlot® Gel Transfer Device (Thermo Fisher Scientific). Membranes were blocked in 5% nonfat milk in 1x Tris-buffered saline-Tween 20 or in 5% BSA buffer for a minimum of 1 hour at room temperature then probed (or re-probed) with primary antibody overnight at 4°C. The membrane was incubated with an appropriate secondary antibody conjugated with horseradish peroxidase and immunoreactive proteins and then visualized using Luminata Forte Western HRP substrate (Millipore, Billerica, MA). The stripping protocol followed the instructions of Restore Western Blot Stripping Buffer (Thermo Fisher). No blots were used more than three times. The following anti-human/mouse antibodies were used for western blot: N-cadherin, E-cadherin, vimentin, ZEB1, SNAIL, SLUG, TWIST, c-MYC, PGRMC1, PGRMC2, β-Actin.

qRT-PCR

To determine the expression levels of TAB1 and PGRMC2 after treatments, cells were collected and lysed using lysis buffer (Qiagen, Valencia, CA, USA). RNA was extracted using a RNeasy kit (Qiagen) per the manufacturer's instructions. Total RNA (500ng) was reverse-transcribed using a High-Capacity RNA-to-cDNA Kit (Applied Biosystems, Foster City, CA). qRT-PCR was performed on an ABI7500 Fast Real-Time PCR System (Applied Biosystems) using Fast SYBR Green Master Mix (Applied Biosystems). The amplification thermal profile was 20s at 95°C and 3 s 95°C, followed by 30s 60°C (40 cycles). To confirm the presence of a single amplicon, a melt curve was carried out: 15s at 95°C, 1 min at 60°C, 15s at 95°C, and 15s at 60°C. Changes in gene expression levels were calculated by using the ΔΔCt method. We used predesigned qRT-PCR primers from Integrated DNA Technologies (Table 4).

Immunocytochemical localization of intermediate filaments cytokeratin and vimentin

Immunocytochemical staining for vimentin (3.7µl/mL;ab92547;Abcam, Cambridge, MA) and CK-18 (1µl/mL;ab668;Abcam) were performed for multiple experimental endpoints [128]. Additionally, vimentin and CK-18 were measured during PGRMC2 overexpression studies. Manufacturer's instructions were used to calculate staining dilutions to ensure uniform staining. After each time point cells were fixed with 4% PFA, permeabilized with 0.5% Triton X, and blocked with 3% BSA in PBS prior to incubation with primary antibodies overnight at 4°C [143]. This protocol is adequate to remove non-specific binding of primary antibodies in our system. After washing with PBS, slides were incubated with Alexa Fluor 488 and 594 conjugated secondary antibodies (Life Technologies, Carlsbad, CA), diluted 1:1000 in PBS, for 1 hour in the dark. Slides were washed with PBS, treated with NucBlue® Live ReadyProbes® Reagent (Life Technologies) and then mounted using Mowiol 4–88 mounting medium (Sigma).

Crystal violet cell viability assay

To document cell viability after 6 day treatments, AECs and AMCs were seed in a 12-well plate and treated as described above. After 6 days, cells were washed with 1× PBS, fixed with 4% PFA for 15 min, washed with water, and stained with 0.1% crystal violet for 20 min. After 20 min, cells are washed, allowed to dry, and 10% acetic acid was added to each well. A 1:4 dilution of the colored supernatant was measured at an absorbance of 590 nm.

Cell shape index quantification

The cell shape index was determined for AEC and AMC 2D cultures by evaluating one frame from each N (total of three images) per treatment for cell circularity using ImageJ software. The shape index was calculated using the following formula: SI= 4π*Area/Perimeter2, which is an established method that was originally reported to determine vascular cell shape [226]. A circle would have a shape index of 1; a straight line an index of 0.

TGF-β ELISA

Human AF was collected at TL, TNIL, pPROM, SPTB, and a human/mouse TGF-β 1 ELISA Ready-SET-Go! ELISA (second generation) (Affymetrix eBioscience) was conducted following the manufacturer's instructions. Standard curves were developed with recombinant protein samples of known quantities. Sample concentrations were determined by correlating the absorbance of the sample to the standard curve by linear regression analysis.

Luminex assay for inflammatory cytokines

The multiplex Luminex-based immunoassay was performed for the cytokines Interleukin-1beta (IL-1β), Interleukin-6 (IL-6), IL-8, and Tumor necrosis factor-alpha (TNF-α) using antibody-coated beads (Biosource International, Camarillo, CA, Luminex

Corporation, Austin, TX) as indicators of SASP profile in murine AF and maternal serum. Standard curves were developed with duplicate samples of known quantities of recombinant proteins that were provided by the manufacturer. Sample concentrations were determined by relating the absorbance that was obtained to the standard curve by linear regression analysis.

Statistics

Statistical analyses for normally distributed data was performed using an ANOVA with the Tukey Multiple Comparisons Test and T-test. Statistical values were calculated using PRISM. P values of less than 0.05 were considered significant. Data is represented as Mean±SEM.

RESULTS

In this study, we sought molecular and cellular evidence of EMT in fetal membranes from term vaginal deliveries and compared them to TNIL membranes collected from scheduled cesarean deliveries. We first examined tight junctions in amnion membranes. Tight junctions are connections between epithelial cells and EMT requires loosening of these junctions to enable transitioning epithelial cells to be shed and or migrate [59, 227]. Migration also requires loosening up of the collagen matrix [59]. As shown in Figure 6.1A, TEM showed smaller desmosome plaques and a significant reduction in tight junction length (TNIL 0.064±0.01nm; TL 0.054±0.01nm) (P=0.0009), accompanied by ECM collagen degradation in TL compared to TNIL membranes. Masson's trichrome staining was used to further show collagen degradation based on the reduced intensity of blue staining marking the membrane epithelium (Fig. 6.1B) and supporting the TEM findings. Next, we examined epithelium (CK18) and mesenchyme-specific (vimentin) intermediate filaments [59-62]. Based on our prior reports that amnion cells normally exist in a 'metastate' expressing both intermediate filament types [128], dual

immunohistochemical staining co-localized CK-18 and vimentin (Fig. 6.1B), however, CK-18 was higher in TNIL, whereas vimentin was increased in TL membranes, suggesting an EMT shift in intermediate filaments with labor. Next, we examined the adherens junction protein, E-cadherin (epithelium-specific) and its mesenchymal homolog N-cadherin. Labor was associated with an increase in the N-cadherin/E-cadherin ratio in favor of N-cadherin, consistent with EMT [228]. Immunohistochemical analyses showed TL membranes had increased N-cadherin and decreased E-cadherin compared to TNIL (Fig. 6.1B) confirmed the EMT shift by AEC in labor. We also examined the key type IV collagenase capable of degrading ECM, MMP9 (Fig. 6.1A and 1B). MMP9, whose AF concentration increase is well documented in labor [124], was increased in TL compared to TNIL membranes (Fig. 6.1B). To confirm histological data, western blot analyses were performed. TL membranes showed higher vimentin (P=0.009) and a lower N-cadherin/E-cadherin ratio (P=0.031) (Fig. 6.1C-D). Specific transcription factors associated with EMT including TWIST, SNAIL, SLUG and ZEB1 and 2, are cell and stimulant specific and time-dependent. As shown in Figure 6.1C-D, TWIST expression was significantly higher in TL than TNIL (P=0.004). Although increasing trends were seen with SNAIL, SLUG, and ZEB in TL, those data did not reach statistical significance (Sup. Fig 6A).

We used a highly validated in vitro organ explant system derived from TNIL membranes to recapitulate the above findings in in vivo clinical specimens [229]. We established conditions that mimic labor via induction of OS, using exposure to a well-characterized CSE [4, 230, 231]. Our prior work has shown that CSE treatment of TNIL membrane explants produces oxidative damage to protein, lipids, and DNA that is identical to changes seen in TL membranes [4]. In particular, activation of the cellular stress mediator p38 MAPK is recapitulated in the explanted membranes (Sup. Fig. 6.1B) [28, 145]. As shown in Figure 6.2A, CSE-treated membranes in culture had reduced tight junctions (P=0.009), as determined by TEM and confirmed by Masson's Trichrome staining (Fig. 6.2B). As seen in TL membranes in vivo, CSE treatment of TNIL membranes

also increased vimentin, N-cadherin and decreased CK-18 and E-cadherin. CSE also induced MMP9 (Fig. 6.2B) and p38 MAPK (Sup. Fig. 6.1C), vimentin, N-cadherin and reduced E-cadherin (P=0.004) (Fig. 6.2C-D). ZEB1 was significantly higher after CSE treatment compared to controls (P=0.036) (Fig. 6.2C-D), whereas SLUG and ZEB increased in response to CSE, but did not reach statistical significance (Sup. Fig 6.1D).

After observing EMT changes in vivo and also in our in vitro model of OS, we proceeded to test whether similar changes could be identified in an animal model of labor. CD-1 mice were selected for examining EMT phenotypic changes in mouse fetal membranes on day (D) 18 (penultimate day of pregnancy) versus D19 (morning of delivery in our colony). Masson's Trichrome staining showed that collagen was more degraded on D19 than D18 and this was accompanied by increased vimentin, N-cadherin and decreased CK-18 and E-cadherin (Fig. 6.3A). MMP9 was also higher in D19 than D18 membranes. Western blot analyses confirmed our histology data, with D19 membranes showing significantly increased vimentin (P=0.005), N-cadherin and decreased E-cadherin (P=0.010) (Fig. 6.3B). SNAIL, one of the murine EMT transcription factors [59] was significantly higher on D19 than D18 membranes (P=0.0016) (Fig. 6.3B), although SLUG did not reach statistical significance (Sup. Fig 6.1E). To test if OS could induce changes similar to those seen on D19, we injected CD-1 mice with CSE on D14 [11]. As shown in Figure 6.3C, vimentin and N-cadherin increased, whereas cytokeratin and E-cadherin were reduced. MMP9 was also higher in animals injected with CSE (Fig. 6.3C). We reported that OS causes significant protein peroxidation (P<.0001), p38 MAPK activation (P<.03), and induced senescence and inflammation (Sup. Fig. 6.2) in this model. To confirm that EMT induction in this model is associated with p38 MAPK activation, animals were co-injected with SB, a p38MAK inhibitor. As shown in Figure 6.3C, SB treatment minimized expression of EMT markers. Additionally, SB treatment reduced pup loss and preserved placental weight (Table 1). These data are supportive of an association among OS, EMT, p38 MAPK activation and senescence during labor in both humans and mouse and EMT.

Descriptive data detailed above used human and mouse TNIL and TL amnion membranes and in vitro models to recreate an in utero environment of OS. We conclude that OS experienced at term prior to labor promotes p38 MAPK-mediated senescence. Further, these studies provided a proof of concept that senescence was a key feature of EMT, likely aided by OS associated p38 MAPK activators [224]. Multiple lines of evidence of EMT in amnion membranes were recreated in these model systems. Inflammatory overload further damages membrane matrix (evidenced by an increase in MMP9 and collagenolysis) that are likely end products of cellular transition associated inflammation.

We next addressed the possible endocrine, paracrine, or autocrine regulation of EMT using human primary AECs derived from normal TNIL membranes. Other investigators established that AECs could be induced by TGF-β to undergo EMT [66, 232] and we have shown that TGF-β, in response to OS, could autophosphorylate p38 MAPK [224]. An alternate signaling pathway has been defined in AECs whereby TAB1, can bypass ASK-1 and MAP3Ks [224]. Therefore, we chose to test the hypothesis that TGF-β -TAB1-p8MAPK might cause EMT. As a rationale to propose TGF-β's role in EMT in amnion cells at term, we examined its concentration in AF samples from various pregnancy conditions. As shown in Supplemental Figure 6.3A, TGF-β was significantly increased in TL compared to TNIL ($P=0.018$). TGF-β concentration was also higher in the AF of subjects with PTB followed by pPROM than women who had PTB with intact membranes ($P=0.037$). Both of these conditions are associated with increased OS [233] and p38 MAPK activation [4, 140]. To verify this hypothesis, primary AECs were treated with TGF-β (15ng/mL) for 6 days. As shown in Figure 6.4A, TGF-β treatment contributed to EMT changes in AECs, altering their typical cuboidal to a fibroblastoid shape with increased expression of vimentin ($P<0.0001$) and reduced CK-18 ($P=0.0002$) (Fig. 6.4A-B). Crystal violet dye exclusion testing showed that morphological changes induced by TGF-β were not an artifact of cell viability or proliferation (Sup. Fig. 6.3B).

Next, we verified the functional role of p38 MAPK in TGF-β -mediated EMT in AECs, using gene silencing with TAB1 siRNA and a pharmacological inhibitor of p38 MAPK (SB). Our prior reports showed that TGF-β mediated p38 MAPK activation was TAB dependent [224]. siRNA to TAB1 reduced the expression of TAB1 mRNA and protein (Sup. Fig. 6.3C) and inhibited p38 MAPK [224]. Morphological changes (Fig. 6.4C), quantified as cell shape indices (Sup. Fig. 6.3D), showed that the TGF-β -induced fibroblastoid shape also was inhibited by TAB1 siRNA or SB. NT siRNA and SB alone did not cause a shift in AEC morphology (Fig. 6.4C) supporting the hypothesis that TGF-β can cause EMT in AECs. To verify parallel changes in EMT transcription factors, we showed that TGF-β increased SLUG and SNAIL expression compared to control (P=0.011; P=0.020, respectively) (Fig. 6.4D and 3E). Co-treatment of TGF-β with TAB1 siRNA or SB reduced SLUG (P=0.026) and SNAIL (P=0.016) expression compared to TGF-β treatment. In accordance with this finding, we noted an increase in N-cadherin and a decrease in E-cadherin (Fig. 6.4E) that corresponded with a higher N-cadherin/E-cadherin ratio (Fig. 6.4E) (P=0.012). This ratio switch was reversed by siRNA to TAB1 and SB co-treatment with TGF-β (Fig. 6.4E). SB treatment alone did not induce changes in morphology, N-cadherin/E-cadherin ratios, or SNAIL and SLUG expression (Sup. Fig. 6.3E). In summary, these experiments show that TGF-β-TGFR1 complex can cause TAB1-mediated autophosphorylation of p38 MAPK (Chapter 5) [224] leading to EMT transcription factor increase, N-cadherin expression and ultimately a fibroblastoid morphology (Fig. 6.4).

EMT is a transition state rather than a stable state, and a homeostatic return of MET phenotype is necessary for the maintenance of membrane integrity. A recent report from our laboratory using scratch assays has shown that wounded primary AECs resemble healing microfractures observed in intact fetal membranes (Chapter 4) [128]. This healing was associated with proliferation, migration, and transition of cells within 38 hours [128]. Proliferative and migrating edges revealed a dominant fibroblastoid shape with superficial

vimentin localization, whereas healed edges were cuboidal with perinuclear vimentin staining. AEC wound healing was accelerated by AF and restrained by OS inducers. Based on these findings, we postulate that MET facilitates reversal of fibroblastoid cells to an epithelial state, as this transition is essential for filling gaps created by epithelial cell exfoliation and migration during gestation. EMT is associated with inflammation and sustained inflammation may damage or weaken membranes [126, 218]. The anti-inflammatory properties of P4 were postulated to minimize EMT's inflammatory effects by transitioning cells back to their epithelial state via MET [223]. Prior to testing the role of P4, we confirmed that AECs do not express the classical nuclear receptors (PRB and PRA) confirming the findings of Murtha et al. [79] and that their actions are likely mediated through membrane progesterone receptors (PGRMC1 and 2).

As shown in Supplemental Figure 6.4A, PGRMC1 expression did not differ between membranes from TNIL and TL; however, we noticed a significant labor-induced decrease in PGRMC2 (P=0.030). This was recapitulated in vitro with AMCs subjected to OS, showing no change in PGRMC1 but a 3-fold downregulation of PGRMC2 (P=0.059) (Sup. Fig. 6.4B-C). Based on these data, we hypothesized that P4 mediates MET in AMCs through PGRMC2. To verify this, primary AMCs were treated with P4 (200ng/mL, to mimic the concentration of P4 at term) for 6 days. As shown in Figure 6.5A, P4 treatment of AMCs was associated with a shift from fibroblastoid to cuboidal shape with increased expression of CK-18 (P<0.0001) (Fig. 6.5A-B). We did not observe changes in vimentin staining. The crystal dye exclusion test showed that morphological changes induced by P4 were not an artifact of apoptosis or cell viability but an indicator of cell rounding (Sup. Fig. 6.4D-E). To confirm the role of PGRMC2 in this transition (Fig. 6.5C) we blocked morphological differentiation with siRNA to PGRMC2. siRNA to PGRMC2 reduced the expression of PGRMC2 mRNA and protein (Sup. Fig. 6.4F). As a control, scrambled siRNA failed to alter mesenchymal morphology validating our gene silencing data. Western blot analysis of AMCs showed upregulation of c-MYC after treatment with P4

(Fig. 6.5D-E) (P=0.010), a signal purported to mediate P4-PGRMC2 effects [234]. Although not significant, we noticed a decreasing trend in c-MYC expression following PGRMC2 siRNA treatment P4 suppressed EMT transcription factors (SNAIL and SLUG) (P=0.015) and this was restored by co-treatment with PGRMC2 siRNA (Fig. 6.5E). Further, P4 treatment decreased N-cadherin while increasing E-cadherin, contributing to an overall decrease in the N-cadherin/E-cadherin ratio (P=0.023) (Fig. 6.5E). siRNA to PGRMC2 reversed this ratio switch supporting P4-PGRMC2 mediated effect producing MET. We then tested if P4 mediated morphologic changes are mediated by c-MYC expression. As shown in Figure 6.6A, P4 treatment of AMCs led to a shift in epithelial morphology that was mitigated by the selective c-MYC inhibitor 10058, confirming the role of c-MYC in MET. In support of this finding, co-treatment of P4 with 10058 increased SNAIL, SLUG and the N-cadherin/E-cadherin ratio (Fig. 6.6B-C). In summary, these experiments show that activation of P4-PGRMC2 complexes can cause c-MYC mediated downregulation of EMT transcription factors and a decrease in N-cadherin expression, contributing to epithelial morphology (Fig. 6.5-6).

To test the effects of P4 on cultured AECs, cells were treated for 6 days and Crystal violet dye exclusion showed no effect on cell viability (Sup. Fig. 6.4G). As shown in Figure 6.7A, P4 treatment maintained epithelial morphology (Sup. Fig. 6.4H) as well as CK-18 expression while significantly reducing (P<0.0001) vimentin compared to untreated cells (Fig. 6.7A-B). In addition, P4 significantly increased c-MYC (P=0.021), decreased SNAIL and SLUG expression (P=0.023; P=0.007, respectively) and reduced the N-cadherin/E-cadherin ratio (P=0.005) (Fig. 6.7C-D). These data supports the theory that the high concentrations of circulating P4 in late pregnancy serve to maintain epithelial characteristics in AECs.

To further confirm that TGF-β and P4 confer opposing effects on AECs, we performed in vitro scratch assays. As shown in Figure 6.8A and B, a scratch in the AEC monolayer normally heals within 38 hours (Chapter 4). As seen with our primary cells

under normal culture conditions healing involves cellular proliferation, migration, and transition. TGF-β substantially prevented the healing of AEC scratches, with full persistence of the wound after 38 hours whereas P4 accelerated the healing process. We tested if TGF-β-induced static, terminal or non-revisable, state of EMT contributed to this process by immunostaining for CK-18 and vimentin. Figure 6.8B shows vimentin dominant and fibroblastoid shaped cells dominating the leading edges of the wound that fails to heal after 38 hours. On the contrary, healed areas after P4 treatment were dominated by CK-18 positive cell with epithelial morphology. These data further support that during pregnancy P4-mediated remodeling of amnion membrane is likely a phenomenon to help membrane homeostasis whereas OS-induced TGF-β may necessitate a non-reversible state of EMT.

We evaluated if mechanistic mediators like TGF-β and c-MYC might also play a role in our murine model. Immunohistochemical localization of TGF-β and c-MYC in mouse AECs and AMCs was assessed on D9, D13, D18, and D19 (Sup. Fig. 6.5A-B). The intensity of staining suggested that TGF-β was higher in AECs ($P<0.0001$) and c-MYC is lower in AMCs on D19 compared to D18 ($P=0.029$) (Sup. Fig. 6.5A-B). This suggests that TL, a condition associated with increased OS, can cause TGF-β to increase and c-MYC to decrease (likely due to systemic P4 withdrawal reported in this model) supporting our notion that activation of EMT is a non-reversible terminal event (static state of EMT) and down-regulation of MET are induced by OS factors associated with parturition at term.

DISCUSSION

In this study, we investigated the mechanisms and mediators through which human fetal amnion membrane cells (epithelial and mesenchymal) undergo cyclic remodeling to maintain membrane integrity during pregnancy. We show that human and murine AEC exist in a "metastate" at term, co-expressing both epithelial (cytokeratin) and mesenchymal (vimentin) markers (Fig. 6.1, Fig. 6.2, and Fig. 6.3). However, mesenchymal features

dominated in laboring compared to non-laboring membranes. We were able to recapitulate these findings in vitro when organ explants of not in labor membranes were exposed to OS mimicking labor (Fig. 6.2). This finding supports previous reports by Janzen et al. [126] and Mogami et al. [141, 218] where similar descriptive evidence of EMT were shown in term laboring membranes. The transition from TNIL to TL is also associated with increased OS, peroxidation of various cellular elements and activation of p38 MAPK. Senescence and SASP (a form of sterile inflammation) were observed [2]. Membranes at TL had more microfractures, degraded basement membranes and augmented cell migration [39]. Based on our findings in Figures 6.1 and 2, we speculate that molecular and cellular senescence is associated with a terminal (irreversible or static) state of EMT. EMT, and associated inflammation and ECM matrix weakening are predisposing factors for mechanical disruption of membranes prompting and facilitating labor and delivery.

The role of TGF-β was investigated as a facilitator of amnion EMT for the following reasons; 1) TGF-β is increased in TL AF compared to TNIL; 2) immunoreactivity of TGF-β is higher in membranes from TL vs. TNIL; 3) in vitro evidence shows that OS can increase release TGF-β from membranes [224]; and 4) it is one of the classical SASP markers. In addition, 5) extracellular vesicles released from AECs under OS are enriched in TGF-β peptides [143] suggesting a paracrine pathway to promote EMT. 6) Amnion cells exposed to OS also undergo TGF-β -mediated autophosphorylation of p38 MAPK [224], a key signal that enforces membrane senescence. In summary, intra-uterine OS at term can initiate a cascade of events mediated by TGF-β-p38 MAPK-senescence-EMT that will weaken the amnion membranes. After EMT, the resultant mesenchymal cells are more susceptible to OS than their epithelial predecessors and produce inflammatory cytokines, MMPs and collagen degradation that can compromise membrane integrity. Loss of tight junctions also promotes disassembly of ECM scaffold structures. As shown in Supplemental Figure 6.5A, the accumulation of mesenchymal cells in TL vs. TNIL supports this concept.

TGF-β mediated EMT is a well-reported phenomenon across development and our data indicate that AEC are no exception. Blocking TGF-β mediated signaling through TAB1 gene silencing of reduced EMT transcription factors and mesenchymal junction markers, maintaining epithelial characteristics. Silencing of TGF-β signaling also reduced p38 MAPK activation [224]. Inhibition of EMT in AECs by treatment with a p38 MAPK inhibitor (SB) further identifies this pathway (Fig. 6.4). In both human and mouse membranes, the p38 MAPK inhibitor reduced mesenchymal intermediate filaments, junction markers, and transcription factors (Fig. 6.3 and Fig. 6.4). TGF-β-p38 MAPK pathway plays a major role in membrane homeostasis and cell remodeling throughout gestation as their functions are regulated by many factors including P4. AEC that are not permanently shed, are transitioned and translocated to the ECM where they remain there as a mesenchymal cell repository, capable of cellular recycling and repair of microfractures and gaps in the amnion membrane. ROS production and p38 MAPK activation peak at term to augment amnion cell senescence and SASP-induced inflammation to promote a terminal state of EMT (Fig. 6.9).

We also examined the mechanisms of recycling of mesenchymal back to an epithelial phenotype. Mesenchymal cells perform endocrine functions during gestation [235]; however, these are tightly regulated and only require a limited number of cells (approximately 10% of amnion membrane cell are mesenchymal). As mesenchymal cells are predisposed to generating inflammatory and ROS signals [236] their numbers need to be tightly regulated and this is achieved by reprograming them back to an epithelial state through MET. MET reestablishes cell-to-cell contacts and increases nascent collagen production to repair degraded matrix. P4 is a known anti-inflammatory hormone that supports pregnancy maintenance, so we tested its ability to reverse EMT to MET. We showed that P4, through PGRMC2, induces MET via proto-oncogene c-MYC expression (Fig. 6.5 and Fig. 6.6). Silencing PGRMC2 with siRNA or reducing c-MYC using a pharmacologic inhibitor, increased mesenchymal transcription factors and a fibroblastoid

phenotype (Fig. 6.5 and Fig. 6.6). Based on these data, we postulateD that P4 in the AF or endogenously produced by membrane cells may play a functional role in maintaining membrane homeostasis. This regulation is further modified as P4 increases PGRMC2 transcripts and protein expression in AMCs (Sup. Fig. 6.4F) providing a feedforward loop to promote MET. To verify these mechanisms, we overexpressed PGRMC2 in AMCs and showed increased P4 mediated MET. MET was evident even under OS conditions (Sup. Fig. 6.6B-C) in cells that overexpressed PGRMC2. However, PGRMC2 is reduced in TL membranes (P=0.03), specifically in the mesenchymal cells (Sup. Fig. 6.4A), likely due to OS in the amniotic cavity. To verify this concept, AMCs in culture were exposed to CSE, an inducer of OS, which showed a 3-fold reduction in PGRMC2 expression (Sup. Fig. 6.4B). No change in PGRMC2 was seen in AECs (Sup. Fig. 6.4C). A 3-fold decrease was observed in PGRMC1 supporting prior reports by Feng et al. [217, 237]. An overall reduction in PGRMC2 induced a localized 'functional P4 withdrawal' that disrupted MET (Fig. 6.9). We propose this as one of the mechanisms leading to a static or terminal state of EMT at term, indicating a new role for P4 as a pregnancy hormone that maintains membrane integrity (Fig. 6.9).

Maintenance of membrane integrity during gestation and its mechanical and functional disruptions at term involve both cellular and matrix levels changes. Although collagenolysis is well reported, this study emphasizes the role played by the amnion cells themselves. AECs and AMCs can undergo cyclic reprograming throughout gestation under the influence of changes in local tissue environment, i.e., localized inflammation promoting EMT whereas P4 supports MET (Fig. 6.9). Increases in intra-uterine OS, TGF-β and p38 MAPK activation mediated senescence, and EMT increase AMCs in membranes. During gestation, P4 through its membrane receptor, regulate the number of AMCs by converting them back to AECs (Fig. 6.9).

This study has some limitations as the amnion layer of the fetal membranes has dominated our focus. Microfractures also have been reported in the chorion layer [96] and

chorion cells undergo a similar type of OS, p38 MAPK activation, and senescence [82]. The chorion trophoblast cells and fibroblastoid cells of its reticular layer also can be susceptible to similar transitions. This region is vulnerable to signals from the maternal decidua and its resident immune cells [24]. TGF-β and P4 are obvious choices in this study as the level of the former are increased and reduced activity of the latter are established in TL. Besides, P4 is a known c-MYC activator and a mediator of MET. Estrogens, IL-6, and other labor-associated growth factors known to increase in AF at term (EGF, FGF, etc.) can also promote EMT [238-240]. Although our model emphasizes the TGF-β effect, it is highly likely that EMT in TL is mediated by synergy and cooperation among multiple factors.

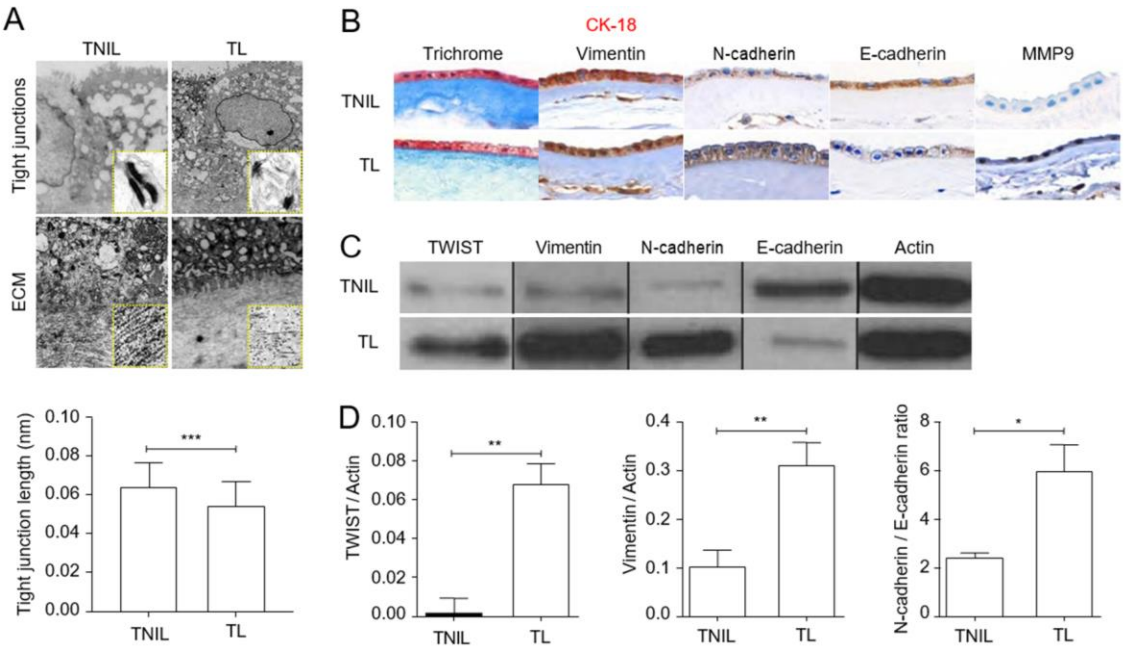

Fig. 6.1 Human amnion membranes from normal TL show evidence of EMT

A) TEM of amnion membranes from TL compared to TNIL (N=3) shows a significant reduction in length of tight junctions (0.06447±0.0125nm vs. 0.05476±0.01173nm; P=0.0009), associated with collagen degradation. (1500x) Enlarged images shown in the inset indicate electron dense desmosomes. This figure shows one representative image from three separate samples. B) Histologic staining (Masson's trichrome) (N=3) of TL membranes show collagen degradation (reduced blue staining) compared to TNIL membranes. Dual IHC staining (N=3) shows a decrease in intermediate filaments CK-18 (pink) and an increase in vimentin (brown) expression in TL compared to TNIL. IHC shows higher expression of N-cadherin and lower E-cadherin expression (both junction markers) in TL compared to TNIL membranes. Basement membrane type IV collagen-specific MMP9 expression was higher in TL than TNIL. These data are indicative of EMT associated changes. (40x) Enlarged images are shown in the insets. This figure shows one representative image from three separate samples. C–D) Western blot analysis (N=5) (C) of EMT associated transcription factors, proteins, and their quantitation. (D) Amnion membranes at TL contained significantly higher EMT transcription factor (TWIST; P=0.004). Intermediate filaments (vimentin; P=0.009), and junction markers (N-cadherin/E-cadherin ratio; P=0.031) were higher in TL than TNIL membranes. Error bars represent Mean ±SEM.

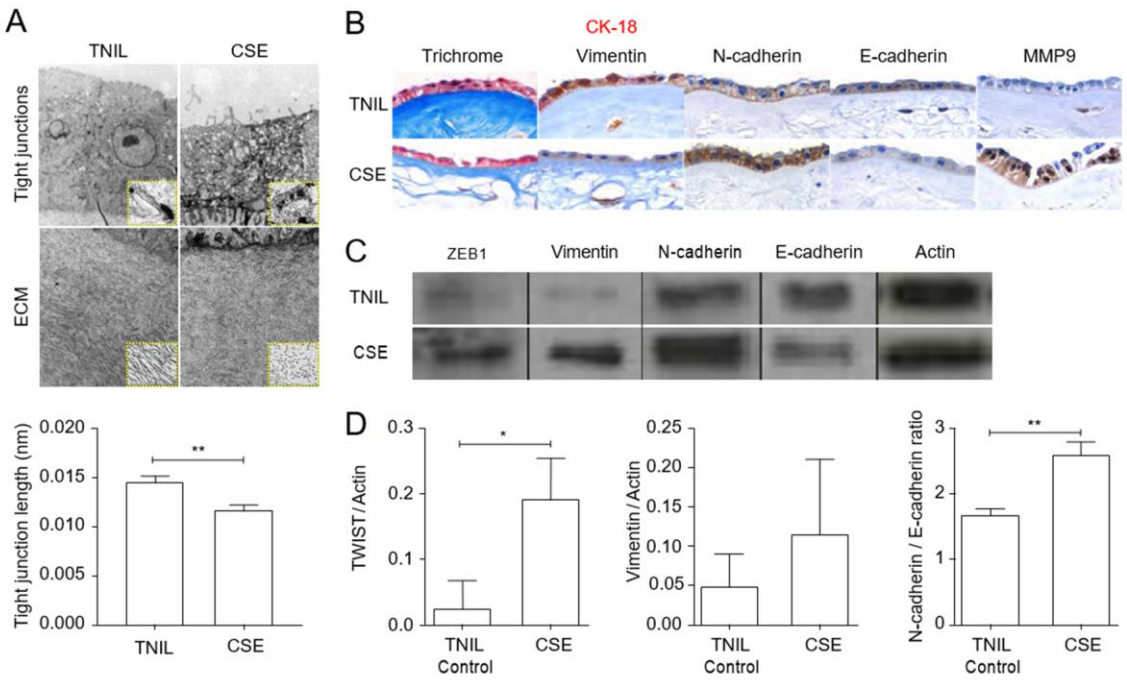

Fig. 6.2 TNIL human amnion membranes exposed to OS show evidence of EMT

A) TEM of amnion membranes cultured in an organ explant system and exposed to CSE (OS) compared to controls (N=3) showed a reduction in tight junction length (0.0145±0.004689nm, and 0.01178±0.00211nm; P=0.0009) and increased collagen degradation. (1500x) Enlarged images are shown in the insets. This figure shows one representative image from three separate samples. B) Histologic staining (Trichrome) of TNIL membranes exposed to CSE in vitro revealed collagen degradation (reduced blue staining) compared to control. Dual IHC staining showed a decrease in intermediate filament CK-18 (pink) (N=3) and an increase in vimentin (brown) after CSE exposure compared to control (N=3). IHC shows higher expression of N-cadherin and lower E-cadherin expression (both junction markers) following CSE treatment (N=3). Basement membrane type IV collagen-specific MMP9 expression was higher in CSE exposed membranes than control. (40x) Enlarged images are shown in the insets. This figure shows one representative image from three separate samples. C-D) Western blot analysis of EMT associated transcription factor, EMT associated proteins, and their quantitation. Amnion membranes after CSE treatment contained significantly higher EMT transcription factor (ZEB1; P=0.035). Supporting IHC data (N=4), intermediate filaments (vimentin), and junction marker ratios (N-cadherin/E-cadherin; P=0.004) were higher in CSE than TNIL control membranes. Error bars represent Mean ± SEM.

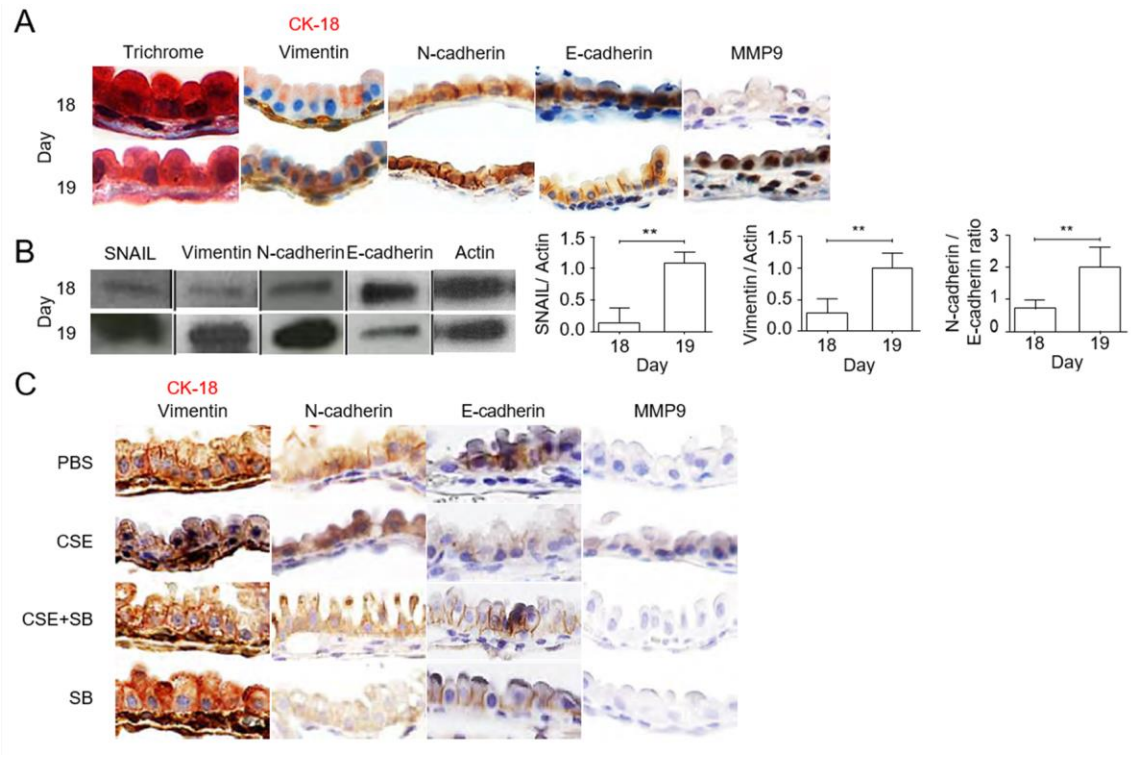

Fig. 6.3 TL and OS treatments induce p38 MAPK dependent EMT in a CD-1 mouse model

A) Histologic staining (Masson's trichrome) Day (D) 19 shows collagen degradation (reduced blue staining) compared to D18 (N=3). Dual IHC staining shows a decrease in intermediate filaments CK-18 (pink) and an increase in vimentin (brown) expression in D19 mouse membranes compared to D18. IHC shows higher expression of N-cadherin and lower E-cadherin expression (both junction markers) on D19 compared to D18. Basement membrane type IV collagen-specific MMP9 expression was higher in D19 membranes than D18. (40x) This figure shows one representative image from three separate samples. B) Western blot analysis of EMT associated transcription factor, EMT associated proteins, and their quantitation. Amnion membranes (N=5) on D19 contained significantly higher EMT transcription factor than D18 (SNAIL; P=0.001). Supporting IHC data (A), intermediate filaments (vimentin; P=0.005), and junction markers (N-cadherin/E-cadherin ratio; P=0.009) were higher in D19 than D18 membranes. This figure shows one representative image from five separate samples. Error bars represent Mean±SEM. C) Histochemistry following CSE injections (N=3) demonstrates disorganized collagen (less light blue stain [Note: ECM in mouse membrane is not as prominent as in humans]), a decrease in IHC signals for epithelial junction markers CK-18 and E-cadherin, and an increase in mesenchymal markers vimentin, N-cadherin, and MMP9 staining. Co-treatment with p38 MAPK inhibitor, SB, prevented CSE induced EMT associated changes in mouse amnion membranes. These data suggest OS-induced EMT at term is partly dependent on p38 MAPK signaling. (40x). Error bars represent Mean ± SEM.

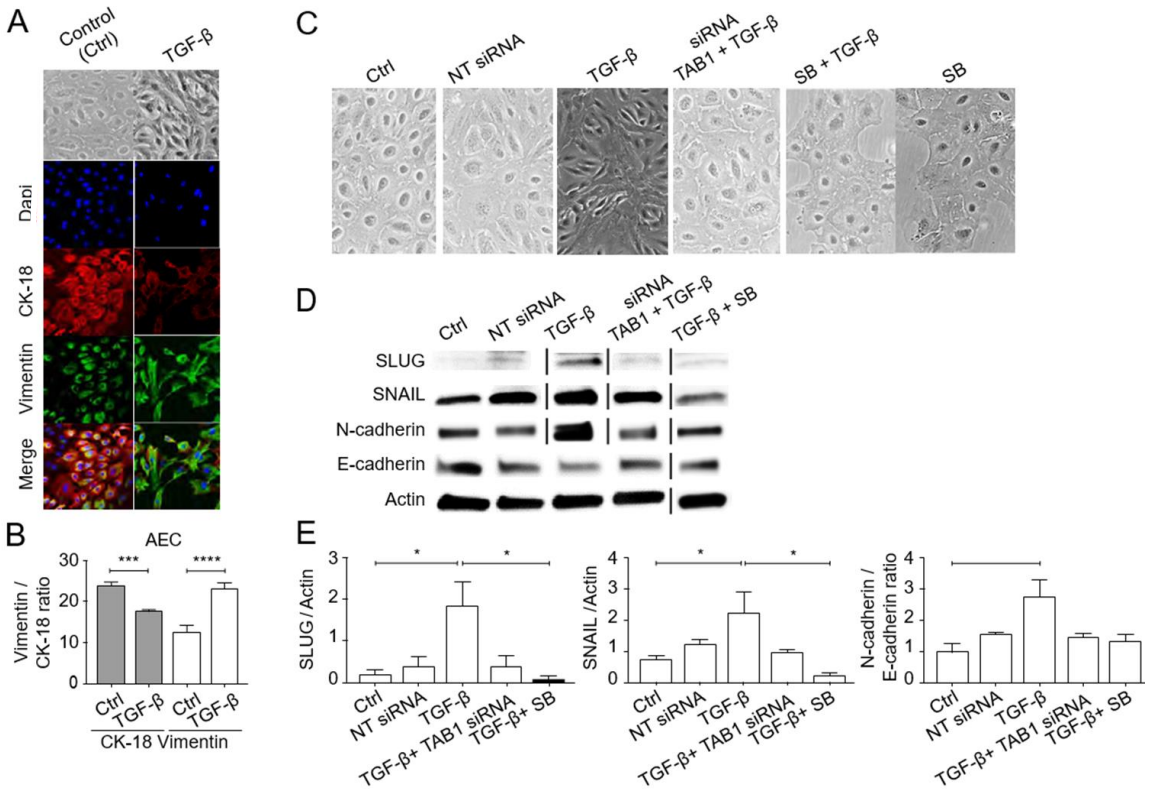

Fig. 6.4 TGF-β quantity and ability to induce EMT in a TAB1-p38 MAPK dependent manner in human AEC

A–B) Bright field microscopy (top panel) shows TGF-β treatment induces mesenchymal morphology of AECs (N=3). Confocal images (bottom panels) show CK-18 expression significantly decreased (Control: 23.81±7.124 vs TGF-β: 17.73±1.416; P<0.0001) and an increase in vimentin expression (Control: 12.66 ± 10.63 vs TGF-β: 23.33 ± 4.751; P=0.0002) (N=3). Confocal images were captured at 63x. Blue-DAPI, red-CK-18, and green–vimentin. Values are expressed as mean intensity±SD. This figure shows one representative image from three separate experiments. Error bars represent Mean ±SEM. C) Bright field microscopy documenting mesenchymal morphology (N=5). TGF-β treatment induces mesenchymal morphology of AECs compared to control cells. Treatment with NT siRNA, siRNA to TAB1, or p38 MAPK inhibitor (SB) or co-treatment of inhibitors with TGF-β retained epithelial morphology suggesting that p38 MAPK activation is required for AEC's mesenchymal transition. (20x). This figure shows one representative image from five separate experiments. D–E) Western blots (D) and densitometry analysis (E) of AECs (N=3) treated with TGF-β significantly increased mesenchymal transcription factors SNAIL and SLUG (P=0.0208; P=0.011) as well as N-cadherin/E-cadherin ratio (P=0.012). Treatment with siRNA to TAB1 or p38 MAPK inhibitor (SB) alone or co-treatment of inhibitors with TGF-β prevented EMT associated changes to various markers. (SNAIL: P=0.026; SLUG: P=0.016; N-cadherin/E-cadherin ratio: P=0.081). This figure shows one representative image from three separate experiments. Error bars represent Mean±SEM.

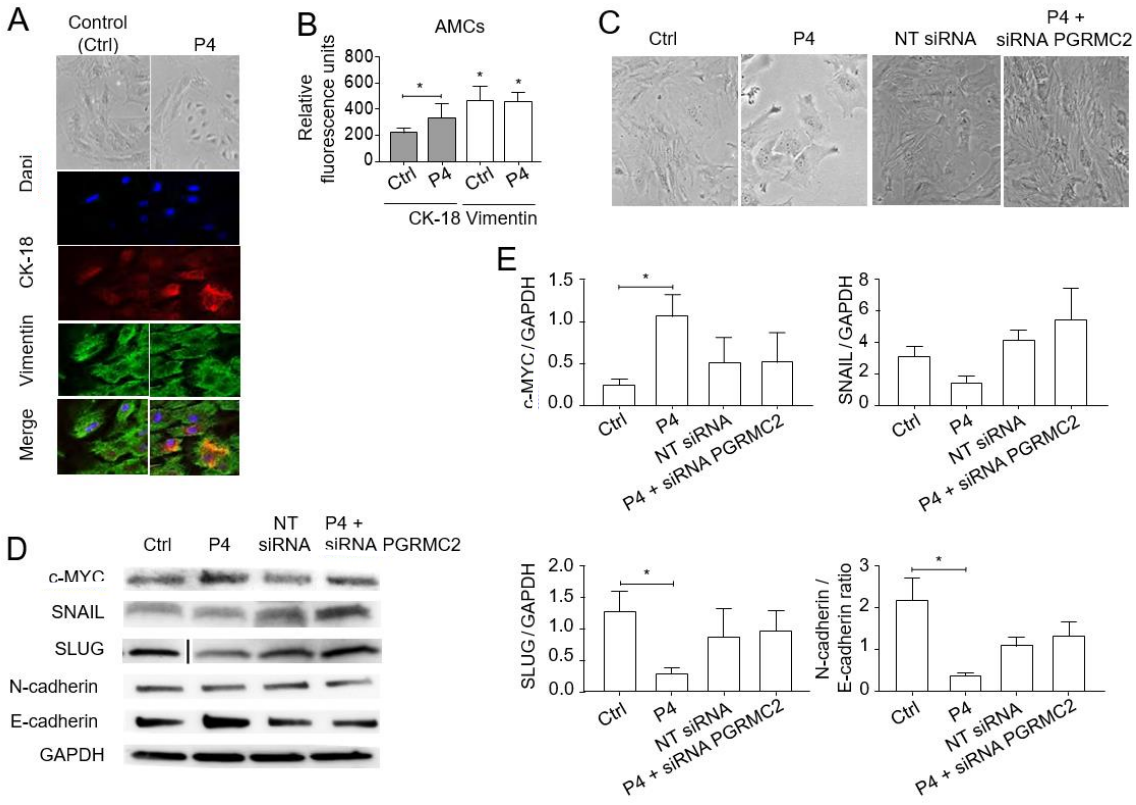

Fig. 6.5 P4 induces MET in a PGRMC2 dependent manner in AMCs.

A–B) Bright field microscopy (top panel) shows P4 treatment reduces mesenchymal morphology of AMCs. Confocal images (bottom panels) show an increase in CK-18 expression (Control (N=3): 226.7±29.01 vs P4: 348.4±111; P=0.002) while vimentin expression remained constant (Control: 467.6±106.6 vs P4: 448.5±82.1; P=0.902). Confocal images were captured at 63x. Blue–DAPI, red–CK-18, and green–vimentin. This figure shows one representative image from 3 separate experiments. Error bars represent Mean±SEM. C) Bright field microscopy documenting P4 induced epithelial morphology. Treatment with siRNA to PGRMC2, NT siRNA, or co-treatment with P4 retained mesenchymal morphology (N=3). This figure shows one representative image from three separate experiments. D–E) Western blot analysis (N=3) of AMCs treated with P4 contained significantly increased epithelial transcription factor c-MYC (P=0.01) while decreasing mesenchymal transcription factors SNAIL and SLUG (P=0.015) as well as N-cadherin/E-cadherin ratio (P=0.023). This figure shows one representative image from three separate experiments. Error bars represent Mean±SEM.

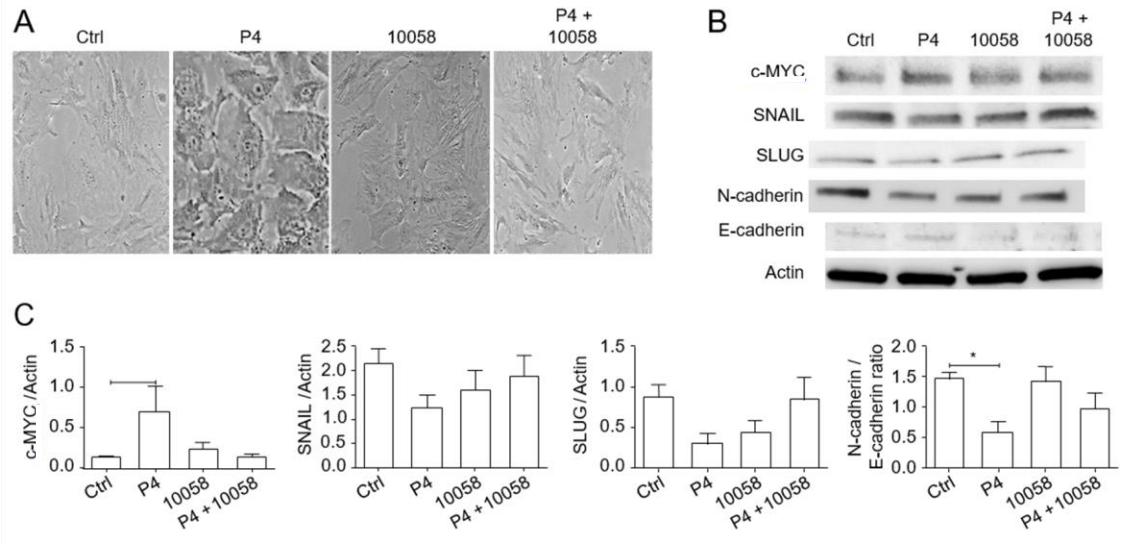

Fig. 6.6 P4 induces MET in a PGRMC2-c-MYC dependent manner in AMCs

A) Bright field microscopy documenting P4 induced epithelial morphology. Treatment with c-MYC inhibitor 10058 or co-treatment of inhibitors with P4 retained mesenchymal morphology (N=3). This figure shows one representative image from three separate experiments. B–C) Western blot analysis (N=3) of AMCs treated with P4 contained increased epithelial transcription factor c-MYC while decreasing mesenchymal transcription factors SNAIL and SLUG as well as the N-cadherin/E-cadherin ratio (P=0.047). This figure shows one representative image from three separate experiments. Error bars represent Mean± SEM.

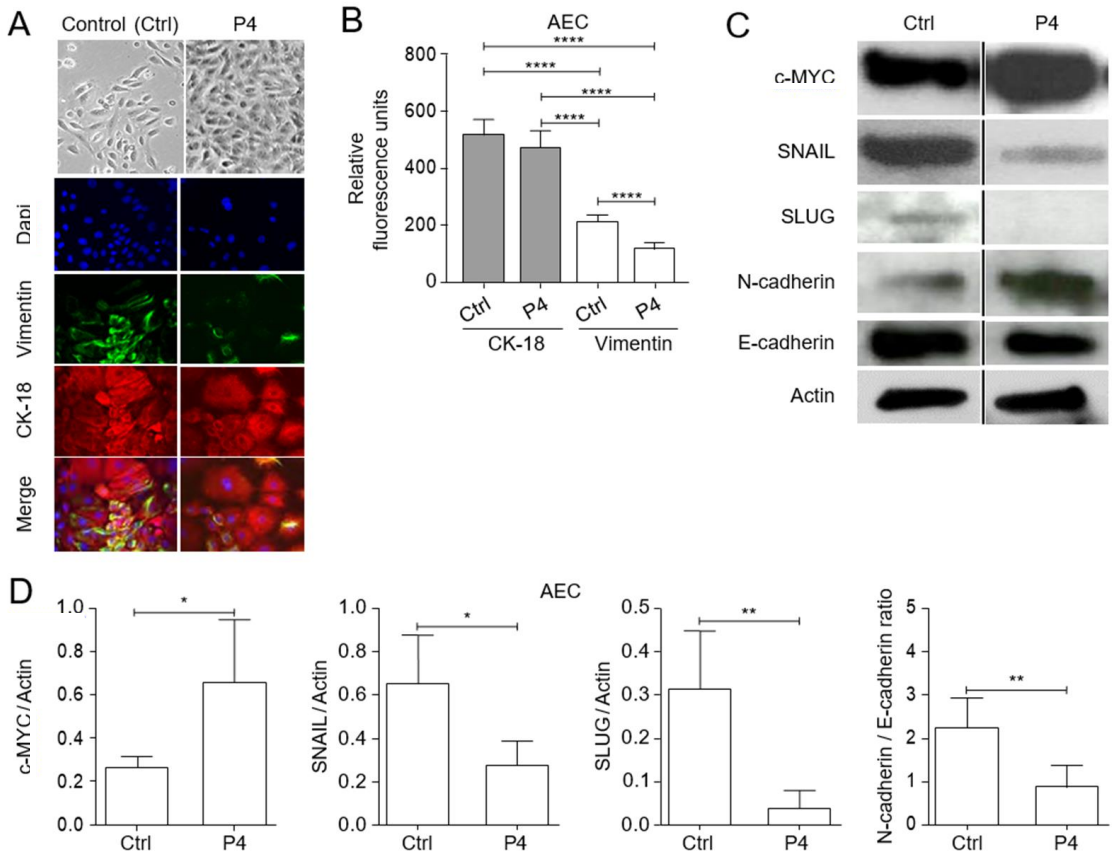

Fig. 6.7 P4 maintains an epithelial state of human amnion cells

A–B) Bright field microscopy shows P4 treatment reducing "metastate" morphology of AECs after six days in culture (N=3). Confocal images show a decrease in vimentin expression (Control (N=3): 223±15.47 vs P4: 130.1±15.68; P<0.0001) while CK-18 expression remained constant (Control: 523±57.5 vs P4: 480.3±52.01; P=0.188). Confocal images were captured at 63x. Blue–DAPI, red–CK-18, and green-vimentin. This figure shows one representative image from five separate experiments. Error bars represent Mean±SEM. C–D) Western blot analysis of AECs treated with P4 (N=5) contained significantly increased epithelial transcription factor c-MYC (P=0.0211) while decreasing mesenchymal transcription factors SNAIL and SLUG (P=0.023; P=0.007) as well as N-cadherin/ E-cadherin ratio (P=0.005). This figure shows one representative image from five separate experiments. Error bars represent Mean±SEM.

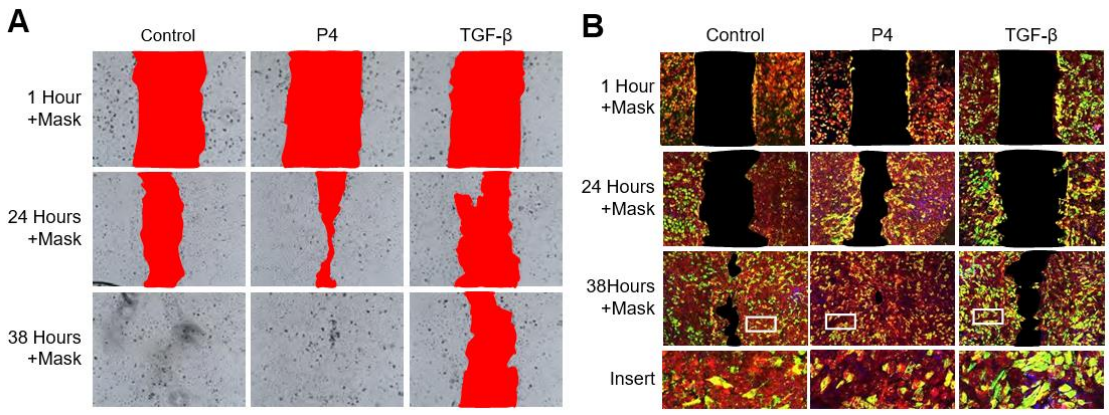

Fig. 6.8 P4 expedites wound healing capacity of human AECs in vitro.

A) AECs under normal cell culture conditions show their natural ability to heal a wound within 38 hours (N=3). P4 expedites wound healing, while TGF-β prevented wound healing as the migrated distance between the two scratch edges never seal. A red mask was applied to help visualization of the wound field (10x). This figure shows one representative image from three separate experiments. B) Scratch assay was performed on primary AECs grown on a slide. Cells were stained with vimentin (green) and CK-18 (red). Cells proliferated and migrated within 22 hours showing mesenchymal morphology and vimentin shifting to the leading edge of migrating cells. Within 38 hours, the scratch was sealed and cells regained their epithelial morphology and CK-18 expression in both control and P4 treated cells. These data show that cells undergo EMT while proliferating and migrating and revert to an epithelial phenotype through MET heal the wound (10x). This figure shows one representative image from three separate experiments.

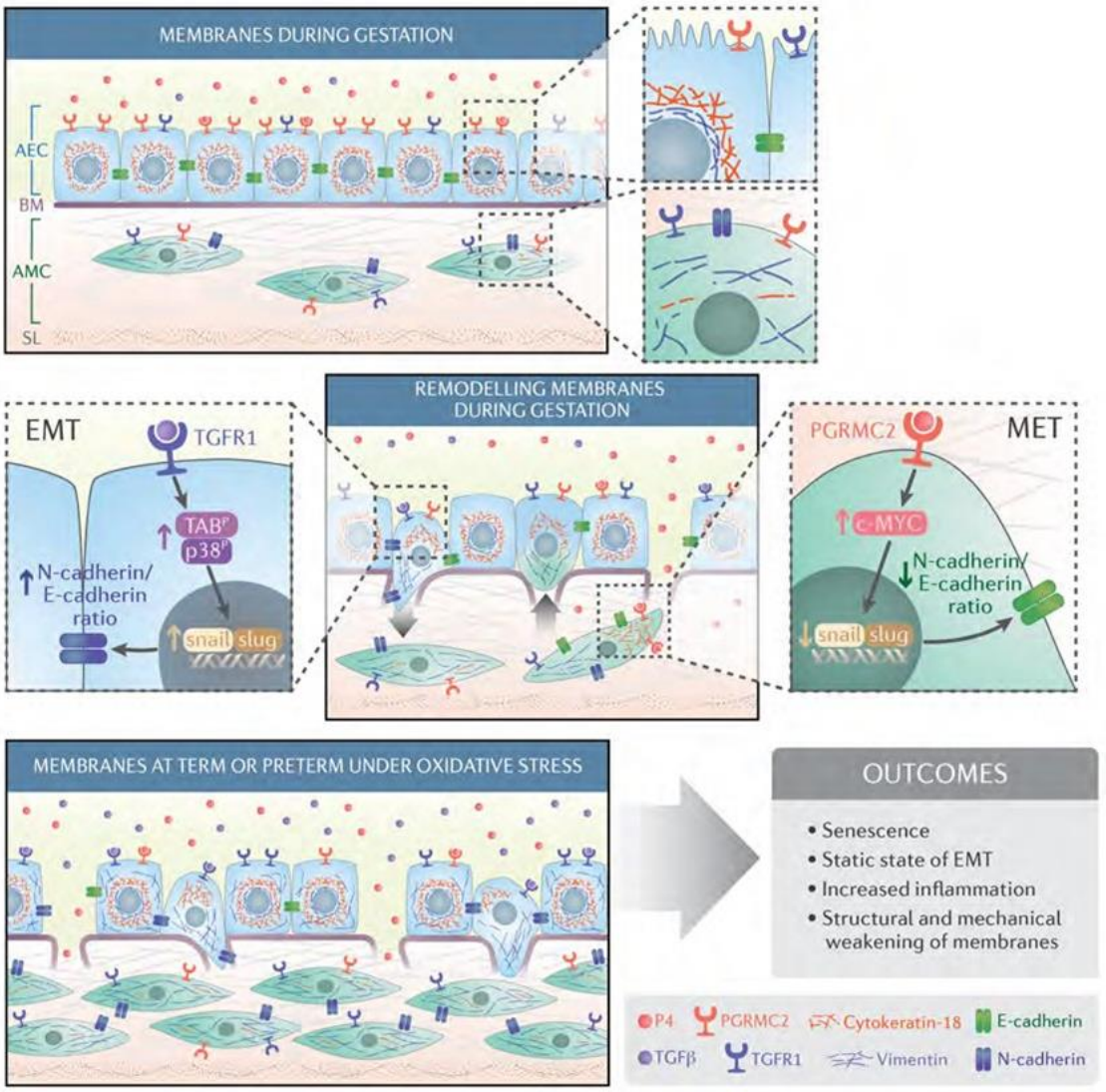

Fig. 6.9 Schematic fetal membrane maintenance and disruption due to cellular transitions

The Amnion membrane is comprised of AEC and AMC separated by a type IV basement membrane collagen and ECM. During gestation, P4 helps to maintain AEC epithelial state. AMCs, located in the ECM, express a fibroblastoid morphology. Based on our data, we hypothesize that the plasticity of fetal membrane cells allows them to undergo MET/EMT-mediated cyclic cellular remodeling, maintaining inflammatory homeostasis via a balanced P4 and TGF-β mediated pathways during gestation to overcome localized inflammation/microfractures. At term and preterm, increased OS and senescence cause intercellular and AF TGF-β increase and functional P4 withdrawal mediated by P4 receptor down-regulation (PGRMC2) in AMCs which induces a terminal state of EMT, increased AMCs, and inflammation contributing to labor associated outcomes.

Treatment	Increased 3-NT	Activated p38 MAPK	Induced senescence	Increased Inflammatory mediators	Increased % pups reabsorbed	Decreased placental weight
Saline Control	-	-	-	-	-	-
CSE	++	++	++	++	++	++
CSE+ SB	+	+	+	+	+	+

Table 8.1 Oxidative stress-induced changes in pregnant CD-1 mice.

Gene of interest	Target sequence 1	Target sequence 2	Target sequence 3	Target sequence 4
NT siRNA	UAAGGCUAUGAAGAGAUAC	AUGUAUUGGCCUGUAUUAG	AUGAACGUGAAUUGCUCAA	UGGUUUACAUGUCGACUAA
TAB1 siRNA	GAUGAGCUCUUCCGUCUUU	GAACAACUGCUUCCUGUAU	GGAGAUUGCUGCGAUGAUU	AAAUAUGGCUACACGGACA
PGRMC2 siRNA	GGCCACUACCGCCGACCACU	CUUCCGCGACCGCCCGUCAC	GACUUGAUCAGUGACCCUGG	UGAAAAAGUGUGAUCUUAAA

Table 8.2 siRNA sequences for genes of interest

Plasmid sequence: GFP-PGRMC2

GACGGATCGGGAGATCTCCCGATCCCCTATGGTGCACTCTCAGTACAATCTGCTCTGATGCCGCATAGTTAAGCCAGTATCTGCTCCCTGC
TTGTGTGTTGGAGGTCGCTGAGTAGTGCGCGAGCAAAATTTAAGCTACAACAAGGCAAGGCTTGACCGACAATTGCATGAAGAATCTGCTT
AGGGTTAGGCGTTTTGCGCTGCTTCGCGATGTACGGGCCAGATATACGCGTTGACATTGATTATTGACTAGTTATTAATAGTAATCAATTA
CGGGGTCATTAGTTCATAGCCCATATATGGAGTTCCGCGTTACATAACTTACGGTAAATGGCCCGCCTGGCTGACCGCCCAACGACCCCCG
CCCATTGACGTCAATAATGACGTATGTTCCCATAGTAACGCCAATAGGGACTTTCCATTGACGTCAATGGGTGGAGTATTTACGGTAAACT
GCCCACTTGGCAGTACATCAAGTGTATCATATGCCAAGTACGCCCCCTATTGACGTCAATGACGGTAAATGGCCCGCCTGGCATTATGCCC
AGTACATGACCTTATGGGACTTTCCTACTTGGCAGTACATCTACGTATTAGTCATCGCTATTACCATGGTGATGCGGTTTTGGCAGTACAT
CAATGGGCGTGGATAGCGGTTTGACTCACGGGGATTTCCAAGTCTCCACCCCATTGACGTCAATGGGAGTTTGTTTTGGCACCAAAATCAA
CGGGACTTTCCAAAATGTCGTAACAACTCCGCCCCATTGACGCAAATGGGCGGTAGGCGTGTACGGTGGGAGGTCTATATAAGCAGAGCTC
TCTGGCTAACTAGAGAACCCACTGCTTACTGGCTTATCGAAATTAATACGACTCACTATAGGGAGACCCAAGCTGGCTAGCGTTTAAACTT
AAGCTTGGTACCGAGCTCGGATCCACTAGTCCAGTGTGGTGGAATTCTGCAGATATCCAGCACAGTGGCGGCCGCTCGAGTCTAGAGGGCC
CGTTTAAACCCGCTGATCAGCCTCGACTGTGCCTTCTAGTTGCCAGCCATCTGTTGTTTGCCCCTCCCCCGTGCCTTCCTTGACCCTGGAA
GGTGCCACTCCCACTGTCCTTTCCTAATAAAATGAGGAAATTGCATCGCATTGTCTGAGTAGGTGTCATTCTATTCTGGGGGGTGGGGTGG
GGCAGGACAGCAAGGGGGAGGATTGGGAAGACAATAGCAGGCATGCTGGGGATGCGGTGGGCTCTATGGCTTCTGAGGCGGAAAGAACCAG
CTGGGGCTCTAGGGGGTATCCCCACGCGCCCTGTAGCGGCGCATTAAGCGCGGCGGGTGTGGTGGTTACGCGCAGCGTGACCGCTACACTT
GCCAGCGCCCTAGCGCCCGCTCCTTTCGCTTTCTTCCCTTCCTTTCTCGCCACGTTCGCCGGCTTTCCCCGTCAAGCTCTAAATCGGGGGC
TCCCTTTAGGGTTCCGATTTAGTGCTTTACGGCACCTCGACCCCAAAAAACTTGATTAGGGTGATGGTTCACGTAGTGGGCCATCGCCCTG
ATAGACGGTTTTTCGCCCTTTGACGTTGGAGTCCACGTTCTTTAATAGTGGACTCTTGTTCCAAACTGGAACAACACTCAACCCTATCTCG
GTCTATTCTTTTGATTTATAAGGGATTTTGCCGATTTCGGCCTATTGGTTAAAAAATGAGCTGATTTAACAAAAATTTAACGCGAATTAAT
TCTGTGGAATGTGTGTCAGTTAGGGTGTGGAAAGTCCCCAGGCTCCCCAGCAGGCAGAAGTATGCAAAGCATGCATCTCAATTAGTCAGCA
ACCAGGTGTGGAAAGTCCCCAGGCTCCCCAGCAGGCAGAAGTATGCAAAGCATGCATCTCAATTAGTCAGCAACCATAGTCCCGCCCCTAA
CTCCGCCCATCCCGCCCCTAACTCCGCCCAGTTCCGCCCATTCTCCGCCCCATGGCTGACTAATTTTTTTTATTTATGCAGAGGCCGAGGC
CGCCTCTGCCTCTGAGCTATTCCAGAAGTAGTGAGGAGGCTTTTTTGGAGGCCTAGGCTTTTGCAAAAAGCTCCCGGGAGCTTGTATATCC
ATTTTCGGATCTGATCAGCACGTGATGAAAAAGCCTGAACTCACCGCGACGTCTGTCGAGAAGTTTCTGATCGAAAAGTTCGACAGCGTCT
CCGACCTGATGCAGCTCTCGGAGGGCGAAGAATCTCGTGCTTTCAGCTTCGATGTAGGAGGGCGTGGATATGTCCTGCGGGTAAATAGCTG
CGCCGATGGTTTCTACAAAGATCGTTATGTTTATCGGCACTTTGCATCGGCCGCGCTCCCGATTCCGGAAGTGCTTGACATTGGGGAATTC
AGCGAGAGCCTGACCTATTGCATCTCCCGCCGTGCACAGGGTGTCACGTTGCAAGACCTGCCTGAAACCGAACTGCCCGCTGTTCTGCAGC
CGGTCGCGGAGGCCATGGATGCGATCGCTGCGGCCGATCTTAGCCAGACGAGCGGGTTCGGCCCATTCGGACCGCAAGGAATCGGTCAATA
CACTACATGGCGTGATTTCATATGCGCGATTGCTGATCCCCATGTGTATCACTGGCAAACTGTGATGGACGACACCGTCAGTGCGTCCGTC
GCGCAGGCTCTCGATGAGCTGATGCTTTGGGCCGAGGACTGCCCCGAAGTCCGGCACCTCGTGCACGCGGATTTCGGCTCCAACAATGTCC
TGACGGACAATGGCCGCATAACAGCGGTCATTGACTGGAGCGAGGCGATGTTCGGGGATTCCCAATACGAGGTCGCCAACATCTTCTTCTG
GAGGCCGTGGTTGGCTTGTATGGAGCAGCAGACGCGCTACTTCGAGCGGAGGCATCCGGAGCTTGCAGGATCGCCGCGGCTCCGGGCGTAT
ATGCTCCGCATTGGTCTTGACCAACTCTATCAGAGCTTGGTTGACGGCAATTTCGATGATGCAGCTTGGGCGCAGGGTCGATGCGACGCAA
TCGTCCGATCCGGAGCCGGGACTGTCGGGCGTACACAAATCGCCCGCAGAAGCGCGGCCGTCTGGACCGATGGCTGTGTAGAAGTACTCGC
CGATAGTGGAAACCGACGCCCCAGCACTCGTCCGAGGGCAAAGGAATAGCACGTGCTACGAGATTTCGATTCCACCGCCGCCTTCTATGAA
AGGTTGGGCTTCGGAATCGTTTTCCGGGACGCCGGCTGGATGATCCTCCAGCGCGGGGATCTCATGCTGGAGTTCTTCGCCCACCCCAACT
TGTTTATTGCAGCTTATAATGGTTACAAATAAAGCAATAGCATCACAAATTTCACAAATAAAGCATTTTTTTCACTGCATTCTAGTTGTGG
TTTGTCCAAACTCATCAATGTATCTTATCATGTCTGTATACCGTCGACCTCTAGCTAGAGCTTGGCGTAATCATGGTCATAGCTGTTTCCT
GTGTGAAATTGTTATCCGCTCACAATTCCACACAACATACGAGCCGGAAGCATAAAGTGTAAAGCCTGGGGTGCCTAATGAGTGAGCTAAC
TCACATTAATTGCGTTGCGCTCACTGCCCGCTTTCCAGTCGGGAAACCTGTCGTGCCAGCTGCATTAATGAATCGGCCAACGCGCGGGGAG
AGGCGGTTTGCGTATTGGGCGCTCTTCCGCTTCCTCGCTCACTGACTCGCTGCGCTCGGTCGTTCGGCTGCGGCGAGCGGTATCAGCTCAC
TCAAAGGCGGTAATACGGTTATCCACAGAATCAGGGGATAACGCAGGAAAGAACATGTGAGCAAAAGGCCAGCAAAAGGCCAGGAACCGTA
AAAAGGCCGCGTTGCTGGCGTTTTTCCATAGGCTCCGCCCCCCTGACGAGCATCACAAAAATCGACGCTCAAGTCAGAGGTGGCGAAACCC
GACAGGACTATAAAGATACCAGGCGTTTCCCCCTGGAAGCTCCCTCGTGCGCTCTCCTGTTCCGACCCTGCCGCTTACCGGATACCTGTCC
GCCTTTCTCCCTTCGGGAAGCGTGGCGCTTTCTCATAGCTCACGCTGTAGGTATCTCAGTTCGGTGTAGGTCGTTCGCTCCAAGCTGGGCT
GTGTGCACGAACCCCCCGTTCAGCCCGACCGCTGCGCCTTATCCGGTAACTATCGTCTTGAGTCCAACCCGGTAAGACACGACTTATCGCC
ACTGGCAGCAGCCACTGGTAACAGGATTAGCAGAGCGAGGTATGTAGGCGGTGCTACAGAGTTCTTGAAGTGGTGGCCTAACTACGGCTAC
ACTAGAAGAACAGTATTTGGTATCTGCGCTCTGCTGAAGCCAGTTACCTTCGGAAAAAGAGTTGGTAGCTCTTGATCCGGCAAACAAACCA
CCGCTGGTAGCGGTTTTTTTGTTTGCAAGCAGCAGATTACGCGCAGAAAAAAAGGATCTCAAGAAGATCCTTTGATCTTTTCTACGGGGTC
TGACGCTCAGTGGAACGAAAACTCACGTTAAGGGATTTTGGTCATGAGATTATCAAAAAGGATCTTCACCTAGATCCTTTTAAATTAAAAA
TGAAGTTTTAAATCAATCTAAAGTATATATGAGTAAACTTGGTCTGACAGTTACCAATGCTTAATCAGTGAGGCACCTATCTCAGCGATCT
GTCTATTTCGTTCATCCATAGTTGCCTGACTCCCCGTCGTGTAGATAACTACGATACGGGAGGGCTTACCATCTGGCCCCAGTGCTGCAAT
GATACCGCGAGACCCACGCTCACCGGCTCCAGATTTATCAGCAATAAACCAGCCAGCCGGAAGGGCCGAGCGCAGAAGTGGTCCTGCAACT
TTATCCGCCTCCATCCAGTCTATTAATTGTTGCCGGGAAGCTAGAGTAAGTAGTTCGCCAGTTAATAGTTTGCGCAACGTTGTTGCCATTG
CTACAGGCATCGTGGTGTCACGCTCGTCGTTTGGTATGGCTTCATTCAGCTCCGGTTCCCAACGATCAAGGCGAGTTACATGATCCCCCAT
GTTGTGCAAAAAAGCGGTTAGCTCCTTCGGTCCTCCGATCGTTGTCAGAAGTAAGTTGGCCGCAGTGTTATCACTCATGGTTATGGCAGCA
CTGCATAATTCTCTTACTGTCATGCCATCCGTAAGATGCTTTTCTGTGACTGGTGAGTACTCAACCAAGTCATTCTGAGAATAGTGTATGC
GGCGACCGAGTTGCTCTTGCCCGGCGTCAATACGGGATAATACCGCGCCACATAGCAGAACTTTAAAAGTGCTCATCATTGGAAAACGTTC
TTCGGGGCGAAAACTCTCAAGGATCTTACCGCTGTTGAGATCCAGTTCGATGTAACCCACTCGTGCACCCAACTGATCTTCAGCATCTTTT
ACTTTCACCAGCGTTTCTGGGTGAGCAAAAACAGGAAGGCAAAATGCCGCAAAAAAGGGAATAAGGGCGACACGGAAATGTTGAATACTCA
TACTCTTCCTTTTTCAATATTATTGAAGCATTTATCAGGGTTATTGTCTCATGAGCGGATACATATTTGAATGTATTTAGAAAAATAAACA
AATAGGGGTTCCGCGCACATTTCCCCGAAAAGTGCCACCTGACGTC

Table 8.3 Plasmid sequence for GFP-PGRMC2

Gene of interest	GeneBank/Ref-Seq ID
GADPH	NM_001115114.1
TAB1	NM_006116
PGRMC2	KT970659.1

Table 8.4 qRT-PCR primer sequences for genes of interest

Do these types of cellular transitions occur in in vivo scenarios?

Here we have documented a new paradigm, focusing on cellular transitions (EMT-MET) to maintain fetal membrane homeostasis throughout gestation and conversely, contributing to dysfunction at term. Although collagenolysis is well reported, this study emphasizes the role played at the cellular level by AECs and AMCs. Amnion cells can undergo cyclic transitions throughout gestation under the influence of changes in local tissue environment promoting membrane homeostasis. During gestation, P4 through its membrane receptor (PGRMC2), regulates the number of AMCs by converting them back to AECs (MET) to fill epithelial gaps or ECM areas void of collagen. This documents a novel role for P4 during pregnancy. At term, increases in the intra-uterine OS induces TGF-β-p38 MAPK meditated senescence and EMT allowing for an increase in AMCs in membranes. This dominate mesenchymal phenotype is very responsive to ROS and contributes to the inflammatory load, propagation of inflammation, and parturition (**chapter 6**).

Though we were able to tease out the mechanisms of cellular transitions (TGF-β-EMT: P4-MET) in standard cell culture conditions, it is unknown if amnion cells interact and maintain their transition properties when cultured in a single dynamic unit as seen in utero. To address this question multiple organ-on-chip (OOC) models were utilized. OOCs are next generation microfluidic co-culture devices containing individual chambers for cells and treatments while still allowing cell-cell and cell-collagen interactions [241-245]. Currently, tissue-specific OOC devices are not commercially available, promoting intra and inter-disciplinary collaborations between labs in order to address specific questions. First, the fetal membrane organ-on-chip (FM-OO-C [fetal-maternal interface]) (**chapter 7**)[246] was used to study signal propagation between fetal and maternal compartments and to document the advantages of OOCs over current transwell models. Next, we recreated the amnion component of the fetal membrane (amnion membrane organ-on-chip [AM-OOC]) (**chapter 8**) to study how co-culture and micro-environmental changes affect cellular transitions and migration. These experiments will help us understand how cellular interactions (e.g., AEC-decidua or AEC-AMC) and micro-environmental changes impact amnion cell properties.

Chapter 7. Fetal membrane organ-on-chip: An innovative approach to study cellular interactions [246]

INTRODUCTION

Human parturition at term is associated with multiple fetal and maternal-derived signals, which coordinate to deliver the fetus. Signals from senescent fetal membranes at term, specifically sterile inflammatory signals, are one of the contributors and initiators of human parturition [2, 4, 13, 28, 41, 145]. Inflammatory signals from fetal tissues are propagated to the maternal tissues, causing immune cell activation and increased decidual inflammation transitioning them to pro-labor status [2]. Our limited understanding of fetal-maternal communications in normal (and diseased) pregnancies is primarily founded upon studies using either intact membrane tissues obtained after deliveries or dispersed cells cultured in isolation. Each of these approaches has significant limitations [247]. Whole tissue explants have limited viability ex vivo and great subject-to-subject variability, while traditional cell culture systems are plagued by dilution effects reflecting the large volumes of culture medium overlying the cells [247]. To address the issue of studying complex multicellular structures (i.e. whole organ cutting-edge 3D cultures [spheroids, organoids]) in vitro systems have been developed to replicate cell-cell and cell-matrix interactions along with paracrine communications [248]. Transwell systems are traditionally used to study cell-cell interactions; however, the usefulness of these static systems is limited; cell migrations are limited and often do not provide reproducible results [249]. Next generation cell coculture models, termed OOC systems, have revolutionized research and medical fields with the development of the brain [250], blood-brain-barrier [251], lungs [252, 253],

heart [254], and liver-on-chip [245] devices that are currently used to test drug pharmacokinetics and pharmacodynamics, biological processes, and disease phenotypes. Additionally, compared to transwell cultures, the two-chamber OOC model uses fewer cells and allows for better interaction between cellular layers while providing a sensitive measurement of membrane permeability, cytokine propagation, and signaling pathways.

The recent development of endometrium-on-chip and placenta-on-chip systems has provided insights into dynamic obstetrics complications [255, 256]. These advanced 3D cell culture systems allow cells to interact with other cells, matrix (e.g., collagen), and blood interfaces while maintaining their viability and function. The microfluidic configuration is ideal for testing the effects of drugs, infectious reagents, and endocrine signals on individual cell compartments and their ability to interact and or affect neighboring cells [247]. Though these models have been developed, additional in utero components such as the umbilical cord, fetal membranes, cervix, and vagina are still lacking complete OOC models.

Fetal membranes, in particular, present an attractive tissue for OOC modeling, becasue there is a fairly well-defined cellular structure and paracrine signaling appears to be central to its dynamic function throughout normal and diseased gestation [39, 256, 257]. It is also a fascinating part of the fetal-maternal interface, containing cells of both fetal and maternal origin. A simple single-chamber model of the decidua, the outermost, maternally-derived cell layer of the fetal membranes, was recently developed by our group to study paracrine signaling between macrophages and decidual cells in the setting of an inflammatory insult (e.g., infection) [258]. However, that model did not incorporate fetal-derived cells. Thus, in the present study, we sought, for the first time, to bring together fetal AECs and maternal decidual stromal cells to assess paracrine signaling in a microscaled environment. Specifically, we investigated the propagation of fetal signals and their ability to induce changes in maternal cells by creating a two-chamber FM-OO-C.

The primary objective of this descriptive study was to develop FM-OO-C device and document its potential usefulness by comparing the interactive properties between primary AEC (fetal) and decidual stromal cells (maternal) cocultured in a two-chamber FM-OO-C device versus traditional transwell plates. Given their relevance to membrane biology [12, 28, 41, 83], we employed models of OS and cellular senescence to assess cell-cell interactions in this environment. Using this model system, we determined the effect of two environmental toxicants (cigarette smoke and dioxin [259]) on AEC and decidual cells separately and tested the impact of exposure effect of one cell type over the other. CSE was chosen as we have shown its ability to induce OS, senescence, and sterile inflammation in AECs and decidual cells [82]. In addition, OS and associated changes induced by CSE mimic such changes observed in fetal-maternal interface cells from term parturition. The present studies illustrate that the FM-OO-C potentially provides a better window through which interactions between cell types that can be observed in fetal-maternal signaling compared to currently employed transwell systems. The FM-OO-C device controls fluid flow rate and cell viability while allowing real-time observation of the cultured cells and the capacity to analyze complex biochemical and physiological responses.

MATERIALS AND METHODS

This study protocol was approved by the institutional review board at UTMB at Galveston, Texas, as an exempt protocol for using discarded placenta after standard term cesarean deliveries (UTMB Project 69693). At Vanderbilt University, human gestational membranes were excised from placental tissues from women who delivered healthy, full-term infants by cesarean delivery without labor. De-identified tissue samples were provided by the Cooperative Human Tissue Network, which is funded by the National Cancer Institute. All tissues were collected in accordance with Vanderbilt University Institutional Review Board (exempt protocol approval #131607) and Declaration of Helsinki. No subject recruitment or consent was required for this study.

Microfluidic FM-OO-C Design

POLYDIMETHYLSILOXANE (PDMS) LAYER DESIGN AND FABRICATION

The device was assembled using two 4.75mm by 6.2mm microfluidic chambers separated by a semipermeable polycarbonate membrane filters (3.0mM, 13mm; Sterlite, CH, M-170098, Kent, Washington, USA). The complete device was fabricated by soft lithography in PDMS (Sylgard 184, Dow Corning, Midland, Michigan, USA) as previously described in Gnecco et al.[247, 255, 256]

ASSEMBLY OF THE TWO-CHAMBERS PLATFORM

The top PDMS layer and the membrane were oxygen-plasma treated (600 mTorr, 100W, 45s) and bonded together. The membrane was then placed over the PDMS with forceps. The second layer was then bonded with the same method on the membrane orthogonally to the top PDMS layer. Oxygen-plasma treatment renders the exposed surfaces hydrophilic. Hence, the assembled devices were immediately filled with sterile DI H2O and stored at 4ºC until used. For static experiments, 500mL cloning cylinders (Fisher Scientific, Pittsburgh, Pennsylvania) were bonded with liquid PDMS to the inlet/outlet regions of each channel to form small reservoirs for the cell medium (Fig. 7.1). Our primary objective of this descriptive study is to show the usefulness of FM-OO-C model compared to the transwell system (3μM) and to project its future advantages.

AEC culture.

Human primary AECs were isolated from the amnion membrane obtained from fetal membranes from TNIL cesareans. Approximately 10g of amnion membrane peeled from the chorion layer were dispersed by successive treatments with 0.125% collagenase and 1.2% trypsin. All cell culture reagents were purchased from Sigma-Aldrich (St Louis, Missouri). Details of AEC isolation protocols can be found in our previous reports (Chapter 4 and 5). Briefly, the dispersed cells were plated in a 1:1 mixture of Ham's F12/ DMEM,

supplemented with 10% heat-inactivated FBS, 10 ng/mL epidermal growth factor, 2 mM L-glutamine, 100 U/mL penicillin G and 100 mg/mL streptomycin at a density of 3 to 5 million cells per T75 and incubated at 37ºC with 5% CO2 until 80% to 90% confluence was achieved. The metastate (coexpression of epithelial and mesenchymal markers)[128] nature of the primary AECs in cultures was verified by immunocytochemistry as reported in our prior reports (Chapter 4), and all cultures showed coexpression of CK-18 and vimentin positive cells.

Decidual cell culture.

Primary decidual cells were isolated and scraped off the chorion from TNIL fetal membranes, that is, decidualized endometrial cells of the feto-maternal interface. Separation of the decidua involved blunt dissection with forceps and a scalpel. The decidual and chorion layers were minced by cross-cutting with scalpel blades. Tissues were processed in a digestion buffer containing 0.125% trypsin (Cat# 85450c, Sigma-Aldrich), 0.2% collagenase (Cat# C0130, Sigma-Aldrich), and 0.02% DNase I (Cat# DN25, Sigma-Aldrich) and incubated at 37ºC for 60 to 90 minutes. Samples were subsequently neutralized with complete medium (1:1 mixture of Ham's F12/DMEM, supplemented with 5% heat-inactivated FBS, 10ng/mL EGF, 100U/mL penicillin G, and 100mg/mL streptomycin; Cat# 30-001-CI, Corning, New York, USA). After filtration, the cell solution was centrifuged at 3000 rpm for 10 minutes. A cell separation gradient was prepared using an Optiprep column (Axis-Shield, Dundee, United Kingdom), with steps ranging from 4% to 40% of 4 mL each (4%, 6%, 8%, 9%, 10%, 20%, 30%, and 40%).

Digested decidual cells were added to the top of the gradient and centrifuged (3000g) at room temperature for 35 minutes. Cell densities of 1.027 to 1.038 g/mL represented cells found within the decidual layer. Harvested cells were washed with DMEM, centrifuged, and resuspended in DMEM, and cell viability was tested using the trypan blue exclusion method. The resuspended cells were subsequently seeded at a density

of 3 to 5 million cells per T75 and incubated at 37ºC with 5% CO2 until 80% to 90% confluence was achieved.

Cell culture seeding

Before using the FM-OO-C or transwells (3.0 µm pore size), devices were washed three times with 1x PBS, coated with Matrigel (Corning Matrigel Basement Membrane Matrix, *LDEV-free; 1:50 in PBS), and incubated at 37ºC with 5% CO2 for 30 minutes. Next, devices were washed three times with complete DMEM/F12 medium before cell seeding. Primary cells were then trypsinized and 25,000 AECs were added in the top chamber and 15,000 Decidua in the bottom chamber of the FM-OO-C; while 50,000 AEC (passage 1) and 30,000 Decidua (passage 6 and 8) were plated into the transwell (3µM pores) (Fig. 7.1, 7.2A-C, and 7.3A-C). Devices were incubated at 37ºC with 5% CO2 for 24 hours before treatment.

Cell culture treatments

To test the effect of OS and environmental toxins on signal propagation and senescence at the fetal-maternal interface, we treated each FM-OO-C with one of the following: (1) DMEM/F12 medium (control), (2) OS inducer CSE 1:50, or (3) the environmental toxin 2,3,7,8-tetrachlorodibeno-p-dioxin (10 nM). Once cells reached 70% to 80% confluence, each OOC was rinsed with sterile 1x PBS, treated, and incubated at 37ºC, 5% CO2, and 95% air humidity for 48 hours. After 48 hours, bright field microscopy (Nikon Eclipse TS100 microscope (10x; Nikon, Melville, New York) was performed to determine cell morphology and staining for each treatment.

Fluorescein Isothiocyanate (FITC) Membrane Perfusion Assay

To determine membrane permeability and medium propagation between both chambers of the FM-OO-C and transwell devices, we designed a set of perfusion assay

experiments (Fig. 7.2D and 7.3D). FITC was added to the top insert and chamber of the devices while PBS was added to the bottom. Collected effluent from the bottom compartment was collected for up to 2 hours to determine membrane integrity. A fluorescence microplate reader (GloMax Multimode Readers, Promega, Madison, Wisconsin, USA) at 470nm excitation and 520 to 550nm emission range was used to measure the intensity of FITC dye that perfused through the membrane layer and into the bottom chamber.

SA-β-Gal Assay

Expression of the SA-β-Gal biomarker is independent of DNA synthesis and distinguishes senescent cells from normal cells [28, 128]. Senescent cells were identified using a histochemical staining kit (ab65351), with blue cells visualized by light microscopy at 48 hours after treatment (Fig. 7.2E and 7.3E). An average of four regions were collected per condition using bright-field microscopy (Nikon Eclipse TS100 (10x; Melville, New York) and the number of cells with positive staining (blue colored cells) were analyzed. Image modifications (brightness, contrast, and smoothing) were applied to all image sets using Lightroom and Image J (National Institutes of Health, rsbweb.nih.gov/ij) and a grading scale was used to measure the staining intensity of five image fields per experiment (Fig. 7.4B).

Analysis and statistics

For this descriptive manuscript, a total of four cell preparations (two AECs and two decidual cell preparations) were used to validate this method. Thus, fold change and trends were reported instead of statistical significance.

RESULTS

Development of FM-OO-C

The FM-OO-C microfluidic coculture platform was composed of two orthogonal stacked chambers, containing equal surface area (29.45 mm^2) that contained primary AECs (fetal) on top and decidual cells (maternal) on the bottom (Fig. 7.1 and 7.2A-C). The two chambers are divided by a semipermeable membrane similar to the ECM component of fetal membranes (Fig. 7.2E, yellow circle). Additionally, this membrane allowed effluent signal propagation and cell migration between compartments permitting for in vitro analysis of complex biological processes (Fig. 7.2D-H). The same cell preparations in traditional transwell cultures were used for comparison purposes (Fig. 7.3).

Cellular Interactions Are Better Determined Using FM-OO-C Than Transwell Cultures

To compare the FM-OO-C to a more conventional transwell, we treated AEC and decidual cells separately with two environmental toxicants (cigarette smoke and dioxin) and examined the changes on AECs and its impact on decidual cells and vice versa. As shown in Figure 7.4, dioxin exposure differentially induced membrane permeability at the fetal-maternal interface, compared to the OS-inducer CSE in the FM-OO-C. The two-chamber FM-OO-C model promoted cellular interactions and allowed sensitive measurement of membrane permeability irrespective of treatment side (AEC vs. decidual cells; Fig. 7.4A). CSE treatment of AEC produced higher membrane permeabilization (1.6-fold) than treatment on the decidual side (1.2-fold); whereas dioxin treatment on the decidual cell side produced higher permeabilization (1.1-fold) than treatment of the same on AEC side (0.7-fold; Fig. 7.4A). In contrast, a minimal effect was notes in corresponding transwell treatments.

FM-OO-C Promotes Biochemical Exchange Between Fetal and Maternal Chambers Leading to Senescence

To identify the ability of OS (CSE treatment) and environmental toxins (dioxin treatment) to induce and propagate signals of cellular senescence between the two

chambers of the FM-OO-C, we designed a scoring system for SA-β-Gal staining (blue) in AECs and decidual cells (Fig. 7.4B). Compared to control cultures, CSE and dioxin treatments induced cellular senescence in AECs and decidual cells after 48 hours. Additionally, both CSE-and dioxin-treated sides in the FM-OO-C induced senescence and forced similar changes on the opposite chamber (i.e., decidua treatment of CSE-induced AEC senescence 1.4-fold higher than controls, while AEC treatment with dioxin-induced decidual senescence 1.4-fold higher than controls), suggesting transfer of biochemical signals between layers that are capable of producing labor-associated changes (Fig. 7.4C). Transwell cultures compared to the corresponding FM-OO-C treatments did not allow propagation of such signals as indicated by the minimal effect on SA-β-Gal levels (Fig. 7.4C).

DISCUSSION

Here, we further developed an OOC model of the human fetal membrane with a device containing human AECs and decidual cells. This system should provide a model for the fetal-maternal interface component of the fetal membranes that can be used to test cell migrations and transitions, intercellular interactions, and signaling. AEC and decidual cells were cocultured in a two-chamber OOC separated by a semipermeable membrane representing the fetal membrane ECM. This device allowed us to test the ability of fetal-derived signals to induce ECM permeability and cellular changes like senescence. Here, we document that the FM-OO-C model (1) maintains physical and fluidic isolation between fetal and maternal compartments (cells), (2) stimulates primary cells to cause biochemical changes, (3) provides better interactions between cell types, and (4) allows for better transfer of biochemicals between compartments compared to transwell cultures to impact changes by the recipient cells. Though more rigorous testing should be conducted before making a definitive statement that the FM-OO-C model is better than transwells,

these results suggest OOC devices are ideal for addressing specific questions related to feto-maternal signaling during pregnancy.

The controlled environment of the FM-OO-C allows improved signal propagation between cells/chambers by minimizing variability while highlighting subtle changes like a cell's ability to induce membrane permeability and transfer biochemicals between treatments compared to transwell systems [247, 255, 256]. On the contrary, transwell systems by nature enhance their nascent signal/noise ratio with different surface areas, cell quantities, and medium volumes between the two chambers. Specifically, negative results in transwell experiments, in part, could be due to the large difference in effluent volume between the top and bottom chambers of the transwell (Top: 600μL; Bottom: 1500μL) which is addressed in most organ-on-chip models (FM-OO-C; top: 800μL; bottom: 800μL). This difference could be one of the reasons fetal and maternal biochemical signals failed to propagate and induce senescence in the transwell system compared to the FM-OO-C. Additionally, stimulant-dependent changes were not detected in transwell membrane perfusion studies. Dilution of the transwell FITC signal (10-fold lower), which crossed to the lower chamber during the membrane perfusion assay, could address these findings. Due to FM-OO-C's ability to amplify small changes in effluent signals, future experiments will be conducted to utilize the dynamic flow of medium in this system to replicate shear stress at the cellular level and to detect the kinetics of various signal generation.

Although FM-OO-C has many advantages to single cell cultures, the model presented here has limitations. Besides the dynamic flow system mentioned above, some other areas to be addressed in future designs include (1) composition of the semipermeable membrane to better mimic ECM in utero, (2) organization of the device to allow for better imaging of chambers and migratory cells, (3) the addition of other collagen types and cell layers to complete the fetal-maternal interface. This model did not include AMCs, chorionic trophoblasts, or immune cells that also play a major role in signaling between

AEC and decidual cells [256, 257], and (4) adaptations in cell loading to produce an even and consistent cell confluence.

In summary, we utilized an OOC model to recreate the fetal-maternal compartment of the fetal membranes (FM-OO-C), which can be used to better understand cellular interactions and paracrine cross-talk between maternal and fetal cells during pregnancy and parturition. OOCs representing a variety of physiological states and organ systems have become a critical step in the drug discovery pipeline and are apart of the future of bench to bedside research. Continual progress of the FM-OO-C model is expected to recreate the entire fetal membrane-on-chip, thus allowing for a full model of pregnancy-on-chip for studying cellular interactions during pregnancy and parturition, screening of drugs, and to advance research activities to reduce the risk of pregnancy-associated complications.

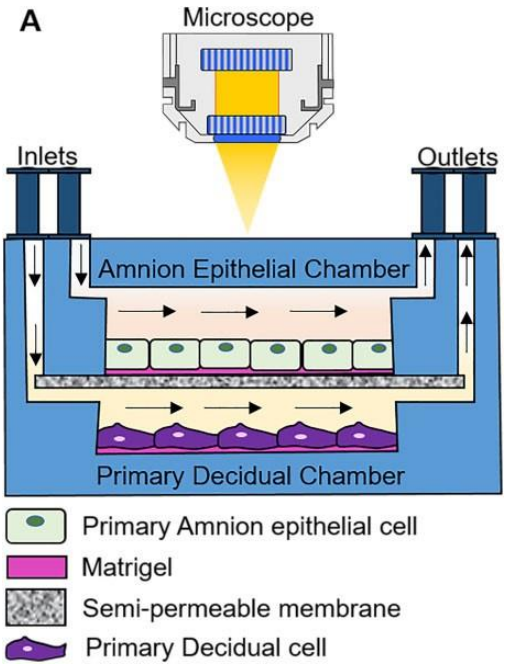

Fig. 7.1 Fetal membrane organ-on-chip schematic.

Schematic of the two-chambered FM-OO-C coated in matrigel. AEC are placed on top of a polycarbonate semipermeable membrane, while decidual cells are placed in a lower chamber.

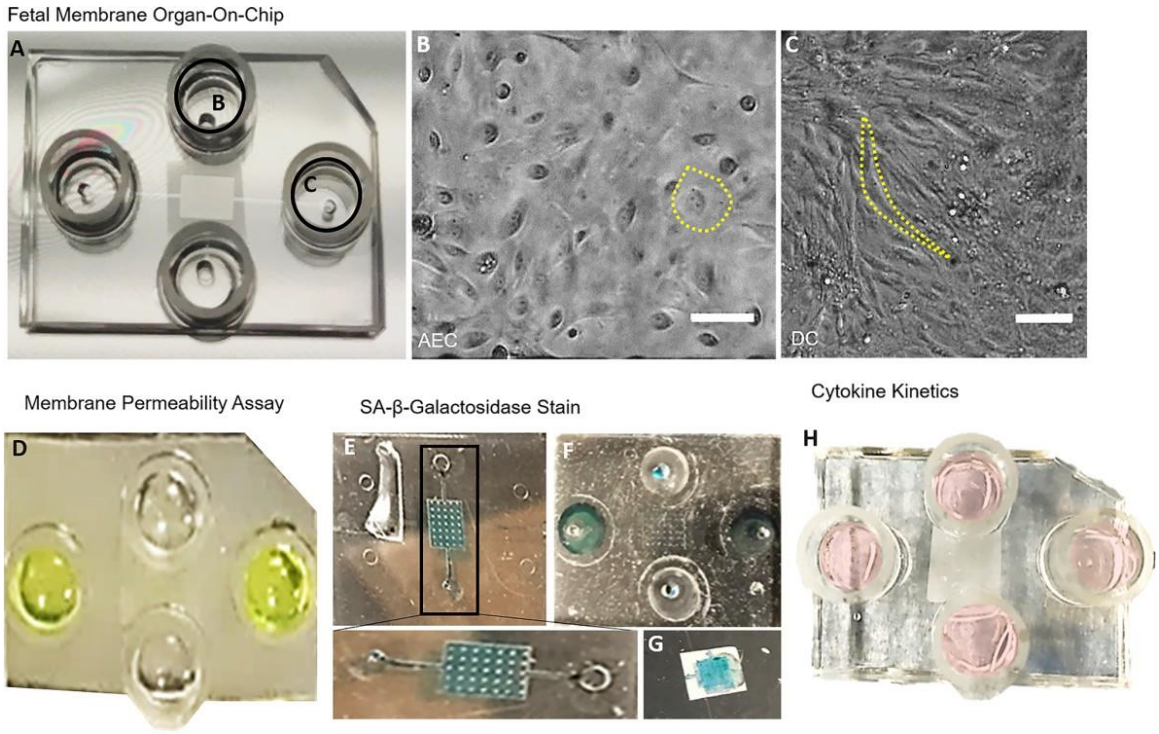

Fig. 7.2 FM-OO-C experimental layout and outcomes

A) Images of the FM-OO-C layout and experimental design. FM-OO-C is a two-chamber device divided by a polycarbonate semipermeable membrane. B) Bright field microscopy image of primary human AECs in the top chamber and (C) primary decidual cells (D-C) in the bottom chamber. Yellow outline documents morphology. Images were captured at 10x and contain 20µm scale bars. D, FITC stain (yellow) is seen in the two horizontal columns feeding into the top chamber AECs. Medium were collected from the bottom vertical columns to measure membrane permeability. E) Bottom chamber showing representative SA-β-Gal stained decidual cells and (F) top chamber of the FM-OO-C along with the (G) the semipermeable membrane containing blue staining representing SA-β-Gal AECs. H) Image of FM-OO-C containing medium from both amnion and decidual cells which can be used to measure cytokine kinetics.

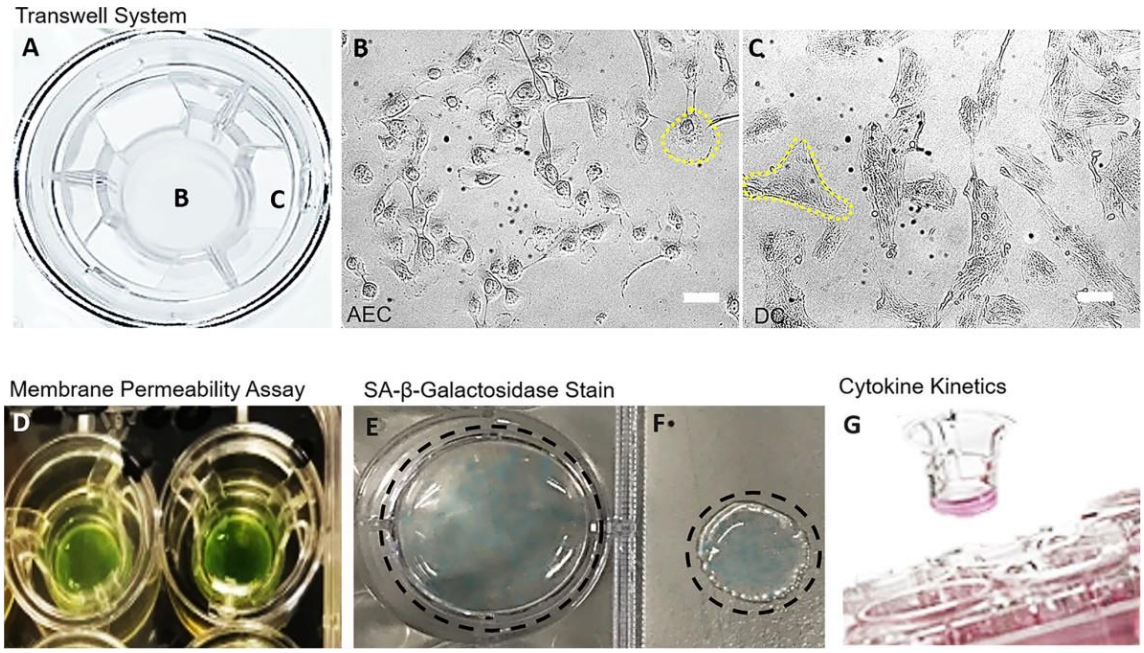

Fig. 7.3 Transwell experimental layout and outcomes.

A) Images of the transwell layout and experimental design. Transwell is a two-chamber device divided by a polycarbonate semipermeable membrane. B) Bright field microscopy image of primary human AECs in the top chamber and (C) primary decidual cells (DC) on the bottom chamber of the transwell devices. Yellow outline documents morphology. Images were captured at 10x and contain 20µm scale bars. D) FITC stain is seen in the two columns (top chamber) feeding into the top chamber AECs. Medium were collected from the bottom columns (bottom chamber) to measure membrane permeability. E) The lower chamber of the transwell showing representative SA-β-Gal stained decidua (blue). F) The semipermeable membrane containing blue staining representing SA-β-Gal AECs are circled in black. G) Image of transwell devices containing medium from both amnion and decidual cells which can be used to measure cytokine kinetics.

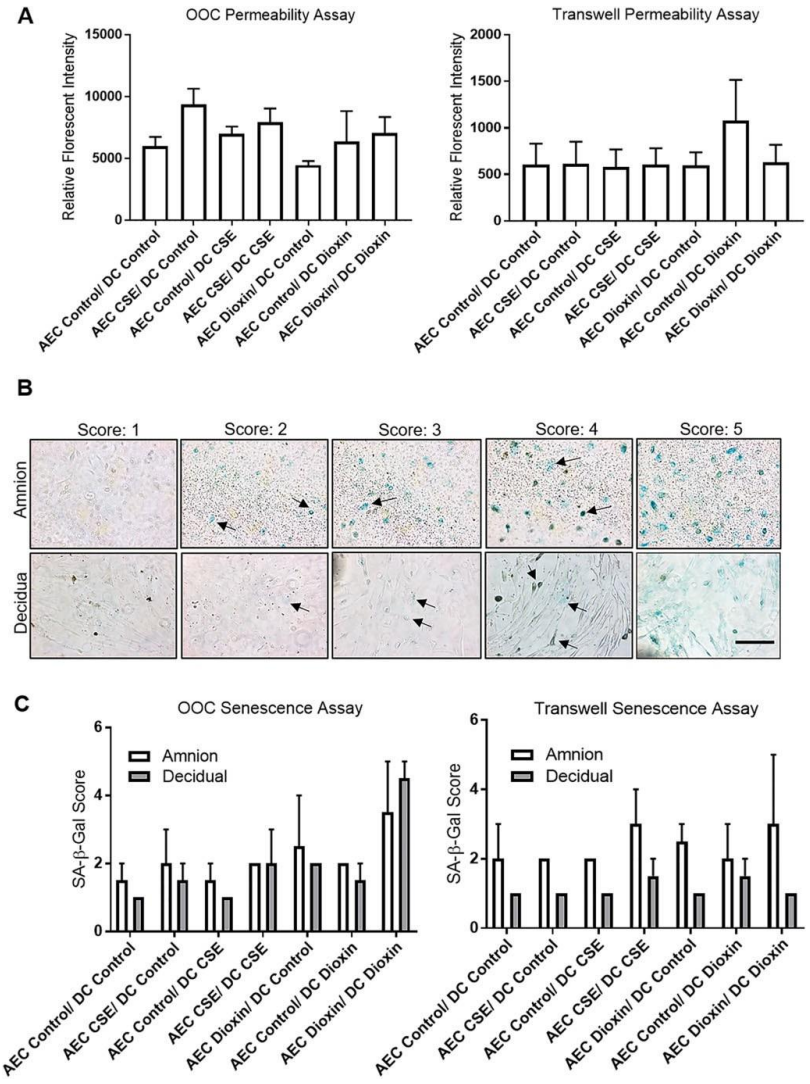

Fig. 7.4 CSE and dioxin differentially induce membrane permeability and senescence in fetal and maternal cells.

A) FM-OO-C and transwell devices were seeded with AEC and decidual cells (AEC/decidual cells), treated with either CSE or dioxin medium for 48 hours. Cells were also maintained in cell culture medium as controls. FITC measured membrane permeability for up to two hours. Compared to transwell cultures, the two-chamber FM-OO-C allowed for more sensitive measurement of membrane permeability regardless of treatment side. Membrane permeabilization was higher with AECs treated with CSE compared to similar treatment on the decidual side. Decidual cells treated with dioxin-induced higher membrane permeabilization compared to dioxin treatment on AEC side in OOC and transwell systems (2-fold). B) Scoring system to determine the amount of SA-β-Gal (blue; arrows) in AECs and decidual cell cultures. All images were taken at 20 and scale bar is set to 20 microns. C) Relative quantitation of SA-β-Gal stain from the FM-OO-C and transwell devices. Treatments are documented as (AEC/DC).

Chapter 8. Amnion membrane organ-on-chip: An innovative approach to study cellular interactions

INTRODUCTION

Membrane homeostasis is vital for the maintenance of pregnancy and fetal growth. Compromise in the fetal membrane's structural [96], biological [28], and mechanical [23] functions or chorioamniotic inflammation [260] are often associated with SPTB and pPROM, two major complications of pregnancy that affect more than 9.6% of all cases in the US alone and 11% worldwide [4, 140, 261]. However, mechanisms that maintain the fetal membrane's homeostasis during gestation and factors contributing to the loss of its functional ability, which could predispose membranes to labor-associated inflammatory changes at term (physiological) or preterm (pathological), are still unclear. A clear understanding of these mechanisms may help fill a major knowledge gap regarding the role of fetal membranes in term and preterm labor, as well as lead to designing better strategies to reduce membrane-associated adverse outcomes.

Fetal membranes are multilayer structures comprising AECs and chorion trophoblasts connected by a collagen-rich ECM that also contains AMCs [20, 39, 40]. The amnion membrane is the most elastic component of the fetal membranes and is composed of an AEC type IV collagen-rich basement membrane with AMCs embedded in ECM [17]. Additionally, the amnion membrane bears a majority of the tensile strength to mechanically keep the tissue intact throughout gestation [23, 51, 107]. AECs and AMCs also provide essential immune and endocrine functions that are critical to the maintenance of pregnancy [19, 262, 263]. Membrane growth and remodeling are essential during gestation and involve both cellular transitions and collagenolytic matrix turnover [39, 128]. Cellular-level changes primarily involve AECs and AMCs that are conventionally considered as purely epithelial and mesenchymal in physiognomies. However, recent findings suggest

that AECs and AMCs are pluripotent stem cells in a “metastate” where they coexpress both epithelial and mesenchymal markers [49, 128]. This metastate is thought to allow amnion membrane cells to readily undergo cellular transitions demanded by intra-uterine micro-environmental cues to either promote membrane remodeling and maintain integrity during gestation or predispose them to weaken in preparation for labor and delivery [39, 128].

The recent discovery of fetal membrane microfractures highlights possible areas of such cellular transitions and remodeling [39, 49, 96]. Microfractures are biologic interruptions in the amnion membrane characterized by AEC puckering or gaps, basement membrane degradation, and tunnels that extend into the collagen matrix with migrating cells [96]. Increased number and morphometry (width and depth) of microfractures at term and in PTB/pPROM suggest that persistence of microfractures may indicate lack of remodeling and membrane dysfunction [96, 140]. Induction of OS in vitro in fetal membrane explants, similar to that seen at term and preterm parturitions, increases microfractures, their morphometry, and their collagenolysis, supporting the hypothesis that the persistence of microfractures may predispose membranes to dysfunctions and instability. This hypothesis was further supported by in vitro scratch assays (mimicking microfractures) (Chapter 3) [128]. Data suggest that AECs can proliferate, migrate, transition, and heal wounds (Chapter 4) [128, 223], supporting the hypothesis that microfractures are likely areas where membrane remodeling occurs. Cell transitions at the scratch site include EMT or the reverse MET [128]. Further, OS prevented cellular transitions and healing [128] and recapitulated similar observations associated with term and preterm parturitions [96].

Despite the recent finding that amnion cells can undergo cellular transitions, it is still unclear if microfractures are formed or healed by fetal cells in vivo. Determining a causal relationship between cellular transitions and environmental stimulants will illuminate the role of fetal cells in membrane remodeling. However, studying such phenomena is extremely challenging due to the lack of available experimental approaches

and models of the multicellular amnion membrane that can be experimentally manipulated and tested. Current experimental approaches of 2D single cell cultures, amnion cell-like organ explant cultures, and transwell coculture systems (of AMCs and AECs) are all insufficient to understand cellular transitions and their roles in tissue remodeling. Conventional mixed culture or coculture methods, where cells are cultured in randomly distributed form or in transwells, often fail to provide means to locally manipulate the physical and biochemical environments of each cell type in culture. Therefore, it is challenging to investigate the interactions between the fetal membrane cells, namely AMCs and AECs, for detailed mechanistic studies. In addition, migratory cells that are thought to play an important role in collagen homeostasis cannot be easily monitored or studied using these methods. Microfractures and scratch assay experiments conducted and terminated at discrete time points may show a snapshot of cellular transition but do not convey the cellular mechanisms involved during membrane remodeling; they also create challenges for understanding the dynamic cell-cell relationships.

To overcome the limitations of these traditional approaches, we developed an AM-OOC, allowing for direct monitoring of amnion cell migration and transition under a coculture condition where the two different cell types could be cultured in two different microenvironments while enabling the application of localized chemical cues to only one cell type. Microfluidic OOC technologies allow for control and manipulation of multiple cell types and their microenvironments with high accuracy and have been demonstrated as a promising technology to achieve in vitro models that more physiologically mimic in vivo structures and functions [242, 243]. Recently, a fetal membrane OOC model was presented [256]; however, this model lacks a degradable basement membrane as well as mesenchymal cells. Thus, this device does not accurately recapitulate how cells migrate through a basement membrane and also lacks critical factors from the mesenchymal cells. A truly physiologically relevant fetal membrane OOC model has the potential to recapitulate inter- and intracellular signaling and the physiological context of tissue

dynamics by compartmentalizing the major cellular components of a fetal membrane while still allowing interactions between these chambers. As a first step in establishing a full fetal membrane OOC system, we initially developed the AM-OOC and tested its usefulness in addressing the experimental limitations described above. Using this OOC approach, we tested and compared, using AECs and AMCs harvested from human placenta, AECs' and AMCs' migration and transitions independently as well as when cultured together under normal and OS conditions. We report that AECs can migrate, degrade basement collagen, and transition to become AMCs. OS induces AECs to undergo EMT and increase collagenolysis and inflammation. Additionally, the presence of AMCs accelerates this process. Conversely, AMCs migrate, degrade basement collagen, and transition to become epithelial cells in the presence of AECs. OS maintains AMCs' mesenchymal phenotype, promotes migration, degrades basement collagen, and propagates inflammation.

MATERIALS AND METHODS

This study protocol was approved by the Institutional Review Board at UTMB at Galveston, TX, as an exempt protocol for using discarded placenta after standard term Cesarean deliveries (UTMB Project 69693). No subject recruitment or consent was required for this study. The AM-OOCs were developed and microfabricated at Texas A&M University (College Station, TX), and cell-based studies were conducted at UTMB.

Clinical samples and cell culture

AEC CULTURE

Primary AECs and AMCs were isolated from amnion membranes obtained from fetal membranes from TNIL cesarean deliveries [82, 143]. Approximately 10g of amnion membrane, peeled from the chorion layer, was dispersed by successive treatments with 0.125% collagenase and 1.2% trypsin. All cell culture reagents were purchased from Sigma-Aldrich (St. Louis, MO). Details of AEC isolation protocols can be found in our

previous report [28]. Briefly, the dispersed cells were plated in a 1:1 mixture of Ham's F12/DMEM, supplemented with 10% heat-inactivated FBS, 10ng/mL epidermal growth factor, 2mM L-glutamine, 100U/mL penicillin G, and 100mg/mL streptomycin at a density of 3–5 million cells per T75 and incubated at 37°C with 5% CO2 until 80%–90% confluence was achieved.

AMC CULTURE

AMCs were isolated from fetal membranes as previously described by Kendal-Wright et al. [42, 225] with slight modifications. Primary AMCs were isolated from the placental membranes of women experiencing normal parturient at term (e.g., not in labor) and undergoing a repeat elective Cesarean section. Reflected amnion (~10 g) was peeled from the chorion layer and rinsed three or four times in sterile Hanks' Balanced Salt Solution (HBSS; Cat# 21-021-CV, Corning) to remove blood debris. The sample was then incubated with 0.05% trypsin/EDTA (Cat# 25-053-CI, Corning) for one hour at 37°C (water bath) to disperse the cells and remove the epithelial cell layer. The membrane pieces were then washed three or four times using cold HBSS to inactivate the enzyme. The washed membrane was transferred into a second digestion buffer containing Minimum Essential Eagle Medium (Cat# 10-010-CV, Corning), 1mg/mL collagenase type IV, and 25μg/mL DNase I, and incubated in a rotator at 37°C for one hour. The digested membrane solution was neutralized using complete DMEM/F12 medium (Cat# 10-092-CV, Corning), filtered using a 70μm cell strainer, and centrifuged at 3000rpm for 10 minutes. The cell pellet was resuspended in complete DMEM/F12 medium supplemented with 5% heat-inactivated FBS (Cat#35-010-CV, Corning), 100U/mL penicillin G, and 100mg/mL streptomycin (Cat#30-001-CI, Corning). The resuspended cells were subsequently seeded at a density of 3–5 million cells per T75 and incubated at 37°C with 5% CO2 until 80%–90% confluence was achieved.

Microfluidic AM-OOC design

The AM-OCC platform was fabricated in PDMS using two-step photolithography and soft-lithography technique [256, 264]. To create the master mold (Fig. 8.1C), two layers of photosensitive epoxy (SU-8, Microchem, Inc., Newton, MA) with different thicknesses were sequentially patterned on a silicon substrate. The first layer forming the 5-μm-deep microchannels was obtained by spin coating SU-8TM 3005 at 4000rpm and soft baking at 95°C for four minutes. It was then exposed to ultraviolet light through a photomask, followed by a post-exposure bake at 95°C for another four minutes. The second layer forming the cell culture chambers was 500μm thick and patterned by spin coating SU-8TM 3050 at 1000 rpm, soft baked first at 65°C for 24 hours and then at 95°C for 40 minutes, exposed to ultraviolet through a second photomask, and then post-exposure baked in two steps, first at 65°C for five minutes and then at 95°C for 15 minutes. The master mold was then coated with (tridecafluoro-1,1,2,2-tetrahydro octyl) trichlorosilane (United Chemical Technologies, Inc., Bristol, PA) to facilitate PDMS release from the master mold after replication.

PDMS devices were replicated from the master mold by pouring PDMS prepolymer (10:1 mixture, Sylgard® 184, Dow Corning, Inc., Midland, MI) on the mold, followed by curing at 85°C for 45–60 minutes. The reservoirs to hold culture medium are punched out using a 5mm diameter punch bit (Technical Innovations, Angleton, TX) mounted on a drill press. To improve the bonding of PDMS devices onto glass substrates and to make the device hydrophilic for easy cell and culture medium loading, the PDMS devices were treated with oxygen plasma (Harrick Plasma, Ithaca, NY) for 90 seconds, followed by bonding onto glass substrates. The PDMS culture devices were then immersed in distilled water. For sterilization, an autoclave was used to sterilize the PDMS culture devices at 121°C for 30 minutes.

Microfluidic AM-OOC device preparation for Matrigel filling of microchannels

Before using the AM-OOC, devices were washed three times with PBS, coated with Matrigel (Corning® Matrigel® Basement Membrane Matrix, LDEV-free; 1:50 in PBS), and incubated at 37°C with 5% CO2 overnight. Diluted type IV basement membrane Matrigel was used to coat the microchannels connecting the outer and inner culture chambers, which mimics the amnion basement membrane in vivo. Through this process, a thin layer of Matrigel is left in the outer and inner chamber after microchannels are filled, where this contact with basement membrane mimics amnion cell growth in utero.

Masson trichrome staining for Matrigel imaging

Before and after AM-OOC experiments, devices were stained with Masson trichrome stain to image type IV collagen inside the microchannels. To show that our Matrigel loading worked, devices were rinsed with PBS and fixed at room temperature with 4% PFA for 20 minutes. The devices were then stained with Biebrich Scarlet / Acid Fuchsin for 10 minutes and then rinsed with water three times. This process stained all the cells and collagen red. Next, phosphomolybdic / phosphotungstic acid was applied for 15 minutes, which removed the red stain from the collagen. Aniline Blue Solution was then added for 10 minutes to stain the collagen blue. Once the device was stained, it was rinsed three times with water and imaged. This procedure was additionally carried out on some devices after 48 hours of cell culture to monitor collagen degradation due to cell migration.

Fluorescent dye perfusion assay

To determine to what degree culture medium in the AM-OOC could diffuse from one culture chamber to the other, which corresponds to how much inflammatory mediators can propagate from one chamber to the other, we conducted a set of perfusion assay experiments. FITC dye was loaded into the inner or outer chambers, and microscopy images were taken over time (0–70 hours). Fluorescent intensity was used to measure the degree of diffusion from the center chamber to the outer chamber, or vice versa. ImageJ

measured the intensity of FITC dye that perfused through the microchannels (with and without type IV collagen Matrigel) and into the opposite chamber over 70 hours. Intensity values were normalized between replicates using the following formula: (intensity at time point - intensity at time zero) / intensity at time zero) *100.

Cell seeding and culture in the AM-OOC

Before using the AM-OOC, devices were washed three times with PBS and coated with Matrigel as described above. The next day, devices were washed three times with complete DMEM/F12 medium before cell seeding. Primary cells were then trypsinized and stained with live cell dyes for GFP (AEC; CellLight Histone 2B-GFP) or RFP (AMC; CellLight Histone 2B-RFP) following the protocol provided by the company (Life Technologies, Waltham, MA; Cat#10594 and #10595). Then, 120,000 AECs were loaded into the outer chamber, and 40,000 AMCs were loaded into the inner chamber of the AM-OOC. The AM-OOCs were incubated at 37°C with 5% CO2 for 24 hours before localized treatment (see next section).

Cell culture treatments in the AM-OOC

To test the effect of OS on cellular transition in the amnion membrane, we treated each AM-OOC with one of the following for 48 hours: 1) normal cell culture conditions (control DMEM/F12 medium), 2) OS conditions (induced by treating cells with CSE) [28, 82] diluted 1:25 in AEC medium or diluted 1:75 in AMC medium, 3) to verify the effect of OS, cells were cotreated with an OS inducer (CSE) and an antioxidant or stress signaler p38 MAPK inhibitor NAC (15mM; Sigma, Cat#A7250) [82, 145] and SB (SB; 13mM, Sigma #S8307) [82, 145], a p38 MAPK inhibitor and a known inducer of EMT.

To induce OS in fetal membrane cells, CSE was used as described previously [28], with modifications. Cigarette smoke from a single commercial cigarette (unfiltered CamelTM, R.J. Reynolds Tobacco Co, Winston Salem, NC) was bubbled into 25mL of

AEC or AMC medium. The stock CSE was sterilized using a 0.22μm Steriflip® filter unit (Millipore, Billerica, MA) and diluted to 1:50 (AEC) or 1:75 (AMC) in cell-specific medium before use. This modification was necessary to minimize any drastic effects of CSE in a microfluidic 3D culture system than a much bigger 2D cell culture system.

Due to AMCs' exaggerated response to OS inducers [265], a different CSE concentration was used to induce OS in AMCs compared to AECs' treatment. Once cells reached 70%–80% confluence, each AM-OOC was rinsed with sterile 1x PBS, serum-starved for 1 hour, treated with the respective conditions, and incubated at 37°C, 5% CO2, and 95% air humidity for 48 hours. After 48 hours, bright field microscopy (Nikon Eclipse TS100 microscope, Nikon, Melville, NY, USA [10x]) or confocal microscopy (Zeiss 880, Zeiss, Germany [10x]) was performed to determine cell morphology, percentage of microchannels containing cells, and number of cells that migrated through the microchannels to the other side of the chamber for each treatment.

Immunocytochemical localization of intermediate filaments cytokeratin and vimentin

CELL STAINING

AEC and AMC immunocytochemical staining for vimentin (3.7μl/mL; ab92547; Abcam, Cambridge, MA) and CK-18 (1μl/mL; ab668; Abcam) were performed after 48 hours as previously described by Richardson et al. [128] (Chapter 4). Manufacturer's instructions were used to calculate staining dilutions to ensure uniform staining. After 48 hours, cells were fixed with 4% PFA, permeabilized with 0.5% Triton X, and blocked with 3% BSA in PBS prior to incubation with primary antibodies overnight at 4°C. After washing with PBS, the AM-OOCs were incubated with Alexa Fluor 488, 594, 647 conjugated secondary antibodies (Life Technologies, Carlsbad, CA), diluted 1:2000 in 3% BSA for two hours in the dark. The AM-OOCs were washed with PBS, treated with

NucBlue® Live ReadyProbes® Reagent (Life Technologies), and imaged as described above.

IMAGE ANALYSIS

Three random regions of interest per AM-OOC were used to determine red (CK-18) and green (vimentin) fluorescence intensity. Uniform laser settings, brightness, contrast, and collection settings were used for all images collected. Images were not modified (brightness, contrast, and smoothing) for intensity analysis. ImageJ software (National Institutes of Health, rsbweb.nih.gov/ij; version 1.51J) was used to measure vimentin and CK-18 staining intensity from two focal plans of three different regions per treatment condition at each time point. Image analysis was conducted in triplicate for all cell experiments.

Multiplex Luminex assays for inflammatory cytokine markers

Supernatant were manually collected from the reservoirs of both chambers after 48 hours of treatment. Multiplex assays were performed with the cytokine IL-8 and Granulocyte-macrophage colony-stimulating factor (GM-CSF) antibody-coated beads (Cat#HCYTOMAG-60K, Merck KGaA, Darmstadt, Germany) as indicators of general inflammation in cell supernatant. Standard curves were developed with duplicate samples of known quantities of recombinant proteins that were provided by the manufacturer. Sample concentrations were determined by relating the absorbance values that were obtained to the standard curve by linear regression analysis.

Statistical analyses

All experiments were conducted and images analyzed using GraphPad Prism 7.0 software (GraphPad Software, Inc., LaJolla, CA, USA). One-way ANOVA and Independent Samples t-test were used, and $P<.05$ was considered significant.

RESULTS

AM-OOC development

The AM-OOC device is composed of two circular chambers, one for AEC culture and one for AMC culture, connected through arrays of microfluidic channels (Fig. 8.1A). The center circular chamber is for AMC culture, and the outer ellipse-shaped chamber is for AEC culture. The outer and inner chambers measure 500μm in height and are connected by 24 microfluidic channels (5μm in height, 30μm in width, 600μm in length; Fig. 8.1B). Each device contained an outer chamber with two reservoirs and an inner chamber with one reservoir (Fig. 8.1C). Due to the device's small height, suspended cells initially loaded into each culture chamber remain in each chamber, while still allowing cellular migration. In addition, in some cases, diluted type IV Matrigel was used to fill these microfluidic channels to mimic the amnion basement membrane (see next section for more details). When applying localized stimuli to only the AECs, the culture medium level of the center AMC culture chamber was maintained higher compared to the outer AEC culture chamber, preventing any biochemicals and metabolites from AECs from diffusing into the AMC chamber due to the hydrodynamic pressure difference created by the different fluidic level. When applying localized stimuli to only the AMCs, the fluid height difference was reversed. Such hydrodynamic pressure difference-based localized coculture has been previously utilized for neuron-glia cell coculture [264, 266].

After sterilization, each device was placed in a conventional 6-well plate (Fig. 8.1D) and coated with type IV collagen Matrigel. Primary cuboidal AECs were loaded into the outer chamber, and primary AMCs were loaded into the inner chamber. Cells were cultured in good health over two days, each showing representative morphologies (Fig. 8.1E). The inner AMC culture chamber was filled with blue dye, and the outer AEC culture chamber was filled with red dye (Fig. 8.1F). Matrigel coating successfully produced

collagen-filled microchannels (blue stain) to mimic amnion basement membrane (Fig. 8.1F), enabling isolation of the two different culture conditions, while still allowing molecular communication as well as cell migration.

Fluidic isolation over time between the AMC and AEC chambers in the AM-OOC

In the multicellular AM-OOC system, fluidic isolation between the two chambers is important to independently control and manipulate the two cell types and their microenvironments, while still allowing interactions between the two cell types. The efficiency to maintain fluidic separation between the two chambers was tested using a FITC-based perfusion assay in the AM-OOC by creating a minute fluidic level difference between the outer and inner chambers that resulted in hydrostatic pressure differences. FITC or PBS was loaded into either the outer or inner chamber, and fluorescent microscopy was used to monitor the rate of perfusion between the two chambers. When the inner chamber had higher fluidic level than the outer chamber, it took more than 24 hours for the FITC in the outer chamber to diffuse into the inner chamber, successfully demonstrating fluidic isolation between the two chambers (Fig. 8.2A-B). The use of type IV collagen-filled microfluidic channels extended this isolation time to 60 hours (Fig. 8.2C-D). Similarly, fluid pressure from the outer to inner chamber counteracted some of the diffusion and allowed fluidic isolation for at least 20 hours (Fig. 8.2E-F). The use of type IV collagen-filled microfluidic channels extended this fluidic isolation time to 40 hours (Fig. 8.2G-H). Additionally, the difference in fluidic levels was also able to prevent proinflammatory cytokine propagation GM-CSF from diffusing from one chamber to the other chamber (Sup. Fig. 8.1B-C), further confirming successful fluid isolation between the two chambers.

Characteristics of monoculture of AECs and AMCs in the AM-OOC

AMNION CELLS SHOW MIGRATORY AND TRANSITION CAPACITY

Monoculture of AECs (outer chamber) or AMCs (inner chamber) in the AM-OCC showed that cells can enter into the type IV collagen-filled microchannels, elongate, migrate through type IV collagen, and exit the microchannel (red outline) within 48 hours (Fig.8.3A-B). Migrated cells either revert to their original epithelial shape or maintain their achieved mesenchymal morphology, clearly showing that direct imaging of cell migration through the collagen-filled microfluidic channel is possible in the developed AM-OOC.

AMNION INTERMEDIATE FILAMENT EXPRESSION AND MIGRATORY POTENTIAL

Increased OS at term has been shown to induce labor-associated changes, such as cellular senescence, MMP9 upregulation, and increased proinflammatory cytokine production in fetal membrane cells, including AECs and AMCs [28, 82]. CSE, a potent and reliable OS inducer [11-13, 28, 41, 82, 96, 131, 143, 224], has been shown to recreate the labor phenotype (OS experienced at TL in amnion membranes) in vitro and to induce a terminal state of EMT in AECs [128, 224]. EMT contributes to sustained inflammation that will promote the labor-related cascade of events.

Data from this study indeed confirmed our earlier findings [128] that CSE treatment for 48 hours induced a fibroblastoid morphology in AECs and vimentin relocalization to the leading edge (white arrow) of migratory cells, and significantly increased vimentin/CK-18 ratio (control: 0.56±0.02, CSE: 0.67±0.02; P=.02) compared to AECs under standard cell culture conditions (vimentin [perinuclear]) and CK-18 (cytoplasmic; Fig. 8.3F-G). These changes are indicative of CSE inducing EMT in AECs, while significantly decreasing their migratory potential (P=.0005). Although mesenchymal characteristics are attained that should contribute to more cellular kinesis, the CSE-induced loss of migratory potential observed in our study is likely due to the senescence of cells and independent of transition status. CSE treatment of AMCs resulted in maintenance of their mesenchymal phenotype (Fig. 8.3F-G) and increased level of migration compared to AECs (Fig. 8.3H).

Characteristics of cellular transition in AM-OOC under normal and OS conditions

Innate transition properties of AECs

Confocal microscopy documented amnion cell morphology, intermediate filament expression, and cellular transitions to better understand how they migrate and degrade basement membrane collagen inside microchannels. Microscopy revealed that AECs under innate conditions express basal levels of vimentin/CK-18 (0.5±0.01), perinuclear vimentin, and an epithelial morphology. Migration of AECs was accompanied by a significant increase of vimentin/CK-18 ratio (0.62±0.02; P=0.0025), vimentin relocalization to the leading edge (white arrow), and a fibroblastoid morphology, suggesting cellular transition (EMT). Once AECs completely migrated to the inner chamber, however, they reverted to basal expression of vimentin/CK-18 ratio (0.48±0.02; P=.0009), perinuclear vimentin, and an epithelial morphology indicative of MET (Fig. 8.4A-B). Thus, the result shows that AECs must undergo two cellular transitions, EMT to migrate and MET to exit, to completely migrate through the type IV collagen-filled microchannels. These transitions are similar to what we have reported in scratch assays that resembled membrane microfractures healing where migrating and healing edges had mesenchymal epithelial phenotypes, respectively [128].

OS-induced terminal state of EMT in AECs

As shown above, 48 hour OS-treated AECs in the outer chamber expressed higher basal levels of vimentin/CK-18 compared to control AECs (Fig. 8.4B vs. 4D), indicative of a mesenchymal phenotype. Migrating AECs maintained their fibroblastoid characteristics while relocalizing vimentin to the leading edge (white arrow); however, due to OS-induced senescence, most cells that underwent EMT were retained inside the microchannels, and the majority of them were unable to transition to an epithelial phenotype to exit, which is in line with our finding that OS inhibits migration in AECs

(Control: 7.4±1.7 cells, CSE: 0.2±0.2 cells; P=.0005; Fig. 8.3H). However, the few AECs that crossed the microchannels did undergo MET, inducing basal vimentin/CK-18 ratio (0.3±0.02; P=.0004) levels and an epithelial morphology (Fig. 8.4C-D), suggesting the influential role of the microenvironment in transitioning amnion membrane cells.

OS DOES NOT CHANGE INNATE TRANSITION PROPERTIES OF AMCS

AMCs in the inner chamber under both normal conditions and after OS exposure expressed relatively high levels of vimentin/CK-18 ratio (control AMC: 1.1±0.2, CSE AMC: 1.1±0.2; P=ns). Migrating AMCs maintained their vimentin/CK-18 ratio (control AMC: 1.0±0.03, CSE AMC: 1.1±0.09) while relocating vimentin to the leading edge. AMCs that migrated into the outer chamber had significantly higher vimentin/CK-18 ratio (control AMC: 2.1±0.14, CSE AMC: 2.4±0.2; migrating vs emigrated AMCs: control: P<.001, CSE: P<.001) while also inducing native vimentin localization and morphology (Fig. 8.4E-H). These data suggests that AMCs do not require cellular transitions (EMT to migrate and MET to exit) to migrate through microchannels, contrary to the behavior of AECs.

Characteristics of cocultured AECs and AMCs in AM-OOC

To recreate the physiological context of the amnion membrane components, AEC and AMCs were cocultured inside the AM-OOCs to study tissue dynamics. To determine the effect of coculture on cellular transitions and migration, we stained live AECs with a histone 2B-green fluorescent protein (GFP) and AMCs with a histone 2B-red fluorescent protein (RFP) to track them during and after migration. We treated each chamber individually with control, CSE, or CSE with OS inhibitor NAC plus p38 MAPK functional inhibitor SB (CSE+; Table 1). Both of these inhibitor compounds have been shown to reduce the deleterious effects of OS- and stress-associated signaling in amnion cells [82, 145], hence why they were selected for our experiment.

COCULTURE EFFECT ON CELLAR TRANSITIONS

After examining what occurs during monoculture in either the outer or inner chamber of the AM-OOC, we performed similar co-culture experiments under fluidic isolation conditions (fluidic isolation shown in Fig.8.2). Under normal coculture conditions, GFP-labeled AECs expressed epithelial morphology in the outer chamber, underwent EMT, migrated, and maintained their mesenchymal morphology to join the AMC population in the inside chamber (Fig. 8.5A; middle column, left cropped area; yellow outline). Similarly, RFP-labeled AMCs migrated, underwent MET to an epithelial morphology while assembling into the AEC population (Fig. 8.5A; middle column, center, and right cropped area; yellow outline), emphasizing AECs' and AMCs' ability to transition under distinct environmental conditions.

OS' EFFECT ON MIGRATION IN COCULTURE

A bright field microscopy analysis showed 48 hour CSE treatment of AECs or AMCs in coculture induced migration more frequently than in respective controls (AEC control: 5.1±0.06, CSE: 7.3±0.3; AMC control: 3.3±0.3, CSE: 5.5±1.5). These results were different compared to our monoculture experiments, highlighting the effect of coculture on cell migration. Localized CSE treatment of each chamber did not affect AECs' or AMCs' migration potential in their adjacent chambers, showing that localized CSE treatment in the AM-OOC is indeed possible. Interestingly, when CSE was cotreated to both chambers, cellular migration was inhibited. These effects were prevented by cotreatment of CSE with NAC and SB (CSE+; Fig. 8.5B) (AECs: CSE/CSE vs. CSE+/CSE+ = 2-fold higher)(AMC: CSE/CSE vs. CSE+/CSE+ = 2.5-fold higher), suggesting that OS and p38 MAPK downstream signaling could regulate AECs' and AMCs' migration.

Propagation of inflammatory mediators in AM-OOC devices

ELISAs for proinflammatory marker GM-CSF was evaluated 48 hours after treatment to determine whether migratory cells induced inflammatory changes in the opposite chambers.

STANDARD AND OS-INDUCED INFLAMMATORY MEDIATOR EXPRESSION

Consistent with the current literature, under coculture condition, AMCs naturally produced more proinflammatory cytokines compared to AECs [49] (Fig. 8.6A). Furthermore, though not significant, CSE treatment of AECs and AMCs increased proinflammatory cytokines in both cell types (AEC: Control: 5.7±1.5, CSE: 8.7±1.9 [black vs. white bars]) (Fig. 8.6B) (AMC: Control: 2208±1629, CSE: 3835±1541 [black vs. light grey bars]) (Fig. 8.6C).

OS-INDUCED INFLAMMATORY MEDIATOR PROPAGATION

The CSE treatment of one chamber was also shown to induce inflammatory mediator (GM-CSF) response in the opposite chamber (CSE AMCs' effect on control AECs [black vs. light grey bars], control/control: 5.7±1.5, control/CSE: 8.2±2.4) (Fig. 8.6B) (CSE AECs' effect on AMCs [black vs. white bars], control/control: 2208 ± 1629, CSE/control: 3835±1541) (Fig. 8.6C), while CSE + treatments lowered proinflammatory cytokine production compared to CSE alone in both cell types (Fig. 8.6B [Dark grey vs. striped bars]) (Fig. 8.6C [Dark grey vs. striped bars]). Since fluid isolation was established (Fig. 8.2 and Sup. Fig. 8.1) and CSE treatment did induce migratory changes in the cell population (Fig. 8.5B), we postulate that inflammatory changes may be initiated from the migrated cells themselves or by supernatant leaking through cell induced tunnels in the collagen-filled microchannels.

DISCUSSION

The AM-OOC that we developed and utilized in this study revealed amnion membrane cells' transition and migratory properties under interactive environmental conditions. We determined the following: 1) amnion membrane cells can transition and migrate through type IV collagen-filled microchannels; 2) OS induces a terminal (nonreversible) state of EMT, decelerates cell migration, and increases proinflammatory mediator production; 3) coculture experiments revealed that both cell types can migrate, transition, and integrate themselves into the emigrated environment; and 4) OS cotreatment propelled transition but inhibited migration of cells in cocultures and induced proinflammatory mediator production in the adjacent cell chamber. Inhibition of OS by antioxidants and functional inhibitors of stress signaler p38 MAPK reversing the changes further confirmed the influence and interaction between the AMCs and AECs.

Recreating the whole organ dynamics using OOCs is an idea that has been around for many years [241]; however, only very recently has their usefulness been explored in the field of reproductive science. The female reproductive tract [267], placenta [268], and endometrium-on-chip [247] have been developed and used to study multiple aspects of reproductive health, which have highlighted the importance of cell-cell and cell-blood interactions in vitro. Although the development of a fetal membrane-on-chip has been postulated [256], no work has been reported yet. We first focused on creating an in vitro culture model of the amnion membrane because it is a key component of the fetal membrane. Another reason we initially focused on the amnion membrane, rather than the entire fetal membrane, is it is only composed of two cell types, compared to the entire fetal membrane, which is composed of five cell types, both from the fetal side as well as the maternal side. We have previously developed a model that tested interactive features between feto-maternal interface cells, AECs, and maternal decidual cells [246]. The current model was used to address the limitations of the previous model, including the following: its lack of an ECM, as cells are directly cultured on a synthetic nondegradable polymer membrane similar to those used in transwell inserts; its inability to locally stimulate only

one cell type to properly study cell-cell interactions and causal relations in their effect; and the vertical organization of the device that prevents direct imaging of the culture chambers and migratory cells that move from one chamber to the other, to name a few. The AM-OOC we developed overcomes these limitations by more accurately mimicking the amnion component of the fetal membrane, especially the existence of ECM, while allowing different cellular components of the amnion to be independently controlled and stimulated and also allowing the direct monitoring of cellular migration through the ECM using microscopy.

The amnion membrane provides the structural framework for the intra-uterine cavity and contributes to pregnancy maintenance by bearing the tensile strain inflicted by the growing fetus [23, 50-52, 106]. The highly elastic amnion layer of the fetal membranes maintains its integrity and function through constant remodeling mediated by cellular transitions and matrix rearrangements. AECs are more dynamic in their transitions as they line the inner surface of the intraamniotic cavity, whereas AMCs serve as reserve cells to fill gaps vacated by AECs in the ECM. Maintenance of membrane integrity during gestation and its mechanical and functional compromise at term involves both cellular and matrix components. ECM turnover by collagenolytic processes are well reported [269], and recent work from our lab has shed some insight into cellular-level changes [96, 128, 224]. In that work, we reported that OS' buildup at term causes stress signaler p38 MAPK-mediated senescence [82, 224], as well as EMT of AECs [128]. Both of these conditions cause endogenous inflammatory responses associated with parturition. Histological examination of senescent membranes revealed biologic microfractures that are sites of remodeling. Although cell scratch assays can determine mechanisms of microfractures' healing, those experiments lacked cellular interactions that may influence transitions and migrations. In addition, even though some level of evidence of cellular migration can be observed at distinct time points through microscopy, such migration could not be directly

monitored. These limitations were addressed by the use of the AM-OOC model we developed.

Our study provides a novel approach to document sites of remodeling in vitro by visualization of cells migrating through collagen filled microchannels (Fig. 8.3). This very well may be facilitated by collagen degradation or even in the absence of this. Our study did not specifically test this aspect; however, based on the nature of amnion cells, it is likely that they will produce type IV collagen-specific MMPs to propel themselves through these microchannels. During gestation, AECs and AMCs undergo cyclic cellular remodeling to heal gaps and microfractures in the membranes, a mechanism required to maintain membrane homeostasis. Membrane remodeling at a cellular level is achieved by EMT of AECs and MET of AMCs, aided by redox radicals, growth factors (e.g., TGFβ), and endocrine mediators (e.g., P4) [66, 128, 223, 224]. Cellular gaps are created [39] when AECs are shed from the membrane due to cellular senescence and/or mechanical disruption due to fetal and AF shear stress. These gaps lead to microfractures' formation by shed AECs, which migrate through the ECM. This migration is aided by the mobility attained by AECs when they transition to AMCs. Endogenous P4 recycles transitioned AMCs back to AECs with the production of nascent collagen to fill any degraded ECM components. These biological processes maintain membrane integrity and cellular homeostasis during gestation. However, at term, an increased OS-induced terminal state of EMT increases inflammatory mesenchymal phenotype, leading to collagen degradation and mechanical failure of membranes

These intrinsic in utero events were recreated in our AM-OOC and documented that treatment of adjacent cell populations in a controlled environment results in OS inducing a terminal state of EMT and inflammation (Fig. 8.3 and 8.4). In single cell culture, OS has also been previously shown to inhibit migration of AECs due to the development of cellular senescence [128]. Data from our AM-OCC also reconfirmed this finding. However, importantly, our model shows that this inhibition can be partially overcome

when AECs are cocultured with AMCs that are maintained in a normal cell culture environment (Fig. 8.5). Conversely, CSE co-treatment induced EMT in AECs but prevented migration and MET in AMCs. Thus, OS treatment induces a terminal state of EMT in the AM-OOC devices, similar to what is observed in term amnion membrane.

By recreating the full amnion component of the fetal membranes, this AM-OCC model provides a physiological context that allows manipulation of multiple cell types and their microenvironments with high levels of accuracy. 3D cell culture models, such as amnion membrane explants, organoids, and transwell systems, offer an alternative approach to multilayer assessment of cell-cell and cell-collagen interactions in vitro. However, the ability to distinguish between individual cell signals and analyze how these signals propagate is lost due to the close proximity of different cell types in explants and organoids, or difficulties in manipulating each cell culture chamber in transwell systems. Additionally, most of these models are not compatible with direct imaging of cellular migration, cellular transition, and ECM degradation, and thus cannot provide a detailed view or direct evidence of cell-cell interactions.

Traditionally, Transwell culture systems are used to study fetal membrane signaling [270]; however, their usefulness is limited due to the following reasons: 1) lack of physiological separation of cell types in coculture; 2) controlling their respective microenvironment in coculture is not possible, and local application of stimuli to only one compartment is difficult; 3) direct monitoring of any collagen matrix degradation due to cellular migration is not possible; 4) imaging of cellular migrations and transitions is limited; and 5) a low signal-to-noise ratio due to a large culture volume hampers studies on biomarker kinetics. Compared to transwell cultures, the AM-OOC model uses a significantly fewer number of cells (2-fold lower than 24-well transwell culture), which is important since the cell source is quite limited from the human amnion membrane. Additionally, it allows for better interactions between cell layers while providing sensitive measurement capabilities of membrane permeability, biomolecule propagation (e.g.,

cytokines, growth factors, extracellular vesicles), and signaling pathways. Overcoming the limitations of conventional approaches, the developed AM-OOC allows for real-time in-depth imaging of cellular processes while controlling fluid / treatment flow in the coculture chambers that are physically and fluidically isolated, yet still allowing cell-cell communication. These unique features of the developed AM-OOC allow analysis of complex interconnected biochemical and physiological responses while maintaining cell viability.

The particular model presented here is focused on visualizing cellular migration and transition, and, therefore, contains few limitations for conducting other types of studies. In utero amnion membranes comprise AECs connected to an ECM containing AMCs by a 13μm thick basement membrane [4]. Although we included type IV collagen in between our cell layers, the ECM fabric where AMCs are often located is not included in the model, and the influence of that component in migration and transition is still unclear. Thus, future improvement to the device will include 1) shortening the microchannels to properly represent microfractures, 2) adding dynamic medium flow to the AEC chamber to induce cellular shear stress normally impacted on AECs by AF, and 3) fabrication of additional chambers to culture primary chorion trophoblast and decidual cells. Such improvements will result in recreating the full fetal membrane on OOC format.

The AM-OOC method developed here allowed us to overcome several limitations of traditional 2D/3D culture systems in investigating amnion membrane cellular and collagen characteristics and interactions. Future designs of this model will include the fetal membrane cells as well as a decidual layer to represent the full feto-maternal interface to study their functions during physiologic and pathologic pregnancies.

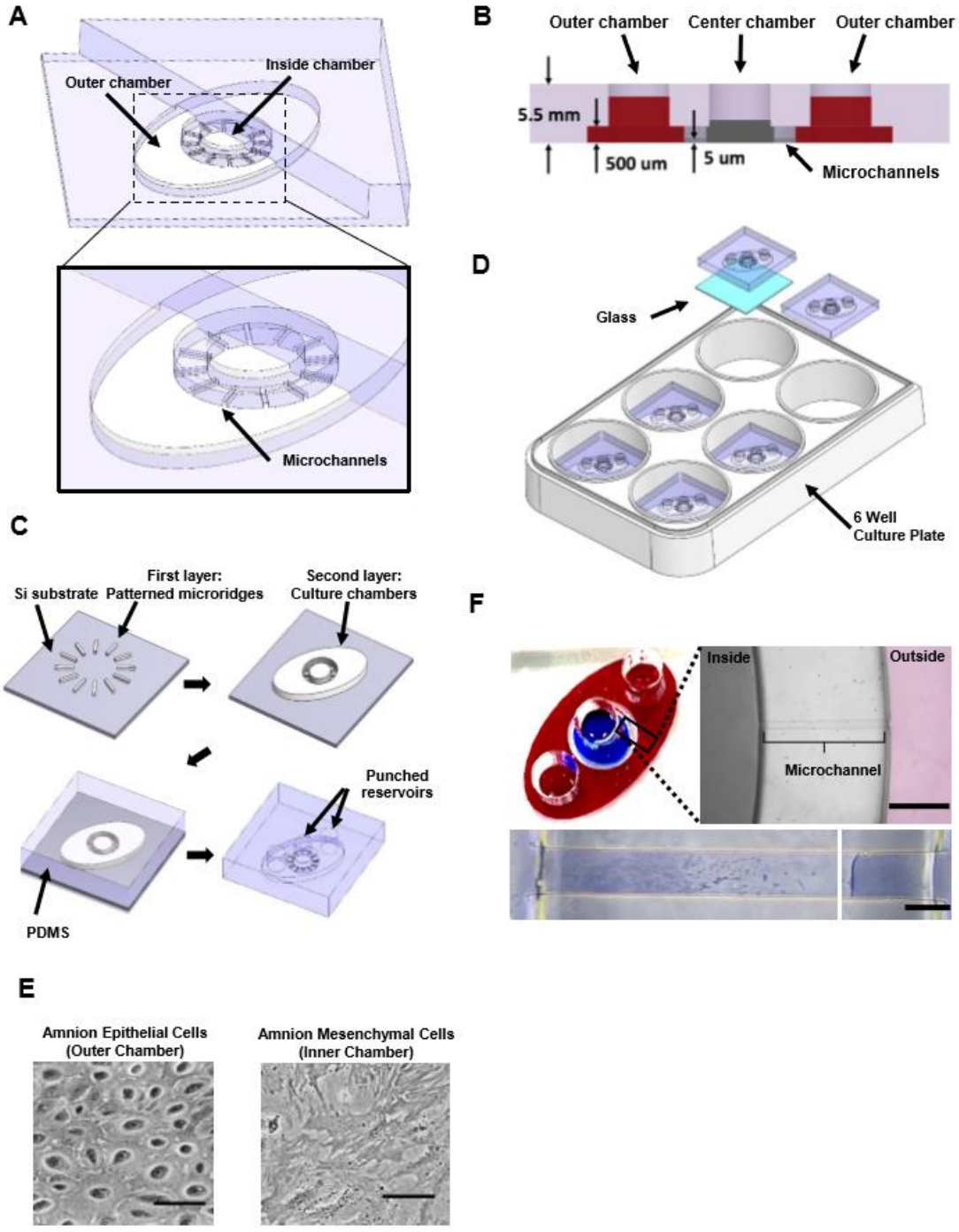

Fig. 8.1 AM-OOC fabrication and layout

The AM-OOC is designed to recreate the amnion membrane in vitro by coculturing amnion epithelial and mesenchymal cells separated by a type IV collagen-filled microfluidic channel array (mimicking basement membrane). A) Schematic illustration of the AM-OOC. 3D and a cross-sectional view showing the physical isolation of AECs and AMCs in each culture chamber, connected by 24 microchannels filled with type IV collagen. B) Cross-section view showing the principle of diffusion barrier formation by

liquid height difference. C) Microfabrication and assembly steps for the AM-OOC device. Two SU-8™ layers with different thicknesses were patterned on top of a silicon substrate to form the microchannels, and the two cell culture chambers (outer chamber: AECs; inner chamber: AMCs). PDMS devices were replicated from the SU-8 master using soft lithography process, and 7mm diameter reservoirs were punched out followed by bonding onto PDL or Matrigel™ coated substrates. D) Each AM-OOC fits into one well of a conventional 6-well polystyrene culture plate. E) Bright field microscopy images of AEC morphology and AMC morphology inside an AM-OOC device. Scale bar is 10μm. F) The outer chamber of the AM-OOC was filled with red dye, and the inner chamber was filled with blue dye. The right image shows that a diffusion barrier has been successfully formed between chambers (indicated by the red dye remaining in the outer chamber; scale bar=300μm). Microchannels filled with type IV collagen Matrigel (stained with Masson trichrome), connecting the two culture chambers (Scale bar=30μm) can also be seen.

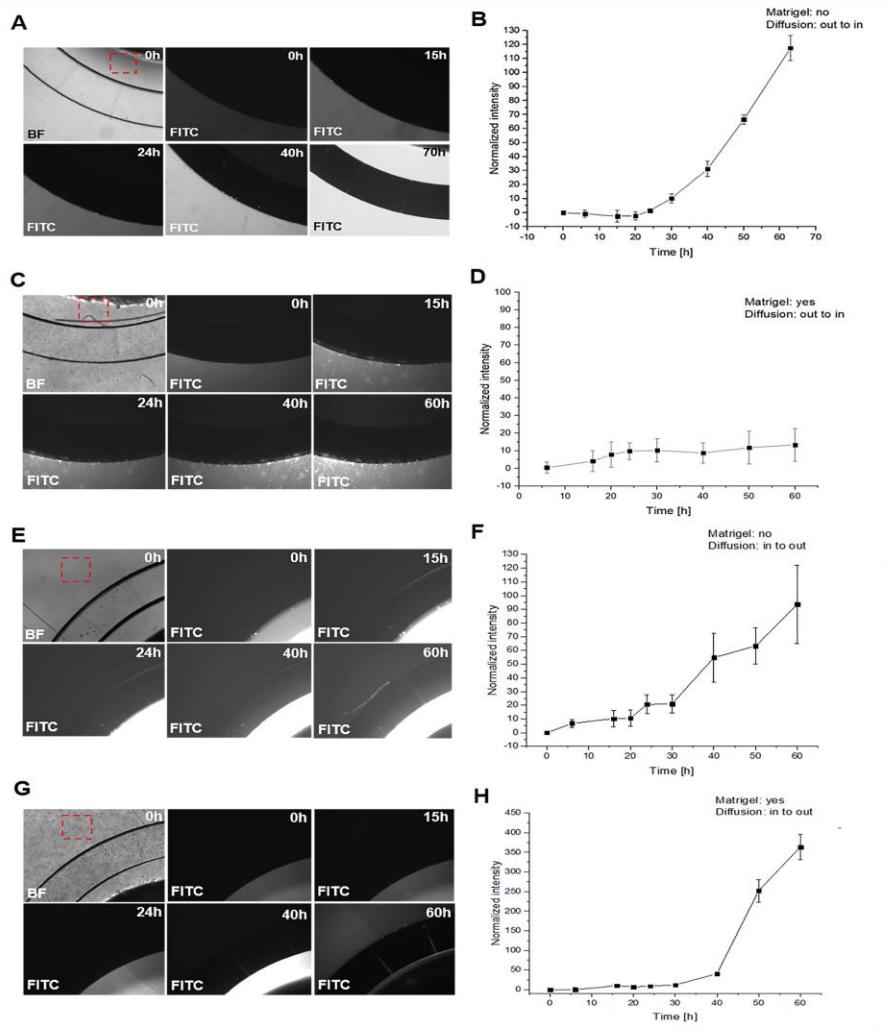

Fig. 8.2 AM-OOC fluid perfusion over time

FITC-based perfusion assay showing fluidic isolation between the two culture chambers of the AM-OOC device over 60 hours. A-D: Inner chamber fluid level is higher than the outer chamber fluid level, countering diffusion from outside to inside. A-B) Brightfield and fluorescent microscopy shows FITC diffusing through microchannels without type IV collagen coating. Red boxes highlight regions where fluorescent intensity was measured (N=3). The graph shows the degree of FITC diffusion from the outside chamber to the inside chamber. C-D) Repeat of A-B, but when the microchannels in the AM-OCC is filled with type IV collagen coating. E-H: Outer chamber fluid level is higher than the inner chamber fluid level, countering diffusion from inside to outside. E-F) Brightfield and fluorescent microscopy shows FITC diffusing through microchannels without type IV collagen coating. Red boxes highlight regions where fluorescent intensity was measured (N=3). The graph shows the degree of FITC diffusion from the inside chamber to the outside chamber. G-H) Repeat of E-F, but when the microchannels in the AM-OCC is filled with type IV collagen coating.

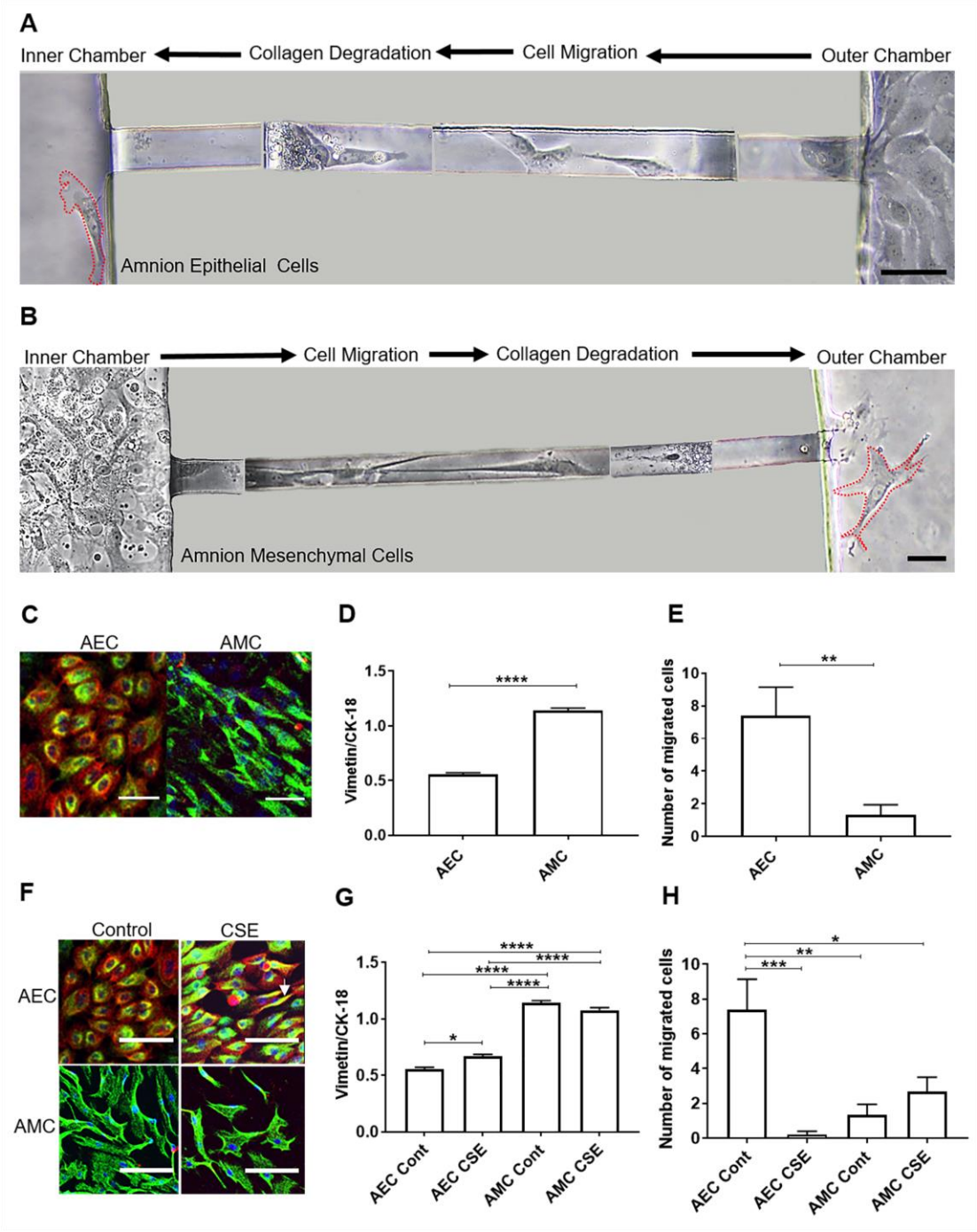

Fig. 8.3 AEC and AMC characteristics inside an AM-OOC device

Characteristics of monoculture amnion cells in an AM-OOC device under control and OS conductions. A) Composite bright field images show that under a normal cell culture condition, AECs can enter into the collagen-filled microchannels, elongate to show a mesenchymal morphology, migrate through type IV collagen, and exit the tunnel (red outline) while potentially retaining this mesenchymal shape (N=6). Scale bar=30 µm.

B) Composite bright field images show that under a normal cell culture condition AMCs can enter into the collagen-filled microchannels, elongate, migrate through type IV collagen during that process, and exit the tunnel (red outline), and then reverting to their original shape (N=6). Scale bar=30 µm. C-D) Confocal images show native levels of vimentin and CK-18 expression in AECs and AMCs (AEC: 0.56±0.02 vs AMC: 1.1±0.02; N=3). AECs are in a metastate, meaning they coexpress both epithelial and mesenchymal markers. AMCs had significantly higher vimentin/CK-18 levels compared to AECs (P<.0001; N=3). Confocal images were captured at 10x. Blue-DAPI, green-vimentin, and red-CK-18. Values are expressed as mean intensity±SEM. Scale bar=10 µm. E) Analysis of bright field microscopy images shows AECs migrated into the opposite chamber more frequently than AMCs. Values are expressed in the number of migrated cells in each device (P=.0064). F-G) Confocal images show native and OS-induced (CSE) levels of vimentin and CK-18 expression in AECs (AEC Control: 0.56±0.02, CSE: 0.67±0.02) and AMCs (AMC Control: 1.1±0.2, CSE: 1.1±0.2; N=3). CSE AECs had significantly higher vimentin/CK-18 levels compared to AEC controls (P=.02) (white arrow showing vimentin on the leading edge of the cell), while AMC intermediate filament expression remained constant regardless of treatment (N=3). Confocal images were captured at 10x. Blue-DAPI, green-vimentin, and red-CK-18. Values are expressed as mean intensity±SEM. Scale bar=30µm. H) Analysis of bright field microscopy images shows CSE treatment inhibited migration of AECs compared to AEC controls (P=.0005), while CSE treatment of AMCs stimulated migration (N=3). Control AECs contain the most migratory potential of all treatments and cell types. Migratory cells were defined as cells that had migrated through the microchannel and were now resident in the opposite chamber.

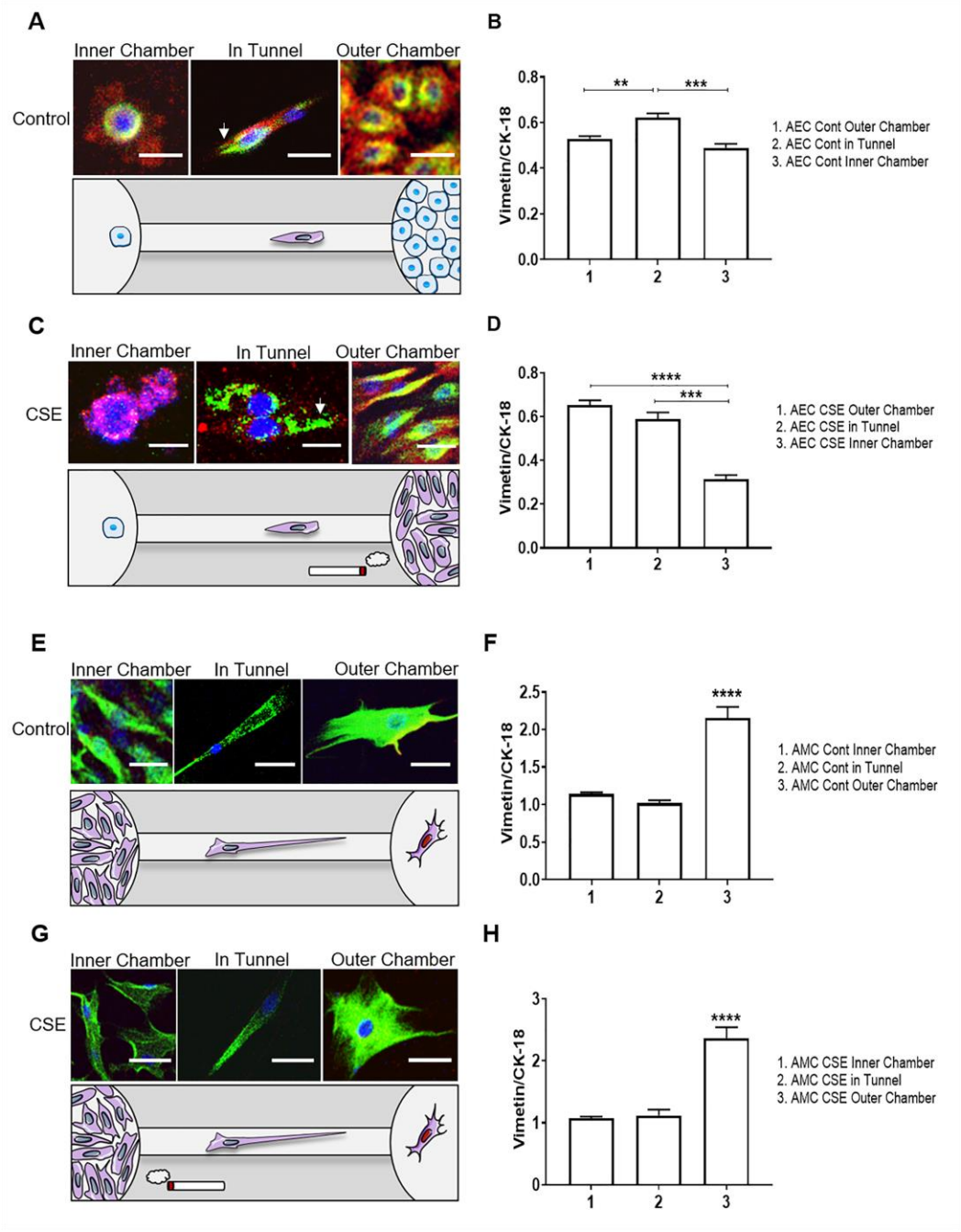

Fig. 8.4 OS effect on cell migration and transition in monoculture

Confocal images measuring vimentin/CK-18 levels in AECs and AMCs during cell migration (N=3). Confocal images were captured at 10x. Blue-DAPI, green-vimentin, and red-CK-18. Values are expressed as mean intensity ± SEM. Scale bar=10 µm. A-B) AECs in the outer chamber under native conditions express basal levels of vimentin/CK-18 ratio (0.5±0.01), perinuclear vimentin, and an epithelial morphology. Migration of AECs is accompanied by a significant increase of vimentin/CK-18 ratio (0.62±0.02; P=.0025), vimentin's relocalization to the leading edge (white arrow), and an elongated mesenchymal

morphology indicative of an EMT. Once AECs completely migrated to the inner chamber, they reverted to basal expression of vimentin/CK-18 ratio (0.48±0.02; P=.0009), perinuclear vimentin, and an epithelial morphology indicative of MET. C-D) AECs in the outer chamber under OS conditions (CSE) express relatively high levels of vimentin/CK-18 ratio (0.65±0.02) compared to control AECs. Additionally, AECs treated with CSE contained vimentin localization at the leading edge (white arrow) and an elongated mesenchymal morphology. Migration of CSE-treated AECs is not accompanied by changes in the vimentin/CK-18 ratio (0.58±0.03), vimentin relocalization, or morphology variations, which shows that CSE maintains AECs in a terminal state of EMT. However, the few AECs able to cross the microchannels did, under MET transitions, revert to basal expression of vimentin/CK-18 ratio (0.3±0.02; P=.0004), very little vimentin, and an epithelial morphology. E-H) AMCs in the inner chamber under native and OS conditions express relatively high levels of vimentin/CK-18 ratio (Control: 1.1±0.2 and CSE: 1.1±0.2) compared to AECs regardless of treatment. Migrating AMCs maintain their vimentin/CK-18 (Control: 1.0±0.03, CSE: 1.1±0.09) while relocalizing vimentin to the leading edge and inducing an elongated cell morphology. Migration of AMCs into the outer chamber significantly increases the vimentin/CK-18 ratio (Control: 2.1±0.14, CSE: 2.4±0.2), while also inducing native vimentin localization and mesenchymal morphology.

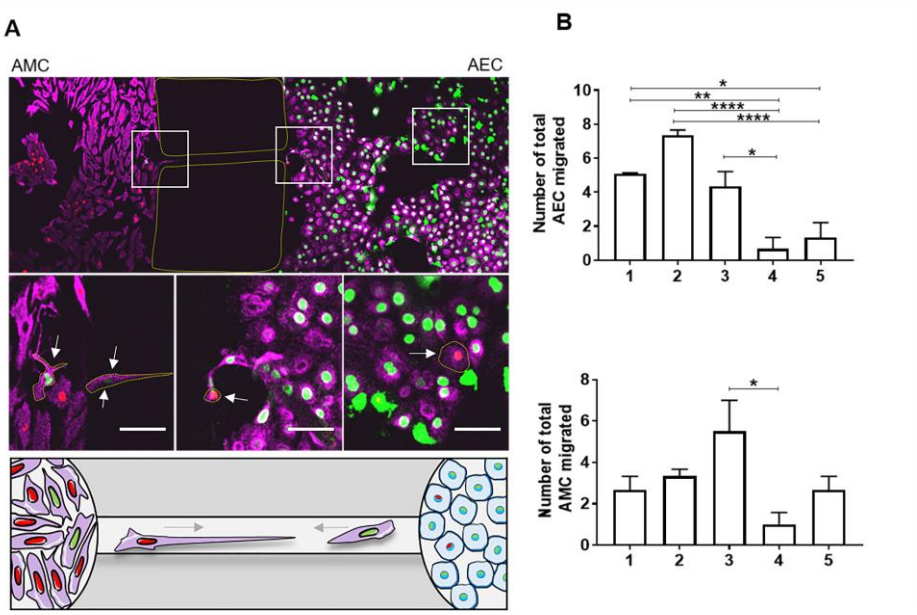

Fig. 8.5 OS' effect on migration and transition in AEC-AMC coculture

Confocal imaging of coculture experiments revealed that both cell types can migrate, transition, and integrate themselves into the emigrated environment (N=3). A) Confocal images show native AECs (green) and AMCs (red), which have transitioned, migrated, and integrated into the opposite population (N=3). Middle right panel highlights (yellow) GFP-AECs that have migrated through the type IV collagen tunnel, relocalized vimentin, and transitioned into a mesenchymal morphology indicative of EMT. Middle left panels highlight (yellow) RFP-AMCs that have migrated through the type IV collagen tunnel, downregulated vimentin, and transitioned into an epithelial morphology indicative of MET. Bottom panel is a schematic representing AEC (green) and AMC (red) cellular transitions. Grey arrows highlight migration direction. Confocal images were captured at 10x. Pink-vimentin, green-histone-2B AEC, and red-histone-2B AMCs. Scale bar=30 µm. B) Top Graph: Analysis of bright field microscopy images shows AECs treated with CSE, in coculture, migrated into the opposite chamber more frequently than the AEC control (AEC Control: 5.1±0.06, CSE: 7.3±0.3) (AEC: bar 1 vs. 2; 1.5-fold increase) (AMC: bar 1 vs. 3; 2-fold increase). CSE treatment of AMCs did not affect AECs' migration (5.1±0.06 vs 4.3±0.8). CSE cotreatment of AECs and AMCs inhibited AECs' migration (0.67±0.6), while cotreatment with CSE+ relieved the effects of CSE (1.3±0.8) (AECs: CSE/CSE vs. CSE+/CSE+ = 2-fold higher) (AMC: CSE/CSE vs. CSE+/CSE+ = 2.5-fold higher). Values are expressed as mean intensity ± SEM. Bottom Graph: Analysis of bright field microscopy images shows AMCs treated with CSE, in coculture, migrated into the opposite chamber more frequently than the AMC control (AMC Control: 2.7±0.6, CSE: 5.5±1.5). CSE treatment of AECs did not affect AMCs' migration (2.7±0.6 vs 3.3±0.3). CSE cotreatment of AECs and AMCs inhibited AEC migration (1±0.5), while cotreatment with CSE+ relieved the effects of CSE (2.7±0.6). Values are expressed as mean intensity±SEM. Migratory cells were defined as cells that had migrated through the microchannel and identified by the opposite color of cell nuclei (i.e. green nuclei AEC cells in the red nuclei AMC population).

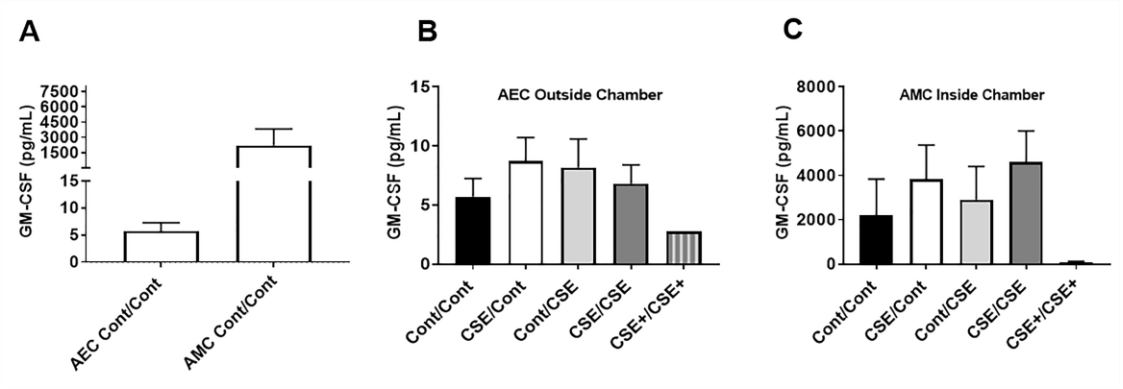

Fig. 8.6 Production and propagation of proinflammatory mediators in the AM-OOC coculture system

OS induced proinflammatory mediator production and propagation in amnion cells (N=3). A) ELISA-measured medium concentrations of GM-CSF from the AEC (outer chamber) and AMC (inner chamber). Though not significant, AMCs naturally have a higher level of GM-CSF expression compared to AECs (AEC: 5.7±1.5 pg/mL, AMC: 2208±1629 pg/mL). B-C) CSE treatment, regardless to which chamber, induced higher expression of GMCSF in AMCs compared to AECs (CSE AMCs' effect on control AECs [black vs. light grey bars], control/control: 5.7±1.5, control/CSE: 8.2±2.4) (Fig. 8.6B) (CSE AECs' effect on AMCs [black vs. white bars], control/control: 2208 ±1629, CSE/control: 3835±1541) (Fig. 8.6C). CSE+ treatment lowered GM-CSF in both AECs (2.8 ±0pg/mL) and AMCs (81.9 ±43pg/mL). Values are expressed as mean intensity±SEM.

CONCLUSIONS

Chapter 9. Summary and future directions

DISSERTATION SUMMARY

The premise of this dissertation is that fetal membrane cells are in a dynamic state during pregnancy undergoing constant transitions and turnovers to maintain homeostasis until term. Disruption in membrane homeostasis due to senescence (mechanism of aging) and inflammation result in the arrest of this process that can be detrimental to pregnancy. This is likely a normal physiologic process at term to promote delivery but pathologic at preterm (i.e., pPROM). We propose that while structural remodeling is innate to the process of pregnancy, disturbances in the remodeling process can be detrimental. Lack of remodeling is indicated by persistence of microfractures which are characterized by 1) altered amnion epithelial layer (puckering) or site of epithelial shedding; 2) deterioration and damage of the basement membrane; 3) tunnels representative of collagen degradation in the ECM that extend from the basement membrane through the spongy layer; and 4) the presence of migrating cells in the tunnel [96]. At term, microfractures increase in number and morphometry compared to normal remodeling tissues. Similarly, examination of membranes from PTB with or without rupture of membranes (i.e., pPROM) also showed an increase in microfractures [96, 140]. This suggests that along with senescence, membrane remodeling dysregulation can also be associated with term or preterm labor. Resealing of microfractures is dependent on its morphometric characteristics as well as cellular-microenvironment. Understanding the pathways and mediators of microfracture development and resealing will help us to determine how pathological conditions (OS and inflammation) can contribute to the persistence of microfractures and dysfunctional membrane status.

By studying amniotic wound healing models in vitro (i.e., AEC scratch assay), we were able to elucidate cellular processes that could contribute to microfracture formation and healing in utero. Amnion cells can naturally proliferate, migrate, and transition undergoing EMT and MET to heal wounds [128]. Throughout gestation components of AF (e.g., P4) may contribute to membrane homeostasis by promoting wound or microfracture closure, while increased OS at term induces a terminal state of EMT, senescence, and inflammation which inhibits wound heal. This data corresponds with the increased number of microfractures observed at term and preterm [96] which could contribute to membrane dysfunction.

Though understanding the cellular processes involved in membrane remodeling is important, the signaling pathways reasonable for cellular transitions deserve equal attention. Prior to our study, upstream regulation of OS-induced p38 MAPK activation was unknown, though it was thought to be comprised of canonical MAPKKK signaling. Systematic analysis using siRNA revealed that p38 MAPK activation at term is not through MAPKKK signaling (e.g., ASK1, MAPK3, MAPK6, or MAPK4), but through TGF-β-TAB1 autophosphorylation of p38 MAPK [224]. OS at term increases TGF-β production and activation of TAB1, which is primarily responsible for p38 MAPK-induced senescence in fetal membranes.

Before determining the role of senescence in preterm membranes, we investigated p38 MAPK-senescence mechanisms at term using membranes at TL (i.e., vaginal term deliveries) compared to TNIL (i.e., schedule cesarian term deliveries). Electron and multiphoton microscopy show swollen organelles [13], constricted desmosomes, amnion puckering and defects in the basement membrane and ECM [96]. Human and mice membranes obtained during labor also express reduced epithelial markers, CK-18 and E-cadherin, and increased mesenchymal markers, vimentin and N-cadherin, transcription

factors-TWIST, SNAIL and SLUG, and MMP9. These changes are characteristic of EMT, a phenomenon associated with tissue inflammation [271, 272]. The same findings were replicated in TNIL explants under conditions of OS, mice injected with CSE, and primary AEC cultured in standard conditions. In the latter, we used siRNA and SB to rigorously define a pathway involving TGF-β, TAB1, and p38 MAPK activation leading to EMT. Induction of terminal EMT is an unstable state and in order to maintain membrane homeostasis, these cells need to revert to an epithelial nature by undergoing MET throughout gestation. Due to local production of P4 via amnion membrane cells, chorion trophoblasts, or AF, stromal AMCs (i.e., a cellular reservoir) can be stimulated to undergo MET through a P4-PGRMC2-c-MYC mediated cascade. Reducing the number of mesenchymal cells in the stroma and contributing to amnion membrane integrity.

Therefore, we hypothesize that during pregnancy, fetal membrane cells are plastic and alternatively undergo EMT-MET remodeling to maintain membrane homeostasis via a balance between TGF-β-TAB1-p38MAPK and P4-PGRMC2-c-Myc pathways. Overwhelming OS at term; 1) downregulates PGRMC2 expression, 2) inhibits P4 mediated MET, 3) induces senescence, and 4) an irreversible (or terminal) state of EMT, 5) promotes an increase in stromal mesenchymal cells, 6) contributs to the inflammatory load and labor initiation. Therefore, discovery and understanding of cellular transitions and signaling mediators at term can help us derive novel therapeutic targets for preterm birth pathways.

Though development of FM-OO-C highlighted the advantages of OOCs compared to current transwell systems [246], in a dynamic in vitro model of the amnion membrane (i.e., AM-OOC), amnion cells were able to proliferate, degrade type IV collagen, migration, and undergo cellular transitions. Use of this model delineated cellular interactions and micro-environmental changes, which can impact amnion cells properties (e.g., AMCs migrating, undergoing MET, and integrating into AEC population) and contribute to fetal membrane remodeling. We propose the process of structural remodeling

during pregnancy and disturbances in the remodeling process at term can be studied using this model.

SIGNIFICANCE

Our research contributes significantly to the field of parturition because it tests a novel hypothesis and mechanistic model that links intra-uterine OS-induced changes in fetal membranes impacting pregnancy outcome. This study for the first time explored fetal membrane cell and matrix remodeling and maintenance during pregnancy and their transition at term to a dysfunctional status under the influence of OS. Successful completion of the proposed studies has elucidated fundamental mechanisms by which fetal membranes maintain their homeostasis through a well-balanced remodeling process mediated by cyclic transitions (EMT-MET) during gestation. By studying the perturbation of this remodeling process at term, we have delineated the role of OS mediated cellular changes. At term, increased OS leads to an acceleration of cellular senescence via p38 MAPK and an irreversible state of EMT capable of increasing inflammation and tissue destruction. Preliminary data suggest dysregulation of EMT or this inflammatory process could also lead to preterm labor; suggesting potential inhibitors of key EMT promoters discovered in this study could be candidate targets for the prevention PTB. The proposed research is important because a clear knowledge of the physiologic mechanisms controlling the onset of labor will facilitate the development of effective therapeutic strategies to prevent preterm labor.

FUTURE DIRECTIONS

The hope is that an explicit knowledge of the physiologic mechanisms (e.g., signaling mediators of senescence and cellular transitions) controlling the onset of 'normal' labor will facilitate the development of effective therapeutic strategies to prevent 'preterm labor.' With that in mind, the Menon lab will conduct a high throughput drug screening

(i.e., FDA approved drugs during pregnancy) on AEC-AMC 3D organoids for inhibitors of OS-induced TGF-β-p38 MAPK EMT. Aspirin, in particular, is a compound of interest due to aspirins current use to manage PE and its ability to directly inhibit TGF-β-induced EMT in cancer cells [273]. Addition of low dose aspirin to the health plan of women predisposed to pPROM could ameliorate infectious or OS derived EMT and inflammation early in gestation (< 34 weeks).

Furthermore, with novel techniques emerging to package drugs or signaling molecules into exosomes, liposomes, or nanoparticles [274-276] new clinical methods of targeted drug delivery are becoming possible. These techniques are beneficial for clinical treatment but also valuable as in vitro tools to tease out signaling mediators responsible for labor associated changes. Specifically, the roles exosomes play in modulating cell-cell, cell-collagen, and micro-environmental factors that contribute to membrane remodeling and labor associated pathways are currently being investigated.

Lastly, the development of an advanced OOC, designed to mimic the full fetal membrane is underway. Containing both AF (on the fetal side) and blood (on the maternal side) interfaces, this device will be able to culture primary human cells (e.g., AEC, AMC, chorion trophoblast, and decidua cells) and primary collagen (e.g., type IV basement membrane and collagen type I and III) while mimicking the mechanical strain and shear stress experienced in utero. This new platform will be crucial for understanding paracrine, endocrine, and cellular propagation between fetal membrane layers and how this contributes to pregnancy maintenance or labor associated changes. Additionally, the advanced fetal membrane-on-chip can serve as a drug screening tool between in vitro cell culture studies and murine/primate models by providing critical pre-clinical data before Phase 1 trials. This device will be developed in my post-doctoral training at Texas A&M in College Station.

Appendix

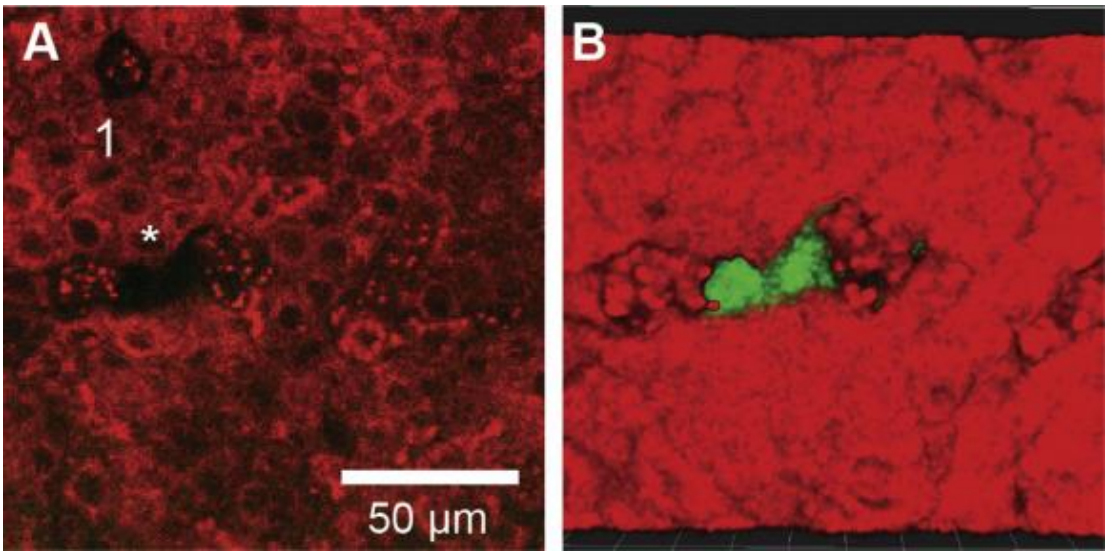

Sup. Fig. 2.1 Cellular characteristics of optically cleared explants using MPAM.

A) A cropped 100µm by 100µm MPAM/SHG single plane image with an asterisk representing an area of epithelial shedding and gap. 1 - Representing an area of epithelial shedding. Measurement bar is 50µm. B) A cropped IMARIS 3D reconstruction of the epithelial shedding and epithelial gap. Green area indicates exposed ECM components through gaps. Contrast and brightness were adjusted to enhance visibility keeping adjustments comparable between images.

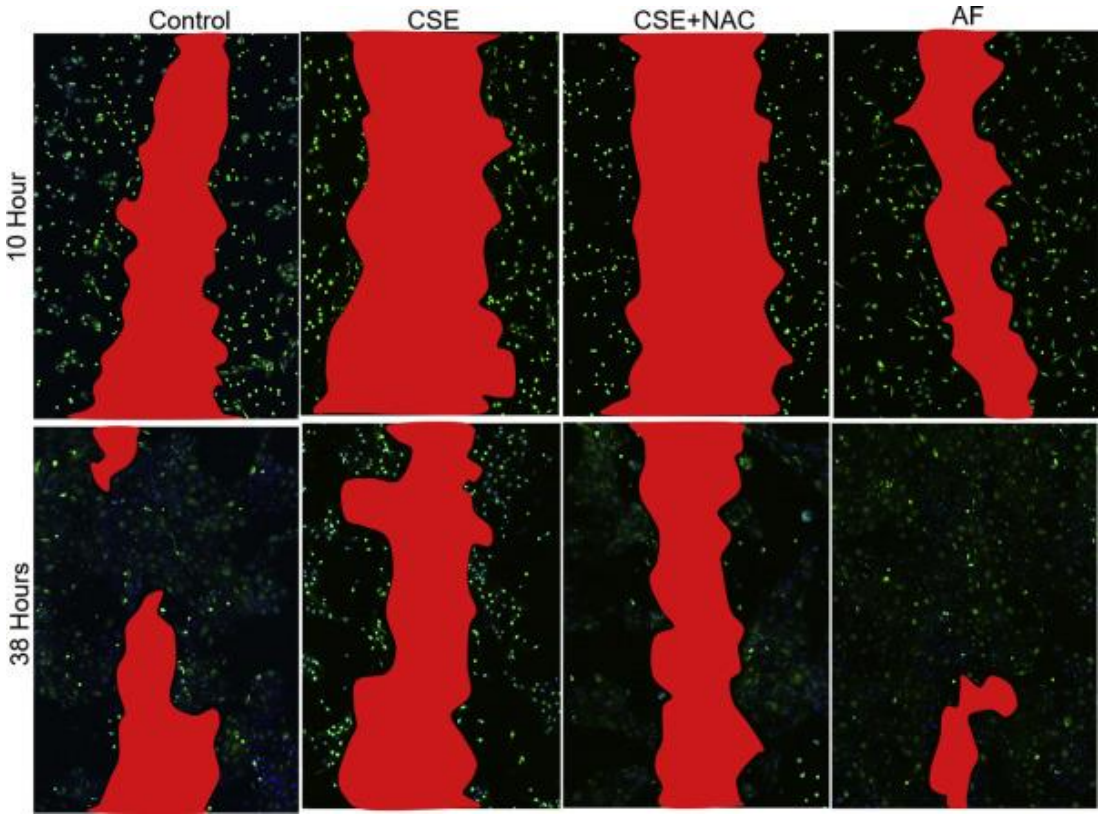

Sup. Fig. 4.1 AECs undergo proliferation and migration to seal the wound.

Representative fluorescence confocal microscopy showing carboxyfluorescein succinimidyl ester (green) localized in AECs at various time points after the scratch. A red mask was overlaid on the wound to highlight the area of AEC proliferation and migration. Carboxyfluorescein succinimidyl ester loses intensity after cell divisions, indicating proliferation compared with cells that are migrating without proliferation to seal the wound. At 10 hours, all treatments retained high fluorescence levels; however, by 38 hours, controls, CSE and NAC, and AF-treated cells decreased their carboxyfluorescein succinimidyl expression along the leading edge, suggesting AEC proliferation and migration to seal the wound. CSE treatment inhibited cell proliferation as indicated by a high degree of fluorescence in cells attributable to OS, an effect minimized by co-treatment with antioxidant NAC. Original magnification, 10x.

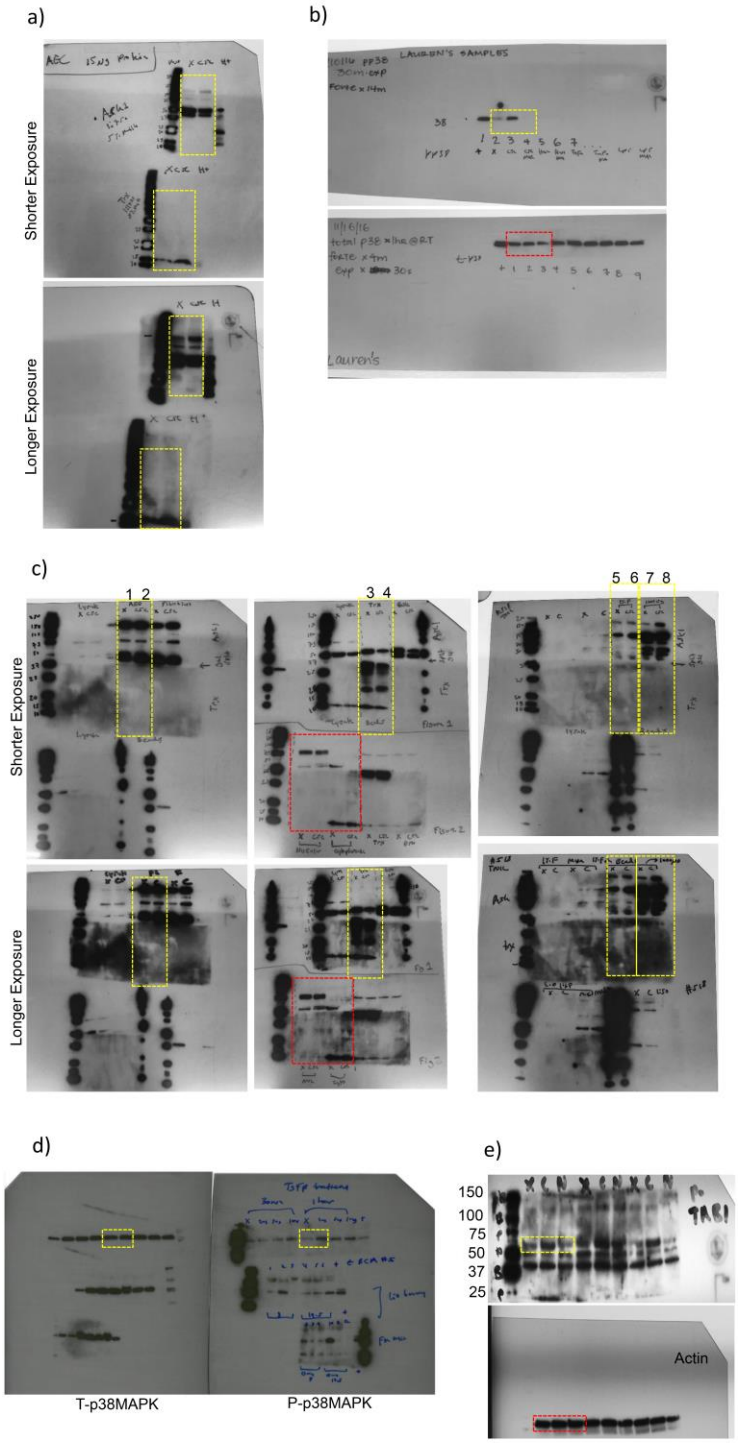

Sup. Fig. 5.1 Original western blot gel images.

A) Two identical western blot gels were probed for ASK-1 or Trx and exposed at the same time. Short exposure image on top and longer exposure image on the bottom. Cropped images (yellow) were used to create Figure 5.1B. B) The same western blot gel was probed for both P-p38 MAPK (yellow) and total p38 MAPK (red) and exposed for

the same time. Cropped images were used to create Figure 5.1D. C) Three individual gels comprise this image and contain components of both Figures 5.1F and 5.2C. Gel 1 contains columns 1 and 2 from Figure 5.1F (yellow). Gel 2 contains columns 3 and 4 for Figure 5.1F (yellow) and all of Figure 5.2C (red), while gel 3 contains columns 5–8 from Figure 5.1F (yellow). Short exposure images on top and longer exposure images on the bottom. Each gel was cut at the 37 MW line and the top half was probed for ASK-1 and the bottom half was probed for Trx. The top and bottom of each gel was then developed together with uniform exposure. D) The same western blot gel was probed for both P-p38 MAPK (yellow; right side) and total p38 MAPK (yellow; left side) and exposed for the same time. Cropped images were used to create Figure 5.4B. E) The same western blot gel was probed for both P-TAB1 (yellow) and actin (red) and exposed for the same time. Cropped images were used to create Figure 5.4F. Uniform contrast/brightness were adjusted with ImageJ for all western blot images.

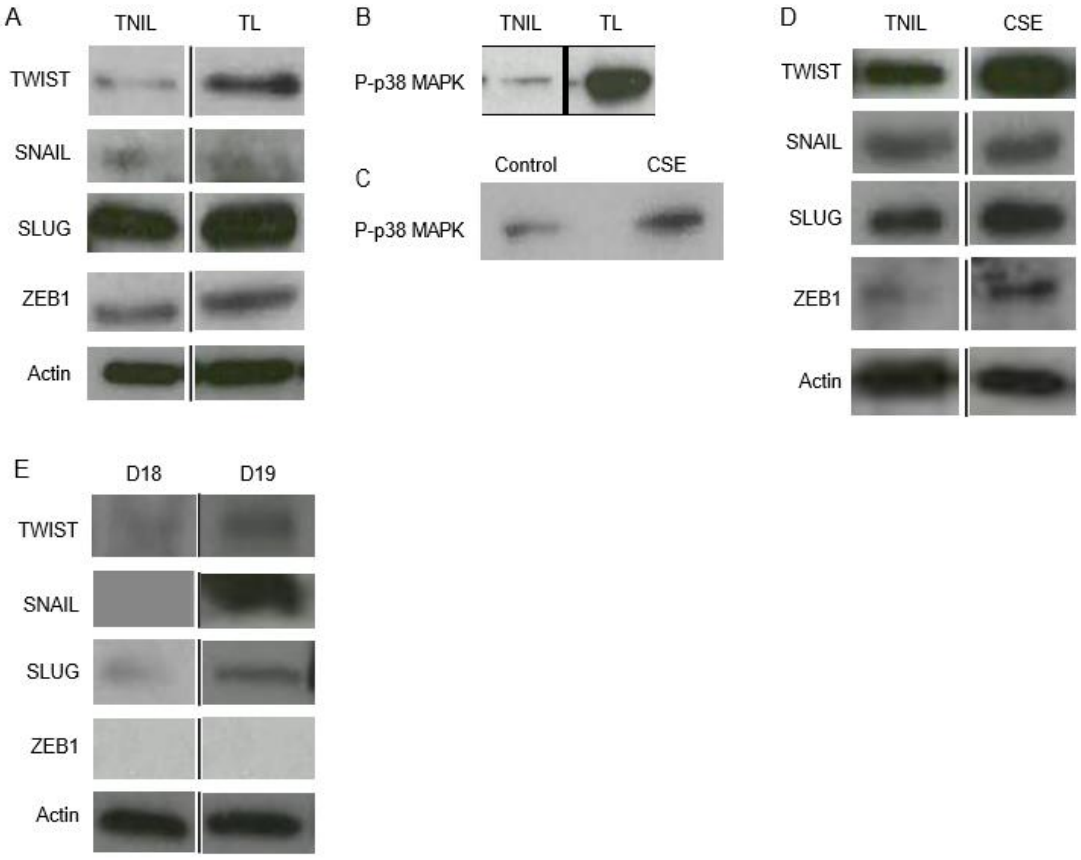

Sup. Fig. 6.1 Mesenchymal transcription factor expression at TL in human and mice models

A) Western blot analysis of human TNIL and TL fetal membranes shows an increase of mesenchymal transcription factors TWIST, SNAIL, SLUG, and ZEB1. This figure shows one representative image from five separate experiments. B) Western blot analysis of human TNIL and TL fetal membranes shows an increase of p38 MAPK activation at TL. This figure shows one representative image from three separate experiments. C) To recreate the labor phenotype in vitro, human TNIL explants were cultured with CSE for 48 hours and western blot analysis shows an increase of p38 MAPK activation after CSE treatment compared to control. This figure shows one representative image from three separate experiments. D) Western blot analysis of human TNIL and CSE fetal membranes shows an increase of mesenchymal transcription factors TWIST, SNAIL, SLUG, and ZEB1. This figure shows one representative image from four separate experiments. E) Western blot analysis of CD-1 mice Day (D) 18 and D19 fetal membranes shows an increase of mesenchymal transcription factors TWIST, SNAIL, and SLUG. This figure shows one representative image from three separate experiments.

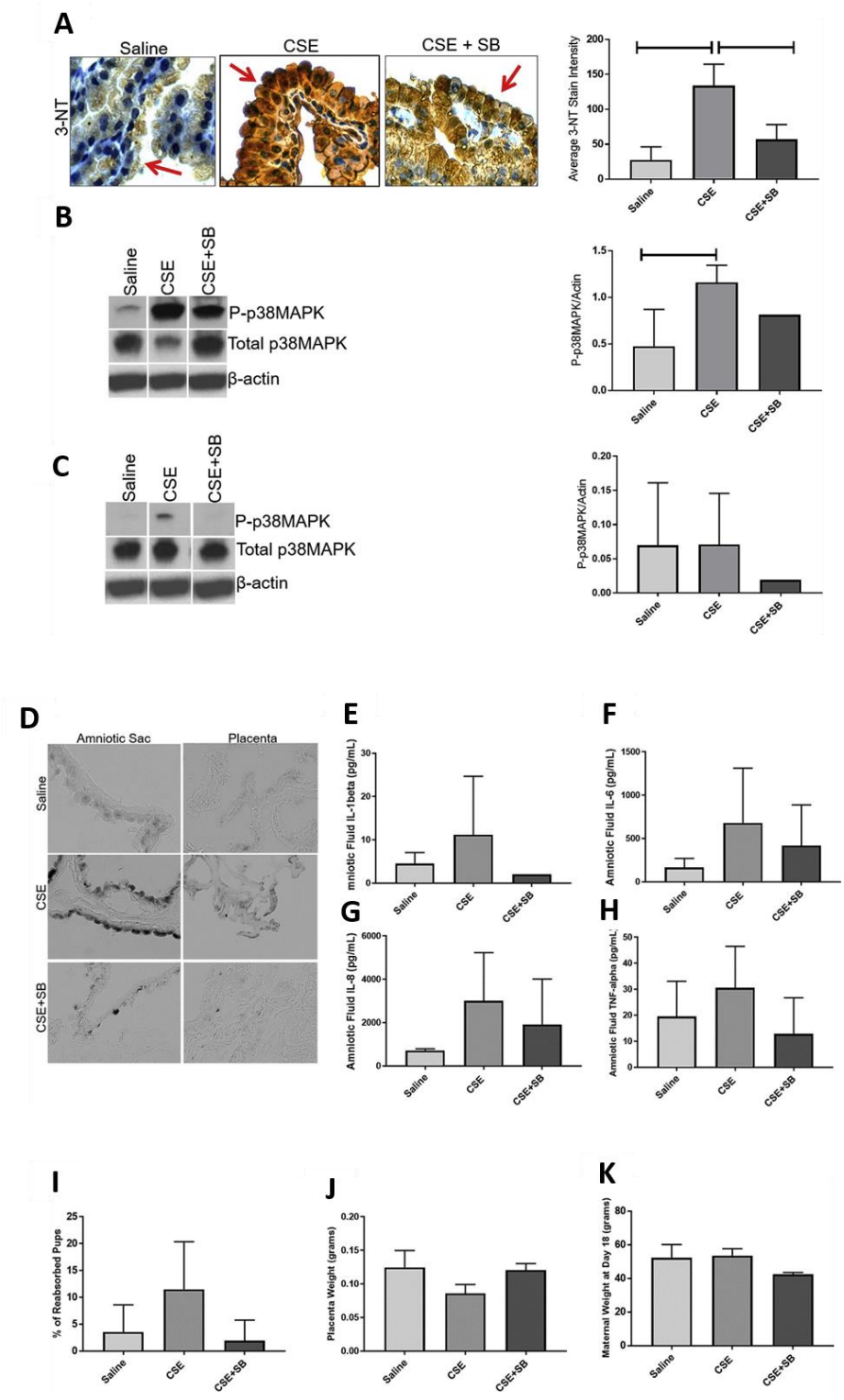

Sup. Fig. 6.2 OS-induced changes in a mice model.

A) CSE injections induced 3-NT in the amniotic sac (P<.0001) (brown Stain) compared to controls, which was reduced by SB, an inhibitor of p38 MAPK (P<.0007) compared to controls. Images were taken at a 40x magnification. CSE injections led to the

phosphorylation and activation of p38 MAPK (P=.0455) in the amniotic sac (B) and placenta (C) compared to controls. SB reduced p38 MAPK activation compared to CSE alone. D) CSE injections induced SA-β-Gal in the amniotic sac and placenta (dark grey). This was prevented by the inhibition of p38 MAPK with SB. Images were taken at a 40x magnification. Amniotic fluid from CSE injected CD-1 mice showed an increasing trend of inflammatory markers IL-1β (E), IL-6 (F), IL-8 (G), and TNF-a (H) Increase in cytokine response was minimized by co-treatment with SB. I) CSE induced pup reabsorption or loss was higher than saline-injected mice. SB, a p38 MAPK inhibitor, prevented pup loss compared to CSE alone. J) CSE injections decreased placental weight compared to saline. Co-treatment with CSE+SB prevented this decrease in weight. K) Co-treatment with CSE+SB decreased maternal weight, which was reversed with CSE.

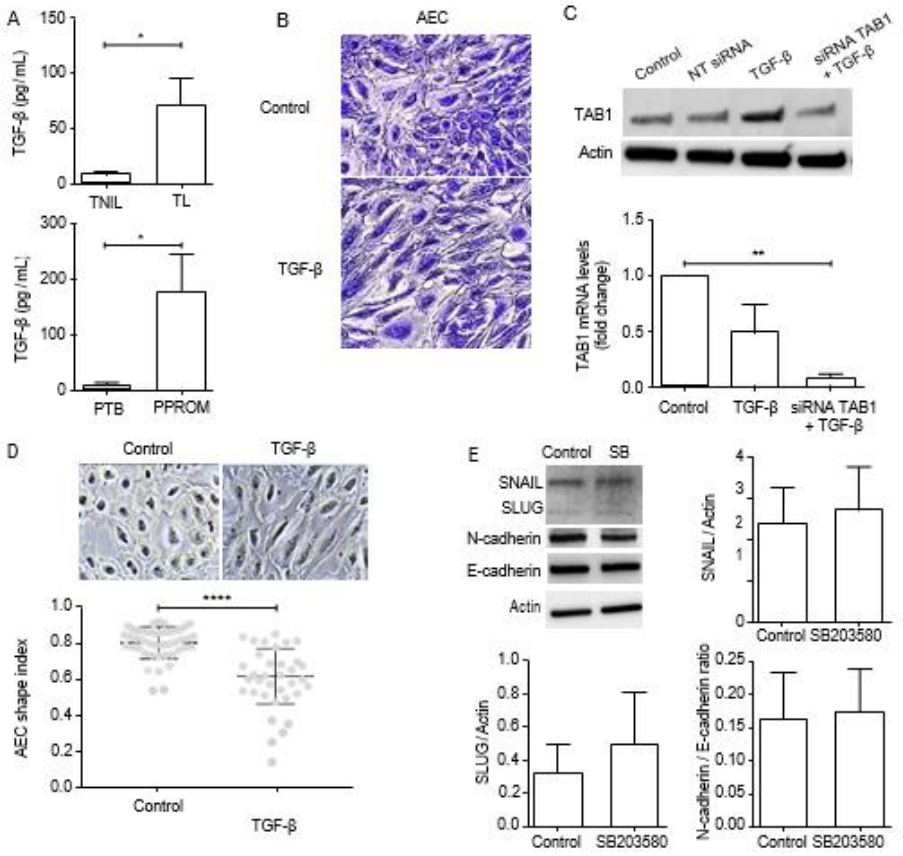

Sup. Fig. 6.3 TGF-β associated changes in AECs

A) ELISA measured AF concentrations of TGF-β. TL samples contained significantly higher amounts of TGF-β (72.6±22.7 ng/mL) compared to TNIL samples (8.8±1.8 ng/mL (N=6, P=0.018). Correspondingly, pPROM samples also contained significantly higher amounts of TGF-β (173.7±69 ng/mL) compared to PTB without rupture (8.4±2.6 ng/mL) (P=0.037) (N=6). This figure shows one representative image from six separate samples. Error bars represent Mean±SEM. B) Bright field microscopy shows AECs taking up crystal violet stain under control and TGF-β treatment documenting their viability. TGF-β treatment induced an elongated mesenchymal morphology after six days in culture (N=3). (10x). This figure shows one representative image from three separate experiments. C) Western blot analysis of AECs treated with TGF-β increased TAB1 protein while co-treatment of siRNA TAB1 with TGF-β decreased protein expression. qRT-PCR analysis additionally documented a significant decrease in TAB1 gene expression compared to controls (P=0.007) (N=3). This figure shows one representative image from three separate experiments. Error bars represent Mean±SEM. D) Bright field analysis shows AECs treated with TGF-β have a significantly lower shape index than untreated cells (P<0.0001). (20x). This figure shows one representative image from three separate experiments. Error bars represent Mean±SEM. E) Western blot analysis of AECs treated with p38 MAPK functional inhibitor SB. SB did not induce protein level changes compared to controls (N=3). This figure shows one representative image from three separate experiments. Error bars represent Mean±SEM.

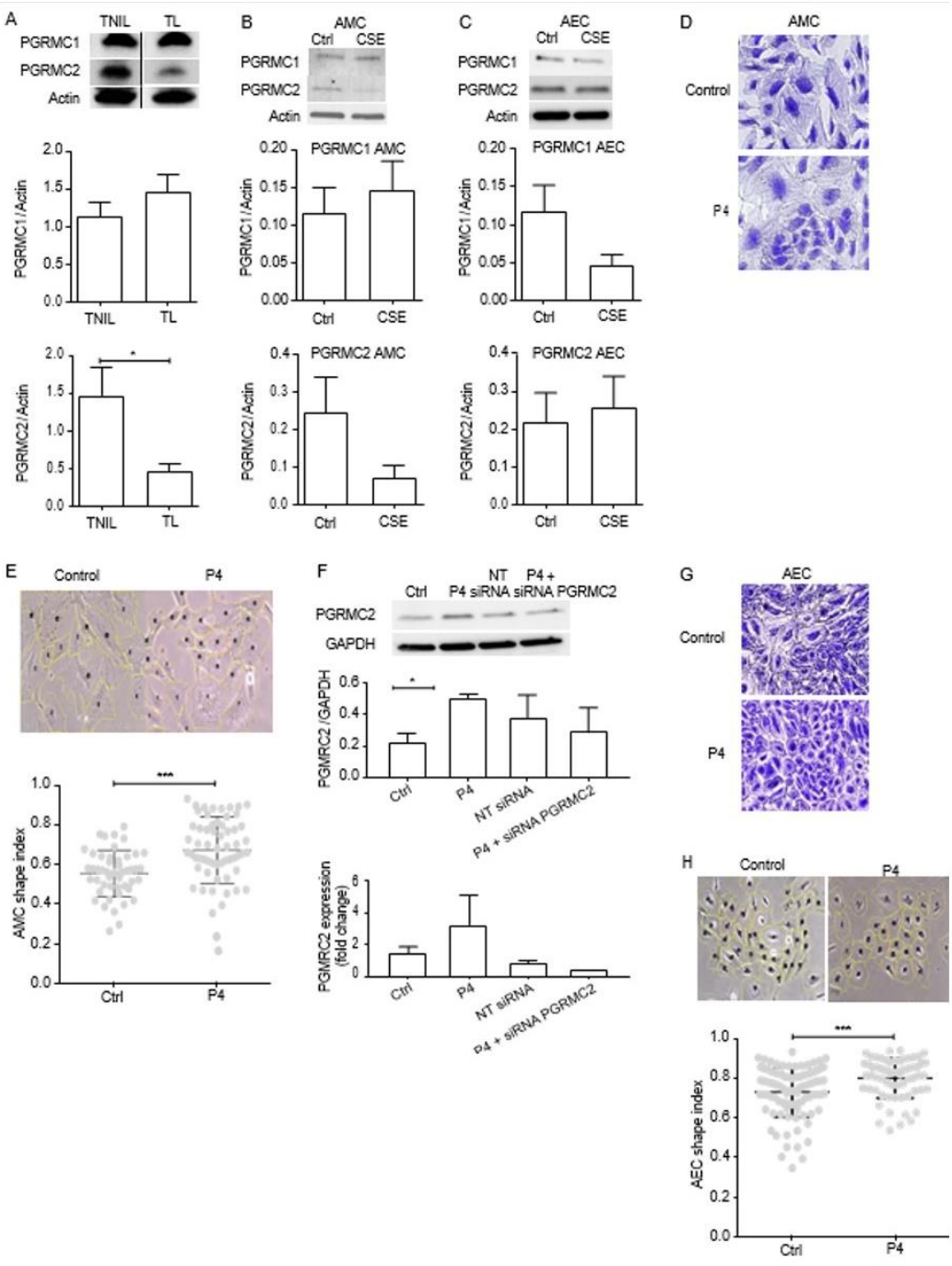

Sup. Fig. 6.4 P4 and P4 receptor associated changes in AMCs and AECs

A) Western blot analysis of TL fetal membranes contained significantly less PGRMC2 (P=0.03) compared to TNIL controls (N=5). PGRMC1 protein levels did not differ between the two groups. This figure shows one representative image from five separate experiments. Error bars represent Mean±SEM. B) Western blot analysis of AMCs treated with OS inducer CSE contained 3-fold less PGRMC2 (P=0.059) compared to control treated cells (N=8). PGRMC1 protein levels did not differ between the two groups. This figure shows one representative image from eight separate experiments. Error bars

represent Mean±SEM. C) Western blot analysis of AECs treated with OS inducer CSE does not change PGRMC2 but induces over 2-fold downregulation of PGRMC1 compared to control treated cells (P=0.054) (N=4). This figure shows one representative image from eight separate experiments. Error bars represent Mean±SEM. D) Bright field microscopy shows AMCs taking up crystal violet stain under control and P4 treatment documenting their viability. P4 treatment induced an epithelial phenotype after six days in culture (N=3). (10x). This figure shows one representative image from three separate experiments. E) Bright field microscopy and analysis of cell shape show that AMCs treated with P4 have a significantly rounder (higher) shape index than untreated cells (P=0.0001) (N=3). (20x). This figure shows one representative image from three separate experiments. F) Western blot analysis of AMCs treated with P4 increased PGRMC2 protein (P=0.017) while co-treatment of siRNA PGRMC2 with P4 decreased protein expression (N=3). qRT-PCR analysis additionally documented a decrease in PGRMC2 gene expression compared to controls and P4 (N=3). This figure shows one representative image from four separate experiments. Error bars represent Mean±SEM. G) Bright field microscopy shows AECs taking up crystal violet stain under control and P4 treatment documenting their viability. P4 treatment induced an epithelial phenotype after six days in culture (N=3). (10x). This figure shows one representative image from three separate experiments. H) Bright field and cell shape analysis shows AECs treated with P4 have a significantly rounder (higher) shape index than untreated cells (P=0.0002) (N=3). (20x). This figure shows one representative image from three separate experiments.

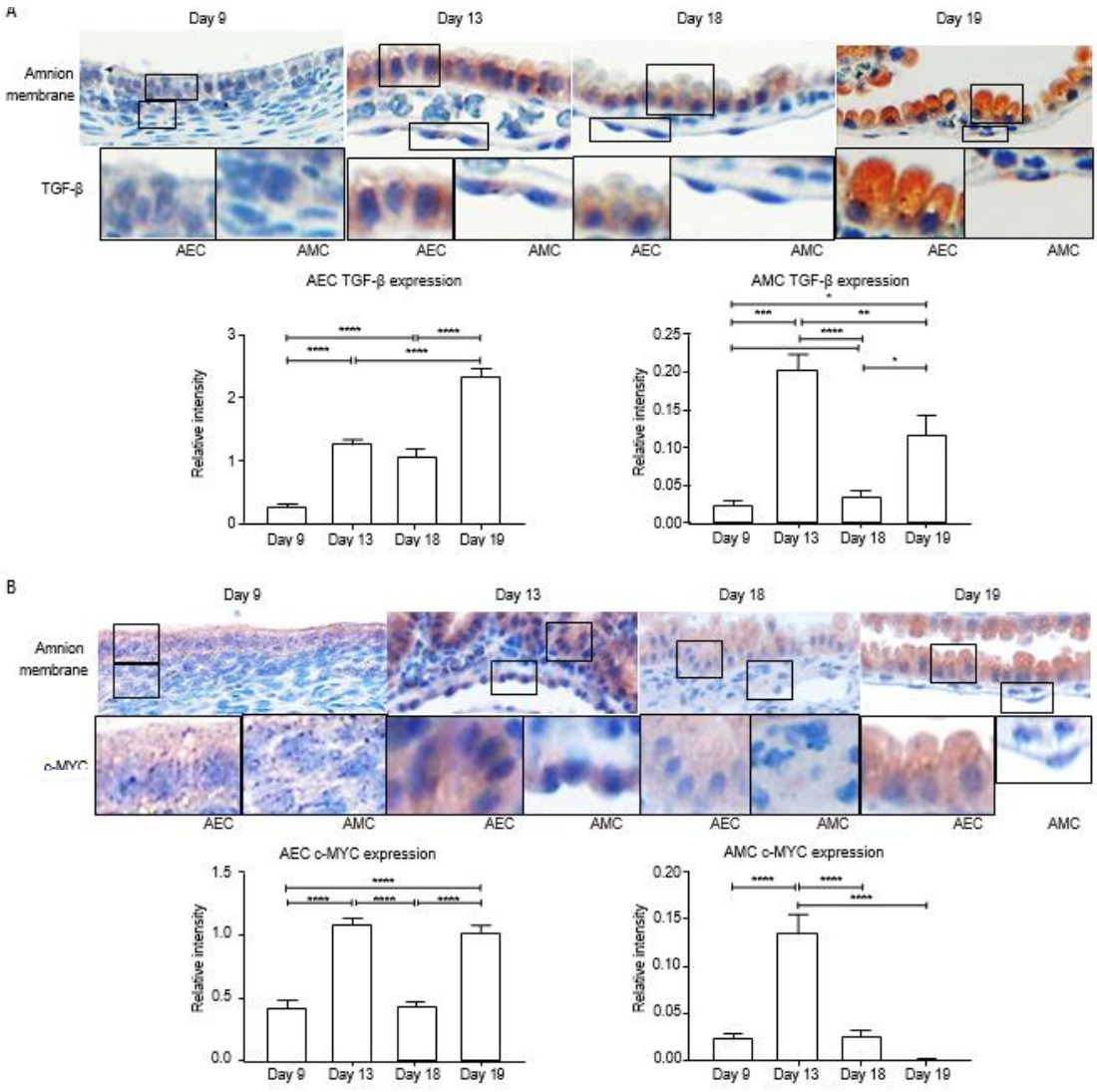

Sup. Fig. 6.5 Fetal membrane TGF-β and c-MYC expression throughout gestation in mice

A) IHC staining shows an increase in TGF-β expression (brown stain) in mice amnion epithelial and mesenchymal cells throughout gestation (N=3) (40x). This figure shows one representative image from four separate experiments. Error bars represent Mean±SEM. B) IHC staining shows an increase in epithelial transcription factor c-MYC expression (brown stain) in AEC throughout gestation while AMC expression of c-MYC (brown stain) decreases after Day 13 (N=3) (40x). Suggesting, a differential role for c-MYC in amnion cells at term. This figure shows one representative image from four separate experiments. Error bars represent Mean±SEM.

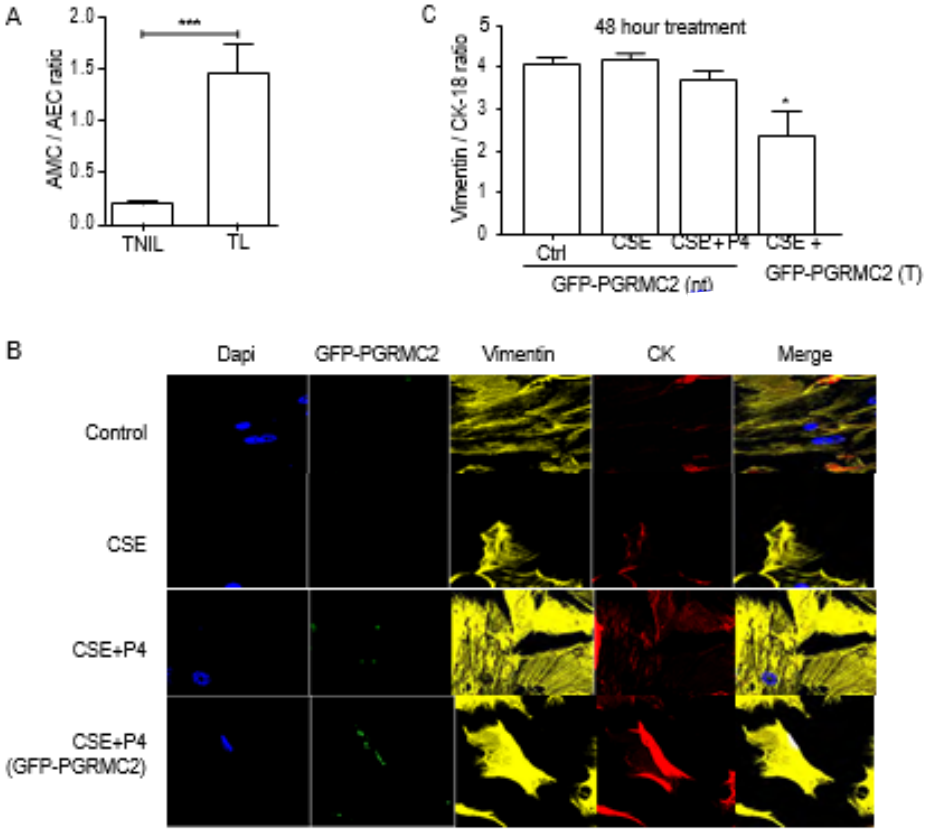

Sup. Fig. 6.6 AMC qualities and characteristics at term

A) AEC and AMCs from 0.0006m^2 in of TNIL and TL fetal membranes were quantitated using two separate approaches. Analysis shows that AMC quantity increased at TL compared to TNIL samples (P=0.0002). A-B) Florescent images showed baseline expression of CK-18 and vimentin in AMCs. AMCs treated with transfection controls maintained baseline expression of vimentin/CK-18 ratios even in the presence of CSE+P4. AMCs transfected with GFP-PGRMC2 and treated with CSE+P4 showed a significant decreased vimentin/CK-18 ratio (P=0.0005). Images were captured at 40x. Blue-DAPI, green-GFP-PRGMC2, red-CK-18, and yellow-vimentin. This figure shows one representative image from three separate experiments. Error bars represent Mean±SEM.

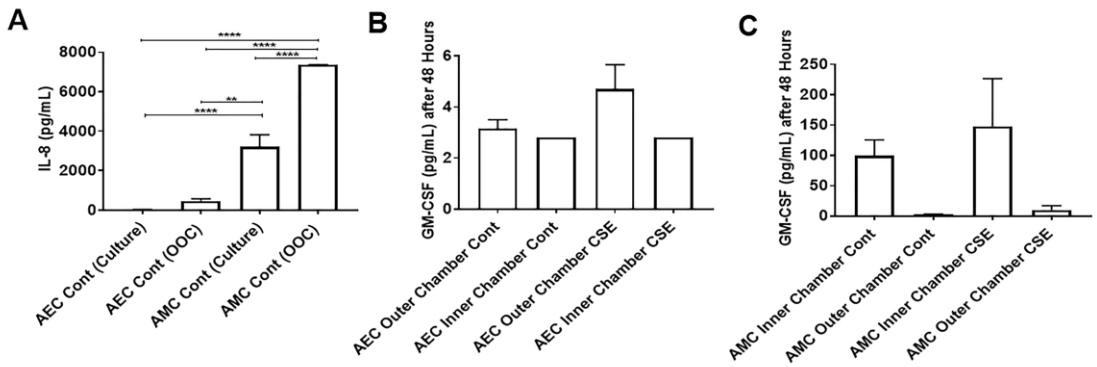

Sup. Fig. 8.1 Production and propagation of proinflammatory mediators in the AM-OOC monoculture system

OS-induced proinflammatory mediator production in AECs and AMCs in single cell culture and did not induce propagation of inflammatory mediators. A) ELISA-measured medium concentrations of IL-8 from the AEC and AMC 2D culture vs. AM-OOC culture. Culturing AECs and AMCs in the AM-OOC innately induced more IL-8 than 2D cultures (N=3). ****P<0.0001. ** P=0.001. B) AECs naturally express very low levels of GM-CSF in the AM-OOC devices (Control: 3.2±0.35ng/mL; CSE: 4.6±0.9ng/mL; N=3) and do not propagate GM-CSF into the inner chamber even after 48 hours. Values are expressed as mean intensity±SEM. C) CSE treatment of AMCs induced GM-CSF production (Control: 99±26ng/mL; CSE: 148±78ng/mL; N=3) compared to controls, but without propagating GM-CSF into the outer chamber even after 48 hours. Values are expressed as mean intensity±SEM.

Vita

NAME: Lauren Richardson

PRESENT POSITION AND ADDRESS:

Predoctoral Research Fellow
University of Texas Medical Branch at Galveston
Department of Cell Biology and Anatomy
Medical Research Building 11.154
301 University Blvd.
Galveston, TX 77555
Email: Lestaffo@utmb.edu
https://www.utmb.edu/obgyn/Research/MenonLab.asp

BIOGRAPHICAL:

Date of Birth:	05/12/1993
Birthplace:	Beaumont, Tx
Citizenship:	USA
Languages:	English

EDUCATION:

08/2016 to present **Predoctoral Research Fellow**
Graduate School of Biomedical Sciences
Department of Cell Biology and Anatomy
The University of Texas Medical Branch, Galveston, TX

08/2011-05/2015 **Bachelor's of Arts and Science in Biology**
Department of Biology
Lamar University, Beaumont, TX

PROFESSIONAL AND TEACHING EXPERIENCE:

Professional Experience:

10/2015 to present **Predoctoral Research Fellow**, Department of Cell Biology,
University of Texas Medical Branch, Galveston, TX
Mentor: Ramkumar Menon
Project: Epithelial to mesenchymal transitions, Cell transitions, Fetal membrane remodeling, cell signaling of p38 MAPK, Senescence, Organ-on-chip

10/2017 to present	**NIEHS Pre-doctoral Fellow in the Environmental Toxicology Training Program (T32)**, University of Texas Medical Branch, Galveston, TX Mentor: Ramkumar Menon Project: Fetal membrane remodeling, dioxin and cigarette smoke extract induced signaling
07/2017-08/2017	**Research Internship**, Department of Infectious Disease, Vanderbilt University, Nashville, Tennessee Mentor: Dr. David Aronoff and Dr. Kevin Osteen Project: Construction of two chamber organ-on-chip devices to recreate fetal membranes. Study cellular signaling directionality between fetal and maternal compartments due to oxidative stress or toxins and their ability to induce senescence.
01/2014-06/2015	**Undergraduate McNair Scholar,** Undergraduate Research, Lamar University, TX Mentor: Dr. Ian Lian Project: Effects of Substrate Rigidity on Cancer Cell Morphology and Metastasis
06/2013-07/2013	**Summer Undergraduate Research Program,** The University of Texas Medical Branch, TX Mentor: Dr. Yong Sun Lee Project: I studied ovarian and gastric cancer and nc886 role as a tumor suppressor

Teaching Experience:

01/2015-05/2015	Lab Instructor for Anatomy & Physiology 2, Department of Biology, Lamar University, TX Mentor: Amanda Posey Project: Taught lab three times a week, developed quizzes and tests, reported final grades
08/2014-12/2014	Lab Instructor for Anatomy & Physiology 1, Department of Biology, Lamar University, TX Mentor: Amanda Posey Project: Taught lab three times a week, developed quizzes and tests, reported final grades

Training and Supervision of Undergraduate, Graduate and Medical Students

012/2015-12/2016	Luke Dixion, Maternal-Fetal Medicine Fellow
01/2016-02/2016	Emily Hadley, Maternal-Fetal Medicine Fellow
06/2016-09/2016	Caroline Marrs, Maternal-Fetal Medicine Fellow

06/2016-07/2016	Martina Ayad, Maternal-Fetal Medicine Fellow
12/2016-12/2017	Jin Jin, Visiting OBGYN from China
12/2016-09/2017	Laura Martin, Visiting Graduate Student from Brazil
06/2017-07/2017	Poorna Menon, High school Student
06/2018-07/2018	Poorna Menon, High school Student
12/2018-02/2019	Violetta Lozovyy, Maternal-Fetal Medicine Fellow
12/2019 to present	Chasey Omere, Maternal-Fetal Medicine Fellow

GRANT SUPPORT:

10/2017 to present	Environmental Toxicology T32 Predoctoral Grant

MEMBERSHIPS IN SCIENTIFIC SOCIETIES:

National:

12/2013 to present	Student Member, Sigma Xi
08/2015 to present	Student Member, Society for Cell Biology
02/2016 to present	Student Member, Graduate Student Organization

HONORS AND AWARDS

12/2018	University Federal Credit Union – GSBS scholarship, UTMB, TX
07/2018	Guest lecturer award, Committee in support of science education, UTMB
06/2018	Elias Hochman Research Award, UTMB, TX
05/2018	Cell Biology outstanding service award, 1st place
05/2018	1st Poster Award in Basic Biology, CIRWH, 2018
03/2018	Society of Reproductive Investigation Poster Award
05/2017	Cell Biology outstanding service award, 2nd place
12/2017	1st place Oral presentation award, Neuro and Cell Biology Dep. Retreat
11/2017	NIEHS Pre-doctoral Fellow in the Environmental Toxicology Training
04/2016	Texas Forum for Reproductive Sciences poster award
08/2015	McNair Scholarship, Lamar University, TX
05/2014	John Ohmstede Biology Scholarship, Lamar University, TX
07/2013	Best Poster in Biochemistry and Molecular Biology, UTMB

COMMUNITY SERVICE AND ACTIVITIES:

12/2018 to present	Teach a fetal development class, Pregnancy Center, Galveston, TX
03/2018 to present	Organizing committee in the Fetal Membrane Club

10/2018-12/2018	Planning committee, Preterm Birth International Collaborative International conference North America Branch, Galveston, TX
07/2017 to present	Current Graduate School of Biomedical Sciences Cell Biology Representative The University of Texas Medical Branch, TX
05/2017 to present	Department of Cell Biology Curriculum Committee Student Representative The University of Texas Medical Branch, TX
01/2017-05/2017	Planning committee, Preterm Birth International Collaborative International conference, Galveston, TX
04/2017	Oral Session Moderator, TFRS Conference, Baylor University Medical Branch, Houston, TX
01/2017-05/2017	Planning committee, Cell Biology Departmental Symposium, The University of Texas Medical Branch, TX
01/2016-05/2016	Planning committee, Cell Biology Departmental Symposium, The University of Texas Medical Branch, TX

BIBLIOGRAPHY:

Poster Presentations:

1. L. Richardson, R. Menon, Transitioning Amnion Mesenchymal Cells Maintain Fetal Membrane Integrity. Society of Reproductive Investigation, International meeting, 2019
2. P. Menon, L. Richardson, R. Menon, The Effects of Extra Cellular Matrix Collagen Rigidity on 3-Dimensional Cultures of Fetal Membrane Cells, Society of Reproductive Investigation, International meeting, 2019
3. Ramkumar Menon, Palle Schelde, Rheanna Urrabaz-Garza, Enkhtuya Radnaa, Lauren Richardson, Katarina Ravn, Inga Baasch Christensen, Lotte Hatt, Ida Vogel, Niels Uldbjerg, Ripudaman Singh, Detection of Circulating Amniochorion (Fetal Membrane) Cells in Maternal Blood Samples Society of Reproductive Investigation, International meeting, 2019
4. L. Richardson, R. Menon. Progesterone accelerates wound healing in human amniotic epithelial cells through mesenchymal to epithelial transition. Society of Reproductive Investigation, International meeting, 2019
5. L. Richardson, R. Menon. Progesterone accelerates wound healing in human amniotic epithelial cells through mesenchymal to epithelial transition. SMFM, 2019
6. L. Richardson, J. Gnecco, T. Ding, K. Osteen, D. Aronoff, R. Menon. Fetal membrane organ on chip. SMFM, 2019
7. V. Lozovyy, L. Richardson, R. Menon, Screening for labor induced functional progesterone withdraw in fetal membranes, SMFM, 2019

8. M. Kuhlmann-Capek, T. Kechichian, L. Richardson, H. Yin, G. Saade, E. Bytautiene-Prewit. Effects of lactation on susceptibility to opioid dependence in the chemically-naive subject. SMFM, 2019
9. L. Richardson, J. Gnecco, T. Ding, K. Osteen, D. Aronoff, R. Menon. Fetal membrane organ on chip: An innovative approach to study feto-maternal cellular interactions. Lone Star Society of Toxicology Conference, 2018
10. L. Richardson, J. Trived,i, R. N. Taylor; J. Yu, R. Menon. Epithelial to Mesenchymal Transition (EMT) in Amnion Epithelium: A mechanism Associated with Parturition? UTMB, CIRWH, 2018
11. L. Richardson, J. Gnecco, T. Ding, K. Osteen, D. Aronoff, R. Menon. Fetal membrane organ on chip: An innovative approach to study feto-maternal cellular interactions. UTMB, CIRWH, 2018
12. L. Richardson, J. Gnecco, T. Ding, K. Osteen, D. Aronoff, R. Menon. Fetal membrane organ on chip: An innovative approach to study feto-maternal cellular interactions. Society of Reproductive Investigation, International meeting, 2018
13. L. Richardson, R. Menon. Progesterone-Driven Mesenchymal to Epithelial Transition (MET): A Mechanism Maintaining Fetal Membrane Integrity. Society of Reproductive Investigation, International meeting, 2018
14. L. Richardson, R. Menon. TGF-β induces Epithelial to Mesenchymal Transitions in Amnion Cells in a TAB1-p38 MAPK Dependent Manor. Society of Reproductive Investigation, International meeting, 2018
15. L. Richardson, J. Trived,i, R. N. Taylor; J. Yu, R. Menon. Epithelial to Mesenchymal Transition (EMT) in Amnion Epithelium: A mechanism Associated with Parturition? Society of Reproductive Investigation, International meeting, 2018
16. L. Martin, L. Richardson, P. Menon, S. Sheller-Miller, R. Menon. Dexamethasone induces amnion cell senescence through p38 MAPK independent but telomere - p21 dependent pathway, Society of Reproductive Investigation, International meeting, 2018
17. S. Sheller-Miller, L. Richardson, L. Martin, J. Jin, R. Menon. Systematic review of p38 MAPK in Reproductive Tissues. Society of Reproductive Investigation, International meeting, 2018
18. J. Jin, L. Richardson, S. Sheller-Miller, N. Zhong, R. Menon. Oxidative stress induces p38 MAPK depended senescence in feto-maternal interface. Society of Reproductive Investigation, International meeting, 2018
19. L. Richardson, R. Menon Elizabeth A Bonney MD MPH. Expression of Phospho-GSK3Beta correlates with p38 MAPK Activation in Human and Mouse Gestation, Ageing conference, UTMB, 2017
20. L. Richardson, L. Dixon, G. Saade, R. Menon. Oxidative Stress Induced p38 MAPK activation in Human Amnion Epithelial Cells are Independent of ASK1-Signalosome. Texas Forum of Reproductive Scientists, 2017
21. L. Richardson, G. Vargas, J. Trivedi, R. Menon. Characterization of Fetal Membrane Microfractures in and Their Potential Significance in Pregnancy and Parturition. South Regional American Physician Scientists Association, 2017
22. Emily E. Hadley, L. Richardson, Maria R. Torloni, Ramkumar Menon. Gestational tissue inflammatory biomarkers at term labor: a systematic review of literature. Society of Reproductive Investigation, International meeting, 2017

23. L. Richardson, G. Vargas, J. Trivedi, R. Menon. Characterization of Fetal Membrane Microfractures in and Their Potential Significance in Pregnancy and Parturition. Society of Reproductive Investigation, International meeting, 2017
24. L. Richardson, R. Menon Elizabeth A Bonney MD MPH. Expression of Phospho-GSK3Beta correlates with p38 MAPK Activation in Human and Mouse Gestation, Society of Reproductive Investigation, International meeting, 2017
25. L. Richardson, G. Vargas, PhD, G. Saade, MD, T. Brown, S. Sheller, J. Trivedi, MS and R. Menon, PhD. Discovery of Microfractures in Fetal Membranes: A Potential Site of Epithelial-Mesenchymal Transition, Texas Forum of Reproductive Scientists, 2016
26. L. Richardson, L. Dixon, R. Menon, G. Sadde. Role of Oxidative Stress Induced ASK1-Signalosome in Amnion Epithelial Cell Senescence ageing phenotype. UTMB Ageing conference, 2016
27. L. Richardson, G. Vargas, PhD, G. Saade, MD, T. Brown, S. Sheller, J. Trivedi, MS and R. Menon, PhD. Discovery of Microfractures in Fetal Membranes: A Potential Site of Epithelial-Mesenchymal Transition, Center for Interdisciplinary Research in Women's Health, 2016
28. L. Richardson, G. Vargas, PhD, G. Saade, MD, T. Brown, S. Sheller, J. Trivedi, MS and R. Menon, PhD. Discovery of Microfractures in Fetal Membranes: A Potential Site of Epithelial-Mesenchymal Transition, Society of Reproductive Investigation, late breaking abstract, 2016
29. Maritza Agular, Gabriel Graham, Nicolas Nikoloutsos, L. Richardson, Hiep-Hury Jamie, Ian Lian. Formation of Physiologically Realistic Cancer Cell Spheroids with Soft Substrate Microenvironment. Poster on the Hill, Washington DC, 2015
30. E. Gutierrez, E. Tkachenko, M. Lopez Ramirez, G.K. Vertelov, L. Stafford, I. Lian, A. Groisman; (2014). Elastic silicone gel substrates control brain endothelial cell explants, and promote rapid cancer cell spheroid formation. Mol. Biol. Cell 25, Abstract P1402.
31. Maritza Agular, Gabriel Graham, Nicolas Nikoloutsos, L. Richardson, Hiep-Hury Jamie, Ian Lian. Formation of in vivo-like Cervical and Breast Cancer Cell Spheroids with Soft Substrate Microenvironments. STEM Conference, Lamar University, 2014
32. L. Richardson, Kwang Soo Lee, Betty H. Johnson, Yong Sun Lee. Nc886 is a Tumor Senor and Gene Regulator of Oncogenesis in Ovarian and Gastric Cancers, Summer Undergraduate Research Poster Presentation, UTMB, 2013

Oral presentations:

1. L. Richardson, Sung Jin Kim, Arum Han, Ramkumar Menon, Amnion Membrane-Organ-On-Chip: An Innovative Approach to Study Cellular Interactions, Society of Reproductive Investigation, International meeting, 2019
2. L. Martin, L. Richardson, R. Menon. Characteristics, properties, and functionality of fetal membranes: The latest findings. 5th international conference on advances in skin, wound care, and tissue, Rome, Italy, October 2018
3. L. Richardson, L. Martin, P. Menon, S. Sheller-Miller, R. Menon. Dexamethasone induces amnion cell senescence through p38 MAPK independent but telomere - p21 dependent pathway, Cell Biology Symposium, UTMB, 2018
4. L. Richardson, R. Menon, PhD. Proliferative and Migratory Properties Reveals Metastate of Amnion Cells Mediated by Epithelial to Mesenchymal and

Mesenchymal to Epithelial Transitions. Texas Forum of Reproductive Scientists, International meeting, 2018

5. L. Richardson, R. Menon, PhD. Proliferative and Migratory Properties Reveals Metastate of Amnion Cells Mediated by Epithelial to Mesenchymal and Mesenchymal to Epithelial Transitions. Society of Reproductive Investigation, International meeting, 2018
6. L. Richardson, R. Menon, PhD. Amnion Epithelial Cells' Role in Wound Healing During Pregnancy and Delivery. NCBA Retreat, Dec. 2017
7. L. Richardson, R. Menon, PhD. Fetal Membrane Integrity is Maintained by Regulators of EMT-MET During Human Gestation. Seminar, 2017
8. L. Richardson, C.L. Dixon, R. Menon . Oxidative Stress Induced p38 MAPK activation in Human Amnion Epithelial Cells are Independent of ASK1-Signalosome. Society of Reproductive Investigation, International meeting, 2017
9. L. Richardson, C.L. Dixon, R. Menon . Oxidative Stress Induced p38 MAPK activation in Human Amnion Epithelial Cells are Independent of ASK1-Signalosome. Neurobiology and Cell Biology Departmental Retreat, 2017
10. L. Richardson, J. Trivedi, MS, G. Saade, MD, S. Sheller, and R. Menon, PhD. Epithelial to Mesenchymal Transition in Placental Membranes: A mechanism associated with parturition? Cell Biology Departmental Symposium, 2017
11. L. Richardson, G. Vargas, PhD, G. Saade, MD, T. Brown, S. Sheller, J. Trivedi, MS and R. Menon, PhD. Discovery of Microfractures in Fetal Membranes: A Potential Site of Epithelial-Mesenchymal Transition, Cell Biology Departmental Symposium, 2016
12. Lauren Richardson, Gabriel Graham, Nicolas Nikoloutsos, Ian Lian. Effects of Substrate Rigidity on Cancer Cell Morphology and Metastasis. McNair Symposium, Lamar University, 2014

Publications:

1. **L. Richardson,** Sehoon Jeong, Sungjin Kim, Arum Han, Ramkumar Menon. Amnion Membrane Organ-On-Chip: An innovative approach to study cellular interactions, *FASEB*, 2019
2. L. Martin, **L. Richardson,** S. Sheller-Miller, R. Menon. Dexamethasone induces amnion cell senescence through p38 MAPK independent but telomere - p21 dependent pathway, *Biology of Reproduction, 2018*
3. **L. Richardson**, J. Gnecco, T. Ding, K. Osteen, D. Aronoff, R. Menon. Fetal membrane organ on chip: An innovative approach to study feto-maternal cellular interactions. *Reproductive* Sciences, *Nov. 2018*
4. R. Menon, **L. Richardson**, M. Lappas. Fetal Membrane Architecture, Aging and Inflammation in Pregnancy and Parturition. *Placenta, Nov. 2018*
5. N. Lavu; **L. Richardson**; E. Bonney; R. Menon. Glycogen synthase kinase (GSK) 3 in pregnancy and parturition: a systematic review of literature. J Matern Fetal Neonatal Med, October, 2018, (In press), PMID: 30278798
6. **L. Richardson**; S. Sheller-Miller; L. Martin; J. Jin; R. Menon. Systematic review of p38 mitogen-activated kinase and its functional role in reproductive tissues. American Journal of Reproductive Immunology, August, 2018, (In press), PMID: 30178469
7. **L. Richardson;** Christopher Dixon; Leopoldo Aguilera-Aguirre; R. Menon.

Oxidative Stress-Induced TGF-beta/TAB1-mediated p38 MAPK Activation in Human Amnion Epithelial Cells. Biology of Reproduction, June, 2018, PMID:29893818

8. **L. Richardson** and R. Menon. Proliferative, Migratory, and Transition Properties Reveals Metastate of Human Amnion Cells. American Journal of Pathology, June, 2018, 188(9):2004-2015, PMID: 29981743
9. J. Jin; **L. Richardson;** S. Sheller-Miller; N. Zhong; R. Menon. Oxidative stress induces p38 MAPK-dependent senescence in the feto-maternal interface cells. Placenta, May, 2018, 67:15-23, PMID: 29941169
10. **L. Richardson**; L. Martin. Characteristics, Properties, and Functionality of Fetal Membranes: an Overlooked Area in the Field of Parturition. *Encyclopedia of Reproduction 2nd Edition,* February, 2018 , 3:387-398
11. J. Polettini; **L. Richardson;** R. Menon. Oxidative stress induces senescence and sterile inflammation in murine amniotic cavity. Placenta, January, 2018, 63:26-31, PMID: 29486853
12. Christopher Dixon; **Lauren Richardson**; Samantha Sheller-miller; George Saade; Ramkumar Menon. Distinct mechanisms of senescence activation in amnion by infection, inflammation and oxidative stress. American Journal of Reproductive Immunology, December, 2017, 79(3), PMID: 29193446
13. **Lauren Richardson;** Gracie Vargas, Ph.D; Tyra Brown; Lorenzo Ochoa; Samantha Sheller-Miller, George R Saade, MD; Robert N Taylor, MD, Ph.D.; Ramkumar Menon, Ph.D. Discovery and Characterization of Human Amniochorionic Membrane Microfractures, AJP, December, 2017, 187(12):2821-2830, PMID: 28939208
14. Ramkumar Menon and **Lauren Richardson**. Preterm Premature Rupture of the Membranes: A Disease of the Fetal Membranes, Seminar Perinatology, November, 2017, 41(7):409-419, PMID: 28807394
15. Emily Hadly; **Lauren Richardson**; Ramkumar Menon. Gestational Tissue Inflammatory Biomarkers at Term Labor: A Systematic Review of Literature. American Journal of Reproductive Immunology, October, 2017, 79(2), PMID: 2907619
16. **Lauren Richardson,** Gracie Vargas , Tyra Brown, Lorenzo Ochoa, Jayshil Trivedi, Marian Kacerovský, Martha Lappas, Ramkumar Menon . Redefining 3Dimensional placental membrane microarchitecture using multiphoton microscopy and optical clearing, Richardson et. al, Placenta, May, 2017, 53:66-75, PMID: 28487023
17. Samantha Sheller, John Papaconstantinou, Rheanna Urrabaz-Garza, **Lauren Richardson**, George Saade, Carlos Salomon, Ramkumar Menon. Amnion-Epithelial-Cell-Derived Exosomes Demonstrate Physiologic State of Cell under Oxidative Stress, Plos 1, 2016, 11(6):e0157614, PMID: 27333275
18. Kwang-Soo Lee, Jong-Lyul Park, Kwanbok Lee, **Lauren E. Richardson**, Betty H. Johnson, Hyun-Sung Lee, Ju-Seog Lee, Sang-Bae Kim, Oh-Hyung Kwon, Kyu Sang Song, Yong Sung Kim, Hassan Ashktorab, Duane T. Smoot, Sung Ho Jeon, Seon-Young Kim and Yong Sun Lee. Nc886, a non-coding RNA of anti-proliferative role, is suppressed by CpG DNA methylation in human gastric cancer, Oncotarget, 2014, 5(11):3944-55, PMID: 25003254

Permanent address: 1590 West Lucas Drive, Beaumont, Tx, 77706

This dissertation was typed by Lauren Stafford Richardson

References

[1] A.J. Watson, The cell biology of blastocyst development, Mol Reprod Dev 33(4) (1992) 492-504.
[2] R. Menon, E.A. Bonney, J. Condon, S. Mesiano, R.N. Taylor, Novel concepts on pregnancy clocks and alarms: redundancy and synergy in human parturition, Hum Reprod Update 22(5) (2016) 535-60.
[3] J.A. Majzoub, J.A. McGregor, C.J. Lockwood, R. Smith, M.S. Taggart, J. Schulkin, A central theory of preterm and term labor: putative role for corticotropin-releasing hormone, Am J Obstet Gynecol 180(1 Pt 3) (1999) S232-41.
[4] R. Menon, I. Boldogh, H.K. Hawkins, M. Woodson, J. Polettini, T.A. Syed, S.J. Fortunato, G.R. Saade, J. Papaconstantinou, R.N. Taylor, Histological evidence of oxidative stress and premature senescence in preterm premature rupture of the human fetal membranes recapitulated in vitro, American Journal of Pathology 184(6) (2014) 1740-51.
[5] B.M. Mercer, D.T. Crouse, R.L. Goldenberg, M. Miodovnik, D.C. Mapp, P.J. Meis, M.P. Dombrowski, The antibiotic treatment of PPROM study: systemic maternal and fetal markers and perinatal outcomes, Am J Obstet Gynecol 206(2) (2012) 145.e1-9.
[6] H. Blencowe, S. Cousens, D. Chou, M. Oestergaard, L. Say, A.B. Moller, M. Kinney, J. Lawn, Born too soon: the global epidemiology of 15 million preterm births, Reprod Health 10 Suppl 1 (2013) S2.
[7] March of Dimes Perinatal Data Center, 2016. http://www.myendnoteweb.com/EndNoteWeb.html?func=downloadInstallers&cat=download&.
[8] S.K. Kota, K. Gayatri, S. Jammula, S.V. Krishna, L.K. Meher, K.D. Modi, Endocrinology of parturition, Indian J Endocrinol Metab 17(1) (2013) 50-9.
[9] E. Joyce, P. Diaz, S. Tamarkin, R. Moore, A. Strohl, B. Stetzer, D. Kumar, M. Sacks, J. Moore, In-vivo Stretch of Term Human Fetal Membranes, Placenta 38 (2016) 57-66.
[10] L. Myatt, K. Sun, Role of fetal membranes in signaling of fetal maturation and parturition, Int J Dev Biol 54(2-3) (2010) 545-53.
[11] J. Polettini, L.S. Richardson, R. Menon, Oxidative stress induces senescence and sterile inflammation in murine amniotic cavity, Placenta 63 (2018) 26-31.
[12] R. Menon, S.J. Fortunato, J. Yu, G.L. Milne, S. Sanchez, C.O. Drobek, M. Lappas, R.N. Taylor, Cigarette smoke induces oxidative stress and apoptosis in normal term fetal membranes, Placenta 32(4) (2011) 317-22.
[13] F. Behnia, B.D. Taylor, M. Woodson, M. Kacerovsky, H. Hawkins, S.J. Fortunato, G.R. Saade, R. Menon, Chorioamniotic membrane senescence: a signal for parturition?, Am J Obstet Gynecol 213(3) (2015) 359.e1-16.
[14] E.A. Bonney, K. Krebs, G. Saade, T. Kechichian, J. Trivedi, Y. Huaizhi, R. Menon, Differential senescence in feto-maternal tissues during mouse pregnancy, Placenta 43 (2016) 26-34.
[15] J. Polettini, F. Behnia, B.D. Taylor, G.R. Saade, R.N. Taylor, R. Menon, Telomere Fragment Induced Amnion Cell Senescence: A Contributor to Parturition?, PLoS ONE [Electronic Resource] 10(9) (2015) e0137188.
[16] G.L. Bourne, The anatomy of the human amnion and chorion, Proc R Soc Med 59(11 Part 1) (1966) 1127-8.
[17] T.M. Malak, C.D. Ockleford, S.C. Bell, R. Dalgleish, N. Bright, J. Macvicar, Confocal immunofluorescence localization of collagen types I, III, IV, V and VI and their

ultrastructural organization in term human fetal membranes, Placenta 14(4) (1993) 385-406.
[18] N.M. Gude, C.T. Roberts, B. Kalionis, R.G. King, Growth and function of the normal human placenta, Thromb Res 114(5-6) (2004) 397-407.
[19] R. Menon, Human fetal membranes at term: Dead tissue or signalers of parturition?, Placenta 44 (2016) 1-5.
[20] G.D. Bryant-Greenwood, The extracellular matrix of the human fetal membranes: structure and function, Placenta 19(1) (1998) 1-11.
[21] V. Nunes, J. Cross, J.E. Speich, D.R. Morgan, J.F. Strauss, 3rd, R.M. Ramus, Fetal membrane imaging and the prediction of preterm birth: a systematic review, current issues, and future directions, BMC Pregnancy Childbirth 16(1) (2016) 387.
[22] J.F. Strauss, 3rd, Extracellular matrix dynamics and fetal membrane rupture, Reprod Sci 20(2) (2013) 140-53.
[23] A. Mauri, A.E. Ehret, M. Perrini, C. Maake, N. Ochsenbein-Kolble, M. Ehrbar, M.L. Oyen, E. Mazza, Deformation mechanisms of human amnion: Quantitative studies based on second harmonic generation microscopy, J Biomech 48(9) (2015) 1606-13.
[24] D. Kumar, R.M. Moore, B.M. Mercer, J.M. Mansour, R.W. Redline, J.J. Moore, The physiology of fetal membrane weakening and rupture: Insights gained from the determination of physical properties revisited, Placenta 42 (2016) 59-73.
[25] J.J. Reynolds, Collagenases and tissue inhibitors of metalloproteinases: a functional balance in tissue degradation, Oral Dis 2(1) (1996) 70-6.
[26] S.J. Fortunato, R. Menon, C. Bryant, S.J. Lombardi, Programmed cell death (apoptosis) as a possible pathway to metalloproteinase activation and fetal membrane degradation in premature rupture of membranes, Am J Obstet Gynecol 182(6) (2000) 1468-76.
[27] G.J. Burton, Oxygen, the Janus gas; its effects on human placental development and function, J Anat 215(1) (2009) 27-35.
[28] R. Menon, I. Boldogh, R. Urrabaz-Garza, J. Polettini, T.A. Syed, G.R. Saade, J. Papaconstantinou, R.N. Taylor, Senescence of primary amniotic cells via oxidative DNA damage, PLoS ONE [Electronic Resource] 8(12) (2013) e83416.
[29] L.S. Cox, C. Redman, The role of cellular senescence in ageing of the placenta, Placenta 52 (2017) 139-145.
[30] N. Gomez-Lopez, R. Romero, O. Plazyo, G. Schwenkel, V. Garcia-Flores, R. Unkel, Y. Xu, Y. Leng, S.S. Hassan, B. Panaitescu, J. Cha, S.K. Dey, Preterm labor in the absence of acute histologic chorioamnionitis is characterized by cellular senescence of the chorioamniotic membranes, Am J Obstet Gynecol 217(5) (2017) 592.e1-592.e17.
[31] E.H. Dutta, F. Behnia, I. Boldogh, G.R. Saade, B.D. Taylor, M. Kacerovsky, R. Menon, Oxidative stress damage-associated molecular signaling pathways differentiate spontaneous preterm birth and preterm premature rupture of the membranes, Mol Hum Reprod 22(2) (2016) 143-57.
[32] Z. Sultana, K. Maiti, J. Aitken, J. Morris, L. Dedman, R. Smith, Oxidative stress, placental ageing-related pathologies and adverse pregnancy outcomes, Am J Reprod Immunol 77(5) (2017).
[33] M.G. Parker, F. Ouyang, C. Pearson, M.W. Gillman, M.B. Belfort, X. Hong, G. Wang, L. Heffner, B. Zuckerman, X. Wang, Prepregnancy body mass index and risk of

preterm birth: association heterogeneity by preterm subgroups, BMC Pregnancy Childbirth 14 (2014) 153.
[34] R. Menon, F. Behnia, J. Polettini, G.R. Saade, J. Campisi, M. Velarde, Placental membrane aging and HMGB1 signaling associated with human parturition, Aging (Albany NY) 8(2) (2016) 216-30.
[35] M. Chai, G. Barker, R. Menon, M. Lappas, Increased oxidative stress in human fetal membranes overlying the cervix from term non-labouring and post labour deliveries, Placenta 33(8) (2012) 604-10.
[36] M. Lappas, M. Permezel, P.W. Ho, J.M. Moseley, M.E. Wlodek, G.E. Rice, Effect of nuclear factor-kappa B inhibitors and peroxisome proliferator-activated receptor-gamma ligands on PTHrP release from human fetal membranes, Placenta 25(8-9) (2004) 699-704.
[37] F. Behnia, S.E. Parets, T. Kechichian, H. Yin, E.H. Dutta, G.R. Saade, A.K. Smith, R. Menon, Fetal DNA methylation of autism spectrum disorders candidate genes: association with spontaneous preterm birth, Am J Obstet Gynecol 212(4) (2015) 533.e1-9.
[38] B.J. Canzoneri, L. Feng, C.A. Grotegut, R.C. Bentley, R.P. Heine, A.P. Murtha, The chorion layer of fetal membranes is prematurely destroyed in women with preterm premature rupture of the membranes, Reprod Sci 20(10) (2013) 1246-54.
[39] Richardson, Lauren, Vargas, Gracie, Brown, Tyra, Ochoa, Lorenzo, J. Trivedi, Kacerovský, Marian, Lappas, Martha, R. Menon, Redefining 3Dimensional placental membrane microarchitecture using multiphoton microscopy and optical clearing, 53(66-75) (2017).
[40] C. Avila, J. Santorelli, J. Mathai, S. Ishkin, M. Jabsky, J. Willins, R. Figueroa, C. Kaplan, Anatomy of the fetal membranes using optical coherence tomography: part 1, Placenta 35(12) (2014) 1065-9.
[41] S. Bredeson, J. Papaconstantinou, J.H. Deford, T. Kechichian, T.A. Syed, G.R. Saade, R. Menon, HMGB1 promotes a p38MAPK associated non-infectious inflammatory response pathway in human fetal membranes, PLoS ONE [Electronic Resource] 9(12) (2014) e113799.
[42] M.L. Casey, P.C. MacDonald, Interstitial collagen synthesis and processing in human amnion: a property of the mesenchymal cells, Biol Reprod 55(6) (1996) 1253-60.
[43] T. Miki, T. Lehmann, H. Cai, D.B. Stolz, S.C. Strom, Stem cell characteristics of amniotic epithelial cells, Stem Cells 23(10) (2005) 1549-59.
[44] W.P. Faulk, R. Matthews, P.J. Stevens, J.P. Bennett, H. Burgos, B.L. Hsi, Human amnion as an adjunct in wound healing, Lancet 1(8179) (1980) 1156-8.
[45] R. Donald E. FetterolfSnyder, Dehydrated Amniotic Membrane Use in Wound Management, (2017).
[46] M. Litwiniuk, T. Grzela, Amniotic membrane: new concepts for an old dressing, Wound Repair Regen 22(4) (2014) 451-6.
[47] B. Zhao, J.Q. Liu, Z. Zheng, J. Zhang, S.Y. Wang, S.C. Han, Q. Zhou, H. Guan, C. Li, L.L. Su, D.H. Hu, Human amniotic epithelial stem cells promote wound healing by facilitating migration and proliferation of keratinocytes via ERK, JNK and AKT signaling pathways, Cell Tissue Res 365(1) (2016) 85-99.
[48] F. Marongiu, R. Gramignoli, K. Dorko, T. Miki, A.R. Ranade, M. Paola Serra, S. Doratiotto, M. Sini, S. Sharma, K. Mitamura, T.L. Sellaro, V. Tahan, K.J. Skvorak, E.C.

Ellis, S.F. Badylak, J.C. Davila, R. Hines, E. Laconi, S.C. Strom, Hepatic differentiation of amniotic epithelial cells, Hepatology 53(5) (2011) 1719-29.
[49] L. Richardson, L. Martin, R. Menon, Functionality of Fetal Membranes: an Overlooked Area in the Field of Parturition. Encyclopedia of Reproduction, 2nd ed., Encyclopedia of Reproduction, 2017.
[50] A. Mauri, M. Perrini, J.M. Mateos, C. Maake, N. Ochsenbein-Koelble, R. Zimmermann, M. Ehrbar, E. Mazza, Second harmonic generation microscopy of fetal membranes under deformation: normal and altered morphology, Placenta 34(11) (2013) 1020-6.
[51] A. Mauri, M. Perrini, A.E. Ehret, D.S. De Focatiis, E. Mazza, Time-dependent mechanical behavior of human amnion: macroscopic and microscopic characterization, Acta Biomater 11 (2015) 314-23.
[52] M. Perrini, A. Mauri, A.E. Ehret, N. Ochsenbein-Kolble, R. Zimmermann, M. Ehrbar, E. Mazza, Mechanical and microstructural investigation of the cyclic behavior of human amnion, J Biomech Eng 137(6) (2015) 061010.
[53] R.M. Moore, J.M. Mansour, R.W. Redline, B.M. Mercer, J.J. Moore, The physiology of fetal membrane rupture: insight gained from the determination of physical properties, Placenta 27(11-12) (2006) 1037-51.
[54] D.J. Forsthoefel, A.E. Park, P.A. Newmark, Stem cell-based growth, regeneration, and remodeling of the planarian intestine, Dev Biol 356(2) (2011) 445-59.
[55] M. Roulis, R.A. Flavell, Fibroblasts and myofibroblasts of the intestinal lamina propria in physiology and disease, Differentiation 92(3) (2016) 116-131.
[56] P. Lu, K. Takai, V.M. Weaver, Z. Werb, Extracellular matrix degradation and remodeling in development and disease, Cold Spring Harb Perspect Biol 3(12) (2011).
[57] P. Lu, V.M. Weaver, Z. Werb, The extracellular matrix: a dynamic niche in cancer progression, J Cell Biol 196(4) (2012) 395-406.
[58] R. Pal, J. Yang, D. Ortiz, S. Qiu, V. Resto, S. McCammon, G. Vargas, In-vivo nonlinear optical microscopy (NLOM) of epithelial-connective tissue interface (ECTI) reveals quantitative measures of neoplasia in hamster oral mucosa, PLoS One 10(1) (2015) e0116754.
[59] R. Kalluri, R.A. Weinberg, The basics of epithelial-mesenchymal transition, J Clin Invest 119(6) (2009) 1420-8.
[60] S. Lamouille, J. Xu, R. Derynck, Molecular mechanisms of epithelial-mesenchymal transition, Nat Rev Mol Cell Biol 15(3) (2014) 178-96.
[61] J.M. Lee, S. Dedhar, R. Kalluri, E.W. Thompson, The epithelial-mesenchymal transition: new insights in signaling, development, and disease, J Cell Biol 172(7) (2006) 973-81.
[62] C.Y. Liu, H.H. Lin, M.J. Tang, Y.K. Wang, Vimentin contributes to epithelial-mesenchymal transition cancer cell mechanics by mediating cytoskeletal organization and focal adhesion maturation, Oncotarget 6(18) (2015) 15966-83.
[63] A. Moustakas, C.H. Heldin, Mechanisms of TGFβ-Induced Epithelial–Mesenchymal Transition, J Clin Med 5(7) (2016).
[64] U. Bedi, Epigenetic plasticity: A central regulator of epithelial-to-mesenchymal transition in cancer, Oncotarget (2016).
[65] M. Sabbah, S. Emami, G. Redeuilh, S. Julien, G. Prevost, A. Zimber, R. Ouelaa, M. Bracke, O. De Wever, C. Gespach, Molecular signature and therapeutic perspective of

the epithelial-to-mesenchymal transitions in epithelial cancers, Drug Resist Updat 11(4-5) (2008) 123-51.
[66] R. Roy, M. Kukucka, D. Messroghli, D. Kunkel, A. Brodarac, K. Klose, S. Geissler, P.M. Becher, S.K. Kang, Y.H. Choi, C. Stamm, Epithelial-to-Mesenchymal Transition Enhances the Cardioprotective Capacity of Human Amniotic Epithelial Cells, Cell Transplant 24(6) (2015) 985-1002.
[67] P.A. R. M. Laberge, J. Campisi, P. Y. Desprez. Epithelial-Mesenchymal Transition Induced by Senescent Fibroblasts. *Cancer Microenvironment*. 2012, -. doi:10.1007/s12307-011-0069-4.
[68] D.S. Fetterolf, Robert, Dehydrated Amniotic Membrane Use in Wound Management, (2017).
[69] M. Kesting, Evaluation of Human Amniotic Membrane as a Wound Dressing for Split-Thickness Skin-Graft Donor Sites, in: M.U.o.T. Department of Oral and Maxillofacial Surgery, Ismaninger Straße 22, 81675 Munich, Germany (Ed.) BioMed Research International, 2017.
[70] C.L. Chaffer, J.P. Brennan, J.L. Slavin, T. Blick, E.W. Thompson, E.D. Williams, Mesenchymal-to-epithelial transition facilitates bladder cancer metastasis: role of fibroblast growth factor receptor-2, Cancer Res 66(23) (2006) 11271-8.
[71] C. Chaffer, Mesenchymal to epithelial transition in development and disease, Cell, Tissue, Organs (2007) 7-19.
[72] L.K. Millar, J. Stollberg, L. DeBuque, G. Bryant-Greenwood, Fetal membrane distention: determination of the intrauterine surface area and distention of the fetal membranes preterm and at term, Am J Obstet Gynecol 182(1 Pt 1) (2000) 128-34.
[73] E.M. Joyce, J.J. Moore, M.S. Sacks, Biomechanics of the fetal membrane prior to mechanical failure: review and implications, Eur J Obstet Gynecol Reprod Biol 144 Suppl 1 (2009) S121-7.
[74] C.E. Kendal-Wright, Stretching, mechanotransduction, and proinflammatory cytokines in the fetal membranes, Reprod Sci 14(8 Suppl) (2007) 35-41.
[75] W.H. Faour, Y. He, Q.W. He, M. de Ladurantaye, M. Quintero, A. Mancini, J.A. Di Battista, Prostaglandin E(2) regulates the level and stability of cyclooxygenase-2 mRNA through activation of p38 mitogen-activated protein kinase in interleukin-1 beta-treated human synovial fibroblasts, J Biol Chem 276(34) (2001) 31720-31.
[76] N.N. Guo, C.L. Meng, W.J. Bai, Q.W. Wei, F.X. Shi, J.S. Davis, D.G. Mao, Prostaglandin F-2 alpha induces expression of activating transcription factor 3 (ATF3) and activates MAPK signaling in the rat corpus luteum, Acta Histochemica 117(2) (2015) 211-218.
[77] M.J. Duchesne, H. Thaler-Dao, A.C. de Paulet, Prostaglandin synthesis in human placenta and fetal membranes, Prostaglandins 15(1) (1978) 19-42.
[78] K.A. Skinner, J.R. Challis, Changes in the synthesis and metabolism of prostaglandins by human fetal membranes and decidua at labor, Am J Obstet Gynecol 151(4) (1985) 519-23.
[79] T.K. Allen, L. Feng, M. Nazzal, C.A. Grotegut, I.A. Buhimschi, A.P. Murtha, The Effect of Progestins on Tumor Necrosis Factor alpha-Induced Matrix Metalloproteinase-9 Activity and Gene Expression in Human Primary Amnion and Chorion Cells In Vitro, Anesth Analg 120(5) (2015) 1085-94.

[80] C. Oner, F. Schatz, G. Kizilay, W. Murk, L.F. Buchwalder, U.A. Kayisli, A. Arici, C.J. Lockwood, Progestin-inflammatory cytokine interactions affect matrix metalloproteinase-1 and -3 expression in term decidual cells: implications for treatment of chorioamnionitis-induced preterm delivery, Journal of Clinical Endocrinology & Metabolism 93(1) (2008) 252-9.
[81] G.T. Sukhikh, N.E. Kan, V.L. Tyutyunnik, M.V. Sannikova, E.A. Dubova, K.A. Pavlov, E.Y. Amiraslanov, N.V. Dolgushina, The role of extracellular inducer of matrix metalloproteinases in premature rupture of membranes, J Matern Fetal Neonatal Med 29(4) (2016) 656-9.
[82] J. Jin, L. Richardson, S. Sheller-Miller, N. Zhong, R. Menon, Oxidative stress induces p38MAPK-dependent senescence in the feto-maternal interface cells, Placenta 67 (2018) 15-23.
[83] S. Sheller-Miller, R. Urrabaz-Garza, G. Saade, R. Menon, Damage-Associated molecular pattern markers HMGB1 and cell-Free fetal telomere fragments in oxidative-Stressed amnion epithelial cell-Derived exosomes, J Reprod Immunol 123 (2017) 3-11.
[84] J.E. Lawn, M.V. Kinney, J.M. Belizan, E.M. Mason, L. McDougall, J. Larson, E. Lackritz, I.K. Friberg, C.P. Howson, Born too soon: accelerating actions for prevention and care of 15 million newborns born too soon, Reprod Health 10 Suppl 1 (2013) S6.
[85] J. Fraser, M. Walls, W. McGuire, Respiratory complications of preterm birth, Bmj 329(7472) (2004) 962-5.
[86] Practice Bulletin No. 160: Premature Rupture of Membranes, Obstet Gynecol 127(1) (2016) e39-51.
[87] V. Agrawal, E. Hirsch, Intrauterine infection and preterm labor, Semin Fetal Neonatal Med 17(1) (2012) 12-9.
[88] A. Martin, C. Faes, T. Debevec, C. Rytz, G. Millet, V. Pialoux, Preterm birth and oxidative stress: Effects of acute physical exercise and hypoxia physiological responses, Redox Biol 17 (2018) 315-322.
[89] K.M. Adams Waldorf, N. Singh, A.R. Mohan, R.C. Young, L. Ngo, A. Das, J. Tsai, A. Bansal, L. Paolella, B.R. Herbert, S.R. Sooranna, G.M. Gough, C. Astley, K. Vogel, A.E. Baldessari, T.K. Bammler, J. MacDonald, M.G. Gravett, L. Rajagopal, M.R. Johnson, Uterine overdistention induces preterm labor mediated by inflammation: observations in pregnant women and nonhuman primates, Am J Obstet Gynecol 213(6) (2015) 830.e1-830.e19.
[90] A.M. Brandao, A.P. Domingues, E.M. Fonseca, T.M. Miranda, A. Belo, J.P. Moura, [Premature labour with or without preterm premature rupture of membranes: maternal, obstetric and neonatal features], Rev Bras Ginecol Obstet 37(9) (2015) 428-33.
[91] G.D. Bryant-Greenwood, S.Y. Yamamoto, Control of peripartal collagenolysis in the human chorion-decidua, Am J Obstet Gynecol 172(1 Pt 1) (1995) 63-70.
[92] E.R. Norwitz, A.B. Caughey, Progesterone supplementation and the prevention of preterm birth, Rev Obstet Gynecol 4(2) (2011) 60-72.
[93] J.A. Carvajal, M.J. Zambrano, N.M. Theodor, L.E. Moreno, T.R. Olguin, P.S. Vanhauwaert, N.B. Rojas, A.M. Delpiano, The Synergic In Vitro Tocolytic Effect of Nifedipine Plus Ritodrine on Human Myometrial Contractility, Reprod Sci 24(4) (2017) 635-640.
[94] M. Hanley, L. Sayres, E.S. Reiff, A. Wood, C.A. Grotegut, J.A. Kuller, Tocolysis: A Review of the Literature, Obstet Gynecol Surv 74(1) (2019) 50-55.

[95] J.W. Lee, J.M. Davis, Future applications of antioxidants in premature infants, Curr Opin Pediatr 23(2) (2011) 161-6.
[96] L.S. Richardson, G. Vargas, T. Brown, L. Ochoa, S. Sheller-Miller, G.R. Saade, R.N. Taylor, R. Menon, Discovery and Characterization of Human Amniochorionic Membrane Microfractures, The American Journal of Pathology.
[97] R. Kiesslich, M. Goetz, E.M. Angus, Q. Hu, Y. Guan, C. Potten, T. Allen, M.F. Neurath, N.F. Shroyer, M.H. Montrose, A.J. Watson, Identification of epithelial gaps in human small and large intestine by confocal endomicroscopy, Gastroenterology 133(6) (2007) 1769-78.
[98] J.M. Williams, C.A. Duckworth, M.D. Burkitt, A.J. Watson, B.J. Campbell, D.M. Pritchard, Epithelial cell shedding and barrier function: a matter of life and death at the small intestinal villus tip, Vet Pathol 52(3) (2015) 445-55.
[99] L. Antoni, S. Nuding, J. Wehkamp, E.F. Stange, Intestinal barrier in inflammatory bowel disease, World J Gastroenterol 20(5) (2014) 1165-79.
[100] K. Edward, S. Qiu, V. Resto, S. McCammon, G. Vargas, In vivo layer-resolved characterization of oral dysplasia via nonlinear optical micro-spectroscopy, Biomed Opt Express 3(7) (2012) 1579-93.
[101] S. Mukherjee, J.S. Wysock, C.K. Ng, M. Akhtar, S. Perner, M.M. Lee, M.A. Rubin, F.R. Maxfield, W.W. Webb, D.S. Scherr, Human bladder cancer diagnosis using Multiphoton microscopy, Proc SPIE Int Soc Opt Eng 7161 (2009).
[102] A. Erturk, D. Lafkas, C. Chalouni, Imaging cleared intact biological systems at a cellular level by 3DISCO, J Vis Exp (89) (2014).
[103] P.L. Appleton, A.J. Quyn, S. Swift, I. Nathke, Preparation of wholemount mouse intestine for high-resolution three-dimensional imaging using two-photon microscopy, J Microsc 234(2) (2009) 196-204.
[104] Y.A. Liu, Y. Chen, A.S. Chiang, S.J. Peng, P.J. Pasricha, S.C. Tang, Optical clearing improves the imaging depth and signal-to-noise ratio for digital analysis and three-dimensional projection of the human enteric nervous system, Neurogastroenterol Motil 23(10) (2011) e446-57.
[105] D.N. Olivieri, C.E. Tadokoro, Techniques for visualization of cell-cell contact at the fetal-maternal interface, Am J Reprod Immunol 69(4) (2013) 419-26.
[106] M. Jabareen, A.S. Mallik, G. Bilic, A.H. Zisch, E. Mazza, Relation between mechanical properties and microstructure of human fetal membranes: an attempt towards a quantitative analysis, Eur J Obstet Gynecol Reprod Biol 144 Suppl 1 (2009) S134-41.
[107] W.L. Chen, P.S. Hu, A. Ghazaryan, S.J. Chen, T.H. Tsai, C.Y. Dong, Quantitative analysis of multiphoton excitation autofluorescence and second harmonic generation imaging for medical diagnosis, Comput Med Imaging Graph 36(7) (2012) 519-26.
[108] R. Ambekar, T.Y. Lau, M. Walsh, R. Bhargava, K.C. Toussaint, Jr., Quantifying collagen structure in breast biopsies using second-harmonic generation imaging, Biomed Opt Express 3(9) (2012) 2021-35.
[109] W.R. Zipfel, R.M. Williams, W.W. Webb, Nonlinear magic: multiphoton microscopy in the biosciences, Nat Biotechnol 21(11) (2003) 1369-77.
[110] R. Yuste, W. Denk, Dendritic spines as basic functional units of neuronal integration, Nature 375(6533) (1995) 682-4.

[111] E.B. Brown, R.B. Campbell, Y. Tsuzuki, L. Xu, P. Carmeliet, D. Fukumura, R.K. Jain, In vivo measurement of gene expression, angiogenesis and physiological function in tumors using multiphoton laser scanning microscopy, Nat Med 7(7) (2001) 864-8.
[112] M.D. Cahalan, I. Parker, S.H. Wei, M.J. Miller, Two-photon tissue imaging: seeing the immune system in a fresh light, Nat Rev Immunol 2(11) (2002) 872-80.
[113] N.J. Durr, C.T. Weisspfennig, B.A. Holfeld, A. Ben-Yakar, Maximum imaging depth of two-photon autofluorescence microscopy in epithelial tissues, J Biomed Opt 16(2) (2011) 026008.
[114] G. Vargas, E.K. Chan, J.K. Barton, H.G. Rylander, 3rd, A.J. Welch, Use of an agent to reduce scattering in skin, Lasers Surg Med 24(2) (1999) 133-41.
[115] G. Vargas, A. Readinger, S.S. Dozier, A.J. Welch, Morphological changes in blood vessels produced by hyperosmotic agents and measured by optical coherence tomography, Photochem Photobiol 77(5) (2003) 541-9.
[116] J. McLaren, T.M. Malak, S.C. Bell, Structural characteristics of term human fetal membranes prior to labour: identification of an area of altered morphology overlying the cervix, Hum Reprod 14(1) (1999) 237-41.
[117] A.P. Murtha, R. Menon, Regulation of fetal membrane inflammation: a critical step in reducing adverse pregnancy outcome, Am J Obstet Gynecol 213(4) (2015) 447-8.
[118] F. Vadillo-Ortega, A. Hernandez, G. Gonzalez-Avila, L. Bermejo, K. Iwata, J.F. Strauss, 3rd, Increased matrix metalloproteinase activity and reduced tissue inhibitor of metalloproteinases-1 levels in amniotic fluids from pregnancies complicated by premature rupture of membranes, Am J Obstet Gynecol 174(4) (1996) 1371-6.
[119] S.J. Fortunato, R. Menon, S.J. Lombardi, MMP/TIMP imbalance in amniotic fluid during PROM: an indirect support for endogenous pathway to membrane rupture, J Perinat Med 27(5) (1999) 362-8.
[120] N. Athayde, R. Romero, R. Gomez, E. Maymon, P. Pacora, M. Mazor, B.H. Yoon, S. Fortunato, R. Menon, F. Ghezzi, S.S. Edwin, Matrix metalloproteinases-9 in preterm and term human parturition, J Matern Fetal Med 8(5) (1999) 213-9.
[121] T.M. Malak, S.C. Bell, Structural characteristics of term human fetal membranes: a novel zone of extreme morphological alteration within the rupture site, Br J Obstet Gynaecol 101(5) (1994) 375-86.
[122] R.S. Pal, Tuya Yang, Jinping Villarreal,Paula Brown, Tyra Qiu, Suimin McCammon, Susan Resto, Vicente Vargas, Gracie, Remodeling of the Epithelial – Connective Tissue Interface in Oral Epithelial Dysplasia as Visualized by Noninvasive 3D Imaging, 76(4637-4647) (2016).
[123] B. Chowdhury, A.L. David, C. Thrasivoulou, D.L. Becker, D.L. Bader, T.T. Chowdhury, Tensile strain increased COX-2 expression and PGE2 release leading to weakening of the human amniotic membrane, Placenta 35(12) (2014) 1057-64.
[124] S. Parry, J.F. Strauss, 3rd, Premature rupture of the fetal membranes, N Engl J Med 338(10) (1998) 663-70.
[125] F. Arechavaleta-Velasco, D. Ogando, S. Parry, F. Vadillo-Ortega, Production of matrix metalloproteinase-9 in lipopolysaccharide-stimulated human amnion occurs through an autocrine and paracrine proinflammatory cytokine-dependent system, Biol Reprod 67(6) (2002) 1952-8.

[126] C. Janzen, S. Sen, M.Y. Lei, M. Gagliardi de Assumpcao, J. Challis, G. Chaudhuri, The Role of Epithelial to Mesenchymal Transition in Human Amniotic Membrane Rupture, J Clin Endocrinol Metab 102(4) (2017) 1261-1269.
[127] S. Sheller-Miller, J. Lei, G. Saade, C. Salomon, B. Irina, R. Menon, Feto-Maternal Trafficking of Exosomes in Murine Pregnancy Models, (2016).
[128] L. Richardson, R. Menon, Proliferative, Migratory, and Transition Properties Reveal Metastate of Human Amnion Cells, Am J Pathol (2018).
[129] A. Gupta, S.D. Kedige, K. Jain, Amnion and Chorion Membranes: Potential Stem Cell Reservoir with Wide Applications in Periodontics, Int J Biomater 2015 (2015) 274082.
[130] E.E. Hadley, L.S. Richardson, M.R. Torloni, R. Menon, Gestational tissue inflammatory biomarkers at term labor: A systematic review of literature, Am J Reprod Immunol (2017).
[131] R. Menon, Oxidative stress damage as a detrimental factor in preterm birth pathology, Frontiers in Immunology 5 (2014) 567.
[132] E. Gratacos, J. Sanin-Blair, L. Lewi, N. Toran, G. Verbist, L. Cabero, J. Deprest, A histological study of fetoscopic membrane defects to document membrane healing, Placenta 27(4-5) (2006) 452-6.
[133] N.A. Papadopulos, S. Klotz, A. Raith, M. Foehn, U. Schillinger, J. Henke, L. Kovacs, R.E. Horch, E. Biemer, Amnion cells engineering: a new perspective in fetal membrane healing after intrauterine surgery?, Fetal Diagn Ther 21(6) (2006) 494-500.
[134] A.F. Borgida, A.A. Mills, D.M. Feldman, J.F. Rodis, J.F. Egan, Outcome of pregnancies complicated by ruptured membranes after genetic amniocentesis, Am J Obstet Gynecol 183(4) (2000) 937-9.
[135] N.S. Carvalho, A.F. Moron, R. Menon, S. Cavalheiro, M.M. Barbosa, H.J. Milani, M.M. Ishigai, Histological evidence of reparative activity in chorioamniotic membrane following open fetal surgery for myelomeningocele, Exp Ther Med 14(4) (2017) 3732-3736.
[136] R. Papanna, L.K. Mann, S.C. Tseng, R.J. Stewart, S.S. Kaur, M.M. Swindle, T.R. Kyriakides, N. Tatevian, K.J. Moise, Jr., Cryopreserved human amniotic membrane and a bioinspired underwater adhesive to seal and promote healing of iatrogenic fetal membrane defect sites, Placenta 36(8) (2015) 888-94.
[137] R.A. Quintero, W.J. Morales, M. Allen, P.W. Bornick, J. Arroyo, G. LeParc, Treatment of iatrogenic previable premature rupture of membranes with intra-amniotic injection of platelets and cryoprecipitate (amniopatch): preliminary experience, Am J Obstet Gynecol 181(3) (1999) 744-9.
[138] L.K. Mann, R. Papanna, K.J. Moise, Jr., R.H. Byrd, E.J. Popek, S. Kaur, S.C. Tseng, R.J. Stewart, Fetal membrane patch and biomimetic adhesive coacervates as a sealant for fetoscopic defects, Acta Biomater 8(6) (2012) 2160-5.
[139] R. Papanna, L.K. Mann, K.J. Moise, Jr., T. Kyriakides, A. Johnson, E. Garcia, C.S. Buhimschi, I.A. Buhimschi, Histologic changes of the fetal membranes after fetoscopic laser surgery for twin-twin transfusion syndrome, Pediatr Res 78(3) (2015) 247-55.
[140] R. Menon, L.S. Richardson, Preterm prelabor rupture of the membranes: A disease of the fetal membranes, Semin Perinatol 41(7) (2017) 409-419.
[141] H. Mogami, A. Hari Kishore, Y. Akgul, R.A. Word, Healing of Preterm Ruptured Fetal Membranes, Sci Rep 7(1) (2017) 13139.

[142] G. Moreno-Bueno, H. Peinado, P. Molina, D. Olmeda, E. Cubillo, V. Santos, J. Palacios, F. Portillo, A. Cano, The morphological and molecular features of the epithelial-to-mesenchymal transition, Nat Protoc 4(11) (2009) 1591-613.
[143] S. Sheller, J. Papaconstantinou, R. Urrabaz-Garza, L. Richardson, G. Saade, C. Salomon, R. Menon, Amnion-Epithelial-Cell-Derived Exosomes Demonstrate Physiologic State of Cell under Oxidative Stress, PLoS One 11(6) (2016) e0157614.
[144] K. Itahana, J. Campisi, G.P. Dimri, Methods to detect biomarkers of cellular senescence: the senescence-associated beta-galactosidase assay, Methods Mol Biol 371 (2007) 21-31.
[145] C.L. Dixon, L. Richardson, S. Sheller-Miller, G. Saade, R. Menon, A distinct mechanism of senescence activation in amnion epithelial cells by infection, inflammation, and oxidative stress, Am J Reprod Immunol (2017).
[146] R.I. Fernando, M.D. Castillo, M. Litzinger, D.H. Hamilton, C. Palena, IL-8 signaling plays a critical role in the epithelial-mesenchymal transition of human carcinoma cells, Cancer Res 71(15) (2011) 5296-306.
[147] H.O. Rennekampff, J.F. Hansbrough, V. Kiessig, C. Dore, M. Sticherling, J.M. Schroder, Bioactive interleukin-8 is expressed in wounds and enhances wound healing, J Surg Res 93(1) (2000) 41-54.
[148] M.S. Kim, M.H. Lee, B.J. Kwon, D. Kim, M.A. Koo, G.M. Seon, J.C. Park, Homogeneity evaluation of mesenchymal stem cells based on electrotaxis analysis, Sci Rep 7(1) (2017) 9582.
[149] M. Lappas, U. Hiden, G. Desoye, J. Froehlich, S. Hauguel-de Mouzon, A. Jawerbaum, The role of oxidative stress in the pathophysiology of gestational diabetes mellitus, Antioxid Redox Signal 15(12) (2011) 3061-100.
[150] A. Asea, C. Jean-Pierre, P. Kaur, P. Rao, I.M. Linhares, D. Skupski, S.S. Witkin, Heat shock protein-containing exosomes in mid-trimester amniotic fluids, J Reprod Immunol 79(1) (2008) 12-7.
[151] J. Pierce, Collection and characterization of amniotic fluid from scheduled C-section deliveries, Cell and Tissue Banking 17(3) (2016) 413-425.
[152] F. Behnia, M.R. Peltier, G.R. Saade, R. Menon, Environmental Pollutant Polybrominated Diphenyl Ether, a Flame Retardant, Induces Primary Amnion Cell Senescence, American Journal of Reproductive Immunology 74(5) (2015) 398-406.
[153] N.X. Landen, D. Li, M. Stahle, Transition from inflammation to proliferation: a critical step during wound healing, Cell Mol Life Sci 73(20) (2016) 3861-85.
[154] R. Menon, S.J. Fortunato, G.L. Milne, L. Brou, C. Carnevale, S.C. Sanchez, L. Hubbard, M. Lappas, C.O. Drobek, R.N. Taylor, Amniotic fluid eicosanoids in preterm and term births: effects of risk factors for spontaneous preterm labor, Obstet Gynecol 118(1) (2011) 121-34.
[155] J.L. Maymo, R. Riedel, A. Perez-Perez, M. Magatti, B. Maskin, J.L. Duenas, O. Parolini, V. Sanchez-Margalet, C.L. Varone, Proliferation and survival of human amniotic epithelial cells during their hepatic differentiation, PLoS One 13(1) (2018) e0191489.
[156] P. Laurila, I. Virtanen, V.P. Lehto, T. Vartio, S. Stenman, Expression and distribution of vimentin and keratin filaments in heterokaryons of human fibroblasts and amnion epithelial cells, J Cell Biol 94(2) (1982) 308-15.

[157] S. Regauer, W.W. Franke, I. Virtanen, Intermediate filament cytoskeleton of amnion epithelium and cultured amnion epithelial cells: expression of epidermal cytokeratins in cells of a simple epithelium, J Cell Biol 100(4) (1985) 997-1009.
[158] S. Begnaud, T. Chen, D. Delacour, R.M. Mege, B. Ladoux, Mechanics of epithelial tissues during gap closure, Curr Opin Cell Biol 42 (2016) 52-62.
[159] M.G. Mendez, S. Kojima, R.D. Goldman, Vimentin induces changes in cell shape, motility, and adhesion during the epithelial to mesenchymal transition, Faseb j 24(6) (2010) 1838-51.
[160] F.C. Nery, J. Zeng, B.P. Niland, J. Hewett, J. Farley, D. Irimia, Y. Li, G. Wiche, A. Sonnenberg, X.O. Breakefield, TorsinA binds the KASH domain of nesprins and participates in linkage between nuclear envelope and cytoskeleton, J Cell Sci 121(Pt 20) (2008) 3476-86.
[161] L. Yu, M.C. Hebert, Y.E. Zhang, TGF-beta receptor-activated p38 MAP kinase mediates Smad-independent TGF-beta responses, Embo j 21(14) (2002) 3749-59.
[162] E. Hedrick, S. Safe, Transforming Growth Factor beta/NR4A1-Inducible Breast Cancer Cell Migration and Epithelial-to-Mesenchymal Transition Is p38alpha (Mitogen-Activated Protein Kinase 14) Dependent, Mol Cell Biol 37(18) (2017).
[163] S. Beck, D. Wojdyla, L. Say, A.P. Betran, M. Merialdi, J.H. Requejo, C. Rubens, R. Menon, P.F. Van Look, The worldwide incidence of preterm birth: a systematic review of maternal mortality and morbidity, Bull World Health Organ 88(1) (2010) 31-8.
[164] O. Institute of Medicine Committee on Understanding Premature Birth and Assuring Healthy, The National Academies Collection: Reports funded by National Institutes of Health, in: R.E. Behrman, A.S. Butler (Eds.), Preterm Birth: Causes, Consequences, and Prevention, National Academies Press (US)
National Academy of Sciences., Washington (DC), 2007.
[165] R. Romero, S.K. Dey, S.J. Fisher, Preterm labor: one syndrome, many causes, Science 345(6198) (2014) 760-5.
[166] T. Cobo, M. Kacerovsky, B. Jacobsson, Amniotic fluid infection, inflammation, and colonization in preterm labor with intact membranes, Am J Obstet Gynecol 211(6) (2014) 708.
[167] K.J. Oh, J.S. Hong, R. Romero, B.H. Yoon, The frequency and clinical significance of intra-amniotic inflammation in twin pregnancies with preterm labor and intact membranes, J Matern Fetal Neonatal Med 32(4) (2019) 527-541.
[168] R. Romero, J. Espinoza, L.F. Goncalves, J.P. Kusanovic, L.A. Friel, J.K. Nien, Inflammation in preterm and term labour and delivery, Semin Fetal Neonatal Med 11(5) (2006) 317-26.
[169] R. Romero, T. Chaiworapongsa, Z. Alpay Savasan, Y. Xu, Y. Hussein, Z. Dong, J.P. Kusanovic, C.J. Kim, S.S. Hassan, Damage-associated molecular patterns (DAMPs) in preterm labor with intact membranes and preterm PROM: a study of the alarmin HMGB1, J Matern Fetal Neonatal Med 24(12) (2011) 1444-55.
[170] V. Topping, R. Romero, N.G. Than, A.L. Tarca, Z. Xu, S.Y. Kim, B. Wang, L. Yeo, C.J. Kim, S.S. Hassan, J.S. Kim, Interleukin-33 in the human placenta, J Matern Fetal Neonatal Med 26(4) (2013) 327-38.
[171] R. Romero, M. Mazor, H. Munoz, R. Gomez, M. Galasso, D.M. Sherer, The preterm labor syndrome, Ann N Y Acad Sci 734 (1994) 414-29.

[172] Y. Hirota, T. Daikoku, S. Tranguch, H. Xie, H.B. Bradshaw, S.K. Dey, Uterine-specific p53 deficiency confers premature uterine senescence and promotes preterm birth in mice, J Clin Invest 120(3) (2010) 803-15.
[173] R. Romero, J. Espinoza, L.F. Goncalves, J.P. Kusanovic, L. Friel, S. Hassan, The role of inflammation and infection in preterm birth, Semin Reprod Med 25(1) (2007) 21-39.
[174] R. Smith, K. Maiti, R.J. Aitken, Unexplained antepartum stillbirth: a consequence of placental aging?, Placenta 34(4) (2013) 310-3.
[175] J. Cha, Y. Hirota, S.K. Dey, Sensing senescence in preterm birth, Cell Cycle, United States, 2012, pp. 205-6.
[176] F. Behnia, S. Sheller, R. Menon, Mechanistic Differences Leading to Infectious and Sterile Inflammation, Am J Reprod Immunol 75(5) (2016) 505-18.
[177] M. Longini, S. Perrone, P. Vezzosi, B. Marzocchi, A. Kenanidis, G. Centini, L. Rosignoli, G. Buonocore, Association between oxidative stress in pregnancy and preterm premature rupture of membranes, Clin Biochem 40(11) (2007) 793-7.
[178] J.S. Arthur, S.C. Ley, Mitogen-activated protein kinases in innate immunity, Nat Rev Immunol 13(9) (2013) 679-92.
[179] A. Cuenda, S. Rousseau, p38 MAP-kinases pathway regulation, function and role in human diseases, Biochim Biophys Acta 1773(8) (2007) 1358-75.
[180] I. Corre, F. Paris, J. Huot, The p38 pathway, a major pleiotropic cascade that transduces stress and metastatic signals in endothelial cells, Oncotarget 8(33) (2017) 55684-55714.
[181] V. Ruiz-Bonilla, E. Perdiguero, L. Gresh, A.L. Serrano, M. Zamora, P. Sousa-Victor, M. Jardi, E.F. Wagner, P. Munoz-Canoves, Efficient adult skeletal muscle regeneration in mice deficient in p38beta, p38gamma and p38delta MAP kinases, Cell Cycle 7(14) (2008) 2208-14.
[182] J.S. Mudgett, J. Ding, L. Guh-Siesel, N.A. Chartrain, L. Yang, S. Gopal, M.M. Shen, Essential role for p38alpha mitogen-activated protein kinase in placental angiogenesis, Proc Natl Acad Sci U S A 97(19) (2000) 10454-9.
[183] E.A. Bonney, Mapping out p38MAPK, Am J Reprod Immunol 77(5) (2017).
[184] Y. Hadjal, O. Hadadeh, C.E. Yazidi, E. Barruet, B. Binetruy, A p38MAPK-p53 cascade regulates mesodermal differentiation and neurogenesis of embryonic stem cells, Cell Death Dis 4 (2013) e737.
[185] J. Yang, D. Zhang, Y. Yu, R.J. Zhang, X.L. Hu, H.F. Huang, Y.C. Lu, Binding of FGF2 to FGFR2 in an autocrine mode in trophectoderm cells is indispensable for mouse blastocyst formation through PKC-p38 pathway, Cell Cycle 14(20) (2015) 3318-30.
[186] A. Sharma, H. Guan, K. Yang, The p38 mitogen-activated protein kinase regulates 11beta-hydroxysteroid dehydrogenase type 2 (11beta-HSD2) expression in human trophoblast cells through modulation of 11beta-HSD2 messenger ribonucleic acid stability, Endocrinology 150(9) (2009) 4278-86.
[187] R.J. Zuo, Y.C. Zhao, W. Lei, T.S. Wang, B.C. Wang, Z.M. Yang, Crystallin alphaB acts as a molecular guard in mouse decidualization: regulation and function during early pregnancy, FEBS Letters 588(17) (2014) 2944-51.
[188] Y. Takanami-Ohnishi, S. Asada, H. Tsunoda, A. Fukamizu, K. Goto, H. Yoshikawa, T. Kubo, T. Sudo, S. Kimura, Y. Kasuya, Possible involvement of p38

mitogen-activated protein kinase in decidual function in parturition, Biochemical & Biophysical Research Communications 288(5) (2001) 1155-61.
[189] K. Takeda, T. Hatai, T.S. Hamazaki, H. Nishitoh, M. Saitoh, H. Ichijo, Apoptosis signal-regulating kinase 1 (ASK1) induces neuronal differentiation and survival of PC12 cells, J Biol Chem 275(13) (2000) 9805-13.
[190] M. Saitoh, H. Nishitoh, M. Fujii, K. Takeda, K. Tobiume, Y. Sawada, M. Kawabata, K. Miyazono, H. Ichijo, Mammalian thioredoxin is a direct inhibitor of apoptosis signal-regulating kinase (ASK) 1, Embo j 17(9) (1998) 2596-606.
[191] C.S. Yang, D.M. Shin, H.M. Lee, J.W. Son, S.J. Lee, S. Akira, M.A. Gougerot-Pocidalo, J. El-Benna, H. Ichijo, E.K. Jo, ASK1-p38 MAPK-p47phox activation is essential for inflammatory responses during tuberculosis via TLR2-ROS signalling, Cell Microbiol 10(3) (2008) 741-54.
[192] G.F. DeNicola, E.D. Martin, A. Chaikuad, R. Bassi, J. Clark, L. Martino, S. Verma, P. Sicard, R. Tata, R.A. Atkinson, S. Knapp, M.R. Conte, M.S. Marber, Mechanism and consequence of the autoactivation of p38alpha mitogen-activated protein kinase promoted by TAB1, Nat Struct Mol Biol 20(10) (2013) 1182-90.
[193] B. Ge, H. Gram, F. Di Padova, B. Huang, L. New, R.J. Ulevitch, Y. Luo, J. Han, MAPKK-independent activation of p38alpha mediated by TAB1-dependent autophosphorylation of p38alpha, Science 295(5558) (2002) 1291-4.
[194] G. Lu, Y.J. Kang, J. Han, H.R. Herschman, E. Stefani, Y. Wang, TAB-1 modulates intracellular localization of p38 MAP kinase and downstream signaling, J Biol Chem 281(9) (2006) 6087-95.
[195] C.C. Hsieh, J. Papaconstantinou, Dermal fibroblasts from long-lived Ames dwarf mice maintain their in vivo resistance to mitochondrial generated reactive oxygen species (ROS), Aging (Albany NY) 1(9) (2009) 784-802.
[196] C.C. Hsieh, J. Papaconstantinou, Thioredoxin-ASK1 complex levels regulate ROS-mediated p38 MAPK pathway activity in livers of aged and long-lived Snell dwarf mice, Faseb j 20(2) (2006) 259-68.
[197] C.C. Hsieh, M. Kuro-o, K.P. Rosenblatt, R. Brobey, J. Papaconstantinou, The ASK1-Signalosome regulates p38 MAPK activity in response to levels of endogenous oxidative stress in the Klotho mouse models of aging, Aging (Albany NY) 2(9) (2010) 597-611.
[198] A. Nawshad, D. Lagamba, A. Polad, E.D. Hay, Transforming growth factor-beta signaling during epithelial-mesenchymal transformation: implications for embryogenesis and tumor metastasis, Cells Tissues Organs 179(1-2) (2005) 11-23.
[199] M. Kretova, L. Sabova, Z. Hodny, J. Bartek, G. Kollarovic, B.D. Nelson, S. Hubackova, K. Luciakova, TGF-beta/NF1/Smad4-mediated suppression of ANT2 contributes to oxidative stress in cellular senescence, Cell Signal 26(12) (2014) 2903-11.
[200] N. Makeeva, G.M. Roomans, J.W. Myers, N. Welsh, Transforming growth factor-beta-activated protein kinase 1-binding protein (TAB)-1alpha, but not TAB1beta, mediates cytokine-induced p38 mitogen-activated protein kinase phosphorylation and cell death in insulin-producing cells, Endocrinology 149(1) (2008) 302-9.
[201] S.I. Kim, J.H. Kwak, M. Zachariah, Y. He, L. Wang, M.E. Choi, TGF-beta-activated kinase 1 and TAK1-binding protein 1 cooperate to mediate TGF-beta1-induced MKK3-p38 MAPK activation and stimulation of type I collagen, Am J Physiol Renal Physiol 292(5) (2007) F1471-8.

[202] L. Kim, L. Del Rio, B.A. Butcher, T.H. Mogensen, S.R. Paludan, R.A. Flavell, E.Y. Denkers, p38 MAPK autophosphorylation drives macrophage IL-12 production during intracellular infection, J Immunol 174(7) (2005) 4178-84.
[203] J. Polettini, M.G. Silva, M. Kacerovsky, T.A. Syed, G. Saade, R. Menon, Expression profiles of fetal membrane nicotinamide adenine dinucleotide phosphate oxidases (NOX) 2 and 3 differentiates spontaneous preterm birth and pPROM pathophysiologies, Placenta 35(3) (2014) 188-94.
[204] K.J. Livak, T.D. Schmittgen, Analysis of relative gene expression data using real-time quantitative PCR and the 2(-Delta Delta C(T)) Method, Methods 25(4) (2001) 402-8.
[205] G.J. Burton, E. Jauniaux, Oxidative stress, Best Pract Res Clin Obstet Gynaecol 25(3) (2011) 287-99.
[206] K.E. Burnum, Y. Hirota, E.S. Baker, M. Yoshie, Y.M. Ibrahim, M.E. Monroe, G.A. Anderson, R.D. Smith, T. Daikoku, S.K. Dey, Uterine deletion of Trp53 compromises antioxidant responses in the mouse decidua, Endocrinology 153(9) (2012) 4568-79.
[207] R. Menon, J. Papaconstantinou, p38 Mitogen activated protein kinase (MAPK): a new therapeutic target for reducing the risk of adverse pregnancy outcomes, Expert Opin Ther Targets 20(12) (2016) 1397-1412.
[208] W.B. Wu, R. Menon, Y.Y. Xu, J.R. Zhao, Y.L. Wang, Y. Liu, H.J. Zhang, Downregulation of peroxiredoxin-3 by hydrophobic bile acid induces mitochondrial dysfunction and cellular senescence in human trophoblasts, Sci Rep 6 (2016) 38946.
[209] H. Shibuya, K. Yamaguchi, K. Shirakabe, A. Tonegawa, Y. Gotoh, N. Ueno, K. Irie, E. Nishida, K. Matsumoto, TAB1: an activator of the TAK1 MAPKKK in TGF-beta signal transduction, Science 272(5265) (1996) 1179-82.
[210] A. Lanna, S.M. Henson, D. Escors, A.N. Akbar, The kinase p38 activated by the metabolic regulator AMPK and scaffold TAB1 drives the senescence of human T cells, Nat Immunol 15(10) (2014) 965-72.
[211] B. Fiedler, R. Feil, F. Hofmann, C. Willenbockel, H. Drexler, A. Smolenski, S.M. Lohmann, K.C. Wollert, cGMP-dependent protein kinase type I inhibits TAB1-p38 mitogen-activated protein kinase apoptosis signaling in cardiac myocytes, J Biol Chem 281(43) (2006) 32831-40.
[212] R.P. Bhattacharyya, A. Remenyi, M.C. Good, C.J. Bashor, A.M. Falick, W.A. Lim, The Ste5 scaffold allosterically modulates signaling output of the yeast mating pathway, Science 311(5762) (2006) 822-6.
[213] J. Polettini, M.G. Silva, M. Kacerovsky, T.A. Syed, G.R. Saade, R. Menon, Screening of lysyl oxidase (LOX) and lysyl oxidase like (LOXL) enzyme expression and activity in preterm prelabor rupture of fetal membranes, J Perinat Med 44(1) (2016) 99-109.
[214] J.J. Lebrun, The Dual Role of TGFbeta in Human Cancer: From Tumor Suppression to Cancer Metastasis, ISRN Mol Biol 2012 (2012) 381428.
[215] A. Alcaraz, A. Mrowiec, C.L. Insausti, E.M. Garcia-Vizcaino, C. Ruiz-Canada, M.C. Lopez-Martinez, J.M. Moraleda, F.J. Nicolas, Autocrine TGF-beta induces epithelial to mesenchymal transition in human amniotic epithelial cells, Cell Transplant 22(8) (2013) 1351-67.
[216] M.L. Casey, C.A. Winkel, J.C. Porter, P.C. MacDonald, Endocrine regulation of the initiation and maintenance of parturition, Clin Perinatol 10(3) (1983) 709-21.

[217] L. Feng, T.K. Allen, W.P. Marinello, A.P. Murtha, Roles of Progesterone Receptor Membrane Component 1 in Oxidative Stress-Induced Aging in Chorion Cells, Reprod Sci (2018) 1933719118776790.
[218] H. Mogami, A.H. Kishore, R.A. Word, Collagen Type 1 Accelerates Healing of Ruptured Fetal Membranes, Sci Rep 8(1) (2018) 696.
[219] A.B. Caughey, J.N. Robinson, E.R. Norwitz, Contemporary diagnosis and management of preterm premature rupture of membranes, Rev Obstet Gynecol 1(1) (2008) 11-22.
[220] K. Rennie, A. Gruslin, M. Hengstschlager, D. Pei, J. Cai, T. Nikaido, M. Bani-Yaghoub, Applications of amniotic membrane and fluid in stem cell biology and regenerative medicine, Stem Cells Int 2012 (2012) 721538.
[221] L.L. Zhang, X.M. Jiang, M.Y. Huang, Z.L. Feng, X. Chen, Y. Wang, H. Li, A. Li, L.G. Lin, J.J. Lu, Nagilactone E suppresses TGF-beta1-induced epithelial-mesenchymal transition, migration and invasion in non-small cell lung cancer cells, Phytomedicine 52 (2019) 32-39.
[222] A. Ooshima, J. Park, S.J. Kim, Phosphorylation status at Smad3 linker region modulates TGF-beta-induced EMT and cancer progression, Cancer Sci (2018).
[223] A. Canciello, V. Russo, P. Berardinelli, N. Bernabo, A. Muttini, M. Mattioli, B. Barboni, Progesterone prevents epithelial-mesenchymal transition of ovine amniotic epithelial cells and enhances their immunomodulatory properties, Sci Rep 7(1) (2017) 3761.
[224] L. Richardson, C.L. Dixon, L. Aguilera-Aguirre, R. Menon, Oxidative Stress-Induced TGF-beta/TAB1-mediated p38MAPK activation in human amnion epithelial cells, Biol Reprod (2018).
[225] B.L. Sato, E.S. Collier, S.A. Vermudez, A.D. Junker, C.E. Kendal-Wright, Human amnion mesenchymal cells are pro-inflammatory when activated by the Toll-like receptor 2/6 ligand, macrophage-activating lipoprotein-2, Placenta 44 (2016) 69-79.
[226] S.C. Schutte, R.N. Taylor, A tissue-engineered human endometrial stroma that responds to cues for secretory differentiation, decidualization, and menstruation, Fertil Steril 97(4) (2012) 997-1003.
[227] I. Pastushenko, C. Blanpain, EMT Transition States during Tumor Progression and Metastasis, Trends Cell Biol (2018).
[228] K. Gravdal, O.J. Halvorsen, S.A. Haukaas, L.A. Akslen, A switch from E-cadherin to N-cadherin expression indicates epithelial to mesenchymal transition and is of strong and independent importance for the progress of prostate cancer, Clin Cancer Res 13(23) (2007) 7003-11.
[229] S.J. Fortunato, R. Menon, K.F. Swan, T.W. Lyden, Organ culture of amniochorionic membrane in vitro, Am J Reprod Immunol 32(3) (1994) 184-7.
[230] S. Carnevali, S. Petruzzelli, B. Longoni, R. Vanacore, R. Barale, M. Cipollini, F. Scatena, P. Paggiaro, A. Celi, C. Giuntini, Cigarette smoke extract induces oxidative stress and apoptosis in human lung fibroblasts, Am J Physiol Lung Cell Mol Physiol 284(6) (2003) L955-63.
[231] E.A. Wahl, T.L. Schenck, H.G. Machens, J.T. Egana, Acute stimulation of mesenchymal stem cells with cigarette smoke extract affects their migration, differentiation, and paracrine potential, Sci Rep 6 (2016) 22957.

[232] A. Alcaraz, A. Mrowiec, C.L. Insausti, A. Bernabe-Garcia, E.M. Garcia-Vizcaino, M.C. Lopez-Martinez, A. Monfort, A. Izeta, J.M. Moraleda, G. Castellanos, F.J. Nicolas, Amniotic Membrane Modifies the Genetic Program Induced by TGFss, Stimulating Keratinocyte Proliferation and Migration in Chronic Wounds, PLoS One 10(8) (2015) e0135324.
[233] E. Ozalkaya, G. Karatekin, S. Topcuoglu, H.O. Karatepe, T. Hafizoglu, P. Baran, F. Ovali, Neonatology oxidative status in preterm infants with premature preterm rupture of membranes and fetal inflammatuar response syndrome, Pediatr Neonatol 58(5) (2017) 437-441.
[234] K.L. Fink, E.D. Wieben, G.E. Woloschak, T.C. Spelsberg, Rapid regulation of c-myc protooncogene expression by progesterone in the avian oviduct, Proc Natl Acad Sci U S A 85(6) (1988) 1796-800.
[235] K. Sun, L. Myatt, Enhancement of glucocorticoid-induced 11beta-hydroxysteroid dehydrogenase type 1 expression by proinflammatory cytokines in cultured human amnion fibroblasts, Endocrinology 144(12) (2003) 5568-77.
[236] W. Li, W. Wang, R. Zuo, C. Liu, Q. Shu, H. Ying, K. Sun, Induction of pro-inflammatory genes by serum amyloid A1 in human amnion fibroblasts, Sci Rep 7(1) (2017) 693.
[237] Y. Meng, A.P. Murtha, L. Feng, Progesterone, Inflammatory Cytokine (TNF-alpha), and Oxidative Stress (H2O2) Regulate Progesterone Receptor Membrane Component 1 Expression in Fetal Membrane Cells, Reprod Sci 23(9) (2016) 1168-78.
[238] C.J. Gu, F. Xie, B. Zhang, H.L. Yang, J. Cheng, Y.Y. He, X.Y. Zhu, D.J. Li, M.Q. Li, High Glucose Promotes Epithelial-Mesenchymal Transition of Uterus Endometrial Cancer Cells by Increasing ER/GLUT4-Mediated VEGF Secretion, Cell Physiol Biochem 50(2) (2018) 706-720.
[239] L. Browning, M.R. Patel, E.B. Horvath, K. Tawara, C.L. Jorcyk, IL-6 and ovarian cancer: inflammatory cytokines in promotion of metastasis, Cancer Manag Res 10 (2018) 6685-6693.
[240] P. Liu, P. Yang, Z. Zhang, M. Liu, S. Hu, Ezrin/NF-kappaB Pathway Regulates EGF-induced Epithelial-Mesenchymal Transition (EMT), Metastasis, and Progression of Osteosarcoma, Med Sci Monit 24 (2018) 2098-2108.
[241] F. An, Y. Qu, X. Liu, R. Zhong, Y. Luo, Organ-on-a-Chip: New Platform for Biological Analysis, Anal Chem Insights 10 (2015) 39-45.
[242] S.N. Bhatia, D.E. Ingber, Microfluidic organs-on-chips, Nat Biotechnol 32(8) (2014) 760-72.
[243] E.W. Esch, A. Bahinski, D. Huh, Organs-on-chips at the frontiers of drug discovery, Nat Rev Drug Discov 14(4) (2015) 248-60.
[244] L.A. Low, D.A. Tagle, Organs-on-chips: Progress, challenges, and future directions, Exp Biol Med (Maywood) (2017) 1535370217700523.
[245] E.M. Materne, I. Maschmeyer, A.K. Lorenz, R. Horland, K.M. Schimek, M. Busek, F. Sonntag, R. Lauster, U. Marx, The multi-organ chip--a microfluidic platform for long-term multi-tissue coculture, J Vis Exp (98) (2015) e52526.
[246] L. Richardson, J. Gnecco, T. Ding, K. Osteen, L. Rogers, D. Aronoff, R. Menon, Fetal Membrane Organ-On-Chip:
An Innovative Approach to Study Cellular Interactions, *Reproductive Sciences*, 2019.

[247] J.O. Gnecco, Kevin, Compartmentalized Culture of Perivascular Stroma and Endothelial Cells, biomedical engineering society (2017).
[248] K. Duval, H. Grover, L.H. Han, Y. Mou, A.F. Pegoraro, J. Fredberg, Z. Chen, Modeling Physiological Events in 2D vs. 3D Cell Culture, Physiology (Bethesda) 32(4) (2017) 266-277.
[249] M.E. Katt, A.L. Placone, A.D. Wong, Z.S. Xu, P.C. Searson, In Vitro Tumor Models: Advantages, Disadvantages, Variables, and Selecting the Right Platform, Front Bioeng Biotechnol 4 (2016) 12.
[250] S. Sances, R. Ho, G. Vatine, D. West, A. Laperle, A. Meyer, M. Godoy, P.S. Kay, B. Mandefro, S. Hatata, C. Hinojosa, N. Wen, D. Sareen, G.A. Hamilton, C.N. Svendsen, Human iPSC-Derived Endothelial Cells and Microengineered Organ-Chip Enhance Neuronal Development, Stem Cell Reports 10(4) (2018) 1222-1236.
[251] M.W. van der Helm, A.D. van der Meer, J.C. Eijkel, A. van den Berg, L.I. Segerink, Microfluidic organ-on-chip technology for blood-brain barrier research, Tissue Barriers 4(1) (2016) e1142493.
[252] D.D. Huh, A human breathing lung-on-a-chip, Ann Am Thorac Soc 12 Suppl 1 (2015) S42-4.
[253] D. Konar, M. Devarasetty, D.V. Yildiz, A. Atala, S.V. Murphy, Lung-On-A-Chip Technologies for Disease Modeling and Drug Development, Biomed Eng Comput Biol 7(Suppl 1) (2016) 17-27.
[254] Y.S. Zhang, J. Aleman, A. Arneri, S. Bersini, F. Piraino, S.R. Shin, M.R. Dokmeci, A. Khademhosseini, From cardiac tissue engineering to heart-on-a-chip: beating challenges, Biomed Mater 10(3) (2015) 034006.
[255] K.L. Bruner-Tran, J. Gnecco, T. Ding, D.R. Glore, V. Pensabene, K.G. Osteen, Exposure to the environmental endocrine disruptor TCDD and human reproductive dysfunction: Translating lessons from murine models, Reprod Toxicol 68 (2017) 59-71.
[256] J.S. Gnecco, A.P. Anders, D. Cliffel, V. Pensabene, L.M. Rogers, K. Osteen, D.M. Aronoff, Instrumenting a Fetal Membrane on a Chip as Emerging Technology for Preterm Birth Research, Curr Pharm Des 23(40) (2017) 6115-6124.
[257] A.P. Anders, J.A. Gaddy, R.S. Doster, D.M. Aronoff, Current concepts in maternal-fetal immunology: Recognition and response to microbial pathogens by decidual stromal cells, Am J Reprod Immunol 77(3) (2017).
[258] L. Rogers, A. Anjali, R. Doster, J. Gnecco, J. Holley, T. Randis, A. Ratner, J. Gaddy, K. Osten, D. Aronoff, Decidual stromal cell-derived PGE2 regulates macrophage responses to microbial threat, American Journal of Reproductive Immunology (2018).
[259] Y. Abe, H. Sinozaki, T. Takagi, T. Minegishi, K. Kokame, K. Kangawa, M. Uesaka, K. Miyamoto, Identification of 2,3,7,8-tetrachlorodibenzo-p-dioxin (TCDD)-inducible genes in human amniotic epithelial cells, Reprod Biol Endocrinol 4 (2006) 27.
[260] E.L. Sweeney, S.J. Dando, S.G. Kallapur, C.L. Knox, The Human Ureaplasma Species as Causative Agents of Chorioamnionitis, Clin Microbiol Rev 30(1) (2017) 349-379.
[261] R.S. Gibbs, J.D. Blanco, Premature rupture of the membranes, Obstet Gynecol 60(6) (1982) 671-9.
[262] M. Castillo-Castrejon, N. Meraz-Cruz, N. Gomez-Lopez, A. Flores-Pliego, J. Beltran-Montoya, M. Viveros-Alcaraz, F. Vadillo-Ortega, Choriodecidual cells from

term human pregnancies show distinctive functional properties related to the induction of labor, Am J Reprod Immunol 71(1) (2014) 86-93.
[263] A.E. King, R.W. Kelly, J.M. Sallenave, A.D. Bocking, J.R. Challis, Innate immune defences in the human uterus during pregnancy, Placenta 28(11-12) (2007) 1099-106.
[264] J. Park, H. Koito, J. Li, A. Han, Multi-compartment neuron-glia co-culture platform for localized CNS axon-glia interaction study, Lab Chip 12(18) (2012) 3296-304.
[265] K. Pomduk, P. Kheolamai, U.P. Y, M. Wattanapanitch, N. Klincumhom, S. Issaragrisil, Enhanced human mesenchymal stem cell survival under oxidative stress by overexpression of secreted frizzled-related protein 2 gene, Ann Hematol 94(2) (2015) 319-27.
[266] J. Park, H. Koito, J. Li, A. Han, Microfluidic compartmentalized co-culture platform for CNS axon myelination research, Biomed Microdevices 11(6) (2009) 1145-53.
[267] S.W. Xiao, Teresa, A microfluidic culture model of the human reproductive tract and 28-day menstrual cycle, Nature Communications (2017).
[268] J.S. Lee, R. Romero, Y.M. Han, H.C. Kim, C.J. Kim, J.S. Hong, D. Huh, Placenta-on-a-chip: a novel platform to study the biology of the human placenta, J Matern Fetal Neonatal Med 29(7) (2016) 1046-54.
[269] M. Bogusiewicz, T. Rechberger, P. Skorupski, K. Postawski, J.A. Jakowicki, Local collagen turnover in human foetal membranes during full term vaginal delivery, Eur J Obstet Gynecol Reprod Biol 77(2) (1998) 141-3.
[270] L.F. Stinson, D.J. Ireland, M.W. Kemp, M.S. Payne, S.J. Stock, J.P. Newnham, J.A. Keelan, Effects of cytokine-suppressive anti-inflammatory drugs on inflammatory activation in ex vivo human and ovine fetal membranes, Reproduction 147(3) (2014) 313-20.
[271] M. Suarez-Carmona, J. Lesage, D. Cataldo, C. Gilles, EMT and inflammation: inseparable actors of cancer progression, Mol Oncol (2017).
[272] C. Zhou, J. Liu, Y. Tang, X. Liang, Inflammation linking EMT and cancer stem cells, Oral Oncol 48(11) (2012) 1068-75.
[273] Y. Liu, X. Yuan, W. Li, Q. Cao, Y. Shu, Aspirin-triggered resolvin D1 inhibits TGF-beta1-induced EMT through the inhibition of the mTOR pathway by reducing the expression of PKM2 and is closely linked to oxidative stress, Int J Mol Med 38(4) (2016) 1235-42.
[274] X. Luan, K. Sansanaphongpricha, I. Myers, H. Chen, H. Yuan, D. Sun, Engineering exosomes as refined biological nanoplatforms for drug delivery, Acta Pharmacol Sin 38(6) (2017) 754-763.
[275] W.H. De Jong, P.J. Borm, Drug delivery and nanoparticles:applications and hazards, Int J Nanomedicine 3(2) (2008) 133-49.
[276] L. Sercombe, T. Veerati, F. Moheimani, S.Y. Wu, A.K. Sood, S. Hua, Advances and Challenges of Liposome Assisted Drug Delivery, Front Pharmacol 6 (2015) 286.